

Copyright

by

Nicholas James Durr

2010

**THE DISSERTATION COMMITTEE FOR NICHOLAS JAMES DURR
CERTIFIES THAT THIS IS THE APPROVED VERSION OF THE FOLLOWING
DISSERTATION:**

**NONLINEAR IMAGING WITH ENDOGENOUS
FLUORESCENCE CONTRAST AND PLASMONIC
CONTRAST AGENTS**

Committee:

Adela Ben-Yakar, Supervisor

Konstantin Sokolov

James Tunnell

Michael Downer

Hans Gerritsen

**NONLINEAR IMAGING WITH ENDOGENOUS
FLUORESCENCE CONTRAST AND PLASMONIC
CONTRAST AGENTS**

by

NICHOLAS JAMES DURR, B.S.; M.S.

DISSERTATION

Presented to the Faculty of the Graduate School of

The University of Texas at Austin

in Partial Fulfillment

of the Requirements

for the Degree of

DOCTOR OF PHILOSOPHY

THE UNIVERSITY OF TEXAS AT AUSTIN

DECEMBER 2010

Acknowledgements

I would like to thank my advisor, Dr. Adela Ben-Yakar, for her enthusiasm, support, and guidance over the course of my dissertation research. Her creativity, desire for excellence, and boldness in venturing into new research areas have been a great source of motivation for me. I would also like to thank all my committee members, particularly Dr. Konstantin Sokolov for his insight in our gold nanorod collaboration, and Dr. Hans Gerritsen, for graciously hosting me as a visiting researcher in his lab. All the graduate students and post-docs of the Ben-Yakar Group also deserve special acknowledgement. Whether it was standing by a chalkboard, working through the night, or toobing down the river—just as your talents and intelligence were essential to me finishing my degree, your camaraderie and humor were crucial to my happiness in Austin. I had a wonderful time working with all of you and hope our friendships will be lifelong.

NONLINEAR IMAGING WITH ENDOGENOUS FLUORESCENCE CONTRAST AND PLASMONIC CONTRAST AGENTS

Publication No. _____

Nicholas James Durr, Ph.D.

The University of Texas at Austin, 2010

Supervisor: Adela Ben-Yakar

Fluorescence from endogenous molecules and exogenous contrast agents can provide morphological, spectral, and lifetime contrast that indicates disease state in epithelial tissues. Recently, nonlinear microscopy has emerged as a potential tool for the early detection, case-finding, and monitoring of epithelial cancers because it permits non-invasive, three-dimensional fluorescence imaging of subcellular features hundreds of microns deep. This dissertation explores the use of nonlinear microscopy for cancer diagnostics on two fronts: (1) we examine the fundamental limitations governing the maximum nonlinear imaging depth in epithelial tissues, and (2) we investigate the use of a new class of nonlinear contrast agent—plasmonic gold nanoparticles—for molecularly specific imaging of cancer cells.

We built and optimized a nonlinear microscope for deep tissue imaging, and studied the image contrast as a function of imaging depth in *ex-vivo* human biopsies and tissue phantoms. With this system we demonstrated imaging down to 370 μm deep in a

human biopsy, which is significantly deeper than imaging depths achieved in comparable studies. We found that the large scattering coefficient and homogenous fluorophore distribution typical of epithelial tissues limit the maximum imaging depth to 3-5 mean free scattering lengths deep in conventional nonlinear microscopy. Beyond this imaging depth, the increasing contribution of out-of-focus emission limits the contrast to insufficient levels for diagnostic imaging. We support these observations with time-dependent Monte Carlo simulations.

We exploited the intense interaction of gold nanoparticles with light, enhanced by surface plasmon resonance effects, to create extremely bright nonlinear contrast agents. These contrast agents proved to be several orders of magnitude brighter than the brightest organic fluorophores and at least one order of magnitude brighter than quantum dots. We targeted gold nanoparticles to a biomarker for carcinogenesis and demonstrated molecularly specific imaging of cancer cells. We demonstrated that unlike emission from traditional bandgap fluorophores, nonlinear luminescence from gold nanoparticles was weakly dependent on excitation pulse length for short pulse durations. This finding supports the hypothesis that nonlinear excitation in plasmonic nanoparticles involves sequential rather than simultaneous absorption of excitation photons. The remarkable brightness of gold nanoparticles makes them an attractive contrast agent for nonlinear diagnostics.

Table of Contents

List of Tables	xi
List of Figures	xii
Chapter 1 Introduction.....	1
1.1. Dissertation overview	2
Chapter 2 Background	4
2.1. Epithelial tissue and carcinoma	4
2.2. Techniques for epithelial cancer imaging	7
2.3. Optical properties of epithelial tissues	9
2.4. Nonlinear luminescence	12
2.5. Nonlinear microscopy	15
2.6. Sources of contrast in nonlinear optical imaging	15
2.7. Plasmonic nanoparticles	17
2.7.1. Surface plasmon resonance	17
2.7.2. Gold nanoparticles as biomedical contrast agents	19
2.7.3. Multiphoton luminescence from plasmonic nanoparticles	20
Chapter 3 Design and characterization of nonlinear scanning microscope for deep tissue imaging	22
3.1. Overview	22
3.2. Excitation path	24
3.2.1. Excitation source	24
3.2.2. Laser scanning system	25
3.2.3. Objective lens	26
Resolution	27
Field of View	28
Olympus XLUMPFL Objective	29
3.3. Focal volume characterization	30
3.3.1. Spatial intensity distribution	30

3.3.2. Temporal characterization	33
3.4. Collection path	34
3.5. Example images	37
3.5.1. Phantoms	37
3.5.2. Three dimensional rendering of healthy tissue biopsies	38
3.5.3. Comparison of normal and cancerous biopsy	39
Chapter 4 A Monte Carlo model for out-of-focus fluorescence generation in two-photon microscopy	41
4.1. Introduction	41
4.2. Monte Carlo vs. analytical approach	43
4.3. Overview of Monte Carlo model	45
4.4. Excitation simulation	46
4.4.1. Focusing	46
4.4.2. Temporal dependence	54
4.5. Collection	54
4.6. Implementation	56
Chapter 5 Deep two-photon autofluorescence microscopy of epithelial tissues	57
5.1. Introduction	57
5.2. Methods	61
5.2.1. 2PAM contrast	61
5.2.2. 2PAM system	63
5.2.3. Monte Carlo model	65
5.2.4. Analytical model	65
5.2.5. Tissue phantom preparation	66
5.2.6. Biopsy preparation	68
5.3. Results and discussion	68
5.3.1. Monte Carlo simulation	68
5.3.2. Phantom imaging	70
5.3.3. Fluorescence decay	75
5.3.4. Contrast decay	78

5.3.5. Human biopsy imaging	80
5.3.6. Fluorescence saturation and photobleaching	83
5.3.7. Maximum imaging depth	85
5.4. Conclusions.....	89
Chapter 6 Multiphoton-induced luminescence from gold nanoparticles	90
6.1. Introduction.....	90
6.2. Nomenclature of gold nanoparticle samples.....	91
6.3. Physical properties	92
6.4. Linear optical properties	96
6.4.1. Absorption and scattering cross sections	96
Measurements.....	96
Simulations.....	97
6.4.2. Absorption and scattering coefficients.....	101
6.5. Calculation of nanoparticle concentrations.....	102
6.6. Nonlinear luminescence properties.....	104
6.6.1. Experimental setup.....	104
Excitation source and power attenuator	106
Pulse stretcher/compressor and autocorrelator.....	106
Laser scanning microscope	108
Sample.....	109
Spectrometer/PMT	110
6.6.2. Spectral features of nanoparticle luminescence	113
6.6.3. Dependence of MPL on excitation intensity.....	115
6.6.4. Dependence of MPL on pulse duration	124
Qualitative description	124
Mathematical description	126
Experimental results.....	129
6.6.5. Quantification of two-photon action cross section	135
Theoretical development.....	136
Collection efficiency	138

Measurement of the two-photon action cross section by reference standard	141
Results	143
Comparison of σ_{TPA} to previous reports	147
6.6.6. Polarization dependence	149
Setup	149
Linear polarization	150
Circular Polarization	151
6.7. Conclusion	152
Chapter 7 Nonlinear imaging of cancer cells with plasmonic contrast agents.....	155
7.1. Preparation of contrast agents	155
7.1.1. CTAB coated gold nanorods.....	155
7.1.2. PEGylated gold nanorods	156
7.1.3. Nanospheres	157
7.2. Sample preparation	158
7.2.1. Tissue phantoms.....	158
7.3. Imaging systems.....	158
7.4. Single layer of labeled cancer cells.....	159
7.4.1. Brightness characterization.....	159
7.4.2. Signal from nanoparticle agglomerates	161
7.4.3. Labeling with PEGylated gold nanorods	162
7.4.4. Optical properties of labeled gold nanorods	164
Dependence of MPL on excitation fluence	165
Dependence of MPL on excitation polarization.....	167
7.5. GNP-Labeled tissue phantoms.....	167
7.6. Biocompatibility	171
Chapter 8 Conclusions and future directions.....	174
References.....	179
Vita.....	197

List of Tables

Table 2.1: High resolution three-dimensional imaging techniques.	9
Table 4.1: Parameters for different focusing schemes.	52
Table 5.1: Measured decay constant compared to phantom mean free scattering length.	77
Table 6.1: Measured nanoparticle dimensions.	96
Table 6.2: Calculated linear absorption and scattering cross sections.	101
Table 6.3: Nanoparticle molar extinction coefficients and concentrations.	104
Table 6.4. Parameters used in calculating absolute emission counts for fluorescein.	140
Table 6.5 Two-photon action cross sections of gold nanorods and other nanoparticles.	149

List of Figures

Figure 2.1: Histology of Stratified Epithelial Tissue.....	6
Figure 2.2: Absorption and scattering mean free path length in the epithelium.....	12
Figure 2.3: Jablonski diagram of one and two photon excited fluorescence and second harmonic generation.....	13
Figure 2.4: Surface plasmon resonance in gold nanospheres and gold nanorods.....	19
Figure 3.1: An upright laser scanning microscope for deep nonlinear imaging.....	23
Figure 3.2: Schematic of laser scanning system.....	26
Figure 3.3: Layout of Olympus Objective.....	30
Figure 3.4: Spatial and Temporal Characterization of the Focal Spot.....	32
Figure 3.5: Optimization of collection optics.....	37
Figure 3.6: Large field of view imaging of unlabeled cancer cells and high magnification view of gold nanorod labeled cells.....	38
Figure 3.7: Autofluorescence and second harmonic generation imaging in an ex-vivo human biopsy.....	39
Figure 3.8: Two-photon autofluorescence images of normal and cancerous biopsy.....	40
Figure 4.1: Qualitative illustration of signal and background two-photon excited fluorescence.....	42
Figure 4.2: Qualitative illustration of different focusing strategies.....	48
Figure 4.3: Parameters describing Gaussian beam focusing in our Monte Carlo simulation.....	50
Figure 4.4: R value vs. r_s for different focusing schemes in a transparent medium.....	53
Figure 4.5: Collection simulation parameters.....	56
Figure 5.1: Schematic of two-photon imaging system collection path.....	64
Figure 5.2: Monte Carlo results for imaging 400 μm deep in $l_s = 80 \mu\text{m}$ tissue.....	69
Figure 5.3: XZ cross sections of phantoms and biopsy.....	72
Figure 5.4: Measured bead size vs depth.....	74
Figure 5.5: Fluorescence signal and background decays.....	76
Figure 5.6: Contrast decays.....	79
Figure 5.7: Biopsy images.....	81
Figure 5.8: Photobleaching test.....	85

Figure 5.9: Maximum imaging depth summary.	88
Figure 6.1: TEM images of nanoparticle samples.	93
Figure 6.2: TEM Image processing sequence for characterizing size distribution of GNR780.	94
Figure 6.3: Plot of measured lengths and widths of GNR780 nanoparticles.	95
Figure 6.4: Measured linear absorbance of gold nanoparticle samples.	97
Figure 6.5: Comparison of measured and simulated absorbance for GNR780.	100
Figure 6.6: Nonlinear optical properties experimental setup.	105
Figure 6.7: Focal plane pulse duration as a function of stretcher position.	108
Figure 6.8: Spectrometer system response and calibration.	112
Figure 6.9: Spectral features of MPL in nanospheres and nanorods	114
Figure 6.10: Nonlinear emission profile of fluorescein	117
Figure 6.11: Nonlinear emission profile of GNR780	119
Figure 6.12: Measured slope vs. λ_x for fluorescein and nanoparticle samples.	122
Figure 6.13: MPL vs. average excitation power for GNR780 detected with PMT.	123
Figure 6.14: Second harmonic generation signal from 160 nm diameter gold nanospheres.	124
Figure 6.15: Band structure of gold near the X and L symmetry points showing sequential one photon absorption.	126
Figure 6.16: MPL vs. excitation intensity and pulse duration for fluorescein and GNR780.	130
Figure 6.17: Comparison of experiment and model for MPL vs τ_p	131
Figure 6.18: Nonlinear order observed in GNR780 at $\lambda_x = 780$ nm versus pulse duration.	132
Figure 6.19: Nonlinear absorption coefficient (β) dependence on pulse duration.	133
Figure 6.20: Simulated MPL rates vs. pulse duration and excitation power for sequential nonlinear absorption.	134
Figure 6.21: Determination of effective collection angle.	138
Figure 6.22: Measured vs. predicted emission counts of fluorescein.	140
Figure 6.23: Validation of reference fluorophore technique for calculating σ_{TPA}	144
Figure 6.24: Measured two-photon action cross sections of gold nanoparticles	145

Figure 6.25: Absolute, area-normalized, and volume normalized σ TPA of gold nanoparticles	147
Figure 6.26: Dependence of MPL on excitation polarization--GNR780 on coverslip. ...	151
Figure 6.27: Determining orientation of gold nanorods from polarization dependence.	152
Figure 7.1: Properties of the CTAB-coated gold nanorods used as contrast agents.	156
Figure 7.2: MPL images of GNR754 labeled and unlabeled A431 cancer cells.	160
Figure 7.3: Wide-field white light and MPL images of non-specifically labeled GNR754 clusters with cells.	162
Figure 7.4: GNR808p labeling of A468 cancer cells.	163
Figure 7.5: Sample movement correction algorithm.	165
Figure 7.6: MPL vs. I_p for GNR808p on a coverslip and labeled to cells.	166
Figure 7.7: Polarization dependence of GNR808p labeled to cells.	167
Figure 7.8: 2PAM and MPL images of tissue phantom.	168
Figure 7.9: Deep MPL imaging in tissue phantom.	170
Figure 7.10: MTT assay after incubation with GNS, GNR, and GNRp.	173

Chapter 1

Introduction

‘Optical biopsy’, as defined over a decade ago as “imaging tissue microstructure at or near the level of histopathology without the need for tissue excision,” [1] remains one of the holy grails of the field of biomedical optics. The conventional excision biopsy is an invasive technique, fraught with high failure rates, patient morbidity, and cost. A tool to compliment, or perhaps replace, even a small fraction of the many biopsies performed each year has the potential to make a dramatic impact on clinical medicine.

Shortly after the first demonstration of nonlinear microscopy by Denk, Strickler, and Webb in 1990[2], its utility in the three-dimensional imaging of living skin was realized[3]. Within the last couple of years, two-photon autofluorescence microscopy (2PAM) has entered the clinic, and *in-vivo* nonlinear images of human skin are now being explored for their diagnostic potential[4],[5]. Several naturally occurring fluorophores provide morphological contrast of the tissue microstructure of human skin[6],[7]. With nonlinear imaging, these fluorophores can be visualized at high resolution, to approximately 150 μm deep[3],[8-10]. However, the epithelium can be several hundreds of microns thick. After a decade of innovation in laser and detector technology, imaging speed, and endoscopic techniques, the limited maximum imaging depth of 2PAM remains as one the hurdles to its translation into a clinically relevant tool for optical biopsy. Though the maximum imaging depth achievable in nonlinear imaging has been studied in stained brain tissue[11], the extension of these results to samples with more scattering and a more diffuse fluorophore distribution, such as that encountered in 2PAM of human skin, has yet to be explored. The first part of this dissertation contributes

to the understanding of the parameters and fundamental limitations that influence the maximum imaging depth in 2PAM of epithelial tissues.

While tissue autofluorescence has the potential to provide some functional contrast, the addition of molecularly-targeted contrast agents allows nonlinear imaging to probe a wide range of important biomarkers. Furthermore, using bright contrast agents instead of the dim endogenous fluorophores can enable imaging in less efficient, more clinically relevant nonlinear endoscopes[12-15]. Towards this goal, the second part of this dissertation focuses on the characterization and application of a new class of extremely bright nonlinear probes—plasmonic contrast agents. Using gold nanoparticles, we demonstrate that plasmonic contrast agents can be used for high-contrast, molecularly-specific imaging of cancer cells at low excitation powers.

1.1. DISSERTATION OVERVIEW

The motivation for the project, as well as the fundamental concepts involved in nonlinear imaging with autofluorescence contrast and with plasmonic contrast agents are presented in Chapter 2. The anatomy and optical properties of epithelial tissue are also discussed, along with a comparison of current imaging modalities for high resolution non-invasive imaging of the epithelium.

Chapter 3 presents the design of a nonlinear microscope for deep imaging in epithelial tissues. Particular attention is paid to the objective lens considerations and a detailed optimization of the collection optics is discussed. The spatial and temporal properties of the focal volume in our nonlinear microscope are characterized. Finally, some example images of cancer cell phantoms and fresh human biopsies are presented.

Chapter 4 details the implementation of a Monte Carlo model to simulate the intensity distribution resulting from a focused pulse of light in turbid media. The

calculated intensity distribution is used to estimate the effect of background fluorescence on two-photon imaging contrast.

Chapter 5 experimentally demonstrates the contrast decay resulting from increased background fluorescence as imaging depth is increased in phantoms and in a human biopsy. These results are compared to the Monte Carlo model developed in Chapter 4. The implications for the maximum imaging depth in conventional two-photon autofluorescence microscopy are also discussed.

Chapter 6 presents a detailed study on the optical properties of multiphoton luminescence from gold nanospheres and gold nanorods. The multiphoton luminescence response to changes in excitation intensity, wavelength, polarization, and pulse duration are explored and the relative brightness of several different gold nanoparticle samples is quantified.

Chapter 7 puts gold nanoparticles to practical use as nonlinear contrast agents. Gold nanorods and nanospheres are used as molecularly specific contrast agents for imaging cultured human cancer cells. Images of single layers of cells as well as three dimensional phantoms are presented. Finally, the biocompatibility of several species of nanoparticles is compared.

Chapter 2 Background

2.1. EPITHELIAL TISSUE AND CARCINOMA

In 2007, one in eight deaths worldwide was caused by cancer, making it the second leading cause of death after heart disease[16]. More than 85% of all cancers begin as precancerous lesions that are confined to the superficial region of the skin, which is typically only a few hundreds of microns thick[17]. It is well-known that the early detection of these lesions can dramatically decrease morbidity and mortality[18]. However, of the currently used clinical imaging modalities, none have sufficient resolution and sensitivity to detect tumors less than a few cubic centimeters in volume ($\sim 10^9$ cells)[19]. Optical technologies can easily exceed this resolution but are limited in imaging depth. However, given the large prevalence of cancer in superficial regions of the body, optical technologies have the potential to aid in case-finding and monitoring of carcinoma.

The skin and its appendages make up the largest organ in the human body. The outermost layer, called the epithelium, can be composed of one or many layers of cells. In the outer layers of the body, the epithelium is most commonly stratified, and generally composed of four layers [Figure 2.1]. The outermost layer, the *stratum corneum*, consists of flat dead cells and can be many cell layers thick. This region of the tissue has high levels of keratin filaments and lipids. The *stratum granulosum* is a thin layer of live cells below the *stratum corneum*. Below this layer is the *stratum spinosum*, which synthesizes the keratin. Both the *stratum granulosum* and *stratum spinosum* are polygonal shaped. The deepest level of the epithelium is the *stratum basale*, which (in healthy tissue) is composed of a single layer of columnar or cuboidal cells which rest on the basement

membrane. The epithelium is constantly being renewed, as the cells from the basal layer differentiate outward, and dead cell layers in the *stratum corneum* are lost. Below this basement membrane is the dermis, which is composed of connective tissue, including high concentrations of collagen fibers.

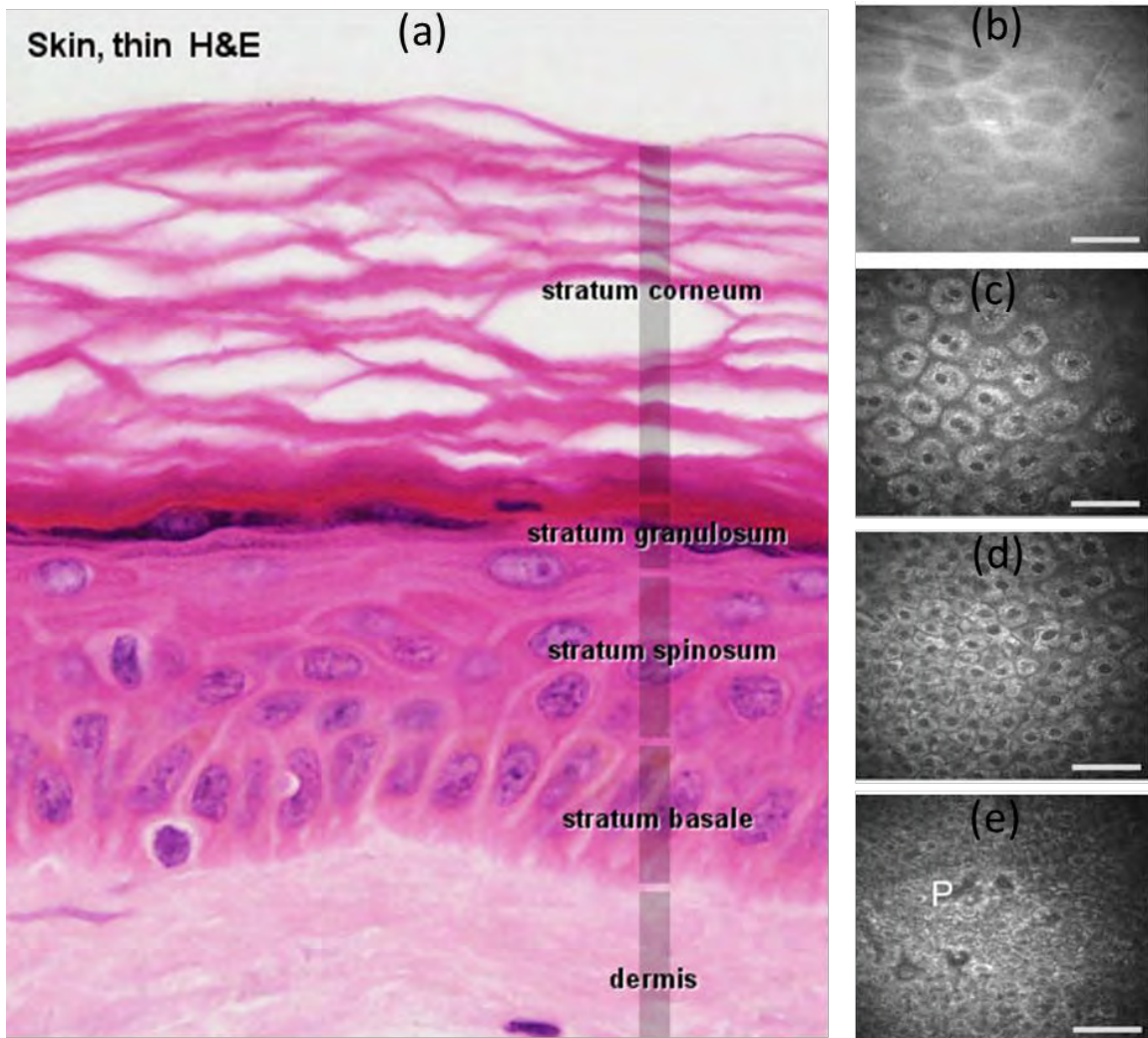


Figure 2.1: Histology of Stratified Epithelial Tissue.

Thin skin is generally composed of 4 different layers of cells: the *stratum corneum* (SC), *stratum granulosum* (SG), *stratum spinosum* (SS), and *stratum basale* (SB). The total thickness can range from a few cell layers, to many hundreds of microns. (a) H&E histology of thin skin slice [20]. Multiphoton autofluorescence lateral images of (b) SC, (c) SG, (d) SP, and (e) SB taken from unspecified depths within 150 μm of the tissue surface[4]. 'P' denotes a breakthrough of the dermal papillae in the field of view. Scale bars are 40 μm . Note that (a) and (b)-(e) are from different samples.

The *stratum spinosum* and *stratum basale* layer are of particular interest for early cancer detection because carcinoma originates and is often most clearly distinguished from normal tissue at these layers[17],[21],[22]. As these layers are sometimes several

hundreds of microns below the surface, it is important for any imaging modality to be used in cancer management to reach at least a few hundred microns deep.

2.2. TECHNIQUES FOR EPITHELIAL CANCER IMAGING

The most commonly used gold standard for carcinoma evaluation is histopathology of an excised biopsy, usually initiated by visual inspection. This is a time-consuming, invasive, and costly procedure. For a histology sample, the tissue is sliced so that the histopathologist can view the depth-resolved structure of the sample. The diagnosis is then based on both the microscopic and macroscopic structure of the tissue. Ideally, alternative techniques for monitoring cancer would then provide three-dimensional, or at least depth-resolved imaging, as well as microscopic resolution and large field of views.

There are several imaging modalities in the research phase that meet these requirements and none are without disadvantages. High frequency ultrasound (HFUS) can image ~ 7 mm deep in skin, but provides a maximum resolution of hundreds of microns. High resolution magnetic resonance imaging (MRI) can reach ~ 100 μm resolution and image the entire body. However, it suffers from being an expensive, time consuming technique, which, along with its poor resolution, make it impractical for replacing biopsy in its current state.

Among optical technologies, confocal microscopy (CM) provides sub- μm lateral resolution, and ~ 1 μm axial resolution, and allows three-dimensional imaging down to tens of microns with autofluorescence contrast, and several hundreds of microns with scattering or exogenous fluorescence contrast[23-26]. Mauna Kea[®] has recently begun selling a commercial device for clinical confocal endoscopy for epithelial tissue imaging[27],[28]. High resolution optical coherence tomography (OCT) provides ~ 10 μm

lateral and sub- μm axial resolution and has the additional advantages of being extremely fast and able to image more than 1 mm deep in epithelial tissues. OCT has found growing success in intravascular imaging over the last decade, and is now being applied towards epithelial tissue imaging (Michelson Diagnostics[©])[5]. However, contrast in OCT is limited to scattering, and convincing subcellular-resolution imaging of epithelial cells has yet to be demonstrated[5],[29]. Photoacoustic imaging (PA) can image several millimeters deep in epithelial tissues but only reaches 50-100 μm resolution and is limited to optical absorption contrast[30],[31].

The focus of this dissertation is on nonlinear microscopy (NM). NM can reach several hundreds of microns deep in epithelial tissue and maintain resolutions less than 1 μm laterally and ~ 1 μm axially. Thus this technique exceeds the resolution of each technique described previously with the exception of CM. In comparison to CM, NM offers equivalent resolution and significantly deeper imaging capabilities when relying on fluorescence contrast. A comparison of the 6 high resolution imaging modalities discussed here is summarized in Table 2.1. A detailed discussion of the achievable imaging depths in NM is presented in Chapter 5.

	HFUS	MRI	OCT	PA	CM	NM
Lateral Resolution	200 μm	25-100 μm	5 μm	50 μm	0.5 μm	0.5 μm
Axial Resolution	200 μm	25-100 μm	< 1 μm	20 μm	1.5 μm	1.5 μm
Contrast	Density	Density	Scattering	Absorbance	Fluorescence, Scattering	Fluorescence, Harmonic Scattering
Imaging Depth Endogenous Contrast	7 mm	Full body	2-3 mm	5 mm	400 μm scattering <100 μm autofluorescence	300 μm
Imaging Depth with contrast agent	7 mm	Full body	2-3 mm	5 mm	400 μm	600 μm

Table 2.1: High resolution three-dimensional imaging techniques.

HFUS: High frequency ultrasound, MRI: Magnetic resonance imaging, OCT: Optical coherence tomography, PA: Photoacoustic imaging, CM: Confocal microscopy, NM: nonlinear microscopy.

In summary, there are several different techniques that are potential suitable to assist or perhaps eventually replace the need for biopsies. All have benefits and drawbacks and several are now being pursued commercially. Only NM has the ability to provide sufficient imaging depth to image the entire epithelium while imaging endogenous fluorescence with subcellular resolution. One major limitation of NM is the limited imaging depth, but at several hundred microns, this may be sufficient for some applications in carcinoma imaging.

2.3. OPTICAL PROPERTIES OF EPITHELIAL TISSUES

The optical properties of the epithelium strongly influence the resolution and imaging depths achievable in the optical imaging modalities discussed in the previous

section. There are generally four parameters that are used to characterize the bulk optical properties of biological tissues[32]. The index of refraction, n , describes the relative speed of light in the sample. The scattering coefficient, μ_s , and absorption coefficient, μ_a , describe the average number of scattering and absorption events seen by a photon per unit length. In this dissertation, the inverse of these parameters is more commonly used—the mean free scattering and absorption length, l_s and l_a , which describe the average path length a photon traverses between scattering and absorbing events, respectively. Lastly, the scattering anisotropy, g , describes the average angle at which the scattered photon propagates relative to its initial direction. A g of 1 means the scattered light is entirely forward scattering while a g of 0 indicates the scattered light is scattered equally in all directions.

For some applications, such as diffuse imaging and phototherapy, the total photon fluence reaching a target is most important to achieve the desired outcome, regardless of temporal or spatial coherence of the incident light. In these applications, photon scattered at a small angle might have a similar effect as the ballistic photons, and the more relevant scattering parameter is the transport corrected scattering length, $l'_s = (1 - g)^{-1}l_s$. This parameter describes the average length a photon travels before it is pointing in approximately a random direction. For tissue microscopy, however, the traditional scattering length, l_s , is more intimately related to imaging performance, as even photons scattered at a small angle will miss the micron-sized focal spot.

Each of the four bulk tissue optical parameters are wavelength dependent and vary between tissue type, site, patient, and even by layer within the tissue. In epithelial tissue, n typically ranges from 1.34 to 1.43 at the basal layer and upper dermis, from 1.36 to 1.43 in the intermediate epithelial layers, and from 1.45 to 1.49 in the *stratum corneum*[33-35]. Scattering in epithelial tissues is typically highly forward scattering, and

g values in the range of 0.8 to 0.9 are typically reported[32],[33]. Relative to g and n , the l_s and l_a of epithelial tissues are a much stronger functions of wavelength, and much more variation in these parameters has been reported in the literature. Generally, the total mean free path of a visible or near-infrared photon (NIR) is dominated by scattering, and l_a is one to two orders of magnitude larger than l_s . The mean free path lengths are largest in the NIR wavelength range, between 700 and 1400 nm. Using a g of 0.8, we can extract l_s and l_a from the data measured in healthy and cancerous tissue by Salomatina et. al.[36] [Figure 2.2]. At 780 nm, a wavelength commonly used in NM, the epithelium has an l_s that ranges from approximately 40~120 μm and an l_a of several millimeters.

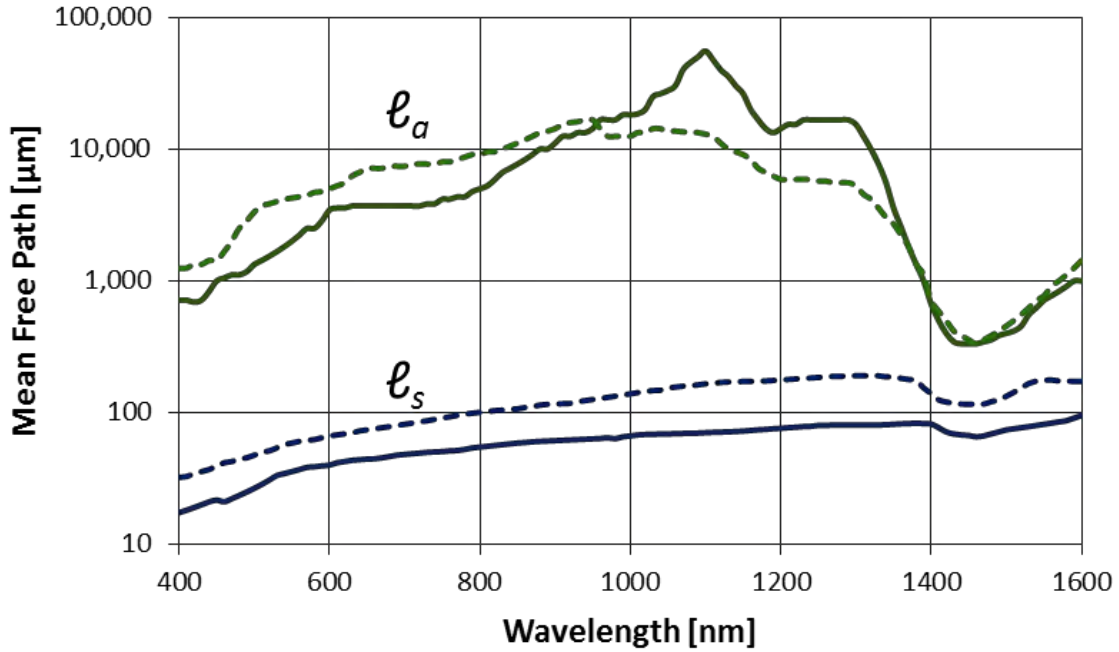


Figure 2.2: Absorption and scattering mean free path length in the epithelium. The mean free scattering length, l_s is much smaller than the mean free absorption length, l_a , and peaks in the near-infrared wavelength range. Solid lines are from normal tissue, dashed lines are from basal cell carcinoma (calculated from Salomatina et. al. using a g of 0.8 [36]).

2.4. NONLINEAR LUMINESCENCE

In linear imaging modalities, the output signal is linearly proportional to the input intensity. In one photon excited fluorescence (1PEF) confocal microscopy, for instance, doubling the excitation intensity produces twice as much fluorescence signal. Conversely, the signal in nonlinear imaging modalities does not change linearly with input intensity. This work focuses primarily on nonlinear imaging with two-photon excited fluorescence (2PEF) and multiphoton-induced luminescence (MPL). In a few cases, we also present some nonlinear images with second harmonic generation (SHG) contrast. 1PEF, 2PEF,

and SHG are described in this section. MPL is introduced here, but discussed in greater detail in Chapter 6.

The processes involved 1PEF, 2PEF, and SHG are illustrated in a Jablonski diagram below [Figure 2.3]. In 1PEF, a high energy photon excites an electron from a ground state, through a bandgap, to an excited state. The excited electron undergoes nonradiative decay and, for bright fluorophores, stays in the excited state for timescales in the nanosecond range. Some percentage of excited electrons will emit a lower energy photon as they return to the ground state. Generally, a longer lifetime in the excited state results in a higher fraction of emission photons produced for each excitation photon absorbed. This fraction is called the quantum yield of the fluorophore.

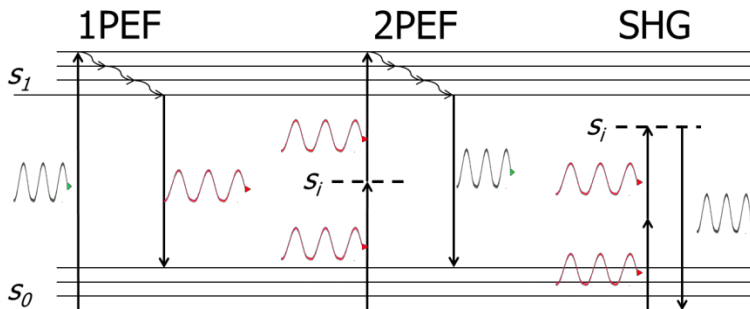


Figure 2.3: Jablonski diagram of one and two photon excited fluorescence and second harmonic generation.

One photon excited fluorescence (1PEF) involves excitation of an electron from the ground state, s_0 , to an excited state, s_1 , from the absorbance of a high energy photon, and the emission of a lower energy photon. Two-photon excited fluorescence (2PEF) involves the excitation of an electron from the simultaneous absorption of two low energy photons through a virtual intermediate state (s_i) and the emission of a higher energy photons. In second harmonic generation (SHG), two photons simultaneously interact with a sample to produce a photon with exactly twice the energy of the excitation photons.

In 2PEF, two lower energy excitation photons “simultaneously” interact with a ground state electron. This process can be thought of as excitation via a very short lifetime intermediate (“virtual”) state. The time scale of interaction necessary for

simultaneous absorption, referred to as the virtual lifetime, τ_i , can be approximated by the Heisenberg relationship[37]:

$$\tau_i = \frac{\hbar}{2\Delta E} \quad (2.1)$$

where \hbar is Planck's constant divided by 2π and ΔE is the energy difference between the excited and ground state. For a 3 eV bandgap (corresponding to the energy of a single photon with a wavelength of 400 nm), τ_i is on the order of 0.1 fs. SHG is an elastic process involving the simultaneous interaction of two low energy photons to produce a photon of exactly twice the excitation photons. Both 2PEF and SHG require two photons to produce luminescence, thus, both processes are quadratically dependent on excitation photon flux. As excitation intensity is doubled, four times as much luminescence is produced.

We use a different term, MPL, to describe nonlinear luminescence originating from gold nanoparticles than from bandgap fluorophores because the processes involved are believed to be fundamentally different than in 2PEF. While fluorophores used in 2PEF are typically excited close to twice the wavelength of their linear absorbance peaks, MPL in gold nanoparticles is efficiently generated at the peak linear absorbance wavelength. Since the intermediate state MPL is an allowed rather than forbidden energy level, the lifetimes of the intermediate state in MPL are many orders of magnitude longer than in 2PEF. MPL is believed to be a serial process involving sequential absorption of photons and emission from the recombination of electrons in the sp-band and holes in the d-band[38],[39]. Convincing evidence supporting this hypothesis is presented in Chapter 7. MPL still exhibits a nonlinear dependence of luminescence on excitation intensity, though not exactly a quadratic one. Further details of MPL are discussed in Chapter 6.

2.5. NONLINEAR MICROSCOPY

The quadratic dependence of luminescence on excitation intensity allows NM to produce three-dimensional images by focusing the excitation light to a small focal spot, and scanning that spot through the sample. The high intensities created at the focal spot confine the luminescence generation almost entirely to the focal volume. Unlike CM, in NM, all the luminescence can be collected to assemble a three-dimensional imaging. This property allows nonlinear imaging to image deeper than CM[40].

The probabilities of nonlinear interaction are, in general, exceedingly small. The 2PEF brightness is quantified by the two-photon action cross section, σ_{2PA} , which is usually reported in Göppert-Mayer, or GM, units ($1 \text{ GM} = 10^{-50} \text{ cm}^4 \text{ s photons}^{-1}$). At intensity levels present in bright sunlight, a bright two-photon fluorophore will undergo 1PEF at a rate of approximately once per second, while 2PEF occurs at a rate of approximately once every 10 million years[41]. Thus to generate appreciable nonlinear signal, very high excitation intensities are needed. In addition to focusing the excitation light to a small focal spot, high intensities are achieved by using pulsed lasers. By compressing the energy of the excitation light to small time durations, extremely high peak intensities can be created. Typically, pulse durations of ~ 100 fs are used, separated by ~ 10 ns. This results in the pulsed excitation producing approximately 10^5 more 2PEF than a continuous wave source at the same average power.

2.6. SOURCES OF CONTRAST IN NONLINEAR OPTICAL IMAGING

There are a variety of sources for fluorescence contrast in nonlinear imaging. Intrinsic fluorophores, such as NAD(P)H, flavins, retinol, and tryptophan can provide a wealth of functional information, but produce weak emission, with σ_{2PA} values on the order of 10^{-4} to 10^{-1} GM[8],[42]. Still, as they are native to the tissue, they provide the

simplest method of functional and morphological contrast. Harmonic generation imaging can also provide contrast to native structures in biological tissues. SHG imaging is sensitive fibrillar structures, such as collagen, axons, muscle filaments, and microtubule assemblies[10],[43-45]. Third harmonic generation imaging, on the other hand, is sensitive to focal-spot sized or larger volumes which exhibit a large difference in refractive index compared to the surrounding medium, which commonly occurs from air bubbles and lipid droplets[46-48].

An alternative strategy to relying on endogenous contrast is to introduce contrast agents into the sample. Though delivery of the contrast agent to the target of interest is sometimes challenging, this technique has two important advantages: (1) a very bright probe can be used, and (2) this probe can be targeted to a ligand of interest. Many exogenous fluorophores used for single-photon fluorescence can also be used as two-photon contrast agents, the brightest of which have a σ_{2PA} on the order of 10-100 GM. There has been some success in engineering organic dyes specifically for large σ_{2PA} , and values on the order of several hundreds of GM have been reported[49]. Quantum dots are increasingly being used as two-photon contrast agents because of their extremely high σ_{2PA} values of up to 50,000 GM[50]. Gold nanoparticles have recently been shown to have relatively large σ_{2PA} values, with rough estimates ranging from 2,000 to 30,000 GM[51],[52]. Our measurements of gold nanoparticle brightness indicate even larger σ_{2PA} values are possible, up to 10^6 GM. Details of these calculations are discussed in detail in Chapter 7.

2.7. PLASMONIC NANOPARTICLES

2.7.1. Surface plasmon resonance

When metals are reduced in size to lengths that are comparable to the mean free path of their conduction band electrons (40-50 nm in gold[53]), they exhibit intense interactions with light[54]. At these size scales, the surface electrons are resonantly oscillated by visible and ultraviolet light. The coherent motion of these free electrons is called the surface plasmon resonance (SPR). Depending on the geometry, orientation, and material of the particle, the SPR leads to intense interactions of the particle with light within a range of optical frequencies.

The interaction of light with particles can be quantified by the scattering and absorption cross sections, C_s , and C_a respectively. The sum of these parameters is defined as the extinction cross section, C_e . These values describe the area of light that interacts with the particle, and can be orders of magnitude smaller or larger than the geometric cross section of the particle. For perfectly spherical nanospheres, Mie showed[55] that these parameters can be calculated exactly by solving Maxwell's equations[56],[55],[57]:

$$C_e = \frac{2\pi}{|k|^2} \sum_{L=1}^{\infty} (2L+1) \text{Re}(a_L + b_L), \quad (2.2)$$

$$C_s = \frac{2\pi}{|k|^2} \sum_{L=1}^{\infty} (2L+1) (|a_L|^2 + |b_L|^2), \quad (2.3)$$

where,

$$a_L = \frac{m\psi_L(mx)\psi'_L(x) - \psi'_L(mx)\psi_L(x)}{m\psi_L(mx)\eta'_L(x) - \psi'_L(mx)\eta_L(x)}, \quad (2.4)$$

$$b_L = \frac{\psi_L(mx)\psi'_L(x) - m\psi'_L(mx)\psi_L(x)}{\psi_L(mx)\eta'_L(x) - m\psi'_L(mx)\eta_L(x)}. \quad (2.5)$$

Here, m is the ratio of the complex index of refraction of the particle to the real index of refraction of the surrounding medium, k is the wave-vector, $x = |k|r$, where r is the radius of the particle, and ψ_L and η_L are the Ricatti-Bessel cylindrical functions[57]. The prime notation indicates differentiation with respect to the argument in parenthesis[57]. In general, for nonspherical particles, the cross sections must be determined numerically. In this work we use the discrete dipole approximation (DDA) to calculate the relevant cross sections of nonspherical particles[58]. In this method, a particle is simulated as an array of polarizable points which become dipoles in response to an electric field. These dipoles interact with each other and results converge to the exact analytical solution for an increasing density of polarizable points.

From Eqs. (2.2)-(2.5), it is clear that by changing the geometry of the particle or the optical properties of the particle or the surrounding material, the spectral shape and magnitudes of the cross sections will also change. Thus the optical properties of metallic particles can be “tuned” to give a desired response at a particular wavelength. At the peak SPR wavelength, metallic nanoparticles can have optical cross sections that are orders of magnitude larger than their geometric cross sections[54],[57],[59]. Peak C_a values can be 5 orders of magnitude larger than that found in conventional absorbing dyes, and peak C_s can be 5 orders of magnitude larger than fluorescence from strongly fluorescing dyes[59]. Gold nanospheres with a diameter of 70 nm exhibit a peak SPR at 530 nm when suspended in water. Gold nanorods with a length of 50 nm and a width of 15 nm exhibit two peaks when isotropically oriented in water—one at 510 nm when the electric field is parallel to the short axis of the nanorod and a second at 780 nm when the electric field is parallel to the long axis of the gold nanorod [Figure 2.4].

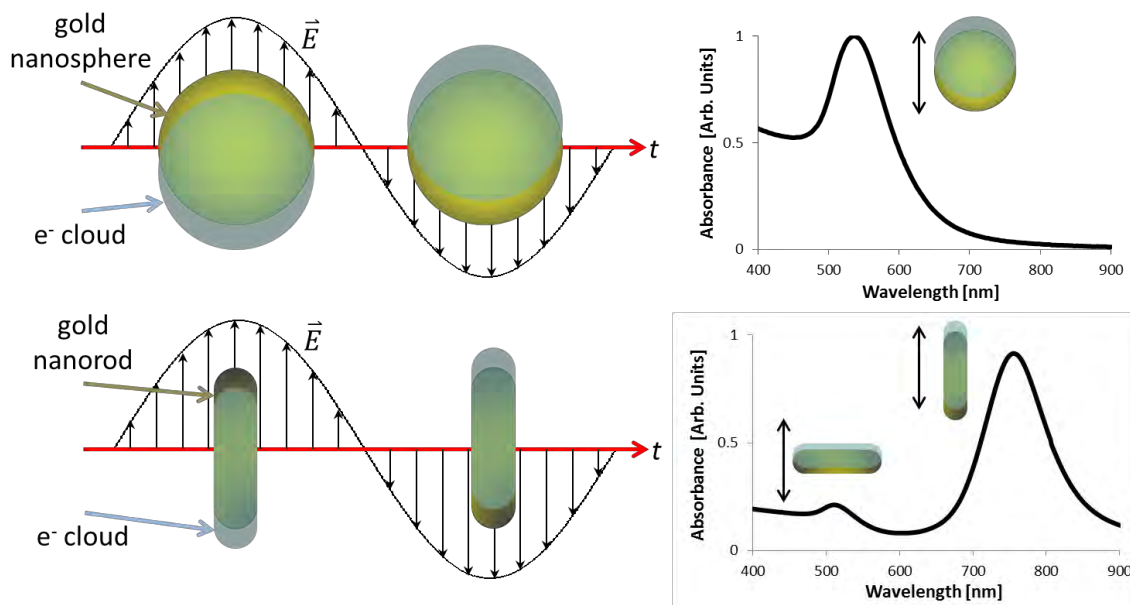


Figure 2.4: Surface plasmon resonance in gold nanospheres and gold nanorods. The material and shape of nanoparticles determines the resonant frequencies of their surface electrons. Due to their radial symmetry, gold nanospheres exhibit a single SPR peak. Gold nanorods, on the other hand, exhibit two peaks, depending on how they are oriented relative to the polarization of the electric field.

2.7.2. Gold nanoparticles as biomedical contrast agents

The large C_s and C_a of metallic particles can be exploited as a bright source of contrast for a variety of optical imaging modalities. As contrast agents, gold nanoparticles in particular have a number of advantages for biomedical use: (1) their peak C_s and C_a values can be tuned by varying particle size, shape, or orientation, (2) the relative contributions of the absorption and scattering cross sections to the total extinction cross section can also be controlled by engineering the particle geometry (especially in the case of nanorod and nanoshell shapes[59]), (3) gold has been shown to have minimal cytotoxic effects and is believed to be relatively biocompatible[60],[61], and (4) the synthesis and conjugation of gold nanoparticles has been well characterized, in part due to their use as stains in electron microscopy over the last several decades[62-64].

Gold nanoparticles were first demonstrated as sensitive probes for Raman spectroscopy[65-67] and single molecule studies[68-70] in the 1990's. Later, Sokolov *et al.* demonstrated the use of gold nanospheres for scattering contrast in vital reflectance confocal imaging of cancer cells and tissues[71]. Since their demonstration, gold nanospheres, nanoshells, and nanorods have also been applied as targeted contrast agents for OCT (which uses large C_s for contrast) [72-74], and PAM (which uses large C_a for contrast)[75-77]. There has also been important progress in using gold nanoparticles as a therapeutic agent. These studies typically utilize the large C_a of gold nanoparticles at NIR wavelengths for targeted thermal therapy[78-84].

2.7.3. Multiphoton luminescence from plasmonic nanoparticles

The large σ_{2PA} values observed in metallic particles are somewhat unexpected—traditionally, gold particles are known for their quenching of fluorescence, rather than fluorescence emission[85]. The lifetime of excited electrons in metals is extremely fast, on the order of tens to hundreds of femtoseconds[86],[87]. Partially due to this short lifetime, the quantum yield of smooth metal surfaces have been measured to be extremely low—on the order of 10^{-10} [38]. Nonetheless, weak luminescence can still be observed.

Single-photon-induced luminescence was first reported from bulk copper and gold by Mooradian in 1969[88]. Later, Boyd *et al.* found that roughened metal surfaces exhibited much higher single-photon-induced luminescence efficiency than smooth surfaces. They also found that while MPL was not measurable in smooth gold films, appreciable MPL could be observed from roughened surfaces[38]. In 2000, Mohamed *et al.* found that gold nanorods offered dramatically larger quantum yield than bulk gold, which they dubbed, the “lightning rod” effect[89]. They measured an enhancement of approximately 10^6 in emission yield when using excitation light at the linear absorbance

peak of gold nanorods. These results support the hypothesis that the presence of an SPR in the sample is important to the efficient generation MPL. However, as we will demonstrate in Chapter 6, the σ_{TPA} of a particle is relatively weakly dependent on the shape of the σ_{ext} —bright MPL can be observed when exciting gold nanoparticles far from their absorbance or scattering peaks. Thus, though SPR does seem to improve the efficiency of MPL, the complicated relationship between the spectral shapes of C_s and C_a indicates that MPL is not simply linearly related to the absorption or scattering enhancement from the SPR.

Gold nanoparticles have previously been used as sources of contrast in nonlinear imaging of biological samples. Yelin et al. demonstrated MPL and harmonic nonlinear microscopy of clusters of gold nanospheres labeled to fixed cell[90]. Unlabeled gold nanorods were used for in vivo MPL imaging of blood vessels by Wang *et al.*[51]. Farrer *et al.* showed that nanosphere can be bright sources of MPL when excited far from their SPR peaks[91]. In this dissertation we expand work done by our group, which demonstrated MPL imaging of cancer cells labeled with gold nanorods[92]. Additional studies have also recently shown that MPL can be used for imaging nanoshells[93], exploring the interaction of nanoparticles with cells[94-96], and even reading optically-encoded data[97].

Chapter 3

Design and characterization of nonlinear scanning microscope for deep tissue imaging

This chapter presents the design and characterization of a laser scanning nonlinear microscope that is optimized specifically for deep tissue autofluorescence imaging. Several important parameters are discussed, including a characterization of excitation source, the parameters related to objective lens performance, and the optimization of the collection optics. A detailed presentation of the control and acquisition software, the specific parts used, and the overall construction of the microscope can be found in the thesis of Benjamin Holfeld[98].

3.1. OVERVIEW

The excitation path consists of a pair of scanning mirrors, two relay lenses, and a long working distance, large field-of-view objective lens. The emission path uses non-descanned collection, large diameter optics, high throughput filters, and a sensitive photomultiplier tube (PMT) to maximize visible-light sensitivity. A customized computer program controls and synchronizes image acquisition, mirror scanning, excitation power control, and sample position. The microscope is configured in an upright configuration—the sample is placed under the objective—to enable the use of a water dipping objective and to facilitate future studies involving *in-vivo* animal studies. Imaging throughput is limited to 5×10^6 pixels per second by the data acquisition card, but imaging is typically performed at 1×10^6 pixels per second to match the bandwidth of our preamplifier.

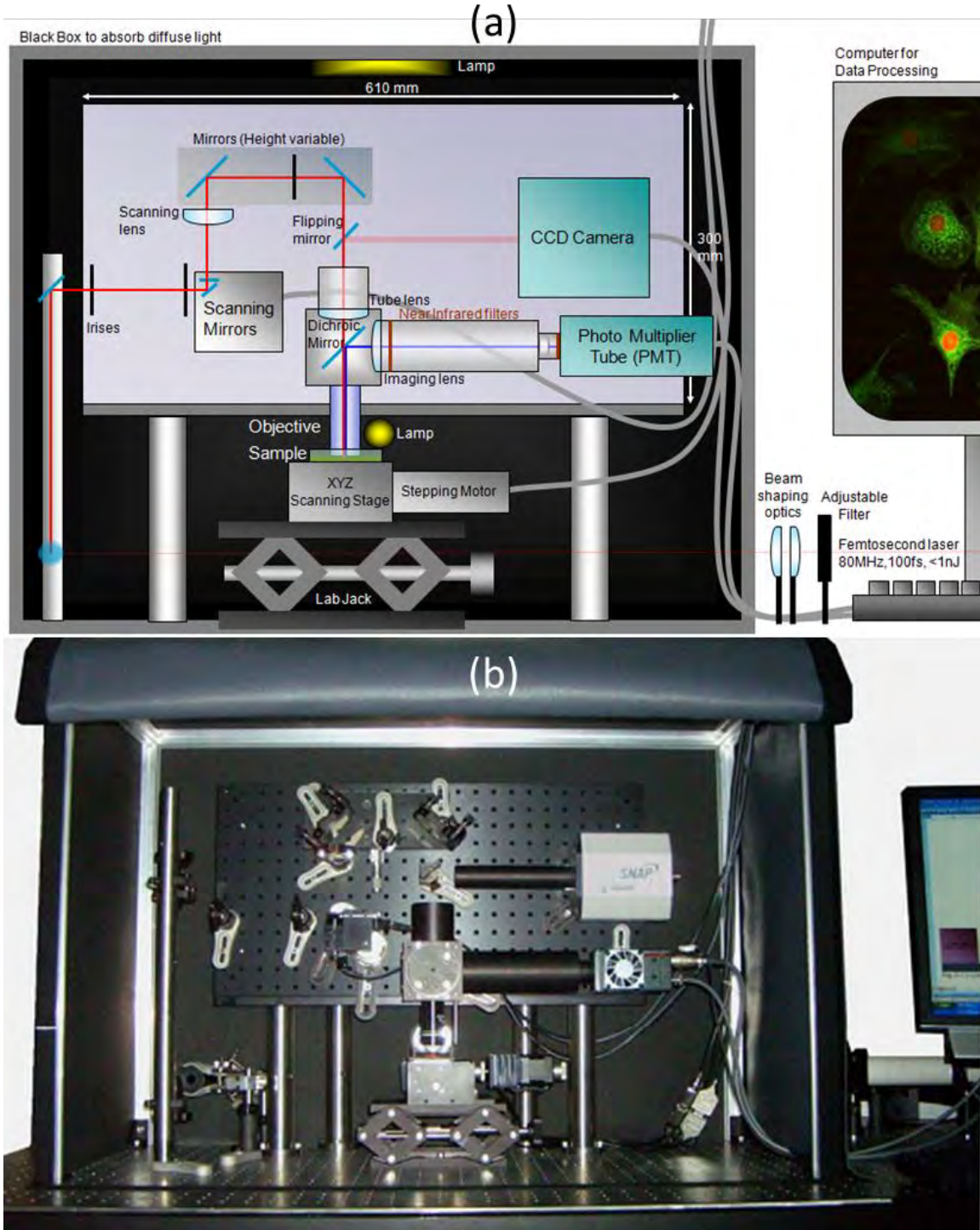


Figure 3.1: An upright laser scanning microscope for deep nonlinear imaging.
 (a) Schematic with labeled parts. (b) Photograph of actual microscope[98].

3.2. EXCITATION PATH

3.2.1. Excitation source

We used a Ti:Sapphire, mode locked laser oscillator (Newport, MaiTai) as our excitation source. This source has a repetition rate of 80 MHz, an excitation wavelength, λ_x , tunable from 710 to 880 nm, and an average power, P_{ex} , of 0.6 to 1.1 W across the tuning range. We measured the full width at half maximum (FWHM) of the spectral bandwidth, $\Delta\lambda$, to be 7.5 nm. Using a time-bandwidth product of 0.44, a transform limited pulse with this bandwidth would have a FWHM pulse duration, τ_p^{FWHM} of 120 fs. The pulse duration at the imaging plane of the objective, which is more relevant to imaging parameters, is discussed in Section 3.3.2. We measured the $1/e^2$ diameter of the excitation beam to be approximately 1.5 mm in the vertical direction and 1.2 mm in the horizontal direction at the output of the laser oscillator. The slightly larger divergence of the smaller (horizontal) axis resulted in the beam shape being relatively circular at the position of the objective back aperture. We used two lenses in a Galileo-configuration beam expander with focal lengths (f) of -30 and 75 mm for a 2.5x increase in beam size.

Two sets of half wave plate (HWP) and polarizing beam cube are used to control the excitation power. We found this solution to have several advantages over the use of reflective neutral density filters: (1) the excitation power may be continuously adjustable and computer controlled, (2) the dispersion introduced into the system is constant as attenuation is changed, and (3) this approach avoids the issue of spatial beam offset associated with the introduction of a neutral density filter at non-perpendicular angles to the excitation beam. One HWP was adjusted by a computer controlled actuator, providing 0.01° resolution. This resolution corresponds to a worst-case attenuation resolution of approximately $\pm 0.08\%$ at 780 nm (Newport, PR50PP, 10RP52-2). This value is calculated assuming the HWP angle is adjusted at the steepest rate of transmission

change versus angle change. The second HWP can be manually adjusted. Combined, the total power attenuation can be varied from less than 0.4 dB to greater than 40 dB within the range of $\lambda_x = 760\text{-}820$ nm. In some cases, additional attenuation was necessary. This was accomplished by inserting additional reflective neutral density filters in the excitation path.

3.2.2. Laser scanning system

Two requirements of the laser scanning system are that (1) the excitation beam is sufficiently expanded to fill the objective back aperture, allowing full use of the objective numerical aperture (NA), and (2) that the scanning mirrors are imaged to the back aperture, resulting in a uniform field of view at the object plane. We use a telecentric two-lens relay system to simultaneously meet these requirements[99],[100] [Figure 3.2]. The scanning mirrors are sufficiently close together that both can be approximately simultaneously imaged to the back aperture. We use an $f = 50$ mm scan lens and an $f = 250$ mm tube lens. The measured $1/e^2$ diameter of the excitation beam at the back aperture was 12 mm.

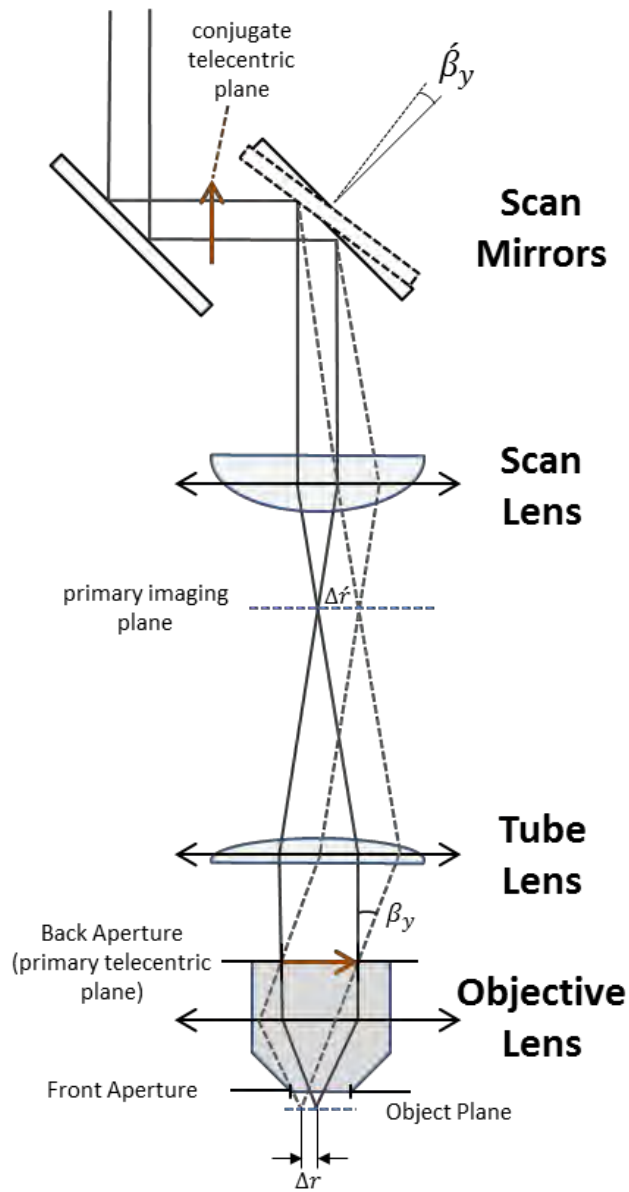


Figure 3.2: Schematic of laser scanning system.

The excitation beam is steered in two dimensions by two scanning mirrors. The scan and tube lens simultaneously image the scanning mirrors to the objective back aperture and expand the beam to fill the objective back aperture (conjugate imaging planes) Drawing not to scale.

3.2.3. Objective lens

The objective lens selection is crucial for deep imaging. A working distance of at least 500 μm is obviously necessary for deep imaging. Using an objective lens with an

immersion medium close in refractive index to the sample minimizes specimen induced spherical aberrations, which helps maintain high intensities necessary for 2PEF[101-103]. The index of refraction of the oil, glycerol, and water used in common immersion objectives are 1.53 (Zeiss Immersol), 1.47, and 1.33, respectively. Though the refractive index of the *stratum corneum* is 1.45~1.5 it generally decreases to 1.36~1.43 closer to the dermis[34],[35]. The tissue phantoms used in this dissertation are composed of greater than 90% water, and are assumed to have a refractive index very close to 1.33. For these applications, we chose a water immersion objective. Ideally, an objective with a correction collar should be used to accommodate samples with $n \neq 1.33$.

Resolution

To create the high intensities necessary for efficient two-photon excitation and the enable high resolution imaging, the objective must have a high numerical aperture (NA). In two-photon microscope the figure of merit for quantifying resolution is the emission spot size, which, because of quadratic dependence of emission on excitation intensity, is typically determined by excitation intensity squared point spread function (IPSF²). Because the IPSF² is approximately a cylindrically symmetrical ellipsoid, it can be succinctly described by quantifying the extent of emission along short and long axes of the ellipsoid. Experimentally, a Gaussian function is usually fitted to the lateral and axial profiles obtained from measuring the spot size of a sub-diffraction sized object. For an NA of greater than 0.7, the full width at half max in the lateral (r_{FWHM}) and axial directions (z_{FWHM}) for a diffraction limited system are given by[42]:

$$r_{FWHM} = \frac{\sqrt{2 \ln 2} 0.325 \lambda_x}{NA^{0.91}} \quad (3.1)$$

$$z_{FWHM} = \sqrt{2 \ln 2} \cdot 0.532 \lambda_x \left[\frac{1}{n - \sqrt{n^2 - NA^2}} \right] \quad (3.2)$$

Field of View

The objective lens field of view (*FOV*) is an often overlooked but important specification that influences collection efficiency[104]. The *FOV* describes the maximum lateral distance from the optical axis a small source at the focal plane can be while being imaged by the objective lens. Since the transmission of light from a point source gradually decreases as the point source is moved off axis, the definition is somewhat arbitrary. In the definition used here, the *FOV* is defined by the radius at which 1/e of the maximum value of a point source is transmitted, r_f . Thus, in order to collect as much scattered emission light as possible, which will appear to originate from large distances from the optical axis, it is important to maximize r_f .

In practice, the r_f of an objective is not usually specified by the manufacturer, as it is the field of view of the integrated system (r_f^{eff}) that is important for most microscopes. The r_f^{eff} is usually limited by the 25 mm diameter tube lens rather than the objectives themselves. However, in nonlinear microscopy with non-descanned detection, the emission is collected as close as possible to the back aperture and r_f is important. In general there is an inverse relation between the magnification, M , of a lens and r_f . Intuitively, this can be inferred by looking at Figure 3.2—the distance Δr in the object plane is related to $\Delta r'$ in the primary imaging plane by: $\Delta r = \Delta r'/M$. Therefore, in choosing an objective for deep imaging, it is important to choose an objective with a low magnification, and ideally, for one to measure the *FOV*.

Olympus XLUMPFL Objective

We chose to use the Olympus 20x/0.95 water dipping objective lens (XLUMPFL) for our system. In the absence of aberrations, this lens would provide an r_{FWHM} and z_{FWHM} of 305 nm and 1.2 μm , respectively, at $\lambda_x = 760$ nm. The r_f of a prototype of this particular objective was measured to be especially large in comparison to others, with $r_f = 1.3$ mm[104]. In comparison to a 63x/0.90 objective lens, this objective collected approximately ten times more emission signal at large imaging depths[104]. Though the exact layout of the objective is a trade secret, we show a prescription for an objective with the same specifications from an Olympus patent[105]. We implemented the patent prescription in Zemax-EE (2009 Version), and found the specifications of our objective are met [Figure 3.3]. However, this layout should serve only as a qualitative picture of the objective.

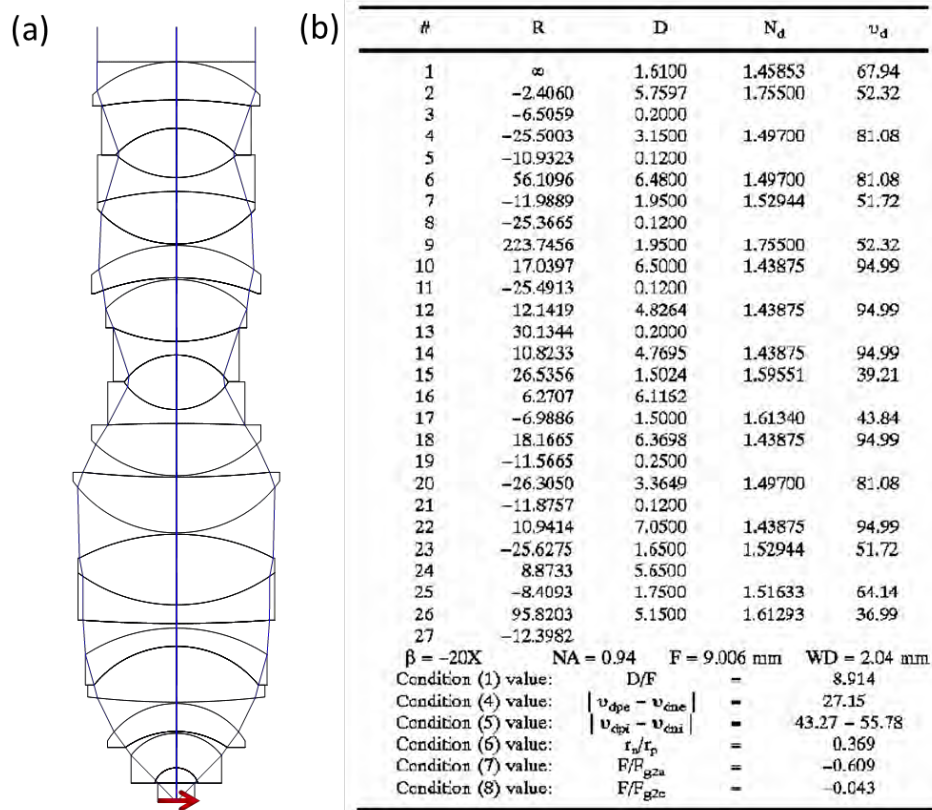


Figure 3.3: Layout of Olympus Objective.

(a) The layout from the prescription in the Olympus patent[105], modeled in Zemax. (b) The patent prescription indicates that the magnification, M is 20x, the NA is 0.94, the focal length, f , is 9 mm, and the working distance, WD , is 2 mm, identical to the objective lens we use.

3.3. FOCAL VOLUME CHARACTERIZATION

3.3.1. Spatial intensity distribution

We characterized the spatial intensity distribution of 760 nm excitation light at the focal volume by measuring the $IPSF^2$ of our system with 100 nm diameter fluorescent beads embedded in agar. A representative $IPSF^2$ measurement is shown in Figure 3.4 (a). We found lateral and axial FWHMs of $r_{FWHM} = 460 \pm 60$ nm and $z_{FWHM} = 1,760 \pm 130$ nm (mean \pm standard deviation), respectively, by fitting Gaussian functions to the profiles drawn through the centroids of 20 beads. These values are approximately 50% larger than

theoretical values expected with a diffraction-limited spot from a 0.95 NA water dipping objective[42], and closer to what would be expected from diffraction-limited focusing from a NA of 0.75. The difference between measured and diffraction-limited IPSF² is too large to be accounted for by our slight underfilling of the back aperture[106],[107], and is likely due to lens aberrations at NIR wavelengths. Similarly large point spread functions have been previously reported from this objective[104],[108],[109]. We found that the PSF was independent of imaging depth through the full working distance of the lens (2 mm) in a transparent sample of 100 nm fluorescent beads embedded in an agar gel. This result indicates that specimen-induced aberrations negligibly affect the shape of the intensity distribution in the perifocal volume in agar phantoms, which is consistent with other studies[110],[111].

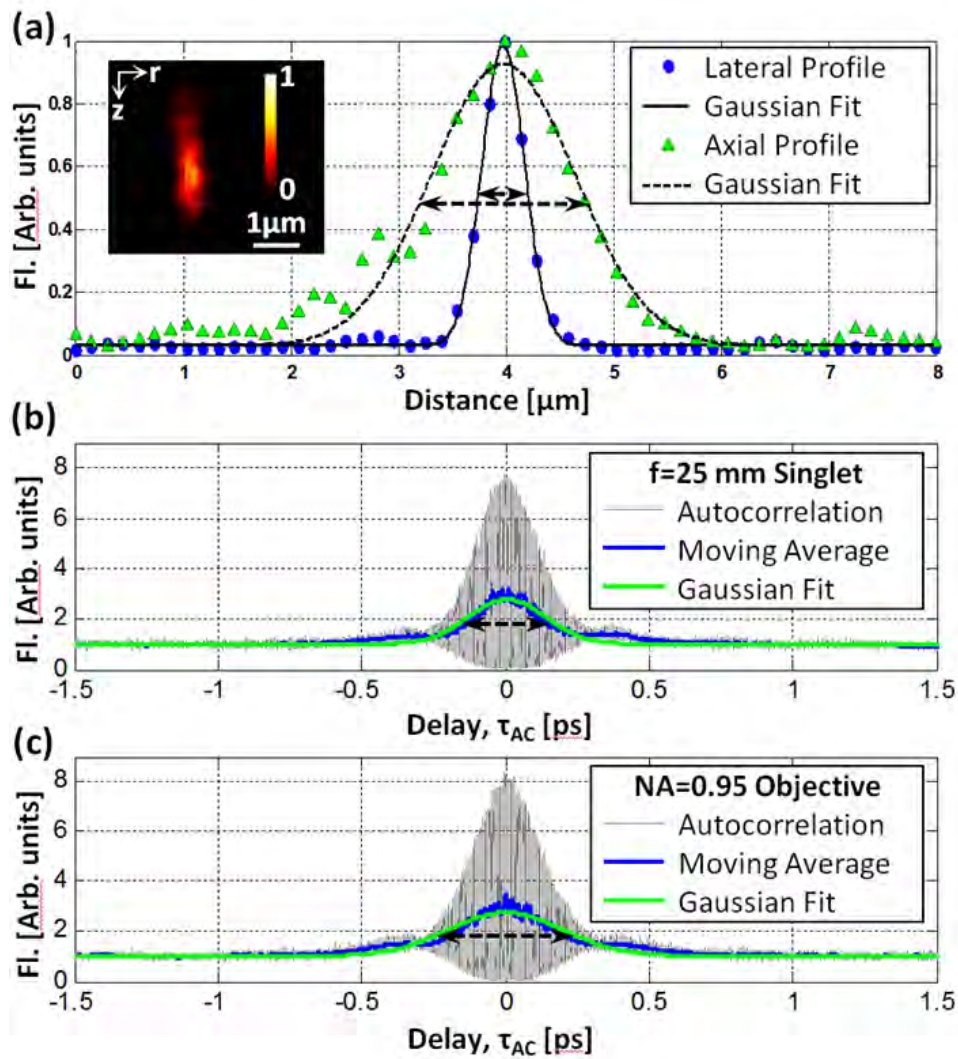


Figure 3.4: Spatial and Temporal Characterization of the Focal Spot.

(a) A representative lateral (r) and axial (z) IPSP² from a 100 nm fluorescent bead. We measured average lateral and axial FWHMs of 460 nm and 1760 nm, respectively. The inset shows the two-photon image of a typical bead in the rz -plane. (b-c) Autocorrelation measurements with a 1" singlet lens and with a 20x/0.95 objective lens indicated duration FWHMs of 185 ± 10 fs and 270 ± 10 fs, respectively. The moving average was performed over 5 fs of distance. Double-headed arrows in each plot indicate where the FWHM was measured. Fluorescent signal (Fl) is normalized to 1 at the center of the bead in (a), and at 1.5 ps in (b-c).

3.3.2. Temporal characterization

We characterized the temporal intensity distribution at the object plane of the microscope by incorporating a Michelson interferometer with a variable delay arm in the excitation path and measuring the autocorrelation function of the focused excitation beam within a sample[112],[113]. We used 25 μM fluorescein in a pH 12 buffer as the sample. We measured the autocorrelation function to estimate the pulse duration at the imaging plane using the 0.95/20x Olympus objective lens. We also measured the autocorrelation where the objective lens was replaced with a 1" diameter singlet lens with a 1" focal length [Figure 3.4 (b) and (c)]. These two measurements allow us to estimate the GDD of the objective lens (ϕ_o). We recorded the FWHM of a Gaussian fit, τ_{AC}^{FWHM} , to the moving average of our interferometric autocorrelation function over 5 measurements in each configuration. Furthermore, we assumed the original pulse shape is a Gaussian, which dictates that the time-bandwidth product, c_B , is 0.44. The FWHM of the original pulse shape, τ_p^{FWHM} , is then related to the autocorrelation trace by:

$$\tau_p^{FWHM} = 0.59 \tau_{AC}^{FWHM} . \quad (3.3)$$

We calculated the pulse duration at the sample plane to be $\tau_{p,s}^{FWHM} = 185 \pm 8$ fs with the singlet lens and $\tau_{p,o}^{FWHM} = 270 \pm 10$ fs with the objective lens from our autocorrelation traces.

To calculate the GDD of the Olympus objective using these two measurements, we use the equation relating the output pulse duration, Δt_{out} , to the input pulse duration, Δt_{in} , for a given GDD, ϕ_2 , and frequency bandwidth, $\Delta\nu$. [114],[115]:

$$\Delta t_{out} = \frac{\sqrt{(c_B/\Delta\nu)^4 + 16(\ln 2)^2 \phi_2^2}}{c_B/\Delta\nu} . \quad (3.4)$$

Note that this equation neglects the contribution from third and higher order dispersion. Solving for ϕ_2 and substituting the GDD of the system leading up to the focusing lens, ϕ_{sys} , and either ϕ_s for ϕ_o the two measurements, we have:

$$\phi_o + \phi_{sys} = \sqrt{\frac{(c_B \tau_{p,o}^{FWHM}/\Delta\nu)^2 - (c_B/\Delta\nu)^4}{16 (\ln 2)^2}}, \quad (3.5)$$

and

$$\phi_s + \phi_{sys} = \sqrt{\frac{(c_B \tau_{p,s}^{FWHM}/\Delta\nu)^2 - (c_B/\Delta\nu)^4}{16 (\ln 2)^2}}. \quad (3.6)$$

Subtracting Eq. (3.6) from Eq. (3.5) and solving for ϕ_o :

$$\phi_o = \phi_s + \frac{c_B}{4 \Delta\nu \ln 2} \left(\sqrt{(\tau_{p,o}^{FWHM})^2 - (c_B/\Delta\nu)^2} - \sqrt{(\tau_{p,s}^{FWHM})^2 - (c_B/\Delta\nu)^2} \right). \quad (3.7)$$

Using the measured spectral bandwidth of 7.5 nm FWHM, our $\Delta\nu$ is 3.7×10^{14} Hz at 760 nm. Assuming a modest ϕ_s of 250 fs² from the 1" singlet lens[113], we calculate the GDD of our objective to be $\phi_o \approx 4,300$ fs² at 760 nm. This value is significantly larger than reports of other similar-NA objectives[113], but not unexpected, given the long physical length of this lens (75 mm long). For reference, the GDD of a 75 mm block of BK7 glass, which has a group velocity dispersion of 50 fs²/mm at 760 nm, would be 3,750 fs².

3.4. COLLECTION PATH

Conventional nonlinear collection optical designs use a low $f/\#$ lens to image the objective back aperture to the detector surface[99]. This approach maximizes emission collection provided the emission is uniform in intensity at the back aperture and the $f/\#$ of the collection lens fills the acceptance angle of the detector. However, neither of these

assumptions are appropriate in deep tissue imaging. For an infinity-corrected objective lens, ballistic emission photons will retrace the path of the ballistic excitation light and come out of the objective back aperture relatively collimated. There may be some deviation between the two paths because many objective lenses are not corrected for chromatic aberrations above ~ 700 nm, and so the focal planes of λ_x and λ_m can be slightly different. But more importantly, the majority of emission light is scattered, even for shallow imaging depths. For instance, imaging one mean free excitation path length deep in epithelial tissue, the scattering length of emission light is typically on the order of half that at the excitation wavelength (i.e. $l_s = 46$ μm at $\lambda_x = 760$ nm and $l_s = 27$ at $\lambda_m = 500$ nm[36]). Using Beer's Law, one can see that when imaging just 50 μm deep in these conditions, less than 20% of the light emitted within the objective acceptance solid angle will exit the tissue unscattered. Imaging 200 μm deep, this fraction drops to less than 0.06%. This underlies the importance of non-descanned detection in deep nonlinear imaging.

The design of a collection system in our system is further complicated by the fact that our detector (Hamamatsu H7422-40), which is commonly used because of its high sensitivity, has a long tunnel surrounding the cathode which prevents high-angle photons from being detected. Accordingly, we employed a computation model to maximize the percentage of emission photons collected in our setup as collection lens parameters are varied.

We optimized the collection optics for maximum emission collection for photons from the diffusive regime using Zemax, similar to a previous approach[116]. We launched the photons with Gaussian spatial and angular distribution with $1/e^2$ radii of 4.25 mm and 11.4° , respectively. This distribution was found from propagating diffuse emission photons through the objective shown in Figure 3.3. Another approach would be

to model the objective as a single 9 mm focal length lens. The collection lens focal lengths and distances were varied using Zemax optimization with a non-sequential incoherent intensity detector data function as the dominant source to the merit function. Due to the size of the dichroic filter holder, the first collection lens was restricted to be greater than 30 mm away from the center of the dichroic mirror. The PMT housing also limits the final collection lens to be greater than 12 mm from the edge of the cathode tunnel. Simulations were typically optimized with 10,000 analysis rays and converged in 12-36 hours. The Zemax Hammer optimization was also used to prevent settling on local maxima.

Examining the conventional approach of imaging the back aperture to the PMT cathode, we observe a collection efficiency of 23% [Figure 3.5 (a)]. Note that the PMT cathode tunnel drastically limits the angle of acceptance. Varying the lens and cathode positions, we found a maximum collection efficiency of 29% by moving the lens and cathode closer to the back aperture [Figure 3.5 (b)]. Note that now that the system is not imaging the back aperture to the cathode—a point source at the back aperture does not map to a point source at the cathode. Introducing a second, 2” diameter lens, and varying the focal lengths and positions of both of the collections lenses and the cathode, we found a maximum collection efficiency of 34% [Figure 3.5 (c)]. This was the configuration implemented in our system. Finally, we examined the case of using a PMT with a larger acceptance angle, which has recently become available commercially (Hamamatsu H7422-40MOD). Without the small cathode tunnel, collection is greatly improved. In a two lens system, we find a maximum collection efficiency of 65% [Figure 3.5 (d)]. Slightly greater efficiency can be achieved by using 2” diameter emission filters, and reducing the length of the housing for the final 1” diameter focusing lens. We found no significant advantage in using a 3 lens system, even with addition of a diverging lens.

However, in the case where it is desirable to move the PMT far away from the objective back aperture (i.e. for including multiple detection channels), additional lenses might further improve collection efficiency.

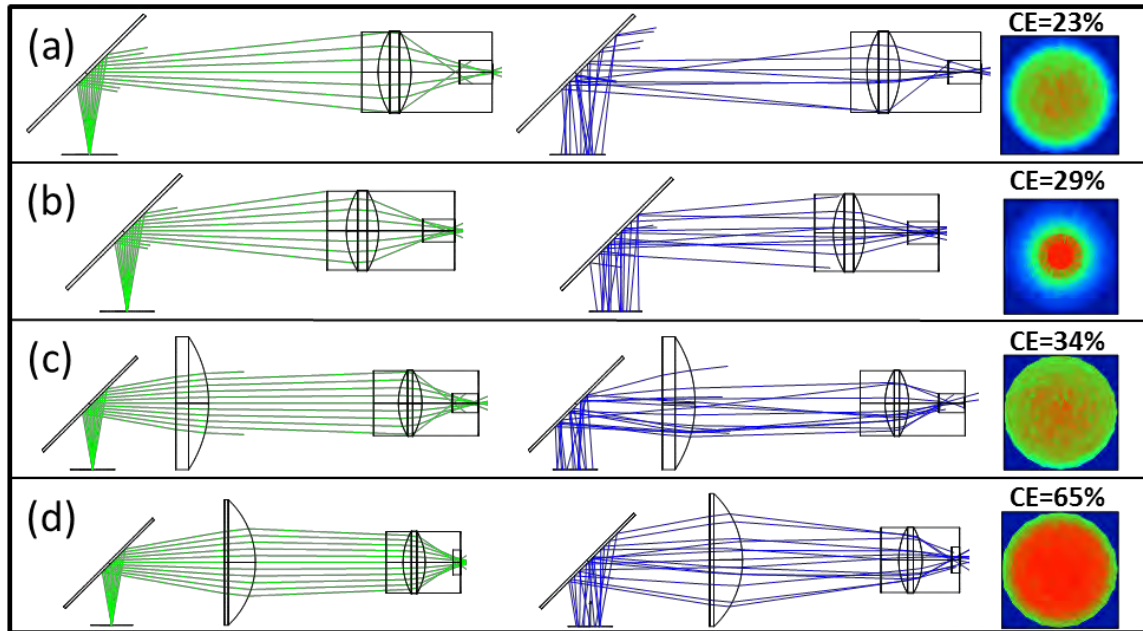


Figure 3.5: Optimization of collection optics.

(a) Conventional imaging approach results in a collection efficiency (CE) of 23%. (b) Optimizing with one lens, the CE is increased to 29%. (c) With two collection lenses, the CE can be increased to 34%. (d) With the new modified PMT available from Hamamatsu, the CE can be increased to greater than 65%. Left column is ray tracing for a point source at different angles. Middle column shows ray tracing of 15 analysis rays with random initial position and angle. Right column shows the intensity distribution at the cathode from the 10^6 random rays. Line traces which end before the cathode indicate emission photons that are not collected

3.5. EXAMPLE IMAGES

3.5.1. Phantoms

The low magnification of the Olympus lens allows us to image at a very large *FOV* while maintaining advantages in collection efficiency and small spot size from the large NA. Figure 3.6 (a) shows an image approximately 30 μm below the surface of a phantom created with autofluorescence from A431 cancer cells embedded in a collagen

matrix. A field of view of 600 μm could be achieved with relatively uniform excitation. Figure 3.6 (b) and (c) show examples of high magnification multiphoton luminescence images of gold nanorod labeled A431 cancer cells. Three dimensional images can be acquired with high resolution.

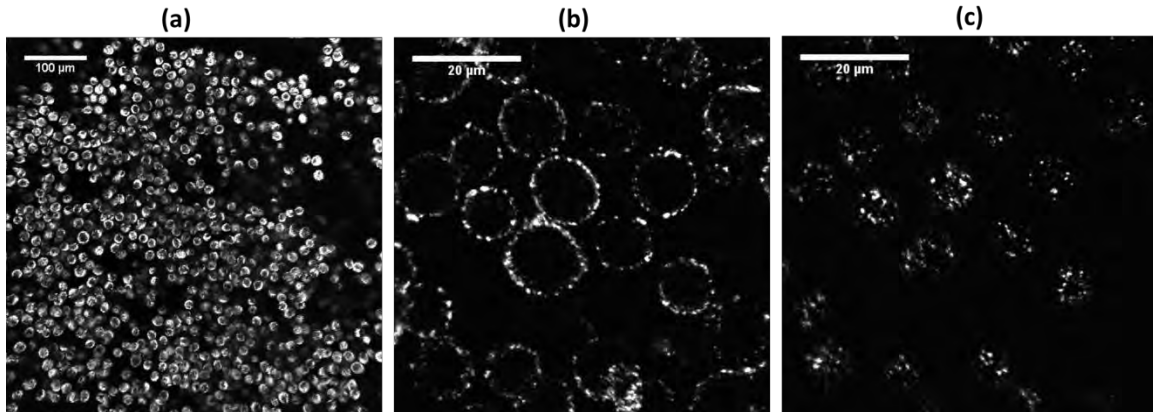


Figure 3.6: Large field of view imaging of unlabeled cancer cells and high magnification view of gold nanorod labeled cells.

(a) The low magnification of the objective lens allowed to image very large field of views. This image of unlabeled A431 cancer cells demonstrates autofluorescence imaging at 600 μm field of view. Scale bar is 100 μm . (b-c) High magnification multiphoton luminescence image of A468 cancer cells labeled with EGFR-targeted, PEGylated gold nanorods. Scale bars are 20 μm . (b) Image at when the focal plane is set to the middle of the cells. (c) Image with the focal plane moved up 5 μm relative to (b). There is little common signal between the two, indicating good axial resolution and corresponding out-of-focus signal rejection. As expected, the gold nanorods form a shell around the cell membranes.

3.5.2. Three dimensional rendering of healthy tissue biopsies

Figure 3.7 shows a three dimensional rendering of a nonlinear autofluorescence image stack from a fresh *ex-vivo* human biopsy of normal tongue tissue (using ImageSurfer software). The different layers constituting the stratified epithelium are clearly visible, and individual cells can be resolved. SHG provides contrast between the epithelium and the collagen-rich epidermis.

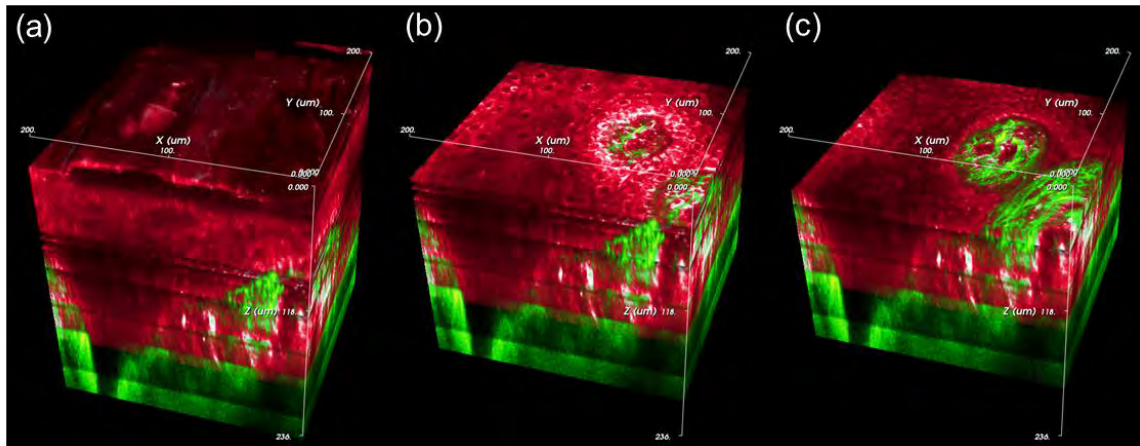


Figure 3.7: Autofluorescence and second harmonic generation imaging in an ex-vivo human biopsy.

A three dimensional rendering of a stack of 250 images acquired over a depth of 250 μm allows different layers of the epithelium to be visualized. Red channel is autofluorescence and green channel is second harmonic generation. (a) the *stratum corneum* is clearly visible on the outer layer of the biopsy. (b) Several layers can be viewed simultaneously when the upper layers of the rendering are removed. The *stratum spinosum* and *stratum basale* are clearly visible. A dermal papillae breakthrough can be seen, marked by strong SHG signal. (c) Deeper still, one can begin to see the collagen structure of the upper dermis in the SHG channel. Note some planes are missing due to PMT saturation. Field of view is $200 \times 200 \times 240 \mu\text{m}^3$. Rendering is achieved with ImageSurfer[117].

3.5.3. Comparison of normal and cancerous biopsy

We imaged a pair of normal and abnormal biopsies to compare the morphological structure of each [Figure 3.8]. The normal biopsy exhibited well differentiated and organized cells that are typical of stratified epithelium. The abnormal biopsy, which was later diagnosed as squamous cell carcinoma, appeared highly irregular and poorly differentiated. These morphological differences are typical of healthy and cancerous tissue[21],[118]. These images provide an idea of capabilities of two-photon autofluorescence imaging as a tool for noninvasive optical biopsy.

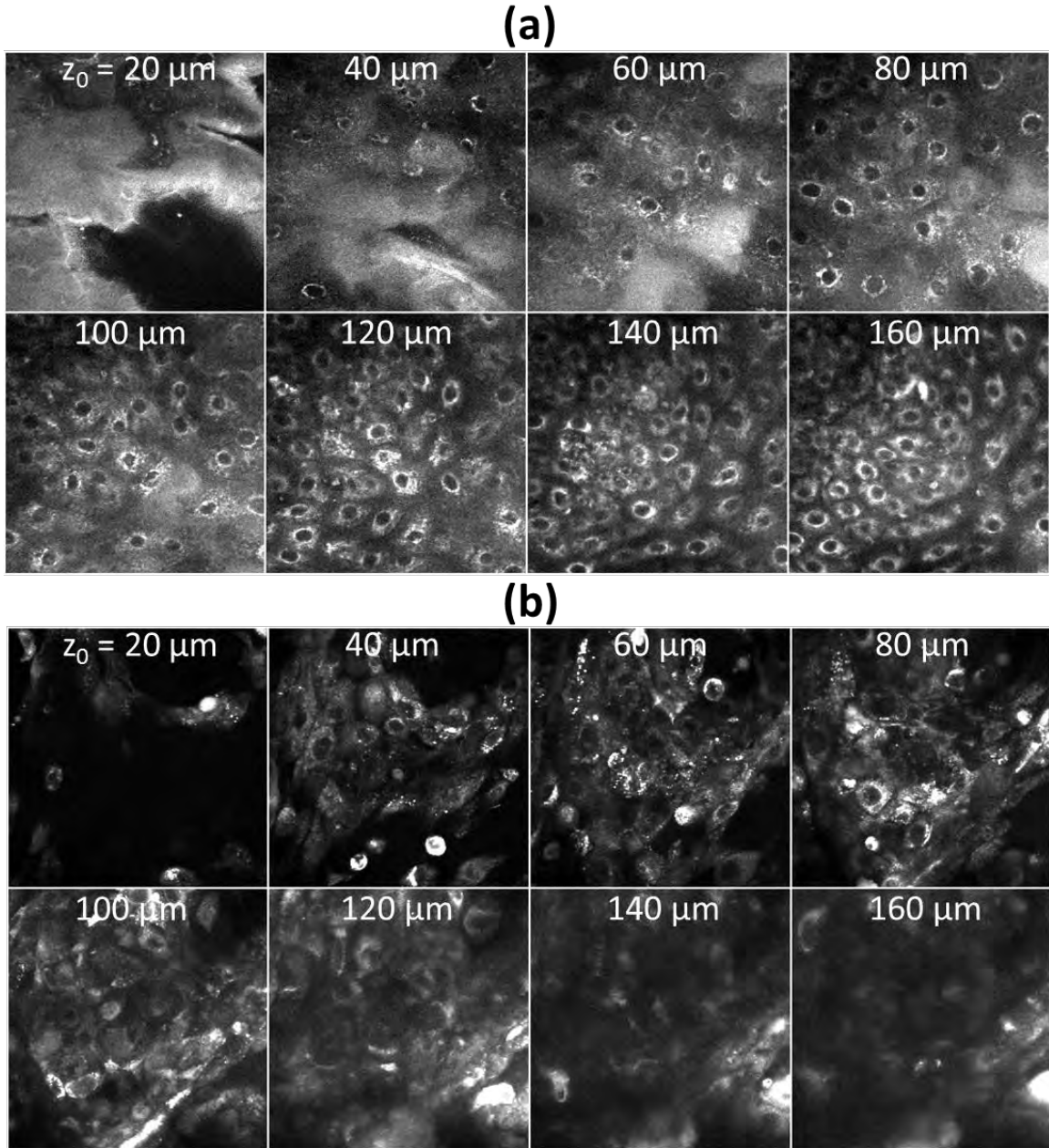


Figure 3.8: Two-photon autofluorescence images of normal and cancerous biopsy.

A comparison of two-photon images obtained from a normal biopsy (a) and contralateral abnormal biopsy (b) shows significant differences in tissue structure. The normal biopsy cells are well-differentiated and organized compared to the cells in the abnormal cells. Field of view is $200 \times 200 \mu\text{m}^2$

Chapter 4

A Monte Carlo model for out-of-focus fluorescence generation in two-photon microscopy

4.1. INTRODUCTION

One of the major advantages of two-photon imaging is that the quadratic dependence of emission signal on excitation fluence results in nearly all the signal being generated within the perifocal volume of a tightly focused beam. This three dimensional confinement allows for intrinsic three-dimensional sectioning and high contrast imaging, provided that: (1) the volume of the feature of interest, V_s , is large relative to the excitation focal spot, and (2) that the fluorophore concentration in the feature of interest is large compared to that in the bulk sample [Figure 4.1 (a)]. When imaging sub-diffraction sized objects, or if the beam spot size is degraded (typically enlarged) by aberrations, V_s is small compared to the focal volume, and the contrast suffers [Figure 4.1 (b)]. Likewise, the contrast decreases if the excitation beam is focused deep within an attenuating sample, wherein appreciable fluorescence can be generated outside of the perifocal volume [Figure 4.1 (c)].

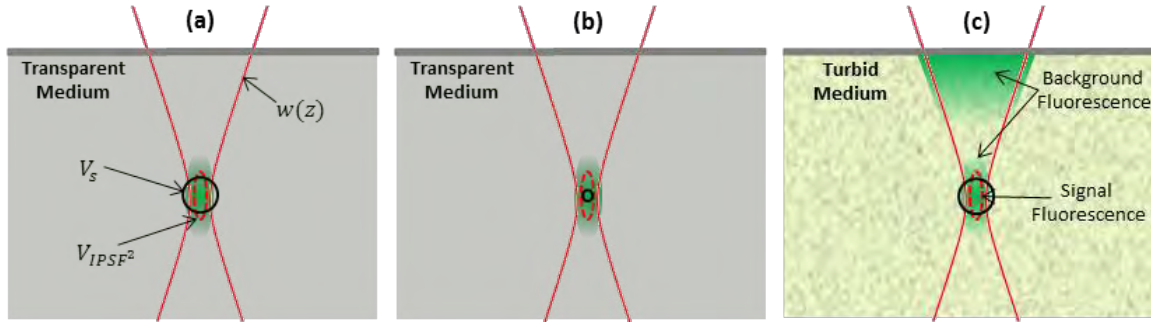


Figure 4.1: Qualitative illustration of signal and background two-photon excited fluorescence.

(a) Focusing in a transparent medium with large signal volume, V_s . If V_s is large compared to the excitation volume, V_{IPSF^2} , there is high contrast between the feature in the volume of interest compared to the background. (b) Focusing in a transparent medium with a small signal volume gives low contrast because significant perifocal fluorescence is generated outside the signal volume. (c) Focusing deep in a turbid medium gives low contrast even with a large signal volume because background fluorescence is generated near the sample surface. Solid red line is $1/e^2$ radius, $w(z)$, of a focused Gaussian beam. Green color represents generated fluorescence. Solid black circles indicate V_s .

The ratio of collected signal fluorescence (F_s) to background fluorescence (F_b) decays with increasing imaging depth in an attenuating medium. In cylindrically symmetric tissues, with a distance from the optical axis, r , and an axial distance from the tissue surface, z , this ratio can be described as:

$$\frac{F_s}{F_b} = \frac{\int_{V_s, -\infty}^{\infty} \int \phi(r, z) C(r, z, t) I^2(r, z, t) dt dV}{\int_{V_b, -\infty}^{\infty} \int \phi(r, z) C(r, z, t) I^2(r, z, t) dt dV}, \quad (4.1)$$

where the signal volume, V_s , is the volume of the feature of interest, the background volume, V_b , is the volume within the sample but outside of the signal volume, ϕ is the collection efficiency, C is the fluorophore concentration, and I is the excitation intensity.

In this chapter, we use a Monte Carlo simulation to calculate the R value, which we define as the ratio of collected fluorescence from the signal volume to background volume, for a homogeneously labeled sample ($C(r, z, t) = C_0$):

$$R = \frac{\int_{V_s}^{\infty} \int_{-\infty}^{\infty} \phi(\rho, z) I^2(\rho, z, t) dt dV}{\int_{V_b}^{\infty} \int_{-\infty}^{\infty} \phi(\rho, z) I^2(\rho, z, t) dt dV} \quad (4.2)$$

The effect of the fluorophore distribution and a quantitative description of two-photon imaging contrast are described in the next chapter.

4.2. MONTE CARLO VS. ANALYTICAL APPROACH

Both the Monte Carlo and Analytical approach to modeling the intensity distribution have advantages and disadvantages. Here we discuss the merits of each approach, and describe why we choose to use a Monte Carlo model.

Previous studies characterizing the IPSF^2 in turbid media have demonstrated that the focal spot size is constant as imaging depth is increased to at least 2 to 5 times the scattering mean free path of the sample[110],[111]. Imaging of the IPSF^2 beyond this depth has not been performed due to limited excitation power and objective working distance. Though there is some debate over these results, our experiments are consistent with this finding [Section 5.3.2]. We are not aware of any experimental reports of an increase in focal spot size when imaging in a refractive-index-matched sample, but it should be mentioned that a recent theoretical investigation has predicted an increase in focal spot size for deep imaging in a turbid medium[119]. A constant spot size for increasing imaging depth implies negligible contribution from scattered light, i.e, that the perifocal fluence is dominated by the unscattered, ballistic light. Assuming the fluorescence in the perifocal volume is caused purely by ballistic photons, the observed IPSF^2 distribution can be predicted using analytical approximations[11],[120],[121]. Conventional Monte Carlo simulations, on the other hand, can recreate the experimental IPSF^2 , but focusing must be arbitrarily constructed to match experimental results.

The background fluorescence for deep nonlinear imaging is predominately generated close to the tissue surface and extends through a few scattering lengths into the sample[11],[122-124]. In this regime, diffraction can be neglected and the photon flux can be accurately described by the time-dependent radiative transport equation. Exact analytical solutions to this equation are extremely complex and do not provide relevant utility[125]. Approximate analytical expressions have been derived to determine fluences in this regime, but the results are inaccurate for large angle scattering and focusing, neglect any backwards propagating component, and are more applicable at more than two scattering lengths deep[11],[125]. Monte Carlo simulations, on the other hand, provide an exact solution to the time-dependent radiative transport equation. In fact, analytical approximations are generally validated against Monte Carlo methods[125].

To summarize, a Monte Carlo approach has the advantage of accurately simulating the superficial fluorescence and the disadvantage of simulating the perifocal volume fluorescence only after arbitrarily aiming ballistic photons to match experimental conditions. Consequently, changes in the IPSF^2 predicted from Monte Carlo models have little bearing on the expected behavior. In comparison, an analytical approach is more rigorous for determine perifocal fluorescence distribution, and less accurate for modeling the superficial fluorescence generation. Given that experimental results suggest the spot size does not appreciably change with imaging depth, we use a Monte Carlo model to determine the R value. For an improved model, it would be possible to combine the two approaches and use the Monte Carlo model to determine background fluorescence and an analytical one to determine signal fluorescence, or perhaps use a Monte Carlo model that includes diffractive effects[119].

4.3. OVERVIEW OF MONTE CARLO MODEL

We used two independent Monte Carlo simulations to find the spatio-temporal distribution of the squared excitation intensity, $I^2(r, z, t)$, and the spatial dependence of the collection efficiency, $\phi(r, z)$. The corresponding results are combined using Eq. (4.2) to determine R for a variety of sample and imaging parameters, and generally, as a function of imaging depth, z_0 . Photon propagation was implemented using the same rules as Wang *et al.*[126]. All simulations (excitation and collection) used a Henyey-Greenstein scattering phase function with a scattering anisotropy set to 0.85. This is the expected value from Mie theory for 760 nm light interacting with 1 μm diameter polystyrene spheres[127], which are used for phantom preparation in Chapter 5. This value is also reasonable for modeling light scattering in epithelial tissue[33],[36],[128],[32]. For the excitation simulations, we use scattering lengths in the range typically found in epithelial tissues at 760 nm and which are later recreated in tissue phantoms: $l_s = 40, 80, \text{ and } 120 \mu\text{m}$. We assume emission photons have a wavelength of 515 nm, which is slightly red-shifted from half of our excitation wavelength, and close to emission peak from other 2PAM studies in epithelial tissues[129],[130]. The ratio of scattering length at 760 nm and 515 nm was found to be 1.7 by Mie simulations for 1 μm diameter polystyrene beads. Thus, for each excitation simulation set, we used a collection scattering length of $l_s^{\text{collection}} = l_s / 1.7$ to create a matching collection efficiency map for each excitation scattering length. To calculate R , the fluorescence grid created from the excitation simulation was integrated over time and every element was multiplied by an interpolated value from the spatial collection efficiency grid.

4.4. EXCITATION SIMULATION

For the excitation simulation, the photon packets were traced through a cylindrically symmetric three-dimensional grid with coordinates for depth z , radius r , and time t . Two grids are used to record excitation photon flux in space and time—a sparse grid for calculating fluorescence generation outside of the focal volume ($\Delta r = 20 \mu\text{m}$, $r_{max} = 1.2 \text{ mm}$, $\Delta z = 20 \mu\text{m}$, $z_{max} = 1.2 \text{ mm}$), and a fine grid within $\pm 20 \mu\text{m}$ of the focal plane ($\Delta r_{focal} = 200 \text{ nm}$, $r_{max} = 20 \mu\text{m}$, $\Delta z_{focal} = 0.5 \mu\text{m}$, $z_{max} = 40 \mu\text{m}$). Both grids had a time spacing of one tenth the excitation pulse duration, ($\Delta t = \tau_p/10$, $t_{max} = 3 \times z_0/c$). These grid spacing were verified to be of sufficient resolution to capture fast changes in fluence by running select simulations at twice the spatial and temporal resolution (resulting in eight times more grid elements for constant total grid size). Photon packets propagate until they exceed the maximum radius, depth, or time; their weight falls to zero (with a roulette procedure); or they exit the tissue.

4.4.1. Focusing

Previous Monte-Carlo models of two-photon microscopy have simulated a focused beam in one of two ways: (1) the geometric focus method, where the fluence at a plane offset from the geometric focus that would give the same width as the diffraction limited spot is measured [Figure 4.2 (a)][131], or (2) the spot focus method, where initialized photons are stochastically pointed towards a radius at the focal plane such that a lateral Gaussian distribution is created [Figure 4.2 (b)][110],[132]. The geometric focus method suffers from a problem of creating a point of infinite fluence, as ballistic rays transmit through an infinitely small area at the geometric focal plane. The spot focus method effectively introduces dispersion in the simulation, as voxels in this simulation

will see ballistic photons pass through at different times, depending on where they are pointed towards at the focal plane.

Our approach focuses excitation light using the hyperbolic method described by Tycho *et al.* for OCT imaging [Figure 4.2 (c)][133]. By skewing the initial trajectory of each photon off of a z - r plane by an angle depending on r , a focused Gaussian beam can be exactly reconstructed in all three dimensions with photons that travel in straight paths. A qualitative visualization of how straight photon rays can recreate a curved focal spot is shown in Figure 4.2 (d). Finally, we note that the spot focus method can have a similar shape to the hyperbolic focus method if the random radius at the focal plane is chosen perpendicular to the initial radius, such that these photons are also skewed off axis (not shown in Figure 4.2). For small focal spots and deep imaging depths, the temporal dispersion introduced from variable-aiming of the initialized photons in the spot focus method becomes negligible. Thus, we would expect similar results in modeling R for both the hyperboloid and spot focusing methods.

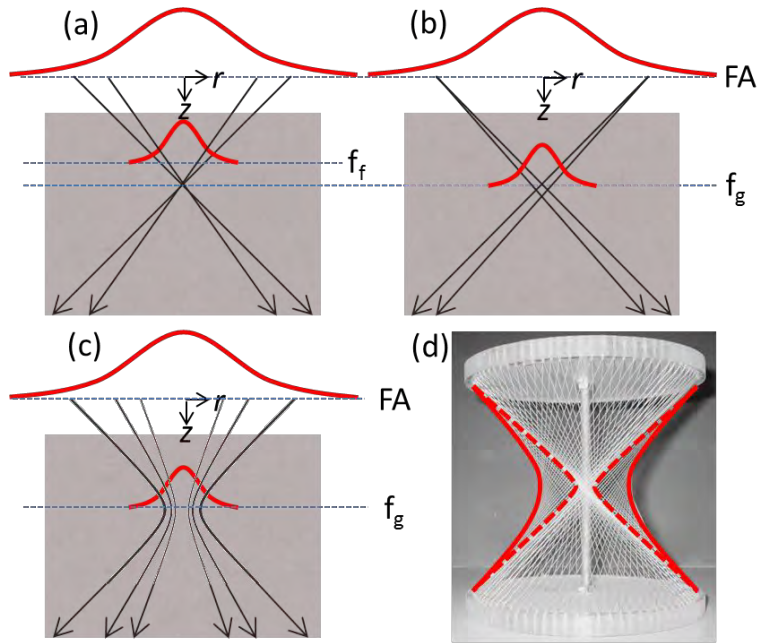


Figure 4.2: Qualitative illustration of different focusing strategies. (a) The geometric focus method. (b) The spot-focus method. (c) The hyperboloid focusing method. (d) Two disks with straight wires are twisted to create two hyperboloids with different beam waists at the focal plane. By varying initial position and the amount skew, the beam waist and Rayleigh range can be adjusted independently to model experimentally observed conditions. Here, the dotted red line follows a Gaussian shape with tighter focus than the solid red line. f_g is the geometric focal plane and f_f is the plane offset from f_g , such that a chosen spot size is created, and FA is the plane of the objective front aperture. Photograph in (d) is adapted from[134].

In the mathematical description of a focused Gaussian beam, there are two parameters available to match experimental conditions when simulating the excitation light as a focused Gaussian beam: the beam waist (w_0) and Rayleigh range (z_r). Note that in the true physical propagation of focused Gaussian beams, w_0 and z_R are not independent. However, our desire, as is the case in all the two-photon Monte Carlo methods discussed here, is not to simulate the diffractive propagation of a Gaussian focus. Instead, our goal is to simulate the measured intensity distribution at known planes and to run a ray-tracing model that satisfies the radiative transport equations as the

imaging depth sample properties are changed. The lateral $1/e^2$ beam radius vs. depth, $w(z)$, is then described by:

$$w^2(z) = w_0^2 \left[1 + \left(\frac{z - z_0}{z_R} \right)^2 \right]. \quad (4.3)$$

And the total (non-normalized) intensity distribution in three dimensions is then:

$$I(z, r) = \frac{1}{w^2(z)} e^{-2r^2/w^2(z)}. \quad (4.4)$$

We measured three parameters in Chapter 3 that characterize the excitation light distribution in our experiments: the beam profile at the back aperture, described by the $1/e^2$ radius of the excitation fluence, w_{BA} ; and the axial and lateral extent of the focal spot, described by the FWHM of the axial and lateral $IPSF^2$ (z_{FWHM} and r_{FWHM}), respectively. In general, with only two parameters that define the shape of a Gaussian focus (z_0 and w_0), all three measurements of our excitation beam shape cannot be modeled simultaneously. Since the purpose of this model is to simulate the ratio of in-focus to out-of-focus fluorescence, and large contributions of out-of-focus fluorescence are known to be generated near the sample surface, it is important that the simulated beam shape matches experimental observations both close and far from the focal plane. Therefore we choose w_0 so that the lateral Gaussian shape is correctly simulated at the focal plane, and z_R such that the lateral Gaussian shape is correctly simulated at the front aperture of the objective (far from the focal plane).

Since z_{FWHM} and r_{FWHM} represents the fluorescence distribution, which is proportional to the square of the excitation intensity, we must convert these parameters to the linear intensity distributions they are the result of to simulate the excitation intensity distribution. The axial $1/e^2$ radius of the excitation intensity, w_0^z , and the lateral $1/e^2$

radius of the excitation intensity, w_0 , are equal to $z_{FWHM} / \sqrt{\ln(2)}$ and $r_{FWHM} / \sqrt{\ln(2)}$, respectively. Furthermore we make the assumption that the fill factor of the Gaussian beam measured at the back aperture is linearly propagated to the front aperture of the objective. That is, that:

$$\frac{w_{BA}}{r_{BA}} = \frac{w_{FA}}{r_{FA}}, \quad (4.5)$$

where w_{FA} is the $1/e^2$ radius of the excitation beam at the objective front aperture, and r_{BA} and r_{FA} are the radii of the back aperture and front aperture of the objective, respectively. The fill factor, F_f , is defined by w_{BA} / r_{BA} . A schematic of the setup with these parameters is shown in Figure 4.3.

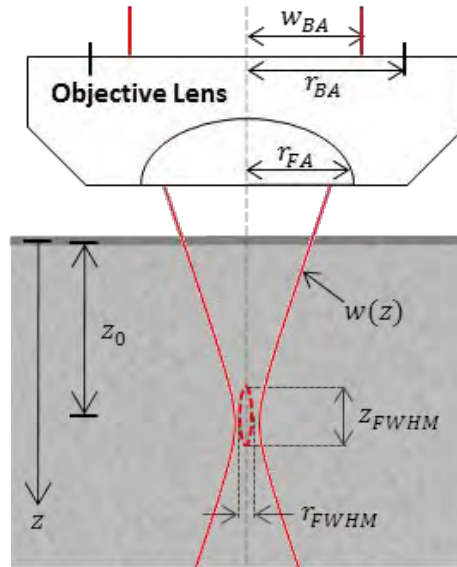


Figure 4.3: Parameters describing Gaussian beam focusing in our Monte Carlo simulation.

Excitation photons are launched in our Monte Carlo simulations to create a three dimensional Gaussian focus distribution. Solid red lines are the $1/e^2$ envelope of the Gaussian beam. Dashed red line outlines the spatial extent of the emission spot. See text for definition of parameters.

The resulting parameters describing the Gaussian distribution of the excitation photons are:

$$w_0 = \frac{r_{FWHM}}{\sqrt{\ln 2}}, \text{ and} \quad (4.6)$$

$$z_R = \frac{wd}{\sqrt{(F_f \cdot r_{ofa})^2 / w_0^2 - 1}}. \quad (4.7)$$

In our simulations, $w_0 = 552$ nm and $z_R = 0.78$ μm for working distance of $WD = 2$ mm and $r_{ofa} = 2.04$ mm. The FWHM of the axial dimension of the two-photon excited focal spot is linearly related to the Rayleigh range by $z_{FWHM} = 1.29 \cdot z_R = 1.06$ μm . Thus the axial resolution of our simulation is 40% smaller than that measured from the IPSF^2 . The effect of this discrepancy in calculating R is shown in Figure 4.4—for a transparent medium, R is approximately twice that if the IPSF^2 is exactly simulated. In our application, we are studying the change in signal when imaging many mean free scattering lengths deep in turbid media. Imaging five mean free scattering lengths deep, for instance, the signal decays by over four orders of (slightly faster than Beer's law with a rate constant of $l_s/2$)[11],[110]. Thus, this inaccuracy in R value has a small effect on calculating the maximum imaging depth. Furthermore, because focal volume intensity distribution is not appreciably changed for moderate imaging depths, this error will be a constant offset with imaging depth from the more accurate value. In Chapter 5 we will show that an offset error will be accounted for in contrast values by the initial choice of staining inhomogeneity.

The Gaussian parameters used for in our simulations and two alternatives—matching the axial and lateral extents of the measured and diffraction limited IPSF^2 , are summarized in Table 4.1.

Parameter	Measured Values	Modeling focal spot with Diffraction-Limited IPSF ² (DL)	Modeling focal spot with Measured IPSF ² (PSF)	Modeling front aperture lateral focal spot with Measured IPSF ² (FA)
w_0	0.552 μm	$\frac{\sqrt{2} \cdot 0.325 \lambda}{NA^{0.91}}$	$\frac{r_{FWHM}}{\sqrt{\ln(2)}}$	$\frac{r_{FWHM}}{\sqrt{\ln(2)}}$
		0.366 μm	0.552 μm	0.552 μm
z_R	1.367 μm	$\frac{z_{FWHM}^{diff}}{2\sqrt{\sqrt{2}-1}}$	$\frac{z_{FWHM}}{2\sqrt{\sqrt{2}-1}}$	$\frac{WD}{\sqrt{\frac{(F_f \cdot r_{ofa})^2}{w_0^2} - 1}}$
		0.926 μm	1.367 μm	0.774 μm
w_{FA}	1.428 mm	$w_0 \sqrt{1 + \left(\frac{WD}{z_R}\right)^2}$	$w_0 \sqrt{1 + \left(\frac{WD}{z_R}\right)^2}$	$w_0 \sqrt{1 + \left(\frac{WD}{z_R}\right)^2}$
		790 μm	808 μm	1.428 mm

Table 4.1: Parameters for different focusing schemes.

Three parameters were measured in our system characterization— w_0 , z_R , and w_{FA} . This table summarizes three options in simulating these measurements—simulating the intensity distribution for a diffraction limited focal spot (DL), simulating the intensity distribution around the focal spot to match the IPSF² (PSF), and simulating the intensity distribution at the front aperture and the lateral distribution of the IPSF² (FA). r_{FWHM} , z_{FWHM} , and z_{FWHM}^{diff} are the measurements of the emission distribution (IPSF²) while other variables refer to the excitation distribution (IPSF) for the measured point spread function and a diffraction limited point spread function. The configuration we use in our system (FA) is matching the measured lateral excitation fluence at the objective front aperture and focal plane ($w_0 = 0.552 \mu\text{m}$ and $z_r = 0.774 \mu\text{m}$). Highlighted cells indicate areas where the simulation exactly matches measurements.

To verify the accuracy of our Monte Carlo model in simulating a Gaussian beam focus, we compared results to an analytical solution for fluorescence distribution in a transparent media from Eqs. (4.3) - (4.4). Evaluating the R value as a function of signal volume radius, r_s , we find excellent agreement between Monte Carlo model and the exact analytical result, indicating that our Monte Carlo model does faithfully reproduce a focused hyperboloid [Figure 4.4]. Results for this simulation were found to be the same

for pulsed and continuous wave Monte Carlo simulations, indicating that pulsed excitation light does not increase the nonlinear imaging resolution in a transparent medium. The spacing in the focal grid in these simulations was increased to $\Delta r = \Delta z = 0.1 \mu\text{m}$ to more smoothly match the exact solution.

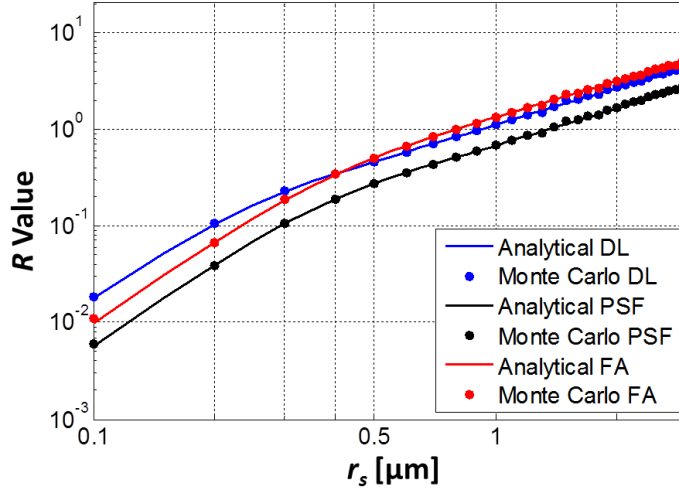


Figure 4.4: R value vs. r_s for different focusing schemes in a transparent medium.

Using the parameters listed in Table 4.1, we plot the Monte Carlo simulated and exact analytical values of the ratio of signal fluorescence and background fluorescence, R , for different signal volumes, r_s , in a transparent medium. DL: using parameters for matching the diffraction-limited focal volume. PSF: using parameters for matching the measured IPSF². FA: using parameters for matching to the front aperture fluence and the lateral measured point spread function fluence.

There are two caveats to consider in using the hyperboloid focusing method to model the focus of pulsed excitation light. First, in this method, excitation photons travel a slightly longer path than they would if aimed to the geometric focus. However this path length difference is small—for a spot size of $0.5 \mu\text{m}$ and an imaging depth of $300 \mu\text{m}$, the maximum relative path length fractional differences are less than 10^{-5} . A second, more significant, limitation to consider in this technique is that at increasing imaging depths, the larger angle excitation photons are attenuated fractionally more than the on-axis photons, leading to a gradual reduction in apparent spot size with imaging depth.

However, for small and moderate angular numerical apertures ($< 45^\circ$) and typical imaging depths ($< 5 l_s$), this effect is relatively subtle—at 5 scattering lengths deep with photons aimed for a 460 nm FWHM spot size, the resulting focal volume produces $\sim 10\%$ more signal at the focal plane than expected from a Gaussian spot size of equal peak intensity.

4.4.2. Temporal dependence

We obtained the intensity temporal impulse response of the system, $G(r, z, t)$, by setting initial photon times such that ballistic photons intercept the focal plane at exactly the same instant and counting the photons per lateral area found in each voxel. The intensity distribution was determined by convolving the impulse response with the Gaussian pulse envelope, f :

$$I(r, z, t) = \int_{-\infty}^{\infty} G(r, z, t') f(t - t') dt'. \quad (4.8)$$

Finally, the fluorescence generated per voxel, \mathcal{F} , was calculated by multiplying the integrated intensity squared by the volume of the voxel, V_v :

$$F(r, z) = \int_{-\infty}^{\infty} I(r, z, t)^2 dt \cdot V_v \quad (4.9)$$

4.5. COLLECTION

We use a second Monte Carlo simulation to model the effect of heterogeneous collection efficiency on maximum imaging depth. In this case, only detected emission is important, so photon time-of-flight tracking, and ray tracing through lateral planes was not necessary. Emission photons are initialized from a range of source positions (z_s, r_s) with an isotropic angular distribution, for each imaging depth (z_θ) . The escape position (r_e) and angle (θ_e) of each photon that leaves the tissue surface is cataloged. We

implemented the approach outlined by Oheim *et al.* to determine the fraction of collected photons[104]. The maximum acceptance radius (r_m) can be derived by examining the geometry of the system [Figure 4.5]:

$$r_m \approx r_f + z_0(r_{FA} - r_f)/WD, \quad (4.10)$$

where r_f is the field of view of the objective. For our 20x/0.95 objective, the field of view was measured by previous studies to be 1.3 mm[104]. We use an effective field of view of 1.0 mm, accounting for the limited collection angle of our PMT [Section 3.4]. The second component of the Oheim *et al.* approach is to account for the coupling between the maximum acceptance angle, θ_m , and r_m . To conserve beam étendue, the product of θ_m , and r_m is assumed to be constant. The value of this constant is found by considering the limiting case where the objective lens focuses to the sample surface, and $r_m = r_f$ [135]. The resulting relation is then:

$$r_m \theta_m \approx r_f \theta_f. \quad (4.11)$$

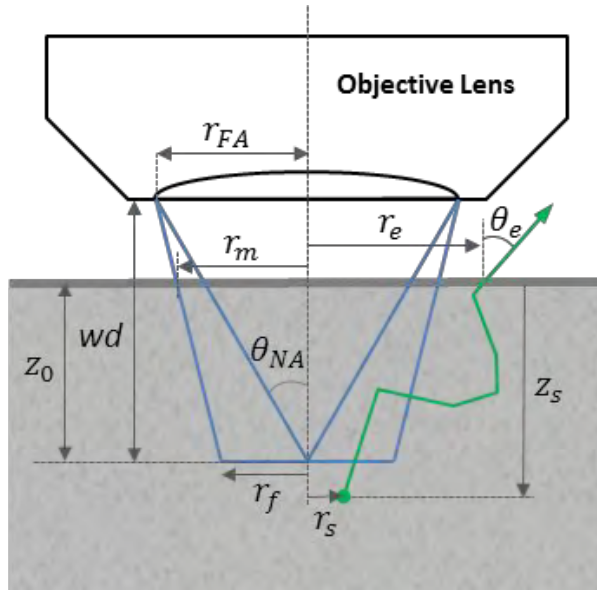


Figure 4.5. Collection simulation parameters. Photons are emitted with an isotropic angular distribution from a range of source positions, (z_s, r_s) , and the percentage of collected photons is recorded for each imaging depth, z_0 . Green line is the path of an emission photon. See text for definitions of parameters. Modified from Oheim et. al.[135].

4.6. IMPLEMENTATION

For shallow imaging depths ($z_0 \leq 3l_s$), 10^6 photon packets were propagated for each excitation simulation, while larger depths required 10^7 photon packets for adequate precision. The computationally intensive part of the program—tracing each photon packet through the excitation grids—was vectorized in Matlab, allowing for execution times close to an equivalent program written in C. The shallow and deep excitation simulations took 0.5 and 5 hours to complete, respectively, using a 3.7 GHz processor running Ubuntu Linux and a 64-bit edition of Matlab (Version 7.9).

Chapter 5

Deep two-photon autofluorescence microscopy of epithelial tissues

Endogenous fluorescence provides morphological, spectral, and lifetime contrast that can indicate disease states in tissues. Previous studies have demonstrated that two-photon autofluorescence microscopy (2PAM) can be used for non-invasive, three-dimensional imaging of epithelial tissues down to 150 μm beneath the skin surface [136]. We report ex-vivo 2PAM images of epithelial tissue from a human tongue biopsy down to 370 μm below the surface. At greater than 320 μm deep, the fluorescence generated outside the focal volume degrades the image contrast to below one. We demonstrate that these imaging depths can be reached with 160 mW of laser power (2 nJ per pulse) from a conventional 80 MHz repetition rate ultrafast laser oscillator. We studied image contrast as a function of depth in tissue phantoms with a range of optical properties typically found in epithelial tissues. The phantom data agree well with the estimated contrast decays from time-resolved Monte Carlo simulations and show maximum imaging depths similar to that found in human biopsy results. This work demonstrates that the low staining inhomogeneity and large scattering coefficient associated with visible-wavelength autofluorescence limits conventional 2PAM from imaging greater than 3-5 mean free scattering lengths deep in epithelial tissue.

5.1. INTRODUCTION

Two-photon autofluorescence microscopy (2PAM) has emerged as a versatile technique for non-invasive three-dimensional imaging of turbid biological samples with subcellular resolution[2],[3],[8]. Spectral and morphological information obtained from

intravital 2PAM of unstained epithelial tissues has shown promise for diagnosing and monitoring of carcinoma[21],[137-141]. Typically, carcinoma originates and is most clearly distinguished from normal tissue at the basal layer, which can be many hundreds of microns below the skin surface. Additionally, the quantification of epithelial layer thickness can be used as an indicator of dysplasia and carcinoma[21]. Thus, in the application of cancer diagnosis, it is particularly important to understand and extend the maximum 2PAM imaging depth in epithelial tissues.

In general, optical imaging depth in skin can be extended by using near-infrared (NIR) wavelengths of 700-1300 nm, which are minimally attenuated in biological tissues[142]. Confocal microscopy can image many hundreds of microns into epithelial tissue using NIR wavelengths and contrast from scattering or exogenous contrast agents[23],[24]. However, the dominant fluorophores naturally present in skin have ultraviolet and blue linear absorption bands[8],[143],[144], requiring low-visible-wavelength excitation and emission to be imaged with confocal microscopy. Consequently, confocal autofluorescence microscopy has been used to obtain axial sectioning in shallow regions of epithelial tissue but has not been reported more than a few tens of microns below the surface[25],[144],[145]. Two-photon imaging, on the other hand, has three working principles that make it particularly advantageous for deep microscopy of endogenous skin fluorescence: (1) the natural fluorophores in epithelial tissues can be excited nonlinearly with NIR light; (2) fluorescence generation in a sample is inherently confined to the focal volume, enabling three-dimensional sectioning while collecting both ballistic and scattered emission light; and (3) resolution is negligibly degraded from scattering because the fluorescence in the perifocal volume is generated almost entirely from ballistic photons[110],[111].

While imaging depth of confocal microscopy is limited by the challenge of getting sufficient levels of ballistic emission photons out of the tissue, nonlinear imaging depth is typically limited by the ability to deliver sufficient levels of ballistic excitation photons to the focal volume. To maintain constant two-photon excited fluorescence signal generated within the focal volume, the pulse energy delivered to the surface of the sample must be exponentially increased with increasing imaging depth. In biological samples, where the attenuation of NIR photons is dominated by scattering processes, the pulse energy must be increased with an exponential length constant of approximately one mean free scattering length, l_s . In practice, the excitation power delivered to the sample surface is increased at a slightly higher rate to compensate for increased losses from fluorescence collection and the longer path length seen by large-angle excitation photons.

Although increasing excitation power with imaging depth can maintain perifocal fluorescence generation at arbitrarily large imaging depths, the approximation that the two-photon excited fluorescence is generated only within the focal volume does not hold beyond ~ 3 mean free scattering lengths deep[122]. Appreciable out-of-focus (background) fluorescence can be generated by ballistic photons near the surface and by scattered photons through several mean free scattering lengths into the tissue, gradually reducing the image contrast[11],[131]. The ratio of collected signal fluorescence (F_s) to background fluorescence (F_b) then decays with increasing imaging depth. In cylindrically symmetric tissue, with a distance from the optical axis, r , and an axial distance from the tissue surface, z , this ratio can be described as:

$$\frac{F_s}{F_b} = \frac{\int_{V_s, -\infty}^{\infty} \phi(r, z) C(r, z, t) I^2(r, z, t) dt dV}{\int_{V_b, -\infty}^{\infty} \phi(r, z) C(r, z, t) I^2(r, z, t) dt dV}, \quad (5.1)$$

where the signal volume, V_s , is the volume of the feature of interest, the background volume, V_b , is the volume within the sample but outside of the signal volume, ϕ is the collection efficiency, C is the fluorophore concentration, and I is the excitation intensity.

The maximum imaging depth, z_m , can be defined as the depth at which the F_s/F_b ratio falls to one[11]. Previous studies have described the maximum imaging depth in units of optical depths, defined as z_m/l_s , for homogeneously stained tissue with similar excitation parameters. Theer *et al.* found a z_m of 3-4 scattering lengths when $l_s = 200 \mu\text{m}$ using an analytical model[11]. On the other hand, Leray *et al.* found a z_m of 5-6 optical depths when $l_s = 350 \mu\text{m}$ using a Monte Carlo model[131]. The difference suggests that z_m is dependent on l_s . Experimentally, z_{max} has also been measured, but only in stained brain tissue and phantoms with $l_s \approx 200 \mu\text{m}$ [11],[146]. Autofluorescence imaging in epithelial tissues presents a particularly challenging set of optical properties for deep two-photon imaging. First, the scattering length of epithelial tissues is typically in range of 40-200 μm —much smaller than those considered in previous studies. Second, endogenous fluorophores are dimmer and more homogeneously distributed than exogenous ones. Previous 2PAM reports have not reached z_m , and imaging depths have, to the best of our knowledge, been limited to 80-150 μm below the surface[3],[4],[129],[136],[137],[147-158]. Some previous studies have reported the ability to image 150-200 μm deep, but either do not present these images, or show images with no appreciable signal at these depths[3],[4].

In this paper, we present 2PAM images of a human tongue biopsy down to and beyond z_{max} . We show that this limit can be reached with a few hundred milliwatts available from conventional, high repetition rate oscillators in phantoms with optical properties in the range typically found in epithelial tissues. We describe the gradual

contrast decay of 2PAM for increasing imaging depths as a function of the fluorescence staining inhomogeneity and a ratio of integrated intensities. We examine the logarithmic dependence of maximum imaging depth on sample scattering length, which becomes important in imaging samples with short scattering lengths such as epithelial tissue. Finally, the F_s/F_b ratio is calculated with time-resolved Monte Carlo simulations and predicted contrast profiles are compared with measurements from tissue phantoms and ex-vivo human epithelial tissue.

5.2. METHODS

5.2.1. 2PAM contrast

In the absence of fluorescence saturation, photobleaching, and sample movement, the fluorophore concentration is independent of time. Assuming the concentration of fluorophores within V_s is a constant, C_s , and that the out-of-focus fluorophore concentration is diffuse enough to be approximated by the average fluorophore concentration, C_b , we can remove the concentration terms from the integral in Eq. (5.1). We define the staining inhomogeneity, χ , as the ratio of the fluorophore concentrations, and a value, R , as the ratio of integrated intensities:

$$\chi = \frac{C_s}{C_b}, \quad (5.2)$$

$$R = \frac{\int_{V_s} \int_{-\infty}^{\infty} \phi(\rho, z) I^2(r, z, t) dt dV}{\int_{V_b} \int_{-\infty}^{\infty} \phi(\rho, z) I^2(r, z, t) dt dV}. \quad (5.3)$$

We can then express the ratio of signal to background fluorescence as the product of χ and R :

$$\frac{F_s}{F_b} = \chi \cdot R. \quad (5.4)$$

Though our definition for F_s / F_b is the same as previous reports, our definition of χ and R differ from that described previously[11]. Our staining inhomogeneity is defined by the absolute concentrations of fluorophores inside and outside a signal volume, and does not depend on the perifocal intensity distribution (i.e. the numerical aperture), while our R value is defined with the volume of the feature of interest rather than the volume of the focal spot. Our approach has the distinction that the χ value is an intrinsic, system-independent property of the sample that scales linearly with changes in background or signal fluorophore concentration.

In this paper, we explore the gradual decay of image contrast, Q , versus depth due to out-of-focus fluorescence. We define the contrast in terms of the measured signal (MS) when the focal spot concentrically overlaps with V_s a bright feature of interest and the measured background (MB) when the focal spot is in a volume that produces relatively weak signal, such that:

$$Q = \frac{MS - MB}{MB}, \quad (5.5)$$

where,
$$MS = C_s \times \int_{V_s} \int_{-\infty}^{\infty} \phi(r, z) I^2(r, z, t) dt dV + C_b \times \int_{V_b} \int_{-\infty}^{\infty} \phi(r, z) I^2(r, z, t) dt dV, \quad (5.6)$$

and
$$MB = C_b \times \int_{V_s} \int_{-\infty}^{\infty} \phi(r, z) I^2(r, z, t) dt dV + C_b \times \int_{V_b} \int_{-\infty}^{\infty} \phi(r, z) I^2(r, z, t) dt dV. \quad (5.7)$$

Note that our measured background includes a fluorescence contribution from within the defined signal volume. This term becomes important for samples where the fluorophore is relatively homogeneously distributed and there are relatively few regions with truly dark signals. Using the definitions in Eqs. (5.2) and (5.3), and rearranging Eqs.

(5.5)-(5.7), we can express the contrast at a given imaging depth, z_0 , as a function of χ and R :

$$Q(z_0) = \frac{\chi - 1}{1 + 1/R(z_0)}. \quad (5.8)$$

This relation shows that the contrast approaches zero as the staining inhomogeneity approaches one (i.e. a uniformly stained sample), or as R approaches zero. If the fluorophore concentration is zero in the focal volume for the *MB* measurement, Q is equal to F_s / F_b . In the more general case, with some fluorescent signal present in the focal volume of the *MB* measurement, $Q(z_0)$ becomes approximately equal to F_s / F_b for small values of R . In this paper, we define our maximum imaging depth as the depth at which the contrast falls to one.

We use a Monte Carlo and an analytical model to calculate $Q(z_0)$, and compare it with the measured values for a variety of sample conditions. For Eq. (5.8) to be accurate, we must choose a signal volume of approximately constant fluorophore concentration, a condition that is closely approximated in tissue phantoms with fluorescent beads by choosing V_s as the volume of the fluorescent bead.

5.2.2. 2PAM system

We used the nonlinear microscope described in Chapter 3 for 2PAM imaging. Briefly, imaging was performed at 760 nm excitation wavelength because it yields the brightest autofluorescence signal with minimal excitation light bleed-through in our system. Two half-waveplate/polarizing beam cube pairs attenuate the excitation beam and a pair of galvanometer scanning mirrors (Cambridge Technologies, 6215h) scans the laser into an upright microscope. We use a high NA, water dipping objective with a large field of view and a 2 mm working distance (0.95/20x Olympus XLUMPFL). A schematic

of the collection path is shown in Figure 5.1 (a). We used the two-lens optimization procedure discussed in Section 3.4, with initial angular and spatial distributions shown in Figure 5.1 (b). The focal lengths and positions of the CL1 and CL2 were found by maximizing the photons hitting the PMT cathode [Figure 5.1 (c)]. The large field of view is especially important for high collection efficiency at large imaging depths[104]. The physical radii of the back aperture, r_{BA} , and front aperture, r_{FA} , of this objective are 8.5 mm and 2 mm, respectively. The measured beam $1/e^2$ radius of the excitation beam, w_{BA} , was 6 mm at the objective back aperture, giving a fill factor of 0.7. We measured the total power transmission through the objective to be 70% at 760 nm.

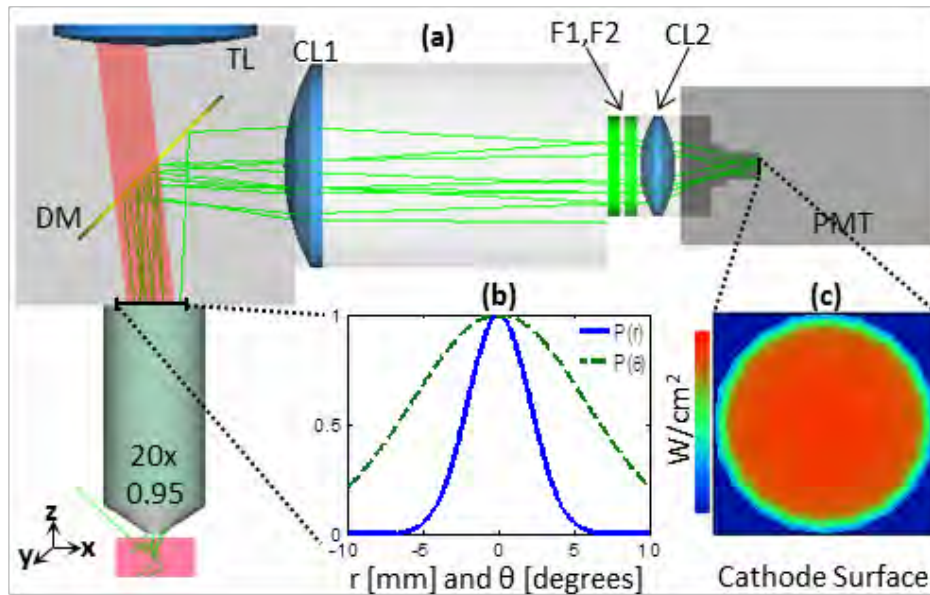


Figure 5.1: Schematic of two-photon imaging system collection path.

(a) Excitation light is scanned through a large field-of-view, long working distance objective. Emission light collection is optimized using stochastic spatio-angular distribution of fluorescence photons at the back aperture of the objective (b) and maximizing photon hits at the cathode surface (c) as CL1 and CL2 are varied. TL: tube lens, DM: dichroic mirror, CL: collection lenses, F: excitation filters, PMT: photomultiplier tube detector. The objective lens choice is especially important to maximize imaging depth.

5.2.3. Monte Carlo model

We used the Monte Carlo model developed in Chapter 4 to calculate R values, and compare to phantom and biopsy results. We used an excitation wavelength of 760 nm, and l_s values of 40, 80, and 120 μm to match phantom results. Focusing was simulated as a Gaussian beam shape, which matched the excitation beam profile at the front aperture of the objective and the lateral extent of the IPSF² at the focal plane. For the collection simulation, we used a collection scattering length of $l_s^{\text{collection}} = l_s / 1.7$, for each of the corresponding scattering lengths at 760 nm.

5.2.4. Analytical model

We applied the analytical model developed by Theer and Denk to calculate the fluorescence distributions for different optical system and sample parameters[120]. In short, we consider the ballistic and scattered light distributions in turbid media independently and then combine the resulting intensities to calculate total fluorescence. The intensity from ballistic photons assumes an incident beam with Gaussian spatial and temporal distributions. Using the spherical wave solution to the telegrapher's equation and the Fresnel approximation, we describe the ballistic intensity as a function of a depth dependent Rayleigh range, which reduced the effective numerical aperture with depth. The scattered light is modeled using a small angle approximation and statistical methods to calculate an effective temporal and transverse spatial beam width. We used a numerical aperture of 0.75, which produces a similar spot size to that measured from our IPSF². All other parameters used in the analytical model were the same as those used in the Monte Carlo model.

5.2.5. Tissue phantom preparation

To measure the experimental contrast decay of two-photon imaging in a turbid media, we prepared twelve scattering agar phantoms with a range of optical properties similar to what is typically observed in epithelial tissues. Low melting point agarose (1.0%, Sigma) was prepared with 0.95 μm diameter polystyrene beads (Bangs Labs, PS03N) to vary scattering coefficient, 1 μm diameter fluorescent polystyrene beads (Invitrogen F-8823) to provide features for contrast measurements, and fluorescein (Fluka 46955) to control staining inhomogeneity. Polystyrene beads were ultrasonicated for 30 minutes to reduce aggregations before they were mixed into the agar phantoms. To increase the two-photon action cross section of fluorescein, we mixed the agar solution with 2% pH 12 buffer. Polystyrene concentrations of 1.7×10^{10} , 0.9×10^{10} , and 0.6×10^{10} particles per mL provided scattering mean free paths of 40, 80, and 120 μm at 760 nm excitation, and 23, 46, and 69 μm at 515 nm emission, respectively. We determined the scattering coefficient with a Mie calculation using polystyrene sphere and agar gel refractive indices of 1.58 and 1.33, respectively[159]. To verify the scattering lengths of our polystyrene solution matched Mie predictions, we measured attenuation of collimated 760 nm light through dilute solutions of polystyrene beads in a cuvette. Fluorescent beads were added to at a constant concentration of 3.5×10^8 particles per mL in all phantoms.

We added increasing amounts of fluorescein to get final concentrations of 0, 4, 10, and 25 μM for each scattering length tested, creating a total of 12 phantoms. This approach allows the formation of phantoms with low staining inhomogeneities without an increase in scattering coefficient that would result from adding high concentrations of fluorescent polystyrene beads. Additional benefit of using this method is that we can increase the background fluorescence immediately adjacent to the fluorescent beads. In contrast, previous studies that varied fluorescent bead concentration could control the

fluorescence only in volumes many microns away from the signal volume[11]. Thus our approach provided a more appropriate model for studying autofluorescence contrast decay, where the local fluorophore concentration changes rapidly in short distances from nucleus to cytoplasm to extracellular matrix. The disadvantage of our approach is that the out-of-focus background fluorescence cannot be measured directly because there is no region without some fluorescent signal—when the focal spot does not overlap with a fluorescent bead, the measured background still includes some contribution from the fluorescein in the focal volume. However, the contrast defined in Eq. (5.5) can still be calculated, given sufficient signal to noise that fluorescent beads can be identified.

We obtained lateral phantom images at one micron depth increments from the surface to the depth where the image contrast fell to approximately 0.1. The contrast for each of the 16 phantoms was analyzed using an automated bead-finding script written in Matlab. We applied a binary mask with a threshold of four standard deviations above the mean pixel value for each lateral image. Beads were then localized by finding the three dimensional position of the centroid of each continuously weighted connected region in the binary stack. We only counted the connected regions of the expected single bead size to exclude clusters and isolated noisy pixels. Beads within 10 μm of the edge of the stack were also ignored. The MS for each bead was then calculated as the average of the maximum 4 voxels (150 x 150 x 1000 nm/voxel) within each region and the MB was calculated as the average pixel value of the non-connected regions at the depth determined by the centroid of the bead. The contrast was monitored for increasing imaging depth, while the excitation power was manually increased to maintain constant detected signal, slightly below the saturation levels of our system.

5.2.6. Biopsy preparation

Human oral cavity biopsies were obtained from The University of Texas M. D. Anderson Cancer Center as part of an ongoing project for two-photon diagnosis of oral malignancies. The study was reviewed and approved by the internal review boards at M. D. Anderson Cancer Center and the University of Texas at Austin. Biopsies were excised from suspicious regions and contralateral normal tissue in the oral cavity and submitted for histopathology. We present two-photon images from the normal biopsy in this paper. The biopsy was approximately 3 mm in diameter and 5 mm thick, delivered in chilled culture media (Phenol Red-free DMEM High, Fisher Scientific) and imaged within 6 hours of excision. The biopsy was stabilized on Petri dishes with low melting point agar and imaged at room temperature in a culture media bath.

5.3. RESULTS AND DISCUSSION

5.3.1. Monte Carlo simulation

We used our Monte Carlo model to calculate R as a function of depth for each phantom. For these calculations, V_s was set to the volume of the 1 μm diameter fluorescent beads which provide the signal in the phantoms. Figure 4 presents the fluorescence distribution for imaging 400 μm deep in a homogeneously labeled sample with an l_s of 80 μm . In this case, the collected background fluorescence overwhelms the signal fluorescence by approximately 30 times. The cross section of the fluorescence generation rate shows that background fluorescence generation density peaks on the optical axis near the focal volume [Figure 5.2 (a)]. When the fluorescence is integrated circumferentially, we observe that the cumulative background fluorescence generation peaks slightly off axis because the off-axis fluorescence is generated in larger volumes [Figure 5.2 (b)]. Finally, integration of this fluorescence radially shows that the total

fluorescence generation at each transverse plane is relatively constant through the first two l_s , and monotonically decreasing at larger depths [Figure 5.2 (c)].

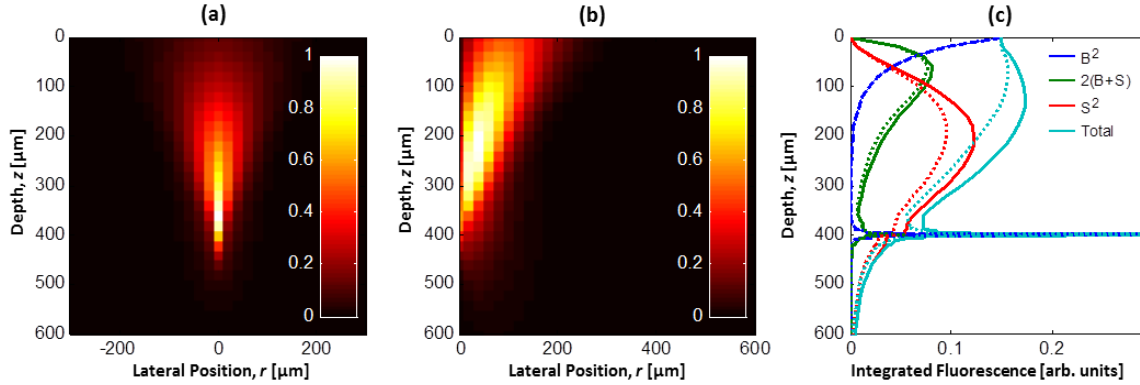


Figure 5.2: Monte Carlo results for imaging 400 μm deep in $l_s = 80$ μm tissue. Monte Carlo simulations of time-integrated fluorescence distribution as generated in the sample for an imaging depth of 400 μm in media with a 460 nm FWHM lateral spot size, $\tau_p = 270$ fs, $l_s = 80$ μm , and $g = 0.85$. These parameters resulted in an R value of $1/70$. (a) Sagittal slice of out-of-focus fluorescence shows increasing fluorescence generation rate close to the optical axis and the focal volume. (b) When out-of-focus fluorescence is integrated circumferentially, it is apparent that total fluorescence peaks off axis, but is fairly diffusely generated. (c) When integrated radially, the contributions from ballistic (B^2), scattered (S^2), and combined $2(B+S)$ photons can be visualized. The total fluorescence generation per transverse slice decreases nearly monotonically from the surface to beyond z_0 . The solid and dotted lines represent simulations with excitation pulse durations of 270 and 135 fs, respectively. (a) and (b) are normalized so that the maximum out-of-focus fluorescence is one, (c) is normalized so the maximum fluorescence is one.

The contributions from ballistic (B) and scattered (S) fluence were separated by tagging scattered photons in the Monte Carlo simulations [Figure 5.2 (c)]. The fluorescence generation at each voxel will then be proportional to $(S+B)^2$. These results can provide some insight into how certain parameters affect the generation of background fluorescence. For instance, previous studies have shown that the R value can be increased by using shorter pulses[11],[131]. Looking at the individual components as the pulse duration is decreased, it is entirely the scattered (S^2) and combined ($2BS$) terms that show a relative reduction in contribution of background fluorescence. Scattering can be thought

of as a source of temporal dispersion from the sample on the scattered fluence. Thus, as the pulse duration is increased, the dispersion of the scattered light reduces its contribution more than for longer pulse durations, resulting in an increase in R for shorter pulsed durations.

Though high collection efficiency is important for reaching large imaging depth with limited excitation power, we found that heterogeneous collection efficiency generally had a small effect on our calculations of R . In the $l_s = 80 \mu\text{m}$ simulation ($l_s^{\text{emission}} = 46 \mu\text{m}$), the collection efficiency only reduced R by 12% at $z_0 = 400 \mu\text{m}$, and by 60% at $z_0 = 800 \mu\text{m}$. The radial dependence of the collection efficiency had an especially weak effect on R , since the majority of the fluorescence generated in the excitation simulations was within $200 \mu\text{m}$ of the optical axis.

5.3.2. Phantom imaging

For all three sets of phantoms ($l_s = 40, 80, \text{ and } 120 \mu\text{m}$), we had sufficient power to reach contrast levels below one. Typically, excitation powers smaller than 1 mW were sufficient to image at the surface, while several hundreds of mW were required at the largest depths. For the phantom with $l_s = 80 \mu\text{m}$ and $\chi = 300$, for example, the power was increased from 0.7 mW at the surface to 483 mW at $510 \mu\text{m}$ depth. We identified an average of 190 beads per $77 \times 77 \times 100 \mu\text{m}^3$ field of view in each of the 12 phantoms using the automated bead-finding script. This number of beads corresponds to a bead concentration of 3.2×10^8 beads per mL , slightly less than the expected value of 3.5×10^8 beads per mL .

Figure 5.3 shows XZ images of the $l_s = 80 \mu\text{m}$ phantom set for different staining inhomogeneities. Each XZ reconstruction is created from a maximum projection through $15 \mu\text{m}$ (45 pixels) of Y . The accompanied biopsy images are discussed in Section 5.3.5.

We estimated the staining inhomogeneity of phantoms using the measured contrast at the surface of each phantom and the R values found from Monte Carlo simulations. The R value since it only changes slightly for shallow imaging depths in our Monte Carlo model—a decrease from 0.51 at the surface to approximately 0.46 at one l_s deep. Substituting an R value of 0.5 in Eq. (5.8), the staining inhomogeneity, χ , becomes approximately equal to 3 times the measured contrast at shallow depths, for large values of χ . Using this approximation, we estimate the average staining inhomogeneities to be $\chi = 300, 62, 25,$ and 10 , by using the average contrast from beads identified within the first 20-40 μm of the three phantoms at each staining inhomogeneity.

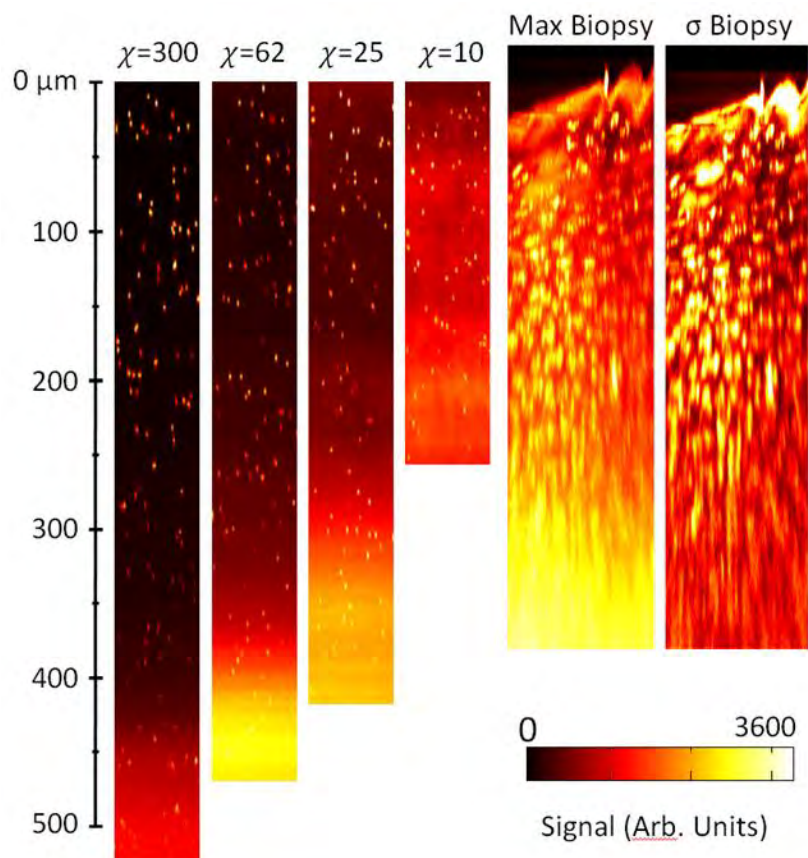


Figure 5.3: XZ cross sections of phantoms and biopsy.

Comparison of XZ images of phantoms with constant scattering length of $l_s = 80 \mu\text{m}$ for increasing staining inhomogeneity, χ , and a human tongue biopsy. Phantom cross sections are maximum projections through $15 \mu\text{m}$ of Y. Biopsy cross sections shown are a maximum projection “max Biopsy” and a standard deviation projection “ σ Biopsy” through $15 \mu\text{m}$ of Y. The standard deviation projection is normalized so that the maximum value is white. Images are stretched in the axial direction by 6.6x so that pixels are equal in size in axial and lateral dimensions.

The measured bead size remained constant with imaging depth for all phantoms. Figure 5.4 shows a representative case for the measured bead size versus depth for the $l_s = 80 \mu\text{m}$, $\chi = 300$ phantom. We determined the FWHMs of bead sizes by fitting a Gaussian function through the centroid of each bead found in the phantom. We found a slightly smaller bead sizes in the direction of our fast moving mirror (horizontal), indicating a slightly smaller resolution in that direction, possibly due to a slight ellipticity of the beam shape at the back aperture of the objective. The apparent axial resolution

measured from the 1 μm beads was noticeably larger than that measured from the IPSF² with 100 nm beads. We attribute this large axial resolution to sparse sampling (axial spacing between images was 1 μm) and long times between imaging the top and bottom of the beads (the time elapsed between the first image and last image 3 μm apart was approximately 10 seconds). Nonetheless, the constant lateral and axial size of the measured beads does indicate minimal specimen-induced aberrations with increasing imaging depth. This result is in contrast to studies without index matching, where spherical aberrations are commonly observed[101],[102].

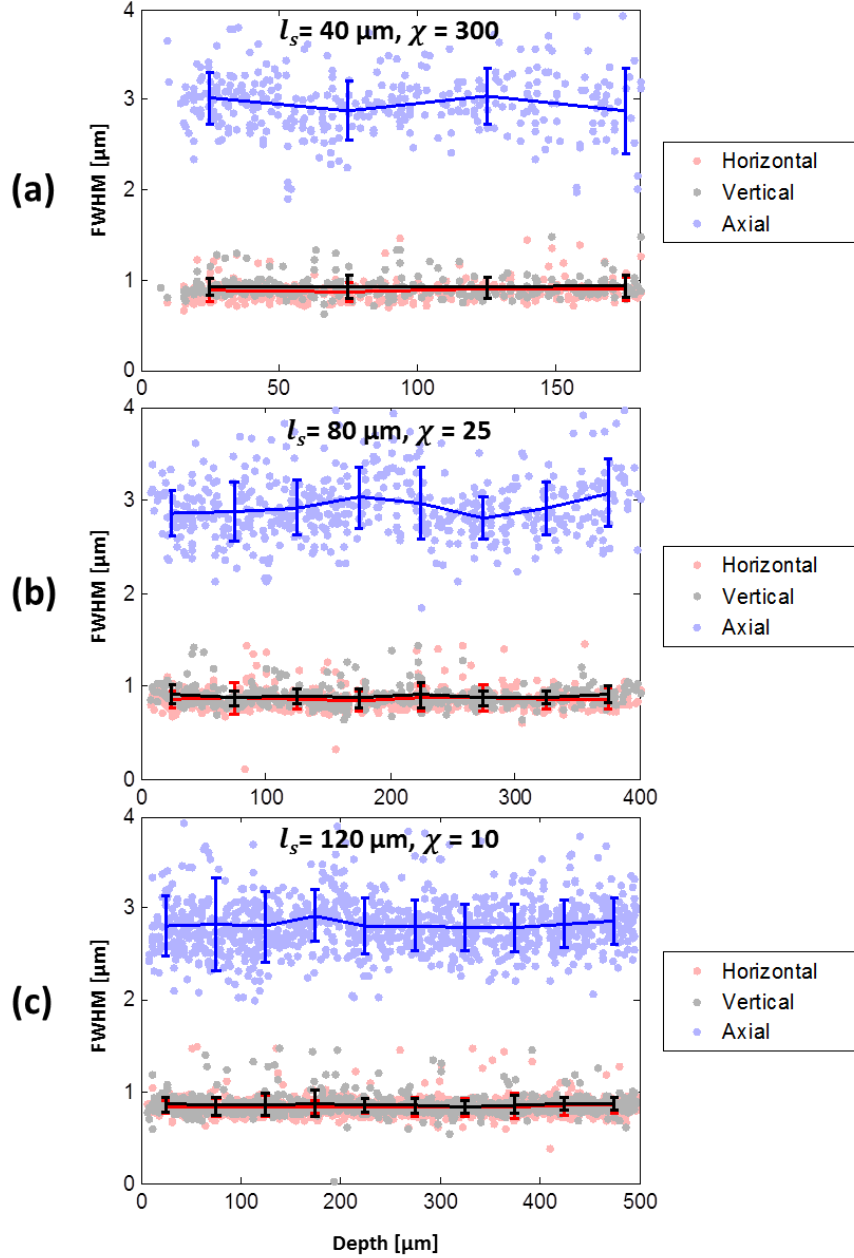


Figure 5.4: Measured bead size vs depth.

Measured sizes of 1 μm diameter fluorescent beads versus depth for the $l_s = 40 \mu\text{m}$, $\chi = 300$ phantom (a), the $l_s = 80 \mu\text{m}$, $\chi = 25$ phantom (b), and the $l_s = 120 \mu\text{m}$, $\chi = 10$ phantom (c), in the lateral and axial directions. The trend and error bars are calculated by the mean and standard deviations of sizes obtained by binning the beads at 50 μm depth increments. We observed no significant increase in bead size and, thus, in system resolution with increasing imaging depth in any of our phantoms.

5.3.3. Fluorescence decay

We measured the decay of the signal, background, and total fluorescence with increasing imaging depth in our twelve phantoms. By increasing the excitation power exponentially with imaging depth and normalizing measured signal at each imaging depth by the expected quadratic increase with the excitation power, $(P(z=0)/P(z=z_0))^2$, we could accurately measure fluorescence decays far beyond the limited dynamic range of our detection system.

Figure 5.5 shows the measured and calculated fluorescence decays of the three $\chi = 62$ phantoms. Looking at the $\chi = 62$, $l_s = 80 \mu\text{m}$ phantom, Figure 5.5 (a) shows the decays of the average value of the measured background at each imaging plane (MB), the measured signal for each fluorescent bead (MS), and the difference (MS-MB). Note that the slopes of the (MS-MB) and MB decays are approximately equal for imaging depths down to three mean free scattering lengths. This result suggests that the contrast, defined as the ratio of (MS-MB) to MB, is relatively constant for shallow depths. At larger imaging depths ($z > 4l_s$) the measured signal, which decays exponentially, is overcome by the background, which decays with z_0^{-1} [11]. Comparing the fluorescence decay in phantoms with different scattering lengths, we found good agreement between the measured data and the Monte Carlo predictions [Figure 5.5 (b) and (c)]. The decay of the fluorescent signal from the biopsy also shown in Figure 5.5 (a), and will be discussed in section 5.3.5.

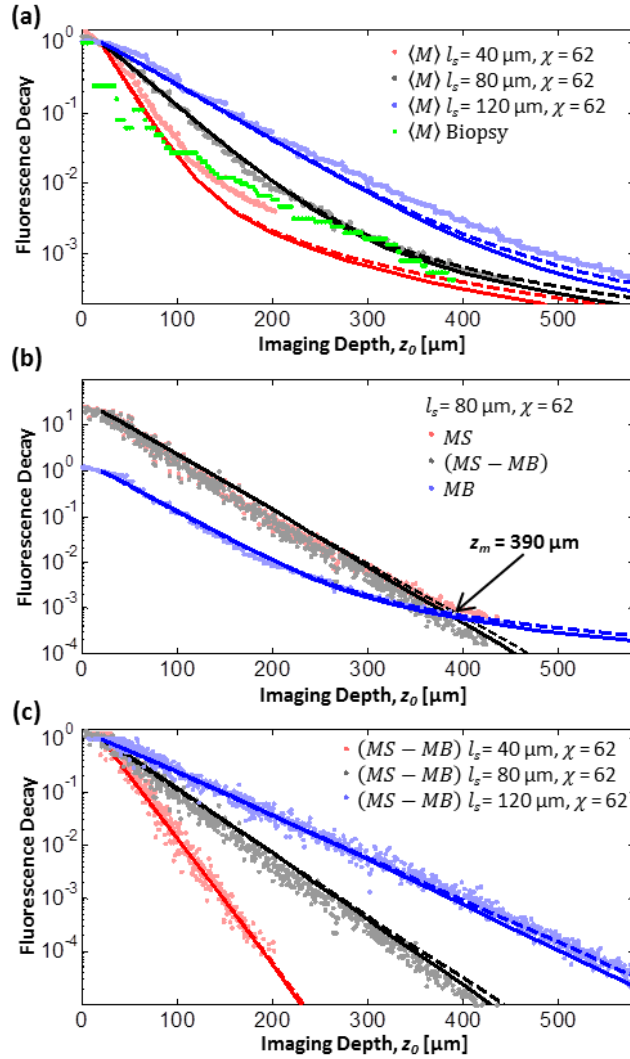


Figure 5.5: Fluorescence signal and background decays.

Plots of normalized fluorescence decays versus imaging depth for constant staining inhomogeneity ($\chi = 62$). Points are data from phantom measurements and lines are the decays predicted by our Monte Carlo simulation with homogeneous (solid lines) and heterogeneous (dashed lines) collection efficiency. (a) The average fluorescence decay, $\langle M \rangle$, represents the average pixel value recorded at each imaging depth. For comparison, the average fluorescence decay of the biopsy is also shown. (b) Examining relative decays for the measured signal (MS), measured background (MB), and difference (MS-MB) versus depth for the $\chi = 50$, $l_s = 80 \mu\text{m}$ phantom, we found a maximum imaging depth of $z_m = 390 \mu\text{m}$. (c) The background-subtracted fluorescence decay exhibits exponential decay for the entire measured range. Monte Carlo simulations agree well with experiments for homogeneous collection efficiency (dashed lines) and heterogeneous collection efficiency (solid lines). Decays are normalized to one at $20 \mu\text{m}$ deep in (a) and (c). In (b), the background is normalized to one at $20 \mu\text{m}$ deep, and the signal and background corrected signal scaled to their values relative to the background.

The effect of heterogeneous collection efficiency has little effect on the calculated decay curves, indicated by the overlap of the Monte Carlo results for shallow and moderate imaging depths. We also found that changing the staining inhomogeneity had little effect on the observed fluorescence decay rate, as summarized in Table 1. Instead, the staining inhomogeneity had the effect of raising or lowering the initial MB value, appearing instead to only change relative difference between MS and MB at the surface.

Table 5.1 summarizes the measured length constants, l_s^m , obtained from the exponential decay rates of the background-subtracted fluorescence in each phantom, and the corresponding decay constants predicted by Monte Carlo models. In all phantoms, the actual scattering length could be estimated to within 10% accuracy by using the approximation: $l_s = 2.3l_s^m$. This is close to a previous report, which found a factor of 2.5 relation between l_s^m and l_s using an NA of 1.2[110].

l_s [μm]	Measured Length Constants, l_s^m / l_s					
	Phantom Measurements				Monte Carlo Data	
	$\chi=10$	$\chi=25$	$\chi=62$	$\chi=300$	Homogeneous Collection	Heterogeneous Collection
40	0.43	0.45	0.43	0.45	0.50	0.48
80	0.40	0.43	0.41	0.41	0.46	0.44
120	0.43	0.45	0.45	0.43	0.46	0.43

Table 5.1: Measured decay constant compared to phantom mean free scattering length.

Summary of fluorescence signal decay length constants from exponential fits to measured phantom data (from $z_0 = 0$ to $3 l_s$) and predicted in Monte Carlo data, with and without including the effect of heterogeneous collection efficiency.

5.3.4. Contrast decay

The measured contrast decay from tissue phantoms showed similar trends to those predicted by Monte Carlo and analytical models (Figure 5.6). The Monte Carlo model matches the analytical model relatively well for the higher χ values tested. For the $\chi = 10$ phantom, the measurements demonstrate shorter z_{max} than predicted, likely due to the high concentration of fluorescein in these phantoms beginning to absorb significant amounts of emission (the “inner filter” effect). If the absorption length is known at the emission wavelength, this effect could be modeled using a shorter mean free absorption length in our collection efficiency calculations.

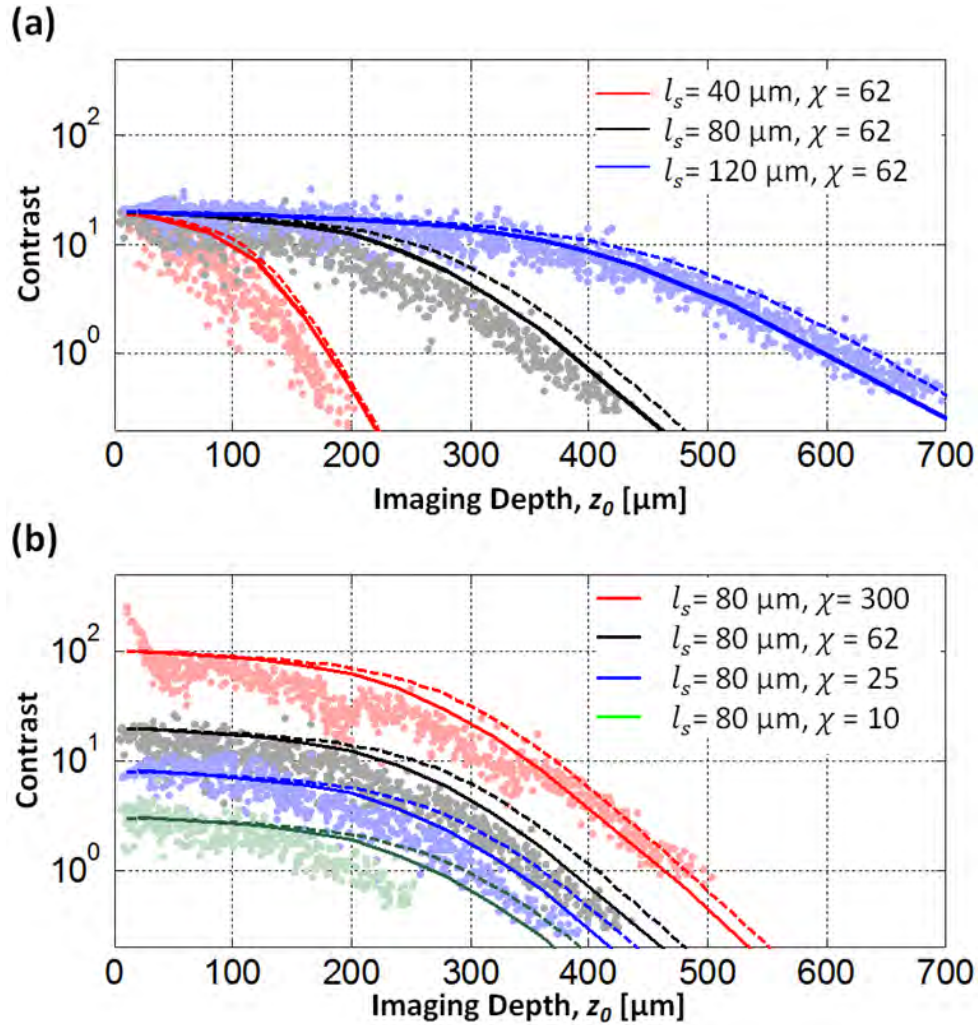


Figure 5.6: Contrast decays.

Contrast decays of phantoms with (a) constant staining inhomogeneity and (b) constant scattering length. Monte Carlo simulations (solid lines) agree well with the analytical model (dashed lines) and the phantom contrast measurements (solid dots). Both models slightly overestimate the maximum imaging depth, increasingly at lower staining inhomogeneities.

We observed that for the $\chi = 300$ phantoms, the contrast was higher than the expected values at shallow depths [Figure 5.6 (b)]. We attribute this large contrast to an effective increase in χ at shallow depths. Because no fluorescein was added in this set of phantoms, the staining inhomogeneity was determined by the influence of background fluorescent beads. For the shallowest beads, there are no background fluorescent beads

directly above them, effectively increasing their apparent staining inhomogeneity. For deeper beads, the fluorescent beads present above the imaging plane produce background fluorescence.

5.3.5. Human biopsy imaging

Figure 5.7 presents a summary of the 200 autofluorescence images collected at 2 μm depth increments from a biopsy of healthy human tongue tissue. The water-dipping objective allowed us to visualize the natural surface roughness of the tissue, which plays a role in collection efficiency [Figure 5.7 (a)][135]. The three dimensional rendering of the biopsy images was performed using Huygens[®] SVI renderer. We defined the surface ($z = 0 \mu\text{m}$) as the depth at which half of the field of view had signal. We increased the excitation power delivered to the tissue surface gradually from 3 mW at the surface to 30 mW at 170 μm deep. At larger imaging depths, we could maintain constant signal detected while increasing the excitation power less rapidly. We used a maximum of 160 mW of excitation power when imaging 380 μm deep.

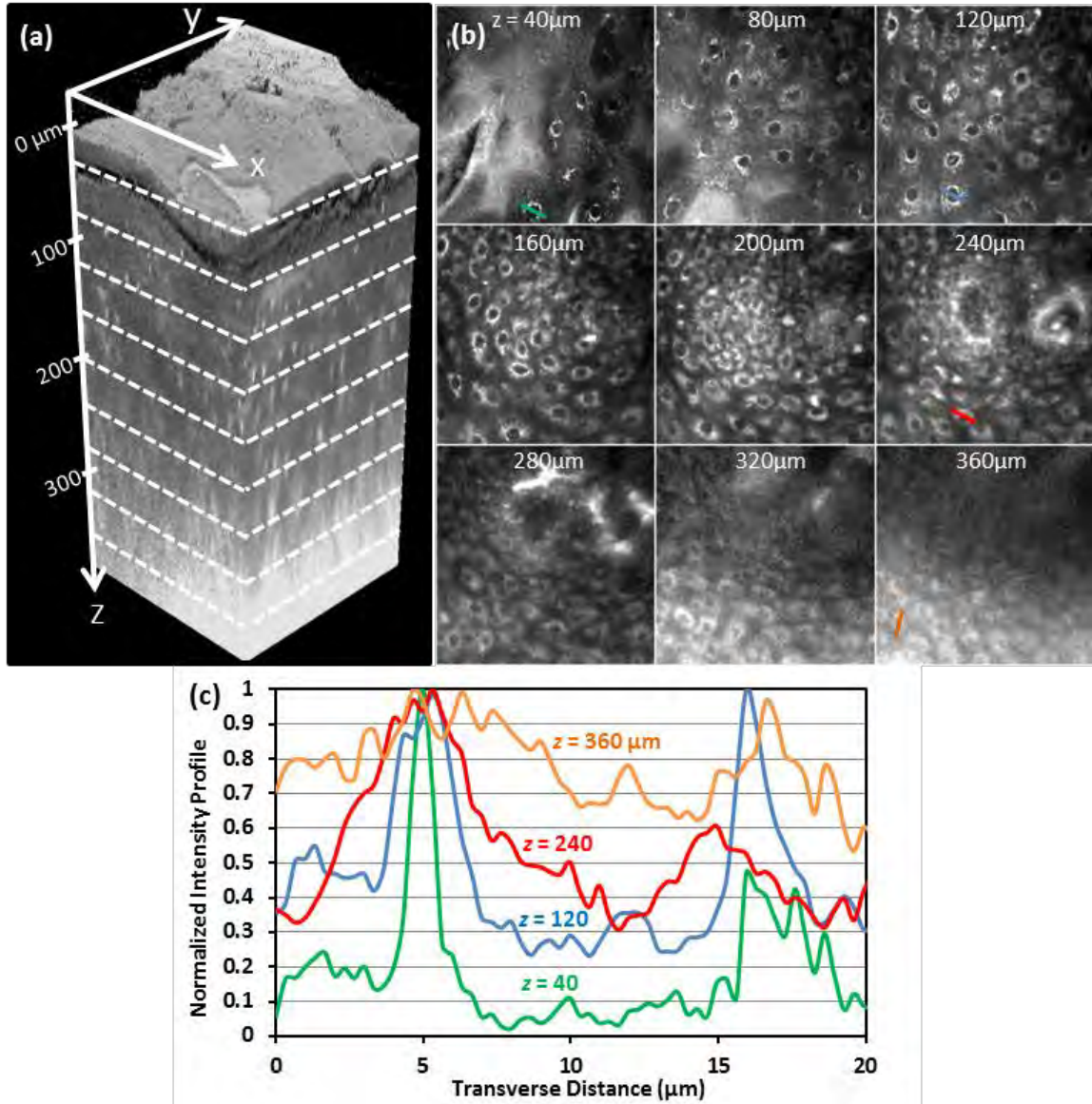


Figure 5.7: Biopsy images.

(a) Three-dimensional rendering of a sequence of 200 lateral 2PAF images acquired from healthy human tongue biopsy. (b) Selection of lateral images from an imaging depth of 40 to 360 μm . Field of view in all lateral images is 170 μm . (c) Normalized signal profile from manually identified cells at imaging depths of 40, 120, 240, and 360 μm . Profiles are taken from lateral lines indicated in (b).

Lateral images show subcellular resolution and cellular morphology with bright cytoplasm to dark nucleus contrast [Figure 5.7 (b)]. Contrast is presumably due to high concentrations of NADH, NAD, and FAD in the cytoplasm, which have been shown to

be the dominant endogenous fluorophores in confocal autofluorescence imaging of cervical and oral epithelial tissues[160],[6], and are efficiently excited in 2PAM at 760 nm excitation[8]. We found especially high signal levels from the stratum corneum, which, based on our Monte Carlo model, would contribute heavily to the out-of-focus fluorescence found at large imaging depths.

A maximum XZ projection through 15 μm of Y shows that at large depths, bright pixels in the background substantially degrade the contrast beyond 300 μm [Figure 5.3]. A normalized standard deviation projection through 15 μm of Y gives values similar to the measured contrast—it shows bright regions where there are large changes in pixel values. At shallow depths, this projection shows large values where there is variation between the bright cytoplasm signal and dark nuclei. At large depths, the increase in low-spatial-frequency, out-of-focus background fluorescence reduces the lateral variation in signal, and the corresponding standard deviation along Y decreases.

We examined the total fluorescence decay with imaging depth to estimate the scattering coefficient of the biopsy. Though fluorescence decay accurately predicted the scattering coefficient in phantoms, extending this method to the biopsy can be complicated by several effects. (1) The scattering length and fluorophore concentrations are likely to change with depth. Previous studies have observed brighter signal coming from the stratum corneum and basal membrane than at the intermediate epithelial layers[6],[130]. (2) As the excised tissue dies, the autofluorescence signal levels will gradually decay with time. We observed that the superficial regions of the tissue begin losing fluorescence signal more rapidly than the interior regions, creating a time-dependent change in relative fluorescence density. (3) Specimen induced aberrations typically become more severe with increasing imaging depths[161], and would result in a higher apparent rate of fluorescence decay. Though we verified aberrations played a

minimal role in degradation of signal in the phantom, without a constant-size point source in our biopsy, we were unable to monitor our excitation spot size with depth in the biopsy. Nevertheless, we obtain an estimate of the biopsy scattering coefficient by comparing our measured biopsy fluorescence decay to phantom experiments [Figure 5.5 (a)]. We fit an exponential curve to the first 200 μm of fluorescence decay obtained from the biopsy and found a length constant of 39 μm , corresponding to a scattering length of 89 μm , assuming $l_s = 2.3l_s'$ [Section 5.3.3]. At larger depths, the fluorescence decayed less rapidly, showing a similar slope to the $l_s = 120 \mu\text{m}$ phantom.

Figure 5.7 (c) presents typical contrast levels obtained from bright features at different imaging depths. We examined the contrast in line profiles drawn through manually identified epithelial cells marked by the lines drawn in the lateral images displayed in Figure 5.7 (b). At 40 μm deep, the brightest signal from the cytoplasm is approximately twenty to forty times larger than the minimum signal from within the nucleus, while the average signal from the cytoplasm is approximately five to ten times the average signal from the nucleus [Figure 5.7 (c)]. Using averaged signal and background as contrast, and employing the same method used with the phantoms, we estimate the χ of the biopsy to be 15-30. The contrast falls to one in our biopsy around 320 μm below the tissue surface, approximately 3-4 mean free scattering lengths deep.

5.3.6. Fluorescence saturation and photobleaching

The analysis presented in this paper has assumed that the intensity ranges used in our experiments are low enough to assume negligible fluorescence saturation and photobleaching—that is, that the fluorescence generation is quadratically dependent on the excitation intensity and is time-independent. However, at high intensities, these

assumptions no longer hold. We performed a series of tests to verify that we do not experience any saturation and photobleaching in our experiments.

Fluorescence saturation can broaden the PSF, as fluorophores in the highest intensity regions no longer generate greater emission signal than fluorophores further away. The resulting decrease in resolution has been previously demonstrated, but is expected to have a significant effect only under a combination of high intensities and especially large two-photon action cross section (> 1000 GM cross section at 1 mW of excitation power delivered to the imaging plane)[162]. Our observation of constant measured bead size with increasing imaging depth indicates a negligible influence of fluorescence saturation in our phantom experiments [Figure 5.4]. To test for fluorescence saturation in our biopsy experiments, we verified that our detected signal scales quadratically with excitation at select imaging depths. We measured power dependencies of 1.94, 2.00, 1.97, and 1.99 at increasing imaging depths of $z_0 = 290, 300, 326,$ and $356 \mu\text{m}$, respectively. In phantoms, we also observed that the signal from the identified beads scaled to the power of 1.98 ± 0.05 at each $100 \mu\text{m}$ imaging depth increment.

We also tested for the presence of photobleaching in 2PAM of the biopsy by measuring the ratio of the average signal of the first and last image taken at every image plane. Each imaging plane was raster scanned 8 times at 3 frames per second. We found an average ratio of 1.002 for the biopsy, and no trend for photobleaching at larger imaging depths [Figure 5.8].

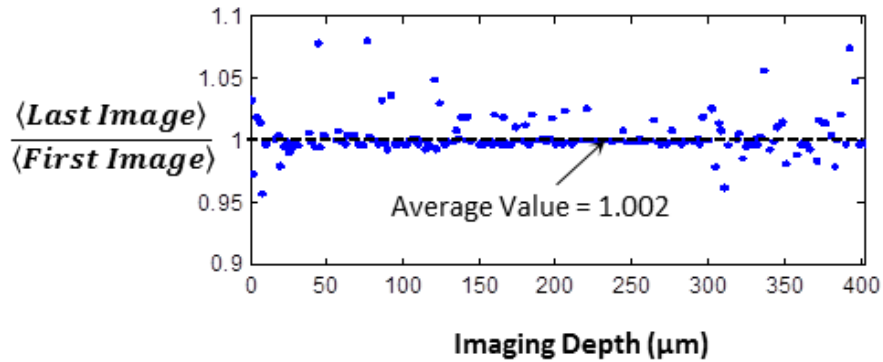


Figure 5.8: Photobleaching test. A plot of the ratio of average pixel intensity observed before and after excitation shows no observable photobleaching.

Finally, we note that in general, both fluorescence saturation and photobleaching become more prominent effects at higher excitation intensities. We found in phantoms and Monte Carlo simulations that the rate of power increase necessary for maintaining constant fluorescence detected is close to that required to deliver constant fluence to the focal point. Thus, though in some cases we imaged with greater than 100 mW delivered to the sample surface, the intensity delivered to the imaging plan at large depths is not significantly greater than that delivered to the imaging plane when imaging the sample surface. In conclusion, we expect that fluorescence saturation and photobleaching did not appreciably influence the results presented herein.

5.3.7. Maximum imaging depth

Figure 5.9 (a) summarizes the maximum imaging depth found in phantom experiments, Monte Carlo simulations, and the analytical model for samples with different scattering lengths and staining inhomogeneities. The approximate position of our biopsy is also indicated, based on extraction of optical properties from biopsy images. Because we estimated an l_s of 90 μm in the first 2 mean free scattering lengths, and an l_s of 120 μm in the last mean free scattering length in Section 5.3.3, we use a bulk l_s of 100

μm for positioning the biopsy region. We found reasonable agreement between the three approaches, with experiments matching the models slightly better for longer scattering lengths and higher staining inhomogeneities. This difference is likely due to the increasing influence of small heterogeneities in our shorter scattering length phantoms, such as spatial variations in fluorescein and polystyrene bead concentrations. The Monte Carlo model showed a slightly weaker dependence of maximum imaging depth on scattering length, partially due to the effect of inhomogeneous collection efficiency.

The maximum imaging depth in the biopsy was slightly less than expected from a phantom with similar optical properties ($l_s = 100 \mu\text{m}$ and $\chi = 20$). We believe this difference is due to the presence of specimen-induced aberrations. Although we could measure the spots size with depth in agar phantoms, there are no bright, fluorescent, sub-diffraction limited features in human biopsies that can be used to reliably measure the excitation spot size. But because the maximum imaging depth was within $\sim 20\%$ of that measured in similar phantoms in which we demonstrate that there is no appreciable specimen-induced aberrations, we believe that the out-of focus fluorescence is still the dominant factor in reducing deep 2PAM imaging contrast in biopsies.

Normalizing the maximum imaging depth by $z_m^n = z_m/l_s$, we observe a logarithmic dependence of z_m^n on l_s [Figure 5.9 (b)]. The origin of the dependence of z_m^n on l_s comes from the fact that as the distances are scaled down by l_s , the photons responsible for the background fluorescence are confined to smaller volumes while the photons generating focal volume signal pass through a constant size signal volume. The dependence of z_m^n on l_s has not been reported before, and has significant implications in comparing maximum achievable imaging depths among samples with different scattering lengths. We recall that Theer *et al.*, and Leray *et al.* found that two-photon imaging depth were limited to $4.5 l_s$ and $6 l_s$ in samples with large l_s and small χ [11],[131]. If one were to

extrapolate those results to samples with scattering lengths commonly found in epithelial tissues, the predicted maximum imaging depth would significantly overestimated [Figure 5.9 (b)].

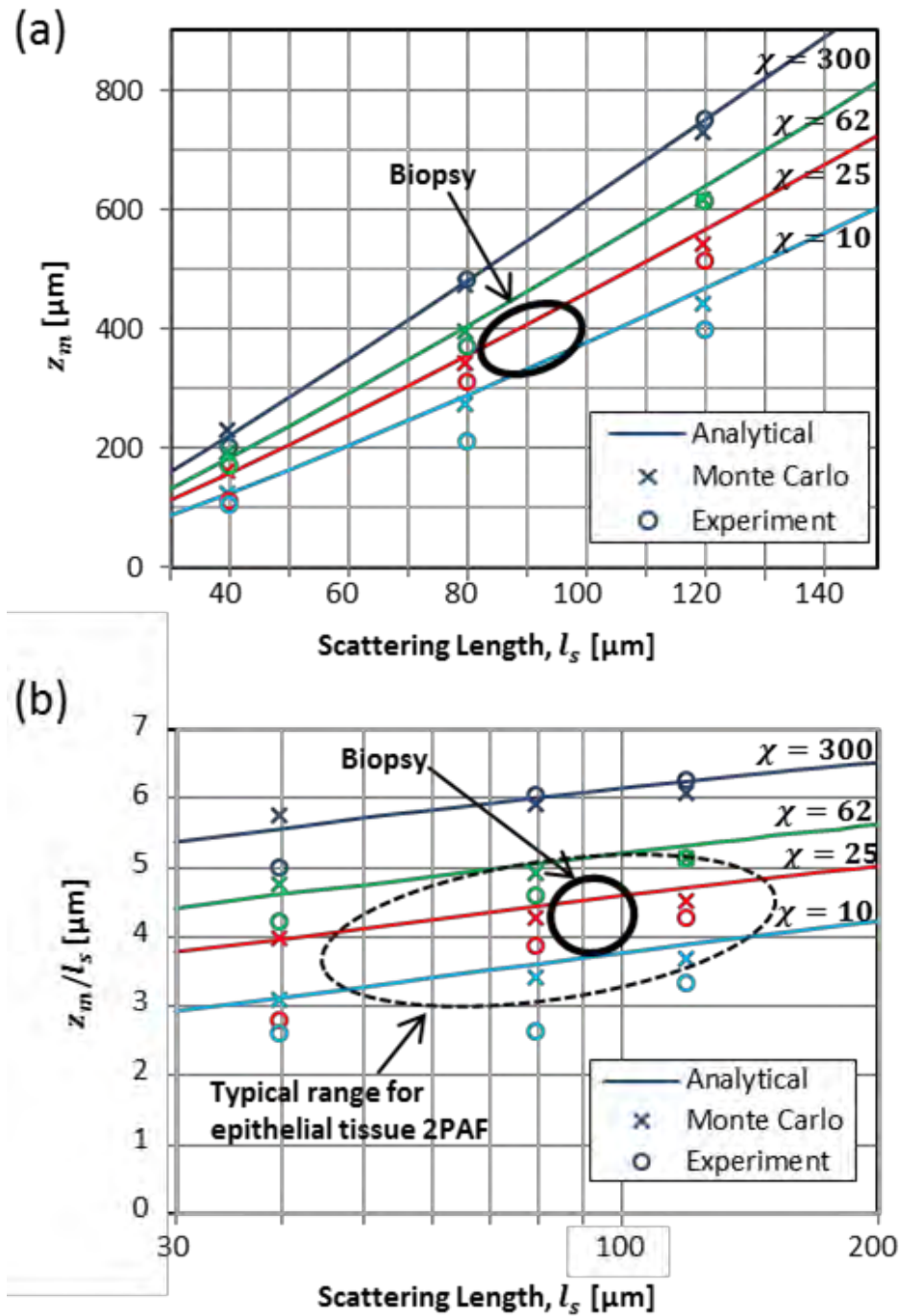


Figure 5.9: Maximum imaging depth summary.

(a) The maximum imaging depth determined by the depth at which $Q = 1$. (b) Expressing the maximum imaging depth in terms of scattering mean free paths, we observed a linear dependence of maximum imaging depth on $\log(l_s)$. Data are plotted from phantom measurements, as well as analytical and Monte Carlo models.

5.4. CONCLUSIONS

With recent technological advances in 2PAM, including the development of 2PAM systems more relevant for in-vivo optical biopsy[12-15], it is increasingly important to understand how out-of-focus background fluorescence affects image contrast and ultimately limits imaging depth. In this paper, we presented experimental data and a computation model that describes the gradual contrast decay of two-photon fluorescence imaging with increasing imaging depth for samples with a variety of scattering lengths and staining inhomogeneities relevant to 2PAM of epithelial tissues. We found maximum imaging depths significantly smaller than those observed in brain tissue. The reasons for a shorter maximum 2PAM imaging depth in epithelial tissue are that the maximum imaging depth decreases with decreasing scattering length, and that the very low staining inhomogeneities typical encountered in 2PAM of epithelial tissues leads to increased out-of-focus fluorescence generation. Based on this analysis, we expect that given range of optical properties typical of epithelial tissue, the 2PAM image contrast decays to one at imaging depths of approximately 160 and 500 μm for scattering lengths of 40 and 120 μm , respectively.

In this chapter, we only considered conventional 2PAM. However, more sophisticated approaches could extend 2PAM imaging depth and contrast by temporal focusing[163],[164], differential aberration imaging[165], optical clearing[166],[167], and/or spatial filtering[11],[168]. It would conceivably also be possible to extend imaging depth by using longer wavelength excitation light[169],[170] to probe dimmer intrinsic fluorophores that have higher wavelength absorption bands, or by using higher order excitation (e.g. three-photon excited fluorescence).

Chapter 6

Multiphoton-induced luminescence from gold nanoparticles

6.1. INTRODUCTION

This chapter presents a detailed exploration of multiphoton-induced luminescence (MPL) from gold nanoparticles. The goal is to quantify the two-photon action cross sections (σ_{TPA}) of a variety of gold nanoparticles and understand how σ_{TPA} relates to various laser and sample parameters. Towards this goal, the physical properties of several gold nanoparticle samples were characterized. The linear absorbance was modeled for each sample using their size and aspect ratio distributions, then calculated absorbance values were compared to measurements to accurately determine nanoparticle concentrations. The calculated linear absorption and scattering cross sections also provide some insight into the sample properties influencing MPL. We present a system to probe the spectrally-resolved nonlinear optical properties of gold nanoparticles as a function of excitation intensity, wavelength, pulse duration (τ_p), and polarization. The three major findings of this chapter are: (1) gold nanoparticles can exhibit extraordinarily large σ_{TPA} values on the order of 10^4 - 10^6 GM, which are significantly larger than any previous reports; (2) MPL deviates from the τ_p^{-1} dependence for short pulse durations, which provides evidence that the mechanism for MPL generation in gold nanoparticles is sequential rather than simultaneous two-photon absorption; and (3) gold nanoparticles exhibit third- and fourth- order luminescence generation, especially at lower emission wavelengths and longer pulse durations.

6.2. NOMENCLATURE OF GOLD NANOPARTICLE SAMPLES

Gold nanoparticle samples used in this chapter are referred to as ‘GNS’ to indicate gold nanospheres, or ‘GNR’ for gold nanorods, followed by the wavelength in nanometers of the linear absorbance peak. In GNR samples, a ‘-25’ suffix indicates 25 nm specified axial width rather than a 10 nm width, and a ‘-p’ suffix denotes a polyethylene glycol (PEG) coating rather than a hexadecylcetyltrimethylammonium bromide (CTAB) coating. The PEG and CTAB coatings add a thickness of approximately 5 nm around the perimeter of the gold nanorods[171]. GNSs are surrounded by sodium citrate ions. Stock solutions of each sample were diluted such that the peak absorbance was approximately one. All nanoparticles were stored at room temperature, except the GNS630, which specified storage at 4° C. We found excellent stability (evaluated by constant absorbance spectra over time) in all samples, except the PEG-coated one, for over a period of greater than one year.

1. **GNS530:** Gold nanosphere sample prepared using a citrate reduction growth method to create a diameter of approximately 50 nm with a linear absorption centered at 530 nm. Specifically, 30 mg of gold chloride was mixed into 300 mL of ultrapure deionized water. In a separate solution, 456 mg of tribasic sodium citrate was added to 40 mL of ultrapure deionized water. The gold solution was stirred and heated to boiling. 2.64 mL of the sodium citrate solution was added to the gold solution and stirred at boiling for an additional 5 minutes to complete the reduction[172-174].
2. **GNS630:** Gold nanosphere sample with a specified diameter of 150 nm and a linear absorption centered at 630 nm. Purchased from BBI Research Inc.® (EM.GC150/4).
3. **GNR750-25:** Gold nanorod sample with a specified width x length of 25 x 86 nm, a peak linear absorption centered at 750 nm, and a CTAB coating. Purchased from Nanopartz®.

4. **GNR780:** Gold nanorod sample with a specified width x length of 10 x 38 nm, a peak linear absorption centered at 780 nm, and a CTAB coating. Purchased from Nanopartz[©].
5. **GNR808p:** Gold nanorod sample with a specified width x length of 10 x 41 nm, a peak linear absorption centered at 808 nm, and a PEG coating. Purchased from Nanopartz[©].
6. **GNR840:** Gold nanorod sample with a specified width x length of 10 x 45 nm, a peak linear absorption centered at 840 nm, and a CTAB coating. Purchased from Nanopartz[©].

6.3. PHYSICAL PROPERTIES

We characterized the physical dimensions of each nanoparticle sample with high resolution field emission scanning transmission electron microscopy (TEM). A 2 μ L volume from the stock solution of each sample was air dried on a copper grid from Grid Tech[©] (Cu-400CN). Imaging was performed on Hitachi S-5500 TEM at 150k magnification. Representative images of each sample are shown in Figure 6.1.

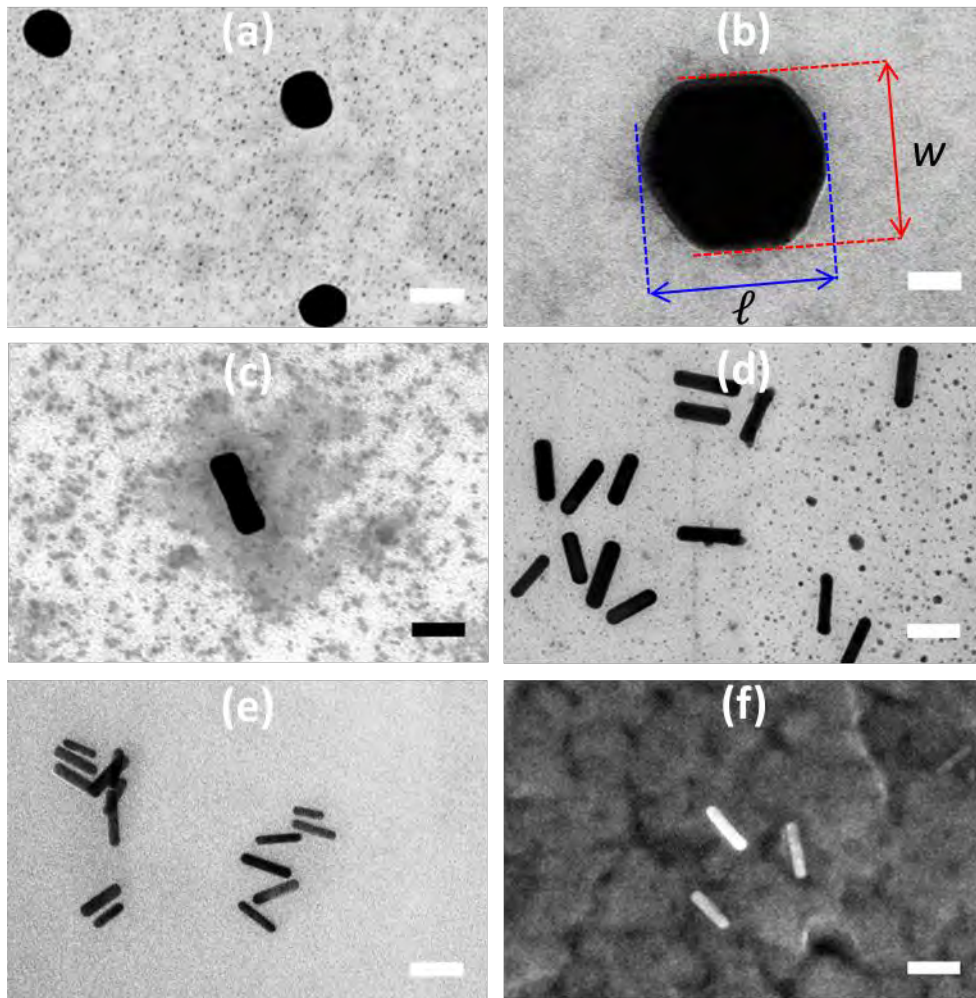


Figure 6.1: TEM images of nanoparticle samples.

(a) GNS530, (b) GNS630, (c) GNR750-25, (d) GNR780, (e) GNR808p, and (f) GNR840. Labels in (b) show how the length (ℓ) and width (w) are defined for a nanosphere. Scale bars are 50 nm.

To characterize the physical dimensions of the nanoparticles in each sample, we used a custom image analysis algorithm implemented in ImageJ [Figure 6.2]. Each image was converted to a binary mask with a threshold set at the average pixel value plus twice the pixel standard deviation. To remove small artifacts and smooth the nanoparticle shapes, images were eroded twice for a 3 pixel (1.9 nm) perimeter loss, followed by a 3 pixel dilation [Figure 6.2(b)]. A particle counting program found particles within the expected size range [Figure 6.2(c)]. Finally, an ellipse was fit to each particle found, and

the dimensions of the long and short axis for each particle were recorded. We counted 30 to 300 particles to get the size distributions in each sample. The GNS630 TEM images were analyzed by manual measurement.

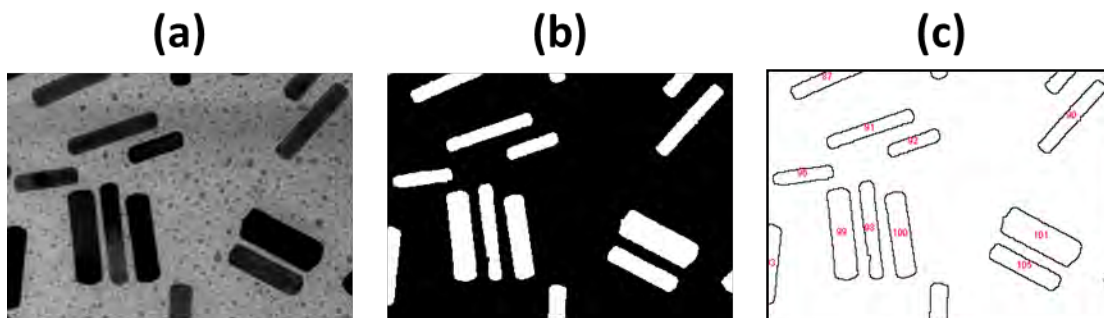


Figure 6.2: TEM Image processing sequence for characterizing size distribution of GNR780.

(a) High resolution TEM images were acquired of each nanoparticle sample. (b) Binary image of same region after binary thresholding and erosion/dilation. (c) Resulting particles found from a particle counting algorithm. Note that typical images were much larger field of view—only a subset of a typical image is shown here.

A typical size distribution scatter plot of the GNR780 sample is shown in Figure 6.3. We observed a small percentage of nanospheres in the nanorod samples. Defining a nanosphere as an object with an aspect ratio less than 2, this sample had 6% nanospheres. From the positive slope of a linear fit to the scatter data, there is some correlation between the length and width distributions, i.e., the ℓ and w values are not independently distributed.

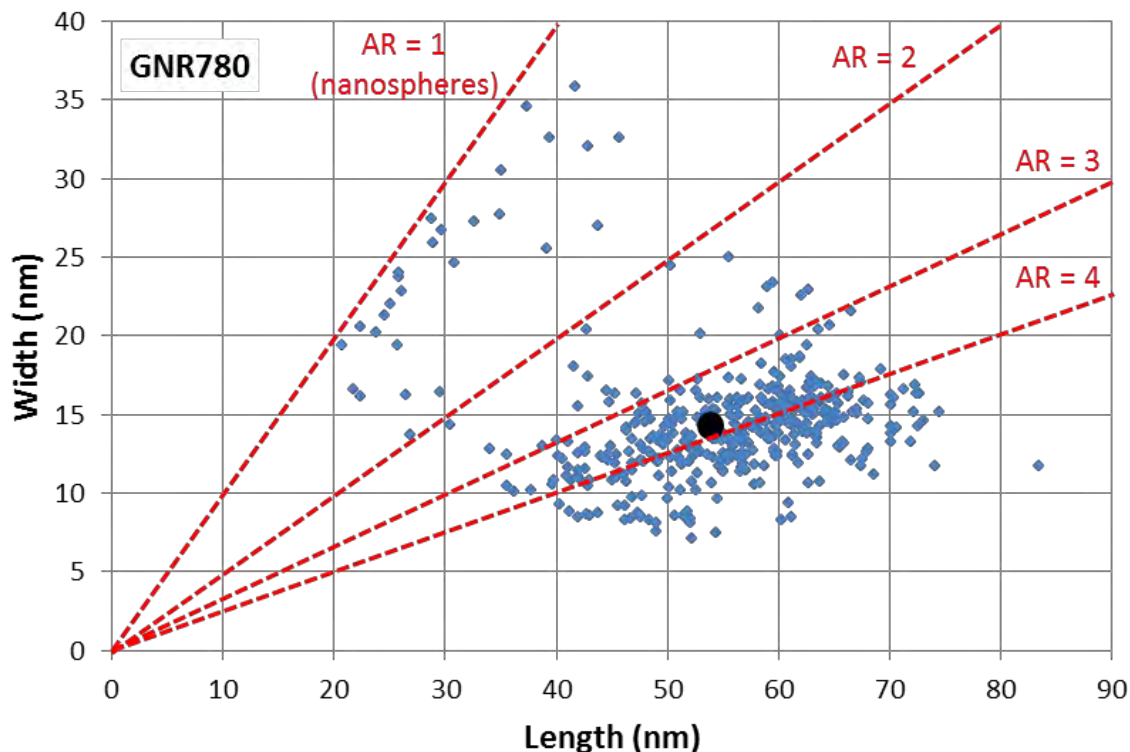


Figure 6.3: Plot of measured lengths and widths of GNR780 nanoparticles. Blue dots are measurements of 430 individual nanorods. Dotted lines are drawn at constant aspect ratios (AR) of 1, 2, 3, and 4. Black dot is average measured length and width for this sample.

Our average measured dimensions were significantly different than the manufacturer's specifications [Table 6.1]. The average aspect ratio, which is important for determining the extinction peak[175], is reported as the average measured from each particle, rather than the ratio of the average length to the average width. We found a slight, but important, ellipticity in the small-diameter nanospheres, which we found must be taken in to account to properly model the absorbance spectrum.

Sample	Coating	Specified Length [nm]	Specified Width [nm]	Measured Length [nm]	Measured Width [nm]	Measured Aspect Ratio
GNS530	Citrate	-	-	54 ± 5	44 ± 4	1.21 ± 0.10
GNS630	Citrate	150	150	173 ± 6	161 ± 10	1.07 ± 0.05
GNR750-25	CTAB	86	25	76 ± 6	25 ± 3	3.05 ± 0.38
GNR780	CTAB	38	10	54 ± 10	14 ± 4	3.95 ± 0.99
GNR808p	PEG	41	10	39 ± 6	9 ± 1	4.24 ± 0.66
GNR840	CTAB	45	10	43 ± 7	9 ± 2	4.75 ± 1.05

Table 6.1: Measured nanoparticle dimensions.

Measured values are reported as mean ± standard deviation. Specified dimensions were taken from manufacturer, if available. Note that average aspect ratios are not the ratio of average length to average width, but rather, the average of the aspect ratios of each individual particle.

6.4. LINEAR OPTICAL PROPERTIES

6.4.1. Absorption and scattering cross sections

Measurements

We measured the linear absorbance for each sample with a path length of 0.95 cm. The normalized linear absorbance spectra are summarized in Figure 6.4. The smaller nanospheres (GNS530) exhibit a narrow absorption peak at 520 nm which is characteristic of a dipole resonance. In the larger gold nanosphere sample (GNS630), the broad, quadrupolar resonance becomes dominant, though the dipolar resonance is still visible in the spectrum as a shoulder at 520 nm. Gold nanorod samples exhibit two peaks at the short and long axis resonances.

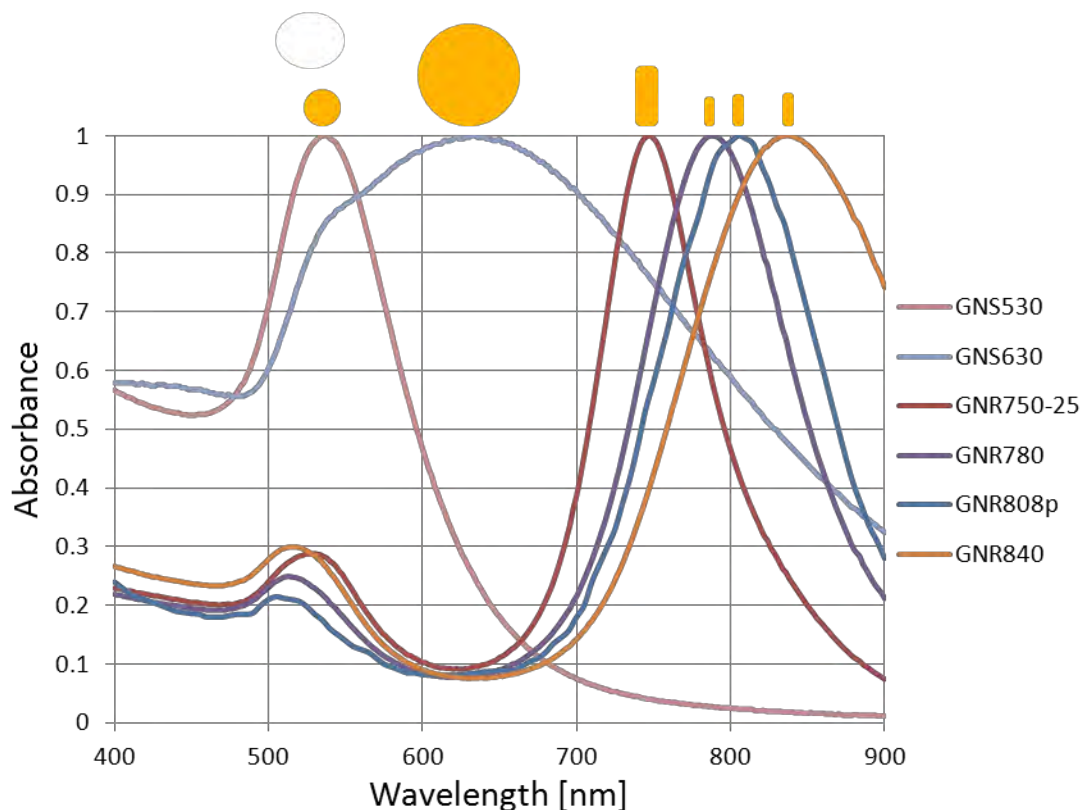


Figure 6.4: Measured linear absorbance of gold nanoparticle samples. Gold nanorod absorbance exhibit the expected double peak—the peak around 520 nm is from light interacting parallel to the short axis of the rod, while the NIR peak is from light interacting parallel to the long axis of the rod. Drawings above the absorbance plot show the relative sizes of the physical cross section of an average particle from the sample with the corresponding the absorbance peak directly below. Data are normalized to a peak absorbance of one.

Simulations

We simulated the absorbance spectrum for each particle, based on the size and shape measurements found in Section 6.3. These simulations were important for two reasons: (1) the knowledge of the extinction coefficient allows for accurate determination of particle concentration, and (2) simulating the absorbance allows us to understand the relative roles of scattering and absorption that contribute to the total extinction coefficient of the particle. The GNS630 sample could be effectively modeled as a sphere of 150 nm using Mie theory, which is an exact solution for the interaction of electromagnetic

waves with spheres. We calculated the absorption and scattering cross sections of all non-spherical shapes using a Discrete Dipole Approximation (DDA) that takes into account the size distribution and orientation of the nanoparticles[176].

For all nanoparticle samples, the colloidal solutions were simulated at intervals of 20 nm across a range of wavelengths from 400 to 900 nm in a water environment. We assumed the particles were far enough apart to be simulated as isolated particles in all cases. The complex gold refractive index at the irradiation wavelength was obtained from a curve fit to experimentally determined refractive index values for bulk gold, and then corrected for size-related surface damping according to the Drude equation with a modified damping constant. DDA breaks apart a simulated geometry into small cube sections across which the induced dipole polarization from the incident light is assumed to be constant, and is a well-established technique for simulating the SPR of colloidal nanoparticles[59]. We observed that the GNS530 sample consisted of elliptical particles, and thus they were simulated as spheroids with a short axis diameter of 44 nm and an aspect ratio of 1.2.

To reproduce the features observed in the absorbance spectra of gold nanorods, we simulated rod shapes at 4 different orientations with respect to the incident light polarization and propagation directions. Specifically, we simulate the nanorod long axis along the x, y, z, and [111] directions for light propagating in the z direction with linear polarization along the x axis. We also simulate a size distribution of plus/minus one standard deviation in the nanorod length at constant width to account for plasmonic peak broadening due to the size distribution of the nanorods. The GNR780, GNR808p, GNR840 samples were simulated as hemispherically-capped cylinders with aspect ratios 3.95, 4.25 and 4.75, respectively. The GNR750-25 sample was found to have an hourglass-like shape with a tapered midsection. We simulated the particles in this sample

as an elliptically-capped rotationally-symmetric shape with a sinusoidally-varying midsection. This rod had an aspect ratio of 2.77 with a diameter of 28 nm. For all samples, we use a minimum of 48 dipoles across the diameter of the nanorod to minimize shape discrepancy and improve the cross-sectional accuracy of the results.

The results of a typical simulation for the GNR 780 sample, in comparison to the measured absorbance are shown in Figure 6.5. The shape around the peak absorbance matches reasonably between the measurement and simulation, while there is a larger error in simulating the lower wavelength peak. We believe this discrepancy is due to the simulation only accounting for gold nanorods, while we do observe a small percentage of nanospheres in each solution. Including a contribution from nanospheres in our simulations would increase the absorbance at 500 to 550 nm, and simulated absorbance would more closely match the observed values.

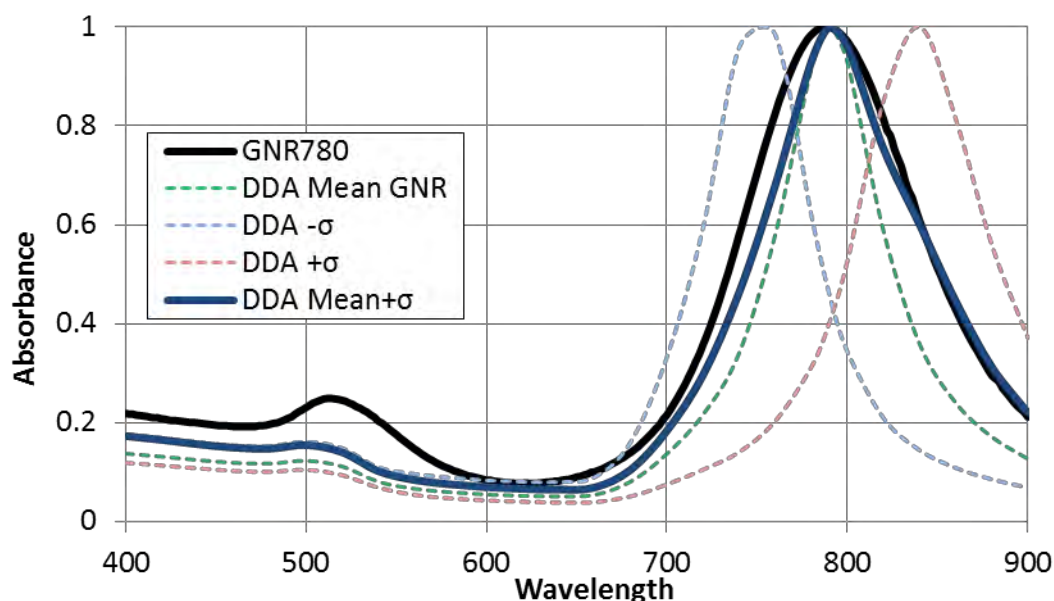


Figure 6.5: Comparison of measured and simulated absorbance for GNR780. The measured absorbance had significantly broader bandwidth than that of a single gold nanorod due to the size distribution of the sample. Summing the contributions of the mean-sized gold nanorod (DDA Mean GNR), weighted by 0.65, a single gold nanorod with the mean plus one standard deviation length (DDA $+\sigma$), weighted by 0.175, and a single gold nanorod with the mean minus one standard deviation length (DDA $-\sigma$), weighted by 0.175, the measured absorbance is much more closely matched. Black line is measured absorbance. Dotted lines are DDA simulations of 3 differently sized nanorods. Solid blue line is resulting simulated absorbance. All plots are normalized to one.

For each simulated sample, we can compare the scattering and absorption cross section. For larger particles, the extinction is dominated by scattering while for smaller particles, the extinction is dominated by absorption. This is consistent with other results[59]. A summary of the absorption and scattering cross sections at the peak wavelength and at 780 nm is shown in Table 6.2. These values will be referred to later in qualitative explanations for the magnitudes of SHG and MPL.

Sample	Peak Absorbance Simulated [nm]	Model	C_a^{Peak} [μm^2]	C_s^{Peak} [μm^2]	C_a^{780} [μm^2]	C_s^{780} [μm^2]	C_a^{780}/C_s^{780}
GNS530	536	DDA	$6.5 \cdot 10^{-3}$	$9.1 \cdot 10^{-4}$	$1.3 \cdot 10^{-4}$	$4.6 \cdot 10^{-5}$	2.7
GNS630	634	Mie	$1.1 \cdot 10^{-2}$	$8.9 \cdot 10^{-2}$	$3.3 \cdot 10^{-3}$	$5.0 \cdot 10^{-2}$	0.07
GNR750-25	754	DDA	$6.5 \cdot 10^{-3}$	$1.8 \cdot 10^{-3}$	$2.5 \cdot 10^{-3}$	$1.6 \cdot 10^{-3}$	1.5
GNR780	788	DDA	$2.3 \cdot 10^{-3}$	$1.0 \cdot 10^{-4}$	$2.1 \cdot 10^{-3}$	$8.9 \cdot 10^{-5}$	23.4
GNR808p	805	DDA	$8.2 \cdot 10^{-4}$	$1.2 \cdot 10^{-5}$	$5.4 \cdot 10^{-4}$	$7.6 \cdot 10^{-6}$	71.6
GNR840	838	DDA	$9.3 \cdot 10^{-4}$	$1.4 \cdot 10^{-5}$	$2.4 \cdot 10^{-4}$	$3.5 \cdot 10^{-6}$	68.7

Table 6.2: Calculated linear absorption and scattering cross sections.

DDA and Mie calculations provide the cross sections of each particle sample with an average size from Table 6.1 at the peak absorbance wavelength and at 780 nm (DDA calculations were performed by R.K. Harrison). The peak absorbance from the simulated geometries was very close the measured absorption peak. As expected, the largest particle (GNS630) primarily scatters the light, while all the other samples primarily absorb light. For nanorods, these values include a 0.33 normalization factor that accounts for an isotropic orientation relative to the excitation polarization.

6.4.2. Absorption and scattering coefficients

For applications involving more than superficial imaging, some care must be taken when using contrast agents that may alter the bulk optical properties of the sample. Thus the change in scattering coefficient ($\Delta\mu_s$) and absorption coefficient ($\Delta\mu_a$) from adding these nanoparticles to a sample are important to understand. These are related to the cross sections by:

$$\Delta\mu_s = C_s [GNP] N_A \quad (7.1)$$

$$\Delta\mu_a = C_a [GNP] N_A, \quad (7.2)$$

where $[GNP]$ is the molar concentration of gold nanoparticles and N_A is Avogadro's Number. We typically had concentrations of approximately 100 pM of gold nanoparticles in the final solution of densely labeled cells. With the GNR780 sample, this concentration amounts to an increase in the peak scattering and absorption coefficients of 0.05 cm^{-1} and

1.3 cm⁻¹, respectively. The scattering and absorption coefficients of skin at 780 nm are on the order of 100 cm⁻¹ and 1 cm⁻¹, respectively[33],[36]. Given these values, we expect that the absorption of the sample will significantly increase (approximately doubled in this case) at 780 nm. Indeed, one sign of successful labeling of sample is that the sample pellet is a dark purple color. However, the extinction coefficient, which is the sum of the scattering and absorption coefficient, ultimately governs the nonlinear imaging depth in a sample. Even with the addition of nanoparticles, the tissue extinction coefficient is dominated by the tissue scattering. Using the values presented above, the mean free path of a 780 nm photon in epithelial tissue decreases from 99 μm without the nanorods to 98 μm with the addition of 100 pM GNR780 nanorods. This approximate calculation is consistent with previous experiments, in which we observed no significant change in extinction coefficient in gold nanorod labeled tissue phantoms[92].

The scattering anisotropy value, g , has been previously measured to be in the range of 0.1 - 0.6 for gold nanospheres and nanorods in water at 780 nm[177]. This parameter is important for applications involving diffuse imaging, where imaging depths scale with the transport corrected scattering, or in methods that rely on backscattered light from nanoparticles as the source of contrast. However, for nonlinear imaging, signal generation is determined by ballistic photons [Figure 5.2 (c)], and g has a relatively small influence on nonlinear excitation.

6.5. CALCULATION OF NANOPARTICLE CONCENTRATIONS

We calculated the peak molar extinction coefficients, ϵ , from the peak effective cross sections calculated in Section 6.4.1 by:

$$\epsilon_{model} = (C_s^{peak} + C_a^{peak})S_F N_A, \quad (7.3)$$

where S_F is a factor accounting for the size distribution and a general decrease in cross section values and the number of dipoles in the DDA simulations are increased. This correction factor was estimated by comparing the extinction from single particles and a mixture of different sized particles (e.g. Figure 6.5), and running some simulations with an increasing number of dipoles. As the number of dipoles were increased, the cross sections were found to decrease asymptotically by $\sim 10\%$. We determined the correction factor to be approximately 0.6 for gold nanorod samples, 0.7 for the GNS530 sample, and 0.9 for the GNS630 sample. We then used the measured peak absorbance values of each sample to estimate their molar concentration in units of nanoparticles per volume [Table 6.3]. Our calculated extinction coefficients are approximately 2.5 times higher than those specified from Nanopartz, which results in an expected concentration 2.5 times lower than that specified. The exception is the GNR780 sample, in which we also observed a large discrepancy between the measured and specified average size. In this sample, our calculated extinction coefficient is eight times higher than that specified. The specified concentrations from Nanopartz are poor approximations because they are calculated using an extinction coefficient determined by an inaccurate model—the simulation of cross sections by Mie-Gans theory[178]. In this method, the nanorods are simulated by ellipsoids. However, the actual geometry is pill-shaped, or hemisphere-capped shaped, and must be modeled numerically[179].

The most common way to estimate ϵ for gold nanorods is by inductively coupled plasma mass spectrometry (ICP), which allows the quantification of gold atoms in a solution[180],[181]. However, this method generally overestimates the nanoparticle concentration, as nanospheres and unreacted gold ions add significant mass to the ICP measurement, but have an insignificant contribution to the longitudinal absorbance. An alternative method has previously been implemented, which gold nanorods on a thin film

are counted with atomic force microscopy (AFM) and the extinction of the film is measured[182]. These extinction values reported in the literature are closer to our measurements than the Nanopartz specifications [Table 6.3].

Sample	ϵ_{spec} [M ⁻¹ cm ⁻¹]	ϵ_{lit} [M ⁻¹ cm ⁻¹]	ϵ_{model} [M ⁻¹ cm ⁻¹]	C_{spec} [pM]	C_{lit} [pM]	C_{model} [pM]
GNS530	-	1.5×10^{10} [183] ⁽¹⁾	2.8×10^{10}	-	67 ⁽¹⁾	36
GNS630	-	-	5.4×10^{11}	-	-	1.9
GNR750-25	1.1×10^{10}	-	2.7×10^{10}	87	-	37
GNR780	9.8×10^8	4.4×10^9 [182]	7.7×10^9	1,020	230	130
GNR808p	1.0×10^9	4.6×10^9 [180]	2.7×10^9	980	227	370
GNR840	1.1×10^9	5.5×10^9 [180]	3.1×10^9	870	182	330

Table 6.3: Nanoparticle molar extinction coefficients and concentrations.

Comparison of peak extinction coefficients and resulting concentrations from Nanopartz (ϵ_{spec} , C_{spec}), reports in previous literature for similar particles (ϵ_{lit} , C_{lit}), and our characterization (ϵ_{model} , C_{model}). Concentrations are calculated from solution with a peak absorbance of exactly 1 in a 1 cm pathlength cuvette. ⁽¹⁾ Extinction and concentration for perfectly spherical gold nanosphere. Our calculation included the ellipticity of our measured particles.

6.6. NONLINEAR LUMINESCENCE PROPERTIES

6.6.1. Experimental setup

We measured the MPL behavior of all samples as a function of excitation wavelength, emission wavelength, excitation power, polarization, and excitation pulse duration. To vary these parameters independently, we implemented a system that incorporates six major parts: (1) an ultrafast laser excitation source; (2) a computer controlled power attenuator; (3) a single grating, double-pass pulse stretcher; (4) an

interferometric autocorrelator; (5) a laser scanning microscope; and (6) a spectrometer and photomultiplier detection system [Figure 6.6].

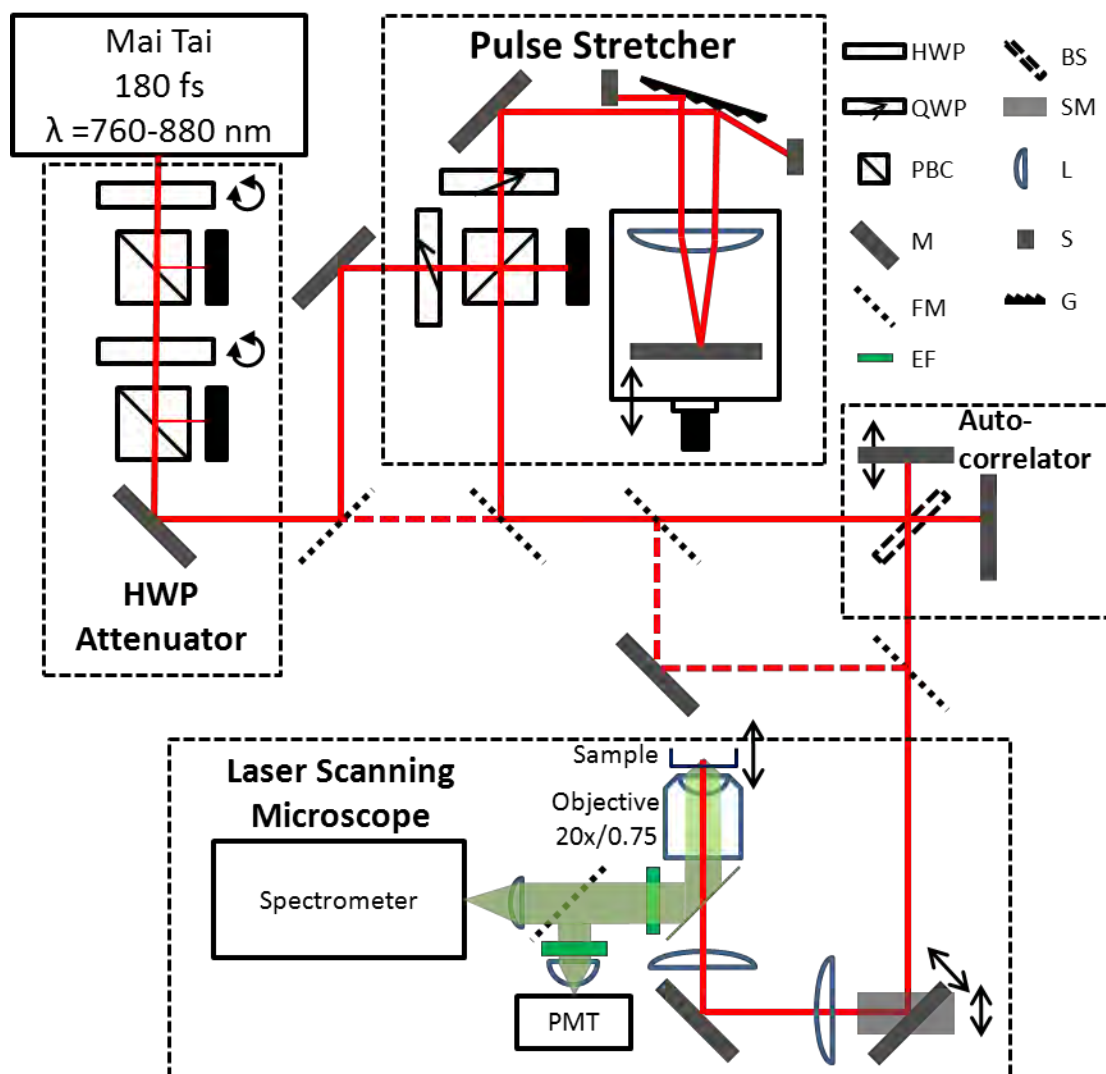


Figure 6.6: Nonlinear optical properties experimental setup.

The linearly polarized, ultrashort pulses from the excitation source (Mai Tai) are attenuated with a pair of half wave plate (HWP) and polarizing beam cubes (PBC). Depending on the desired configuration, the excitation light can then be directed straight into the laser scanning microscope, or sent into the pulse stretcher and/or the autocorrelator first. Luminescence is epicollected from the sample and directed to a spectrometer or a photomultiplier tube (PMT). Double arrows indicate moving parts. QWP: quarter wave plate, M: mirror, FM: flip mirror, EF: emission filter, BS: beam splitter, SM: scanning mirror, L: lens, S: beam stop, G: diffraction grating.

Excitation source and power attenuator

The laser source is a Ti:Sapphire oscillator, tunable in the range of 760 to 880 nm, with an average power of 1 W (Newport, MaiTai). At an excitation wavelength, λ_x , of 780 nm, the output of the laser source had a spectral bandwidth of 7.5 nm and a pulse duration of 120 fs. The repetition rate, R , was 80 MHz. We measured the pulse duration at the sample plane of the nonlinear microscope, τ_p , to be 250 fs (FWHM) when bypassing the stretcher. The $1/e^2$ beam diameter is 2.1 mm exiting the cavity. To have precise control over the laser power, we found that reflective neutral density filters were insufficient. Instead, we used two sets of half wave plates and polarizing beam cubes to continually adjust the power. One of the half wave plates was adjusted by a computer controlled actuator, providing 0.01° resolution, corresponding to a worst-case attenuation resolution of approximately $\pm 0.08\%$ at $\lambda_x = 780$ nm (Newport, PR50PP, 10RP52-2). This value corresponds to the change in excitation power when the HWP is adjusted at the steepest rate of transmission change versus angle change. Using the two attenuators in series allowed us to continuously attenuate the excitation power from less than 0.4 dB to greater than 40 dB within the range of $\lambda_x = 760$ -820 nm

Pulse stretcher/compressor and autocorrelator

We built a single grating, double pass pulse stretcher, similar to the designs of [184],[185]. The grating had a line spacing of 1480 lines/mm grating with an 800 nm wavelength blaze. We used a 2" diameter focusing lens ($f = 200$ mm) and mirror to allow enough space for the light to reflect off the grating twice. To adjust the pulse duration, the lens and mirror after the grating were positioned on an optical rail that could slide tens of centimeters [Figure 6.6]. This apparatus can impart negative or positive GDD on our excitation pulse, and vary the pulse duration at the objective focal plane from 220 fs to

beyond 8 ps. With proper alignment, the pulse duration could be tuned with no observable change in system power transmission, or an significant misalignment.

To measure the autocorrelation of our excitation pulse at the sample, we used a Michelson interferometer with a computer controlled delay arm. Changing the distance of one arm of the interferometer changes the temporal overlap of excitation pulses at the focal plane. The resulting autocorrelation was analyzed to find pulse duration at the sample, as described in Section 3.3.2 and Figure 3.4 (b). We characterized the effect of the pulse stretcher position, s , on the excitation pulse duration at the objective focal plane using the autocorrelator and an Olympus 20x/0.75NA air objective. The pulse duration as a function of stretcher position is shown in Figure 6.7. When not performing an autocorrelation, we found it necessary to bypass the autocorrelator, as even with the autocorrelator stationary, minute vibrations in the system caused the intensity at the focal plane to fluctuate rapidly.

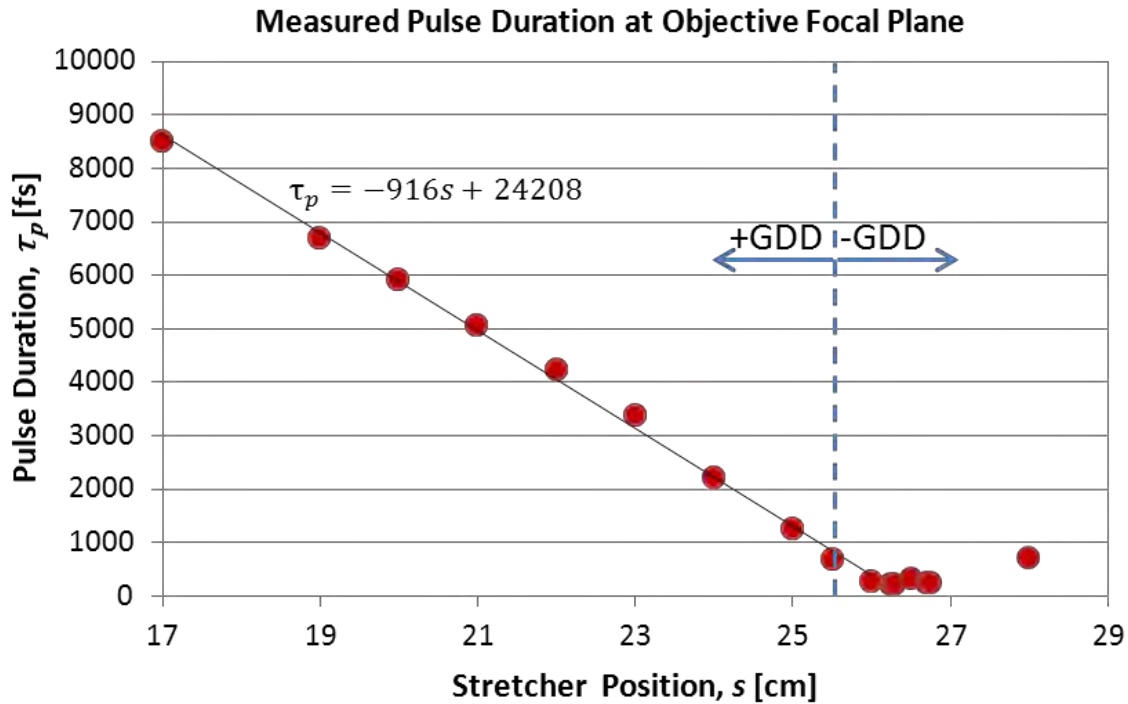


Figure 6.7: Focal plane pulse duration as a function of stretcher position. The change in measured pulse duration, τ_p , was nearly linear with stretcher position, s . The zero GDD position is 25.5 cm. Below this point, the stretcher imparts negative GDD on the pulse, while sliding the stretcher above this point adds positive GDD. A linear best fit is shown that relates τ_p in femtoseconds to s in centimeters by the equation: τ_p [fs] = -916 s [cm] + 24,208, for 17 cm $\leq s \leq 26$ cm.

Laser scanning microscope

The inverted laser scanning microscope used a pair of galvometric mirrors to scan the beam through two relay lenses ($f = 75$ mm / $f = 160$ mm), and into the back aperture of an Olympus 20x/0.75 air objective with a 13.5 mm back aperture. A key parameter of this system that was considered for sensitive MPL measurements is the focal spot size. We purposely underfilled the back aperture of our objective to have large excitation focal volumes. This large volume allowed us to probe many nanoparticles simultaneously at low intensities, while utilizing the full NA for large solid-angle epicollection. The $1/e^2$ beam diameter of the laser beam at the objective back aperture was 4 mm, giving a fill

factor of 0.3. At 780 nm excitation, we measured an IPSF^2 of $1.4 \pm 0.2 \mu\text{m}$ and $9 \pm 1 \mu\text{m}$ FWHM in the lateral and axial dimension, respectively. These numbers represent the average \pm standard deviation across measurements of ten fluorescent beads (Invitrogen, 100 nm diameter FluoSpheres) embedded in a 2% agar gel. The dimensions of the linear intensity distribution (the IPSF) are a factor of $\sqrt{2}$ larger than the dimensions IPSF^2 . The peak excitation intensity, I_p , was then calculated by using the focal spot area, A_f , calculated from the $1/e^2$ radius of the excitation intensity by:

$$I_p = \frac{P_{ex}}{R\tau_p A_f} \quad (7.4)$$

The peak excitation intensities used were typically reported as MW/cm^2 , or millions of Watts per square centimeter.

During spectra acquisitions, the scanning mirrors were rotated at 1 kHz at small angles, which translated to maximum scanning distances of $\pm 10 \mu\text{m}$ at the focal plane. This scanning method minimized accumulated damage or photobleaching effects, while minimizing any likelihood of optical trapping. Because of the large slit size in the spectrometer, we found that this lateral movement had no effect on our measurements in a fluorescein reference standard.

Sample

Samples were placed on a #1.5 coverslip-bottom petri dish (Matek Corp), and adjusted relative to the objective lens with a three axis piezo actuator, first to find the coverslip/sample interface, and then move a constant $10 \mu\text{m}$ into the sample. For aqueous solutions, samples were concentrated to a peak optical density of 10, and $400 \mu\text{L}$ was placed on the coverslip (resulting in a nanoparticle concentration 10x higher than those reported in Table 6.3). For a nanoparticle concentration of 1 nM, using an ellipsoidal

focal volume determined by the IPSF (~ 25 fL), the average nanoparticle concentration is approximately 15 particles per focal volume. In a homogeneously dispersed solution at this concentration, a nanoparticle will be separated from its nearest neighbor by an average distance $1.2 \mu\text{m}$.

To examine the polarization dependence of the luminescence, we analyzed stationary particles dried on a coverslip. We prepared these samples by diluting the stock solution five times (to a peak optical density of 0.2), depositing $5 \mu\text{L}$ of the dilute solution on a #1.5 coverslip, and evaporating the solvent at 90°C .

Spectrometer/PMT

Nanoparticle luminescence was detected by either a spectrometer or a PMT. We used an SRS163 nonimaging spectrometer (f/3.6) with 163 mm focal length, a 300 line/mm grating (500 nm blaze), and a $100 \mu\text{m} \times 3 \text{ mm}$ slit (Andor Technology). We used an f/4 focusing lens so that no light would be lost outside of the acceptance cone of the spectrometer, assuming perfectly collimated light from the objective (Thorlabs $D = 25 \text{ mm}$, $f = 100 \text{ mm}$). We verified that the small amount of focal point movement from the scanning mirrors did not appreciably affect spectra or photon counts from a sample of fluorescein. The $100 \mu\text{m}$ slit also played the role of a spatial filter, rejecting some of the scattered MPL light that is not collimated out of the objective. This filtering of the scattered light was important to our cross section measurements that are made in reference to fluorescein, because a constant collection efficiency is required for an accurate measurement, and fluorescein and nanoparticles scatter visible wavelength emission quite differently. Our spectrometer was cooled with a thermoelectric cooler (TEC) with an additional liquid cooling unit that flowed 25°C water through the TEC heatsink. We found the liquid cooling unit to be essential for low signal measurements, as

it allowed us to reduce the detector temperature from -60°C to -75°C . This 15° temperature change led to a decrease of dark current by one order of magnitude, in agreement with the specifications.

Many previous studies on nonlinear luminescence from nanoparticles ignore the far red regions of the luminescence spectra by using non-ideal emission filters and dichroic mirrors[186],[97],[187]. We used ion-beam-sputtered filters that are relatively flat up to 750 nm, while performing deep attenuation of the laser bandwidth ($\text{OD} > 7$ above 760 nm). Our dichroic mirror limits the spectral sensitive of our system to 380 nm to 720 nm. We calibrated the wavelength response of our spectrometer using a NIST-traceable Tungsten-Halogen lamp and precision current source (Optronic Laboratories, 245 and OL 65A). The actual spectrum was divided by the measured spectrum to determine a correction factor, CF [Figure 6.8]. To get a smooth calibration, we fit a 5th order polynomial function to the CF , resulting in:

$$CF = -6.201\lambda^5 + 1.699\lambda^4 - 1.864\lambda^3 + 1.028\lambda^2 - 2.851\lambda + 320.769. \quad (7.5)$$

All spectra presented in this chapter were multiplied by this correction factor. This calibration ensured the shape of the luminescence we recorded reflects the actual spectral content of the emission. Acquisitions were done over 4 accumulations at 10 second exposures, with full vertical binning and 4 pixel horizontal binning to improve signal to noise ratio.

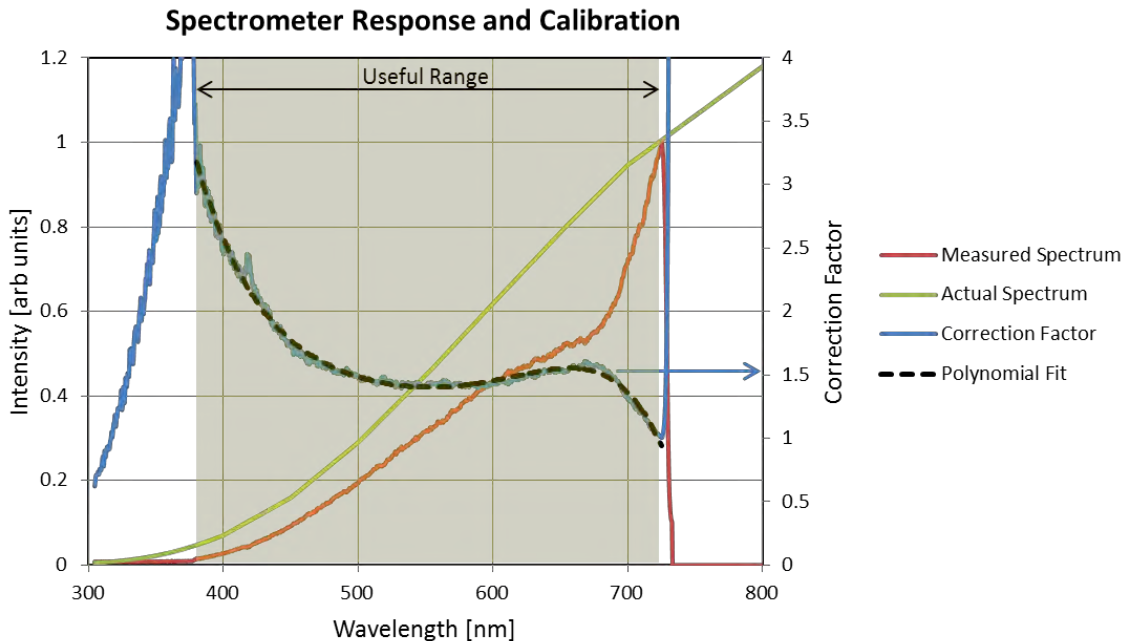


Figure 6.8: Spectrometer system response and calibration.

The spectral system response of the objective, dichroic mirror, and excitation filters was determined using a NIST-traceable lamp. The actual spectrum of this lamp is plotted from the specifications, the measured spectrum was taken with the lamp placed above the objective, with a diffuser close the objective focal plane. The system was more sensitive to higher wavelengths, indicated by the smaller correction factors at the higher wavelength end of the spectrum. The useful range of the spectrometer system was 380 to 720 nm. We used a 5th order polynomial fit to the correction factor to obtain a smooth calibration.

For select experiments, we validated our spectrometer results by measuring luminescence with a PMT and select emission filters. The PMT allows for greater sensitivity at lower excitation intensities, at the loss of spectral resolution. All measurements in this chapter are background corrected by subtracting the signal obtained with equivalent laser parameters and deionized water as the sample. The background signal was almost entirely above 700 nm, and from 700 nm to 720 nm, it amounted to less than a 30 counts per second (cps) at 600 μ W average power and 780 nm excitation

wavelength. Occasional 2-3 pixel signal peaks from cosmic rays were removed manually by setting the pixel spikes to the average value of the adjacent pixels[188].

6.6.2. Spectral features of nanoparticle luminescence

This section presents a qualitative comparison of the MPL spectra of each of the gold nanoparticle samples in solution. In general, the MPL spectra from gold nanoparticles are very broad and significantly red-shifted compared to band-gap fluorophores. All experiments presented in this section were performed bypassing the pulse stretcher and autocorrelator, which resulted in a measured pulse duration of 250 fs at the objective focal plane.

Comparing the spectral features of MPL from each nanoparticle sample, we observe appreciable second harmonic generation (SHG) peaks only in the nanosphere samples [Figure 6.9 (a)] and in the largest size nanorod sample [Figure 6.9 (b)]. As expected, significant SHG signal correlates to samples with low C_a/C_s ratios summarized in Table 6.2. As the MPL is epicollected, the harmonically generated light must scatter backwards to be detected. Therefore the relative size of the SHG peaks to the broad MPL outside $\lambda_x/2$ is a function of the scattering of the sample, and is not directly indicative of relative magnitude of signal generated at the focal volume.

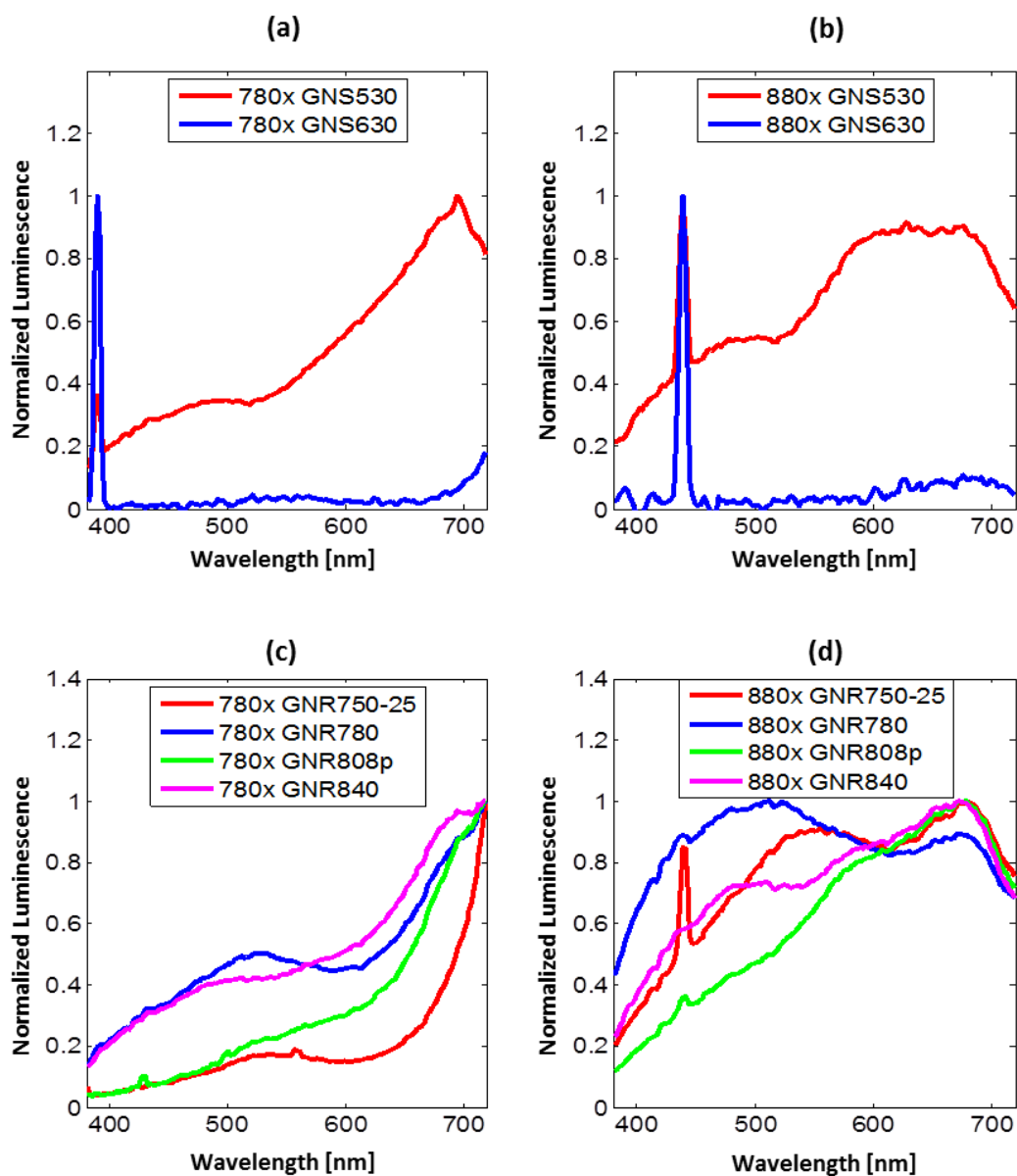


Figure 6.9: Spectral features of MPL in nanospheres and nanorods
 Normalized MPL of nanospheres and nanorods illuminated with 780 nm excitation light (panels (a) and (c), respectively) and 880 nm excitation light (panels (b) and (d), respectively). Note that maximum MPL counts are normalized to 1, i.e. the relative brightness between samples cannot be inferred from this plot.

For 780 nm excitation, MPL rose nearly monotonically up to the limit of our system sensitivity range at 720 nm. For 880 nm excitation, MPL peaked at slightly lower wavelengths—approximately 680 nm. This 680 nm peak is commonly attributed to the X

symmetry point in the first Brillouin zone of gold[39],[189],[190]. One important feature, which will be discussed more in the following section, is the presence of luminescence below $\lambda_x/2$, which has also been reported by other groups[191-194]. This contrasts to two-photon excited fluorescence, which, by energy conservation, must be at larger wavelengths than $\lambda_x/2$. Thus we would expect that MPL in this spectral range should increase at a faster than quadratic rate with increasing excitation intensity (three- or four-photon induced luminescence). To investigate this hypothesis, we studied the dependence of the spectrally resolved MPL on excitation intensity. This approach will also verify that the high wavelength MPL observed here is not due to bleed through of the excitation light[195].

6.6.3. Dependence of MPL on excitation intensity

We investigated the dependence of MPL on excitation intensity in two ways. Using the spectrometer, we recorded MPL counts as we increased power. We also measured the MPL response to power changes with a PMT and a variety of bandpass emission filters. In both methods, we found that different spectral regions of the nanoparticle MPL increased at different nonlinear rates. In all cases, we found that lower wavelength luminescence increased at higher nonlinear orders than the higher wavelength MPL (i.e. MPL at 400 nm increased at higher rates than MPL at 650 nm).

To start, we tested a fluorescein sample, which serves to validate our method—we expect that all regions of the fluorescence should quadratically increase with excitation power. We prepared a 25 μM solution of fluorescein (Fluka) in a pH 12 buffer, and recorded spectra for increasing power. As we exponentially increased the power in approximately $10^{0.1}$ intervals, we observe that the emission shape is constant and emission counts increase at intervals of $10^{0.2}$ [Figure 6.10 (a)]. Looking at the emission

profiles on a logarithmic scale, we see that the emission counts are spaced at equal increments for the exponentially increasing excitation power [Figure 6.10 (b)]. We also visualized the nonlinear trends by taking the ratio of two full spectra at two different excitation powers and dividing the spectral ratio by the ratio of the power increase (i.e. ~ 1.26). The result describes the nonlinear order at which each wavelength behaved during the power increase. As we expected, fluorescein exhibited a quadratic dependence on excitation power across its entire emission spectra [Figure 6.10 (c)]. We also looked at the integration of photon counts within fixed emission wavelengths, and found a slope of ~ 2 on the double-logarithmic MPL vs. I_p plot, as the power was increased within each emission window [Figure 6.10 (d) - (f)]. We tested fluorescein and rhodamine 6G in every condition applied to gold nanoparticles, and found no deviations in these trends at different pulse durations, excitation powers, excitation wavelengths, or emission windows.

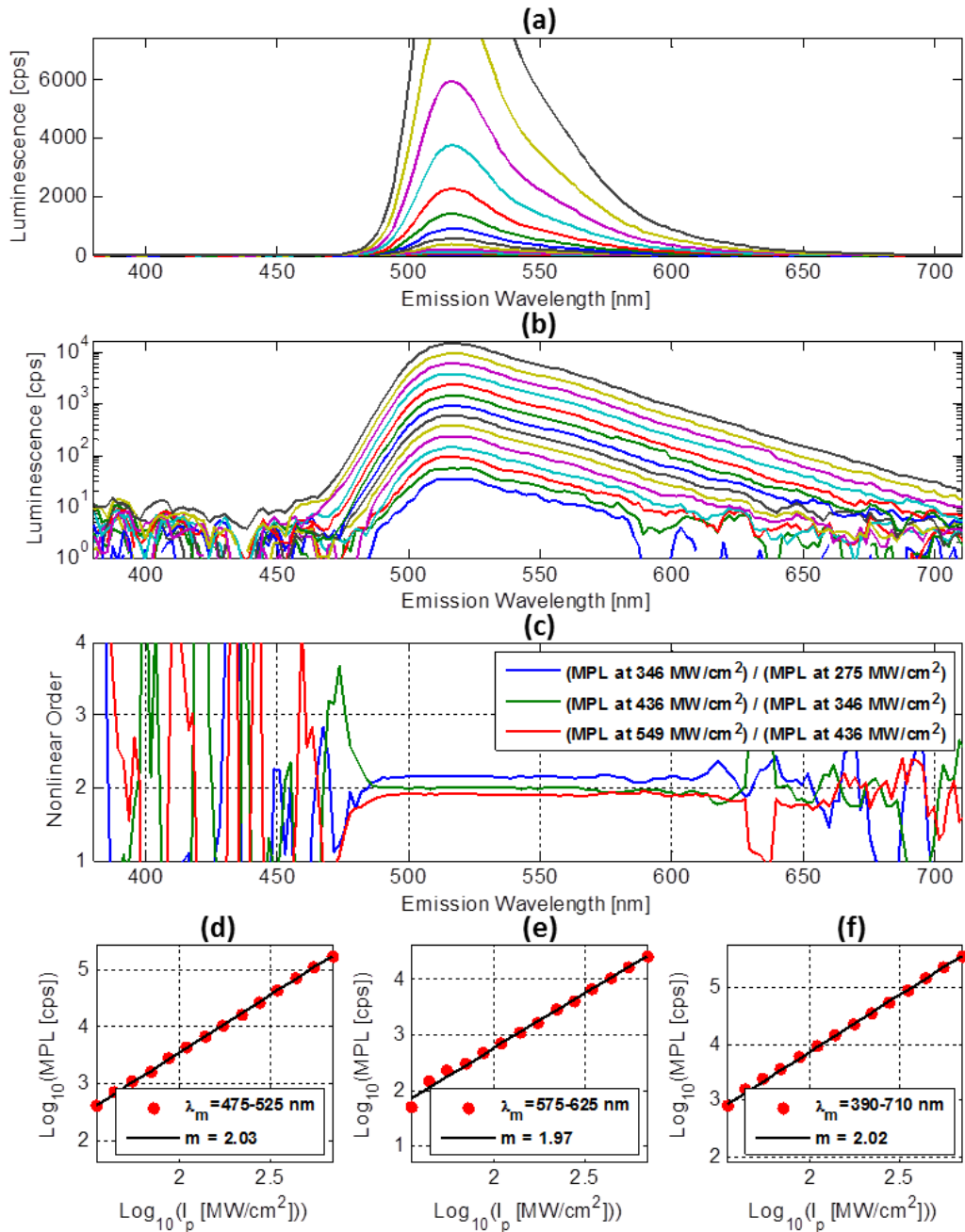


Figure 6.10: Nonlinear emission profile of fluorescein

25 μM fluorescein at $\lambda_x = 780 \text{ nm}$, $\tau_p = 250 \text{ fs}$. (a) Emission counts versus wavelength for exponentially increasing peak intensity, I_p , from 34 MW/cm² to 700 MW/cm² (30 μW to 614 μW average power). (b) Same data as (a), but plotted on logarithmic scale. (c) Ratio of spectrum for several different powers divided by the power ratio. Thus a value of 2 indicates a second order process. (d), (e), and (f) Sum of MPL emission counts versus average power within ranges of 475 to 525 nm, 575 to 625 nm, and 390 to 720 nm, respectively. Best fit linear lines to data above a total of 1000 counts per second (cps) are shown with resulting slope.

Applying this analysis to the GNR780 sample, we found several interesting deviations from the quadratic power dependence that we observed in fluorescein and rhodamine 6G experiments [Figure 6.11]. Qualitatively, the shape of the luminescence curve changes with excitation power, including the formation of a low wavelength peak around 520 nm [Figure 6.11 (b)]. This shape change with varying excitation powers is indicative of different order processes and/or saturation effects. Looking at the spectral ratio, we observe that for constant excitation wavelength, at lower luminescence wavelengths, the luminescence increases at nonlinear orders of up to four, while at higher wavelengths, the nonlinear rate of increase is closer to second order [Figure 6.11 (c)].

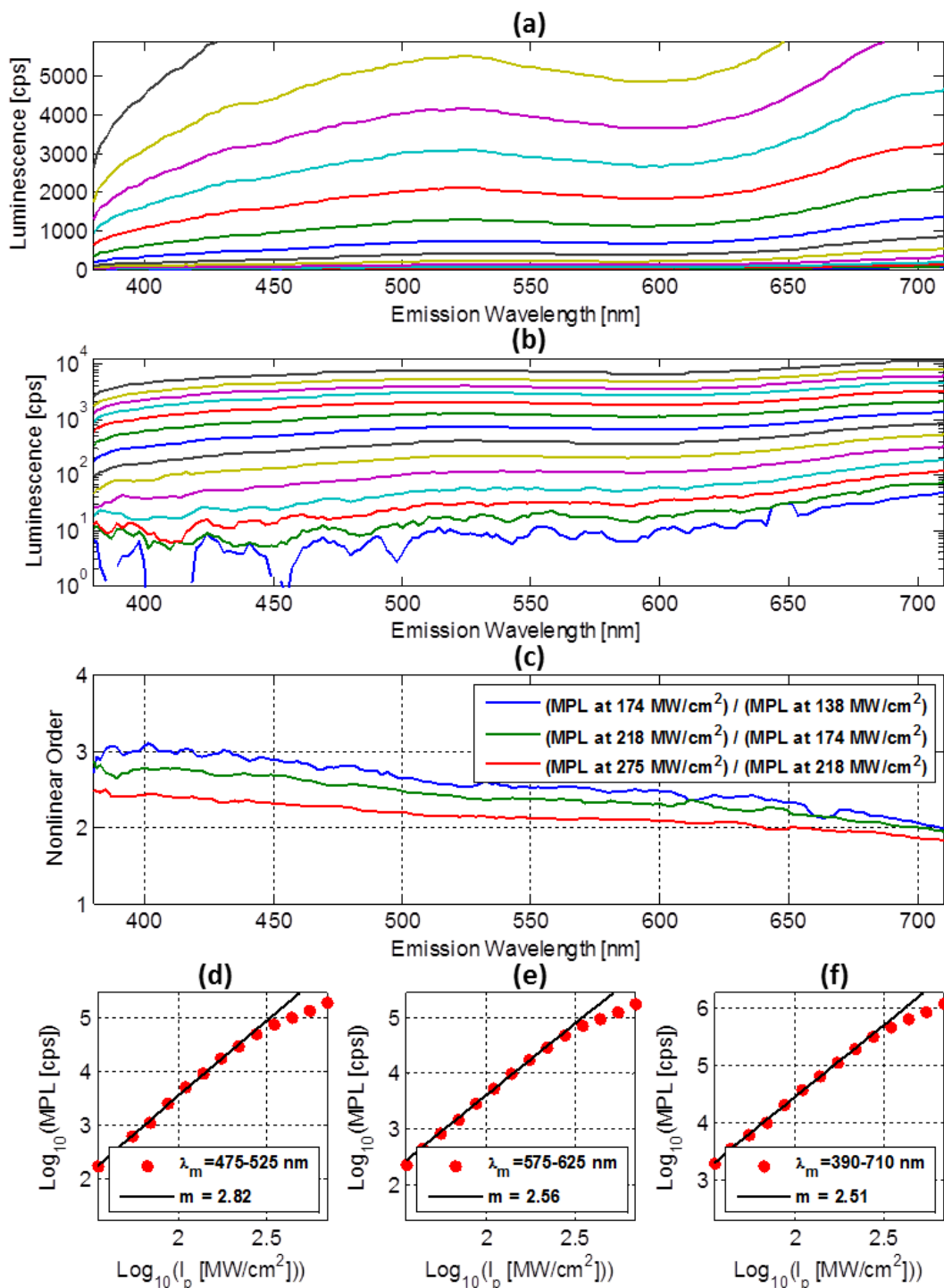


Figure 6.11: Nonlinear emission profile of GNR780

1 pM GNR780 at $\lambda_x = 780$ nm, $\tau_p = 250$ fs. Same format as Figure 6.10. We observe higher order nonlinearity at lower luminescence wavelengths. Saturation can be observed at excitation intensities above ~ 300 MW/cm² (d-f).

At peak excitation intensities greater than $\sim 300 \text{ MW/cm}^2$ (corresponding to an average intensity of $61 \text{ }\mu\text{J/cm}^2$ per pulse), the luminescence begins to saturate, and lower order power dependencies are observed. Plasmon saturation has been observed recently in two reports. Pelton *et al.* observed the onset of plasmon saturation at average intensities of approximately $32 \text{ }\mu\text{J/cm}^2$ per pulse at 800 nm excitation of similarly-sized, single gold nanorods[196]. Park *et al.* found evidence of plasmon saturation in colloidal, randomly oriented, gold nanorods[197]. They observed that when excited at resonant wavelengths at above 1.5 nJ per pulse (approximately 1.9 GW/cm^2), the absorption from the gold nanorods begins to be dramatically reduced[197]. In both studies, though the origin of the plasmon saturation was not fully elucidated, the saturation was attributed to changes in the mechanisms of damping of the surface plasmon and possibly the generation of highly energetic electrons[196],[197]. There are some differences in these previous studies and our results. Pelton *et al.* probed a single gold nanorod aligned to the electric field of the excitation light, while our setup and Park *et al.* probed an ensemble of different nanorod sizes at isotropically distributed orientations with respect to the electric field. Both Pelton *et al.* and Park *et al.* measured the transient linear transmission (and corresponding linear absorption) rather than the multiphoton induced luminescence. However, one would expect that the observation of a reduction in linear absorption would correspond to a change in MPL, especially in the case where MPL is a result of sequential linear absorption events, which we will provide evidence for in Section 6.6.4.

Though the majority of previous MPL studies with nanoparticles report a second order dependence[92],[93],[97],[186],[198-203], the range reported is typically small, and measurements tend to be noisy and difficult to interpret. In these studies, the peak intensities, if indicated, are typically in the GW/cm^2 range. We note that slopes taken in our experiments at this range (above our saturation threshold) would also yield slopes

close to 2. We also reproduce this observation using high numerical aperture focusing in Chapter 7. Some reports do show nonlinear dependencies that are non-integer orders, with values that range from 2.2 to 7[191],[194],[187],[204],[205].

In Figure 6.11 (a), the different rates of increase across the luminescence spectra result in a dramatic peak at 520 nm forming at high intensities. A similar phenomenon was reported previously in an experiment that probed large nanorods fabricated on a substrate with ultrafast excitation[191]. This low wavelength luminescence was attributed to white-light supercontinuum generation, while the longer wavelength luminescence was believed to be MPL. We will demonstrate evidence for an alternative possible origin for this higher order dependence in Section 6.6.4.

Across all nanoparticle samples and excitation wavelengths, we observed a higher order nonlinear dependence at the lower wavelengths of the luminescence range [Figure 6.12]. Slopes were measured by fitting lines at the lower range of I_p used in each sample. There was no clear dependence of nonlinear slope on excitation wavelength, that is, the slopes observed were not necessarily higher or lower when different samples were excited with higher or lower excitation wavelengths.

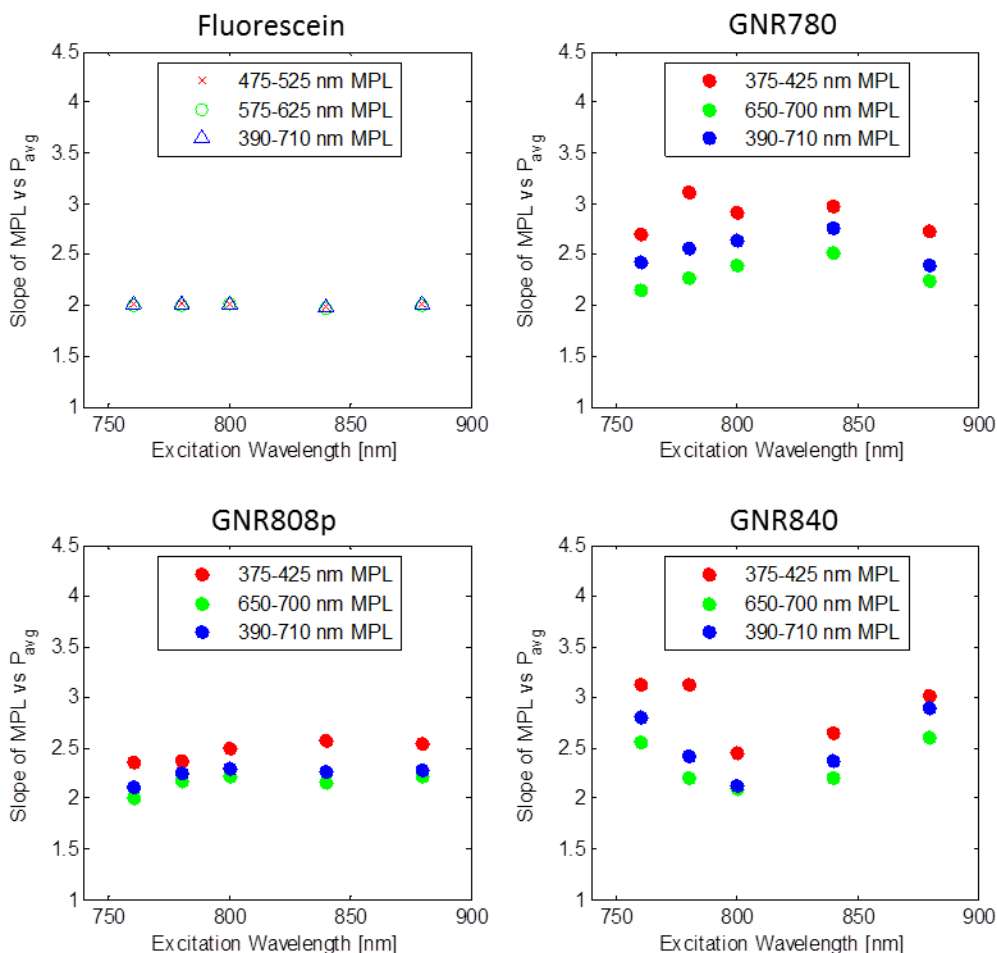


Figure 6.12: Measured slope vs. λ_x for fluorescein and nanoparticle samples. While fluorescein gave a constant quadratic dependence of luminescence on excitation power, our gold nanoparticle samples exhibited a more complicated relationship. One trend observed over all nanoparticle samples and excitation wavelengths was that the lower wavelength luminescence (shown here as red dots) increased at higher rates with excitation power than higher wavelength luminescence (green dots).

We also tested the dependency of MPL on excitation power in a PMT with a series of different bandpass emission filters. The higher sensitivities afforded by a PMT allowed us to probe MPL at slightly lower peak excitation intensities. We observed the same trends found in the spectrometer experiments. In the GNR780 sample, we found a slope of 3.5 through a 436 ± 10 nm bandpass filter (Chroma D436/20x), a slope of 3.0

through a 515 ± 7 nm filter (Chroma HQ515/15m), a slope of 2.4 through a 617 ± 36 nm filter (Semrock FF01-617/73), and a slope of 2.8 across the whole detectable range, with only the 720 nm low pass laser blocking filter in place [Figure 6.13].

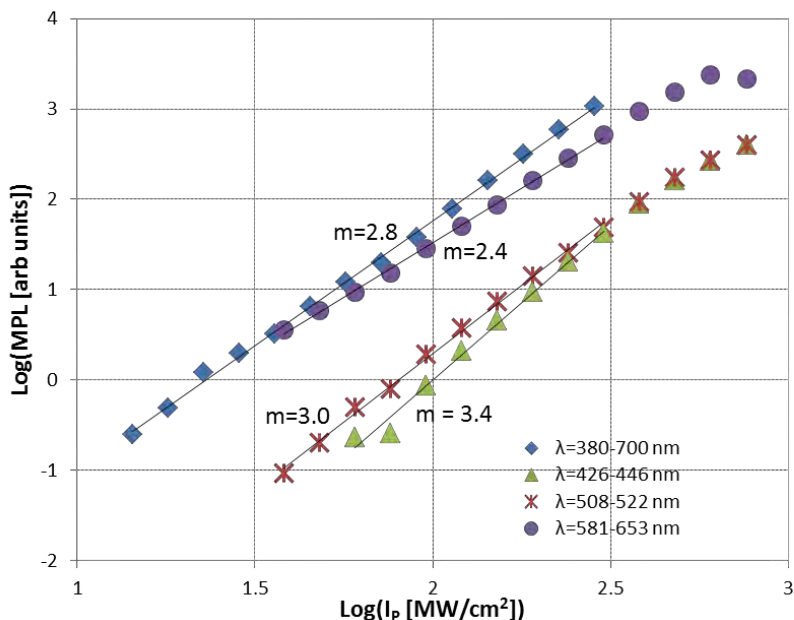


Figure 6.13: MPL vs. average excitation power for GNR780 detected with PMT. We used a PMT for MPL detection with 15 to 800 MW/cm² peak intensity, with various bandpass filters. We observed the similar dependencies found with the spectrometer as the detector. Excitation wavelength was 780 nm and the pulse duration was 250 fs.

The GNS630 sample exhibited weak broadband MPL. However, we did observe a strong backscattered second harmonic generation signal. The SHG signal was well-behaved—it scaled quadratically with excitation power and was centered at half the excitation wavelength [Figure 6.14]. Similarly, the SHG signal observed in other samples with small C_d/C_s ratios scaled quadratically.

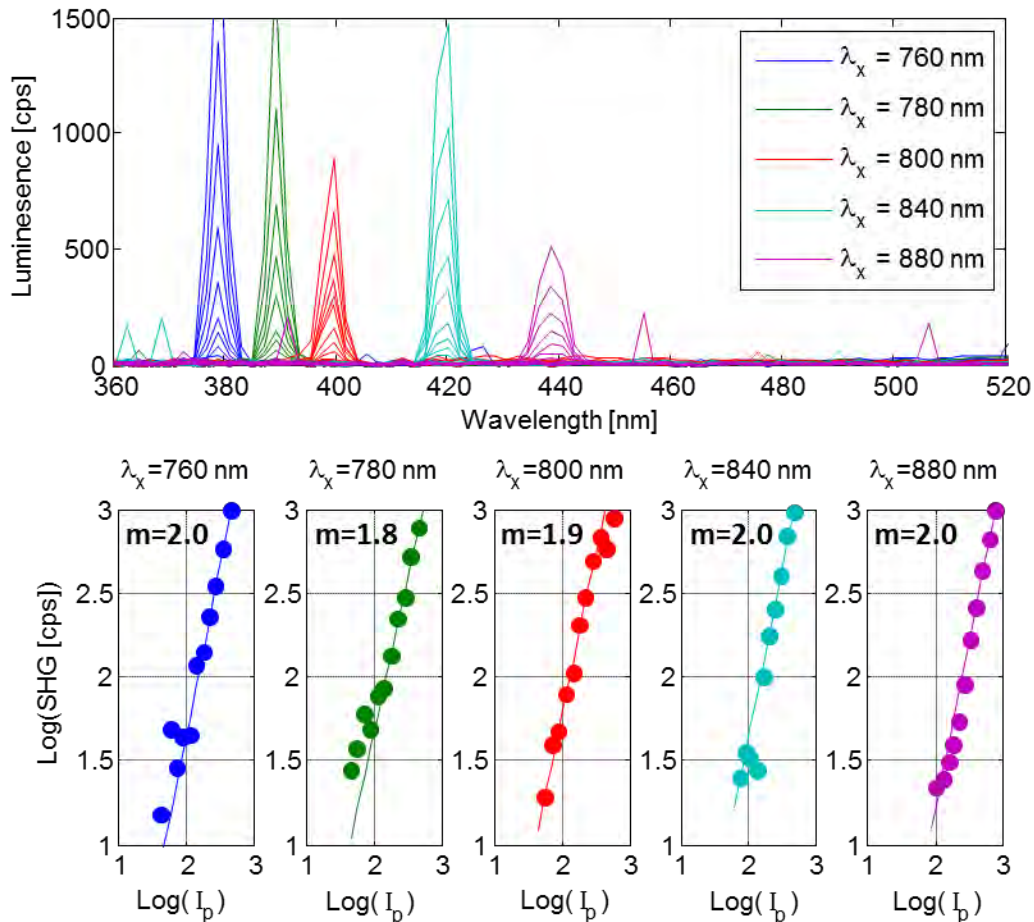


Figure 6.14: Second harmonic generation signal from 160 nm diameter gold nanospheres.

Top: Emission was centered at half the excitation wavelength. Bottom: SHG signal increased quadratically with peak excitation intensity. Units of I_p are MW/cm^2 . No appreciable MPL was observed from this sample.

6.6.4. Dependence of MPL on pulse duration

Qualitative description

As described in Section 2.4.5, two-photon excitation in conventional band-gap fluorophores requires near-simultaneous absorption of two photons. This process can be thought of as excitation through an intermediate virtual state, with an extremely short lifetime. The lifetime, τ_i , of this virtual state dictates the timescale of this interaction,

which was approximated to be 0.1 fs in Section 2.4. For excitation pulse durations much longer than this lifetime ($\tau_p \gg \tau_i$), an electron sitting in this intermediate state will decay before it sees most of the remaining photons in the excitation pulse. In this case, the fluorescence rate will strongly depend on the pulse duration. However, as τ_p approaches τ_i , an electron in the intermediate state stays there long enough to interact with most of the photons in the excitation pulse. At this limit, as the pulse duration becomes shorter and the fluorescence rate becomes independent of τ_p . This limit has not been explored experimentally in band gap fluorophores because: (1) it is difficult to create excitation pulse durations below a few femtoseconds while maintaining the short pulse durations through a high NA objective, and (2) the spectral bandwidth of an excitation pulse grows linearly with a decrease in pulse duration to maintain the time-bandwidth product—and as the pulse duration drops below ~ 10 fs, the spectral bandwidth outgrows the two-photon absorption linewidth of most molecular fluorophores, leading to inefficient excitation[206].

In the case of MPL, the lifetime of the intermediate state is believed to be much longer than 0.1 fs. Unlike multiphoton excitation with a bandgap fluorophore, MPL from gold nanoparticles is excited at the linear absorption bands of the nanoparticle. As a result, the intermediate state is not a forbidden one, and is not determined by the Heisenberg relationship (i.e. ΔE is ~ 0 in Eq. (1)). The band structure diagram in Figure 6.15 illustrates one proposed scheme for two-photon induced luminescence in gold nanoparticles[39],[198]. In this model, the lifetime of the intermediate state is governed by the relaxation time of the holes created in the *sp* band. The lifetime of this *sp* hole has been measured in nanowires and gold films to be on the order of 0.2 - 1 ps[87],[198],[207]. Because our excitation pulse duration can be varied from 200 fs to

greater 8 ps, we expect to be able to detect the deviation from the luminescence dependence on τ_p^{-1} .

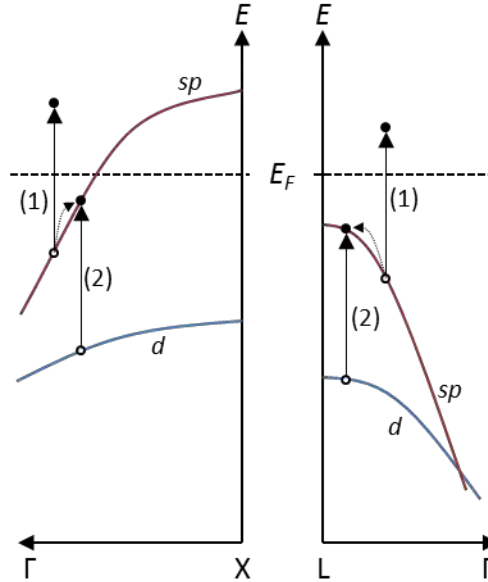


Figure 6.15: Band structure of gold near the X and L symmetry points showing sequential one photon absorption.

One proposed mechanism for MPL in gold is absorption in a two step process: (1) The first photon excites electrons from the sp conduction band below the Fermi energy level (E_F) to the sp conduction band above the Fermi energy level. (2) A photon excites an electron from the d band to combine with the hole produced in the sp conduction band. The excited electron from step (1) can then radiatively decay when it relaxes to the hole created in step (2). Modified from [208].

Mathematical description

In this section, we derive an equation for the TPL rate as a function of pulse duration by modeling the processes illustrated in Figure 6.15 with a set of rate equations (following the approach taken by Biagioni et al.[198]). We assume that the rate of MPL emission is proportional to the rate of d holes produced in the second step of the two-photon absorption. The rate of change in hole density in the sp band below the Fermi level is equal to the rate of electrons excited from this band to sp band above the Fermi

level, minus the loss of hole due to relaxation and recombination with electrons excited from the d band to the sp band. Conversely, the rate of change in hole density in the d band is equal to the rate at which electrons are excited from the d to the sp band minus the rate of d band holes lost to relaxation. The rate equations for these processes can be formulated as:

$$\frac{dN_{sp}}{dt} = \sigma_{sp \rightarrow sp} N F(t) - \frac{N_{sp}}{\tau_{sp}} - \sigma_{d \rightarrow sp} N_{sp} F(t) \quad (7.6)$$

$$\frac{dN_d}{dt} = \sigma_{d \rightarrow sp} N_{sp} F(t) - \frac{N_d}{\tau_d}, \quad (7.7)$$

where N_{sp} and N_d are the densities of holes in the sp and d bands, N is the electron density in the sp conduction band, $\sigma_{sp \rightarrow sp}$ and $\sigma_{d \rightarrow sp}$ are the cross sections for the first and second absorption events, respectively, $F(t)$ is the instantaneous excitation intensity, and τ_{sp} and τ_d are the relaxation times of the holes in the sp and d bands, respectively. In the small perturbation regime, where $N_{sp} \ll N$, the third term in Eq. (7.6) can be ignored. Taking the Fourier transform of Eqs. (7.6) and (7.7), the rate equations be rewritten as:

$$\hat{N}_{sp}(\xi) = \left(\frac{\sigma_{sp \rightarrow sp} N}{2\pi i \xi + 1/\tau_{sp}} \right) \hat{F}(\xi) \quad (7.8)$$

$$\hat{N}_d(\xi) = \left(\frac{\sigma_{d \rightarrow sp}}{2\pi i \xi + 1/\tau_d} \right) \hat{N}_{sp}(\xi) * \hat{F}(\xi), \quad (7.9)$$

where the caret ('^') indicates the Fourier transform of the function over ordinary frequency, ξ , and '*' denotes a convolution. Combining Eqs. (7.8) and (7.9) and taking the inverse Fourier transform, we obtain an expression for the instantaneous density of holes in the d band:

$$N_d(t) = N \sigma_{d \rightarrow sp} \sigma_{sp \rightarrow sp} \left(e^{-\frac{t}{\tau_d}} u(t) \right) * \left(F(t) \int_{-\infty}^{\infty} e^{-\frac{T}{\tau_{sp}}} u(t) F(t - T) dT \right), \quad (7.10)$$

where $u(t)$ is the Heaviside step function. For the purposes of our experiments, we are interested in the time-averaged rate of two-photon luminescence, $\langle TPL \rangle$. Assuming the

excitation source consists of pulses separated by the inverse of the laser repetition rate, ν_{rep}^{-1} , the time averaged density of holes in the d band, $\langle N_d \rangle$, is given by:

$$\langle N_d \rangle = \nu_{rep} \int_0^{\nu_{rep}^{-1}} N_d(t) dt \quad (7.11)$$

Combining Eqs. (7.10) and (7.11), we can use Fubini's theorem to separate the integral of the convolution to a product of integrals. In the limit where the excitation pulses are far enough apart in time to act independently of each other ($\tau_d \ll \nu_{rep}^{-1}$), the expression for $\langle TPL \rangle$ can be reduced to:

$$\begin{aligned} \langle TPL \rangle \propto \langle N_d \rangle &= \nu_{rep} N \sigma_{d \rightarrow sp} \sigma_{sp \rightarrow sp} \tau_d \\ &\times \int_{-\infty}^{\infty} F(t) \int_0^{\infty} e^{-\frac{T}{\tau_{sp}}} F(t-T) dT dt \end{aligned} \quad (7.12)$$

To gain more insight into the parameters affecting $\langle TPL \rangle$, we can define $F(t)$ as the product of a constant and a time-dependent function: $F(t) = E_{pulse} h_\delta / A$, where E_{pulse} is the total number of photons contained within a single excitation pulse, A is the area of the focused spot, and $h_\delta(t)$ is a time-dependent function which describes the temporal profile of the excitation pulse and is normalized to integrate to one. The time-independent constants can then be taken out of the integrals and the TPL rate is given by:

$$\begin{aligned} \langle TPL \rangle \propto \nu_{rep} N \sigma_{d \rightarrow sp} \sigma_{sp \rightarrow sp} \tau_d &\left(\frac{E_{pulse}}{A} \right)^2 \\ &\times \int_{-\infty}^{\infty} h_\delta(t) \int_0^{\infty} e^{-\frac{T}{\tau_{sp}}} h_\delta(t-T) dT dt \end{aligned} \quad (7.13)$$

From this equation, we see that TPL increases linearly with the cross sections from each linear sequential absorption event, the excitation pulses per second (ν_{rep}), and longer d band hole relaxation times. The quadratic dependence of TPL on excitation intensity is correctly derived by the $(E_{pulse}/A)^2$ term.

The integration terms in Eq. (7.13) describe the influence of the excitation pulse dynamics and the lifetime of the intermediate state. For $\tau_{sp} \ll \tau_p$, which is the regime typically probed in conventional band-gap fluorophores, the TPL rate is proportional to the integration of the squared energy per pulse, which scales as τ_p^{-1} . For $\tau_{sp} \gg \tau_p$, on the other hand, the TPL rate is proportional to the integral of the pulse autocorrelation, which is independent of τ_p . This result is consistent with the qualitative discussion in the preceding section.

Experimental results

We tested the MPL versus pulse duration for gold nanorods and nanospheres (the GNR780 and GNS530 samples). Again, we also tested fluorescein and rhodamine 6G as a validation set, which should exhibit a τ_p^{-1} dependence. We changed the pulse duration from 220 fs to 8.5 ps. Typical results for the total integrated luminescence (380 to 720 nm) as a function of excitation power and pulse duration in a gold nanoparticle sample and fluorescein are shown in Figure 6.16. As in Section 6.6.3, the GNR780 sample exhibited a nonlinear order of slightly greater than two. We also observe the onset of saturation around the same intensity regime (170 μW , or peak intensities of approximately 200 MW/cm^2) as found in Section 6.6.3. Plotting the luminescence vs. pulse duration, we observe the expected τ_p^{-1} dependence in the fluorescein sample, and a clear deviation from this dependence at pulse durations shorter than ~ 4 ps in the GNR780 sample [Figure 6.16 (b)].

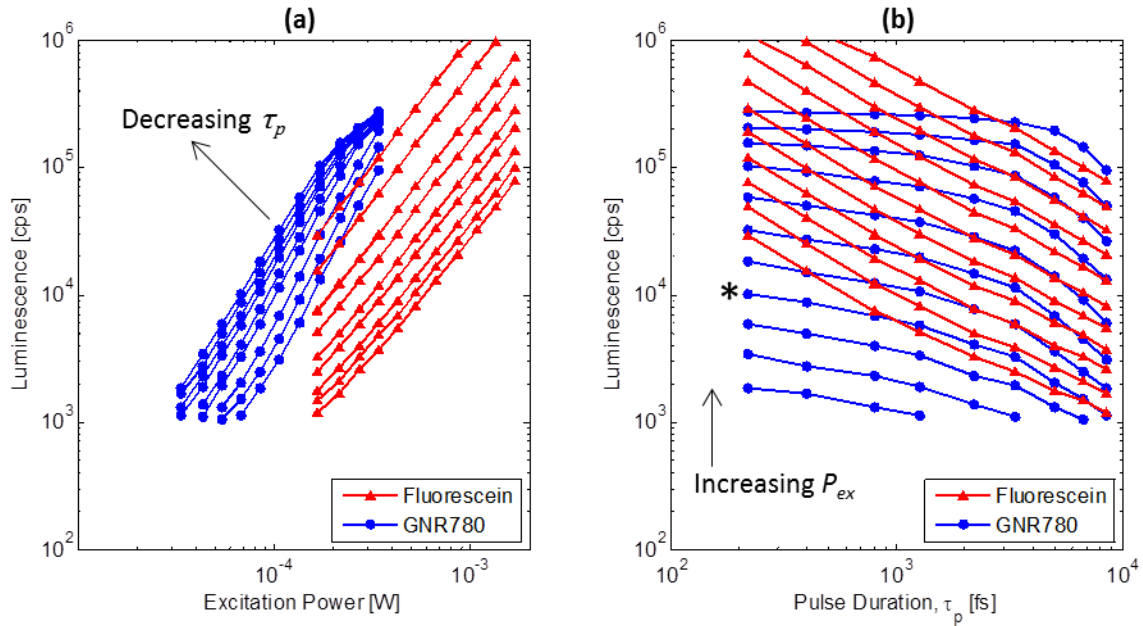


Figure 6.16: MPL vs. excitation intensity and pulse duration for fluorescein and GNR780.

(a) Luminescence vs. excitation power for given pulse durations in 25 μM fluorescein and 1 nM GNR780. Saturation is observed above 170 μW average power in the GNR780 sample with 250 fs pulse duration. (b) Luminescence vs pulse duration for increasing excitation power. The fluorescein behaves as expected for a conventional band gap fluorophore. GNR780, on the other hand, deviated from the τ_p^{-1} dependence for $\tau_p < 4$ ps. The starred line in (b) is used to compare to our model in Figure 6.17 because it doesn't exhibit saturation effects.

To compare the observed luminescence vs. pulse duration to the model described in Eq. (7.13), we assume a Gaussian pulse shape:

$$h_\delta(t) = \sqrt{\frac{\ln(2)}{\pi}} \left(\frac{2}{\tau_p}\right) e^{-\frac{4 \ln(2) t^2}{\tau_p^2}}. \quad (7.14)$$

The trend from Eq. (7.13) is then normalized to give the same initial value as the experiments and compared to measurements in the GNR780, GNS530, and fluorescein samples. We observed good fits to the nanorod, nanosphere, and fluorescein sample using τ_{sp} lifetimes of 500, 1000, and 0.1 fs, respectively [Figure 6.17].

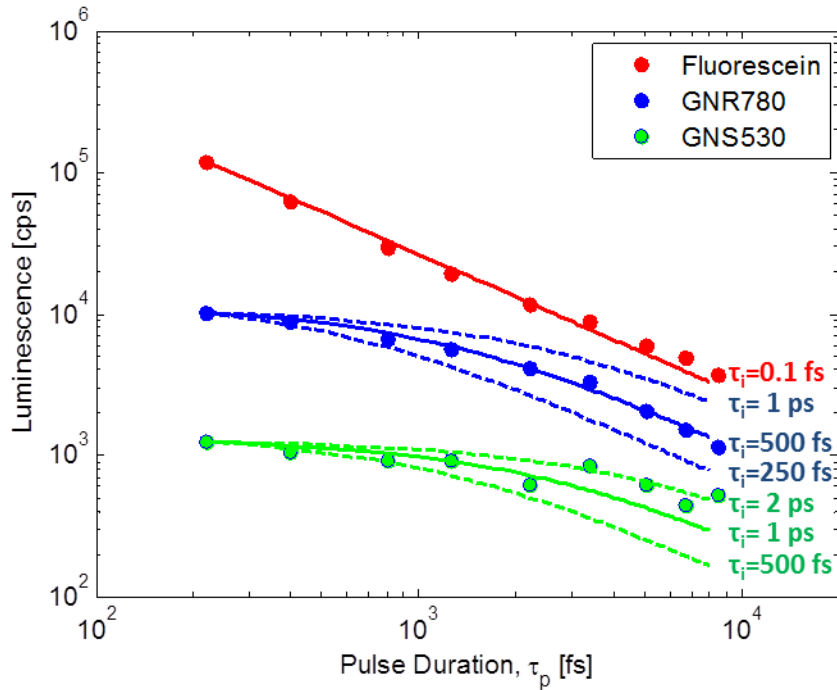


Figure 6.17: Comparison of experiment and model for MPL vs τ_p . Luminescence vs pulse duration for Fluorescein, GNR780, and GNS530 at constant average powers of 420, 85, and 500 μW , respectively (dots). Lines are the result of modeling the MPL using Eq. (7.12) and normalizing to match the luminescence values at the shortest pulse duration. Blue and green solid lines are for the GNR780 and GNS530 samples with a τ_{sp} of 500, and 1000 fs, respectively. Dashed lines are for models with twice and half the τ_{sp} modeled in the respective solid lines. The red line is a τ_p^{-1} fit to the fluorescein measurements.

The ability to match the observed luminescence trend by the model described in Eq. (7.13) provides evidence that TPL is due to a sequential two-step absorption process rather than simultaneous two-photon absorption. However, the model does not match the measurement exactly—it predicts a purely quadratic dependence of MPL on excitation power, whereas we observe nonlinear order of slightly greater than two, and increasing nonlinearity at longer pulse durations [Figure 6.18].

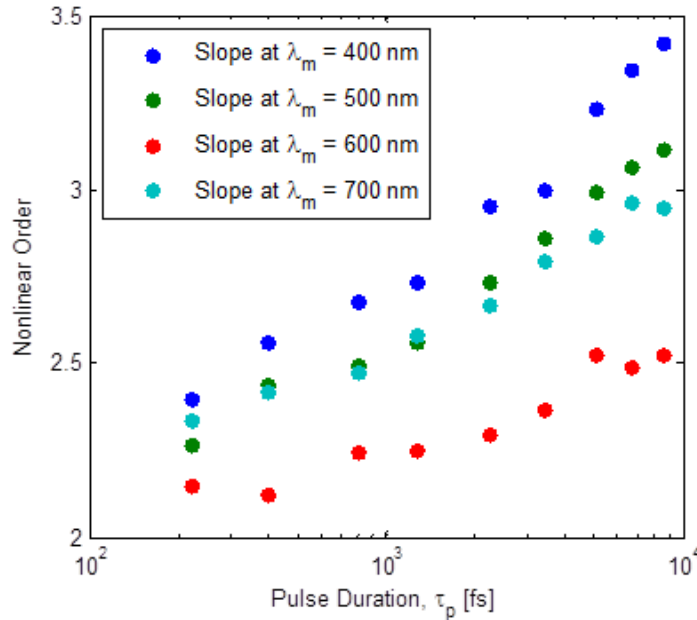


Figure 6.18: Nonlinear order observed in GNR780 at $\lambda_x = 780$ nm versus pulse duration.

We observed increasing contribution of higher order nonlinear effects at longer pulse durations within shorter emission windows. This result is consistent with other findings, which attributed the phenomena to white light supercontinuum generation (WLSC).

A nonlinear absorption cross section that increases with pulse duration has been reported previously in experiments with thin gold films. Rotenberg *et al.* observed an increase in the nonlinear absorption by two orders of magnitude as they increased pulse duration from 0.1 to 5.8 ps [Figure 6.19][209]. They explained the dependency of the nonlinear absorption on pulse duration by the change of the electron temperature during the duration of the excitation pulse. For long pulse durations, the electrons have enough time to change temperature, increasing the effective absorption coefficient.

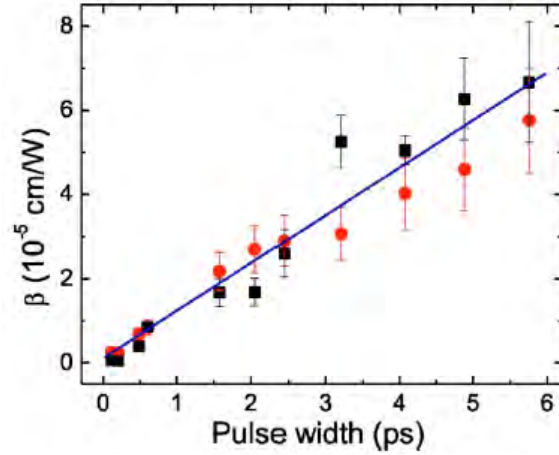


Figure 6.19: Nonlinear absorption coefficient (β) dependence on pulse duration. Using a z-scan technique, β of a thin gold film was observed to linearly increase with pulse duration. Squares are experiments, circles are simulation points, and the line is to guide the eyes. Figure from [209].

Incorporating a nonlinear absorption cross section into the rate equations described in Eqs. (7.6) and (7.7), the deviation from the quadratic dependence of MPL on excitation power can be appropriately modeled. We substituted the linear cross section term in Eq. (7.6) with a term which contains the linear cross section and an intensity-dependent nonlinear one:

$$\sigma_{sp \rightarrow sp} \rightarrow \sigma_{sp \rightarrow sp} + \beta_{eff} F(t) \quad (7.15)$$

We solved the new rate equations numerically with a Runge-Kutta method. We found that as the quantity $I \beta_{eff} / \sigma_{sp \rightarrow sp}$ becomes large, MPL becomes proportional to P_{avg}^3 , and as it goes to zero, MPL is proportional to P_{avg}^2 . If both cross sections in Eq. (7.7) ($\sigma_{d \rightarrow sp}$ and $\sigma_{sp \rightarrow sp}$) are modeled to have a nonlinear component, the MPL rate can show a second- to fourth- order power dependence, depending on the values of the σ and β parameters, and the intensity regime simulated. Furthermore, based on the data from Figure 6.19, the increase in slope with increasing pulse duration that we observe in our measurements [Figure 6.18] can be reproduced with this model. Figure 6.20 plots the simulations of MPL rates vs. pulse duration and excitation power for moderate $I \beta_{eff} /$

$\sigma_{sp \rightarrow \sigma_{sp}}$ values. Pollnau *et al.* have also explored models using excited state absorption and energy-transfer upconversion to explain complex nonlinear dependencies in multistate systems[210].

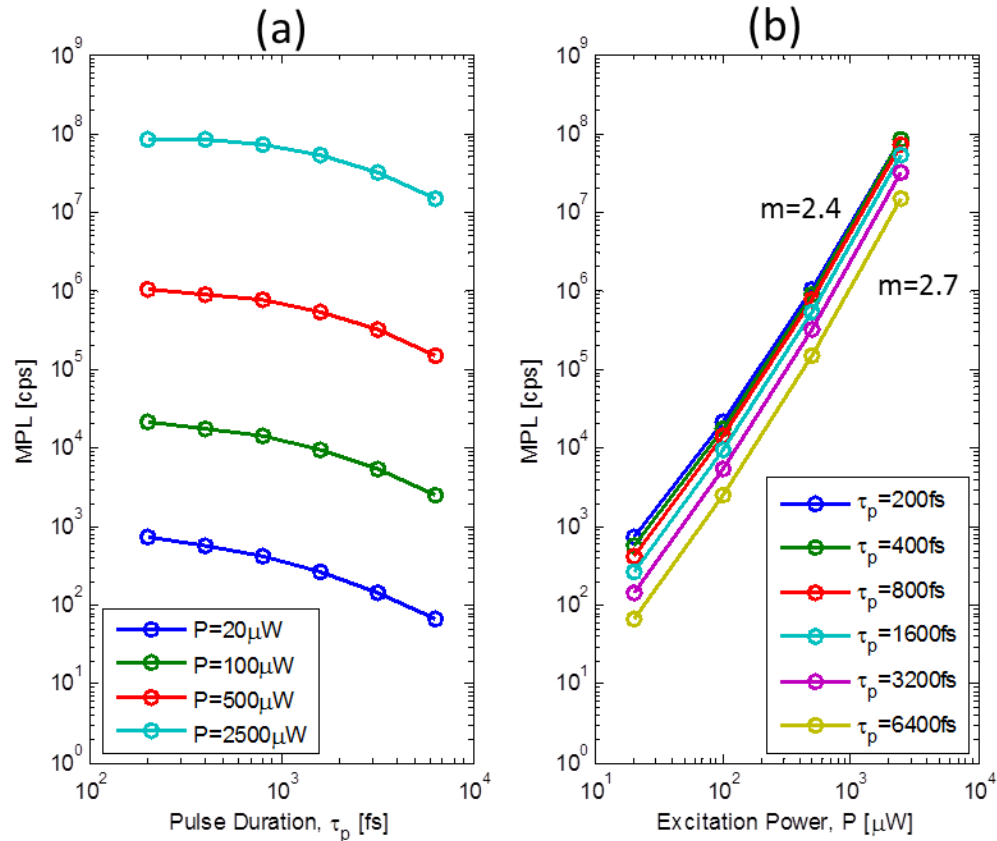


Figure 6.20: Simulated MPL rates vs. pulse duration and excitation power for sequential nonlinear absorption.

Numerical solutions to sequential absorption with a nonlinear expansion to the cross sections. This model exhibits a deviation from the τ_p^{-1} dependence for small τ_p (a). Using the trend of β_{eff} with pulse duration from previous studies [209], we expect an increasing slope on the MPL vs. power curve for longer pulse durations (b). Using this model, we find that slopes of 2 to 4 are possible, depending on the ratio of β to σ , which could explain our experimental observations.

In conclusion, we have found that unlike two-photon excited fluorescence in bandgap fluorophores, MPL rate is weakly dependent on excitation pulse duration for pulse durations shorter than several hundred femtoseconds (below the lifetime of the

intermediate state). This observation can be accurately explained by the sequential photon absorption hypothesis[39],[198], using an intermediate state lifetime of approximately 500 fs. This lifetime value is in good agreement with previous studies, assuming the origin is the relaxation of holes in the *sp* conduction band[87],[198]. The higher order nonlinear dependencies of MPL on excitation power, which become more prevalent at longer pulse durations, can be explained by either or both of the absorption cross sections being modeled with a nonlinear component whose contribution increases with pulse duration.

6.6.5. Quantification of two-photon action cross section

In Sections 6.6.3 and 6.6.4 we showed that instead of a purely second order process, the MPL from gold nanoparticles exhibits a slightly higher order nonlinear dependence on excitation power. At the shortest pulse durations we can achieve in our system (220 fs), we found a $\log(\text{MPL})$ vs $\log(P)$ slope of 2.3 to 2.5 if the whole luminescence spectrum is considered and a slope of 2.1 to 2.3 when monitoring only the higher luminescence wavelengths. Because MPL is a complex, non-quadratic process, the traditional two-photon action cross section does not apply. In this section we calculate an effective cross section by comparing measurements performed at short pulse duration and low excitation power regions from gold nanoparticles and to a reference dye of known two-photon action cross section (fluorescein). In these regions, the slopes observed are relatively close to two. This measurement, of course, is meaningful only when paired with the excitation pulse duration, since the measured effective two-photon action cross section will increase with increasing pulse duration for pulse durations less than the lifetime of the intermediate state. It is also worth noting that this strategy results in a conservative calculation of nanoparticle σ_{TPA} ; using longer pulse durations or comparing

brightness at higher I_p values (while still below the saturation threshold) would result in larger values of σ_{TPA} .

Theoretical development

In this section we derive the relationship between the rate of emission photons and the parameters of our system and sample, and then compare predicted rates to our measured values. Following the work of Xu and Webb[211], we can calculate the expected number of emission photons produced under our experimental conditions. The instantaneous rate of detected emission photons, $F(t)$ [photons s^{-1}], is related to the rate of two-photon-absorbed photons, N_{abs} [photons s^{-1}], the fluorescence quantum yield, η_2 , and the system collection efficiency, ϕ , by:

$$F(t) = \frac{1}{2} N_{abs}(t) \eta_2 \phi \quad (7.16)$$

As a second order process, N_{abs} , is related to the square of the excitation intensity, I [photons $s^{-1} \text{ cm}^{-2}$], the concentration of the molecule, C [molecules cm^{-3}], and the two-photon absorption cross section, δ [units of GM, or $10^{-50} \text{ cm}^4 \text{ s photons}^{-1}$] in a sample volume V [cm^3] by:

$$N_{abs}(t) = \int_V I^2(\vec{r}, t) C(\vec{r}, t) \delta(t) dV \quad (7.17)$$

Given a homogenous distribution of fluorescent molecules, and in the absence of saturation and photobleaching, C and δ are constant in time and space and can be removed from the integral. Assuming the intensity can be separated into a spatially- and temporally-dependent expression, $I(\vec{r}, t) = S(r)I_0(t)$, we can rewrite Eq. (7.17) as:

$$N_{abs}(t) = C \delta I_0^2(t) \int_V S^2(\vec{r}) dV \quad (7.18)$$

Substituting Eq. (7.18) into Eq. (7.16), the time averaged fluorescence emission rate is then:

$$\langle F(t) \rangle = \frac{1}{2} \eta_2 \phi C \delta \langle I_0^2(t) \rangle \int_V S^2(\vec{r}) dV \quad (7.19)$$

The average intensity squared can be rewritten in measurable terms utilizing the second-order temporal coherence parameter $g = \langle I_0^2(t) \rangle / \langle I_0(t) \rangle^2$:

$$\langle F(t) \rangle = \frac{1}{2} \eta_2 \phi C \delta g \langle I_0(t) \rangle^2 \int_V S^2(\vec{r}) dV \quad (7.20)$$

For a Gaussian temporal distribution, g is $0.664/(f\tau)$ [212], where f is the pulse repetition rate, and τ is the pulse duration FWHM. Neglecting absorption and scattering loss, the average intensity is related to the average excitation power, P , by the lateral spot size, which is defined by the excitation wavelength, λ , and the numerical aperture, NA:

$$\langle I_0(t) \rangle = \langle P(t) \rangle \frac{\pi NA^2}{\lambda^2} \quad (7.21)$$

The spatial distribution of the excitation light has been evaluated numerically for thick samples to be approximately[211]:

$$\int_V S^2(\vec{r}) dV \approx \frac{8n\lambda^3}{\pi^3 NA^4} \quad (7.22)$$

where n is the index of refraction of the sample. Combining Eqs (7.20)-(7.22), we arrive at an expression for the time averaged rate of emission photons:

$$\langle F(t) \rangle = \frac{1}{2} \eta_2 \phi C \delta g \frac{8n\langle P(t) \rangle^2}{\pi\lambda} \quad (7.23)$$

With this expression we calculate the expected signal acquired by our detector. For cross section measurements with fluorescein, all the parameters are approximately known, so we also compare the theoretical rate of detected emission photons to the measured rate. Finally, we note that the product of δ and η_2 , called the two-photon action cross section (σ_{TPA}), is the relevant measure of brightness for a fluorophore. It describes the magnitude

of the emission to be expected for a given excitation intensity, and as a result, is easier to measure and the more often reported value for two-photon excitation fluorophores.

Collection efficiency

We estimate the collection efficiency of our system by finding the average throughput of each element in the detection path. To determine the throughput of our objective, ϕ_{obj} , we calculate the effective numerical aperture using geometric ray tracing at the refractive index mismatch induced by the sample [Figure 6.21].

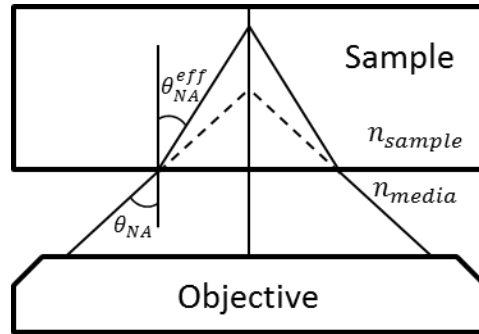


Figure 6.21: Determination of effective collection angle. Due to refractive index mismatch (air to water), the collection angle of our objective, θ_{NA}^{eff} , is less than the angular numerical aperture, θ_{NA} .

From Figure 6.21, using Snell's law, the effective angular numerical aperture is:

$$\theta_{NA}^{eff} = \sin^{-1} \left(\frac{n_{media} \sin \theta_{NA}}{n_{sample}} \right), \quad (7.24)$$

The collection efficiency of the objective is then simply the product of the fractional solid angle collected and the transmission efficiency of the objective, T_{obj} :

$$\phi_{obj} = \frac{1}{2} (1 - \cos \theta_{NA}^{eff}) T_{obj}, \quad (7.25)$$

In our cross section experiments, we used an Olympus 20x/0.75NA objective (UPLSAPO), with an average T_{obj} of 0.89 throughout the visible range. Our objective throughput, assuming $n_{media} = 1$ and $n_{sample} = 1.33$, is $\phi_{obj} = 0.078$.

The throughput of the rest of our detection path was calculated by the specifications of each component. The throughputs of our dichroic mirror (Semrock FF720), focusing lens (Thorlabs $f = 100$ mm), and excitation blocking filter (Semrock FF01-750) in the visible range, are $\phi_{dc} = 0.92$, $\phi_{fl} = 0.96$, and $\phi_{ef} = 0.98$, respectively, from the manufacturer's specifications. Assuming the emission light collected out of the objective is perfectly collimated, we estimate the only loss coupling the light into the detector is from the grating efficiency, $\phi_{gr} = 0.65$. The spectrometer detector was a cooled back-illuminated CCD (DV401-BC, Shamrock). Using the average quantum yield as the source of loss in the CCD, the throughput of the detector is approximately $\phi_{det} = 0.95$. Our total emission detection throughput can then be found by:

$$\phi = \phi_{obj}\phi_{dc}\phi_{fl}\phi_{ef}\phi_{gr}\phi_{det} \approx 0.04 \quad (7.26)$$

With an estimated value for system collection efficiency, we can now use Eq. (7.23) to estimate emission detection rate in our system and compare to an experiment with fluorescein. The values used are summarized in Table 6.4. The calculated and predicted emission rates for fluorescein in a pH 12 buffer solution are displayed in Figure 6.22.

Parameter	Symbol	Value	Units
Wavelength	λ	[760, 780, 800, 840, 880]	nm
Index of refraction	n	1.33	
Two-photon action cross section	σ_{TPA}	[36, 37, 36, 12, 11]	$\text{cm}^4 \text{s photons}^{-1}$
Collection efficiency	Φ	0.04	
Concentration	C	25 $=1.50 \times 10^{16}$	μM molecules cm^3
Second order temporal coherence	g	3.00×10^4	
Excitation Power	P	[244, 244, 251, 654, 689] $=[9, 9, 10, 28, 30] \times 10^{14}$	μW photons s^{-1}

Table 6.4. Parameters used in calculating absolute emission counts for fluorescein. Two-photon action cross sections for fluorescein are from[213].

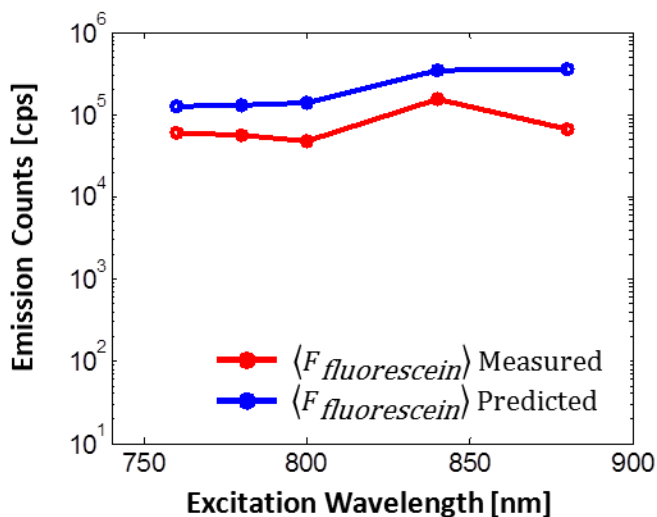


Figure 6.22: Measured vs. predicted emission counts of fluorescein. The rate of emission photons collected from a fluorescein solution is within a factor of four of that predicted from Eq. (7.23).

Though of the same order of magnitude, our measured emission rate is approximately 2-4x less than the predicted rate. This difference could be due to a number of factors, including (1) the model does not account for any collection efficiency losses from misalignment or deviations of optical element performance from specifications; (2)

the focusing lens into our spectrometer is not an achromat, so we expect some system loss coupling into the spectrometer from chromatic aberrations; and (3) the second order temporal coherence was calculated from a measured autocorrelation, which resulted in a pulse duration of $\tau_{\text{FWHM}} = 250$ fs. However, the temporal pulse shape is likely more complicated than the smooth Gaussian assumed, but after the autocorrelation, any rapid changes in the pulse envelope are smoothed out[114]. (4) Finally, though Eq. (7.23) is independent of NA for perfect Gaussian focusing, an aberrated beam may introduce focal spot dependencies—for complicated intensity distributions, it may be difficult to predict S^2 .

The absolute two-photon action cross section can be measured by Eq. (7.23) [97],[213]. However, the equation is sensitive to a number of parameters that are difficult to characterize. As a result, given the values from measured emission rate for fluorescein, we would have measured a two-photon action cross section that is two to four times lower than the actual value. Consequently, we adopt a different technique that utilizes a reference measurement to a molecule with a known two-photon action cross section, σ_{TPA}^r , and is independent of focal spot geometry, g , and ϕ [214].

Measurement of the two-photon action cross section by reference standard

If the two photon action cross section for a reference molecule (σ_{TPA}^r) is known, the ratio of the emission rates for an unknown sample, $\langle F_s(t) \rangle$, to the reference, $\langle F_r(t) \rangle$ eliminates some of the dependencies of Eq. (7.23). For similar emission spectra, the collection efficiencies are approximately equal. At the same excitation wavelength, g and λ also cancel out, leaving us with:

$$\frac{\langle F_s(t) \rangle}{\langle F_r(t) \rangle} = \frac{C_s \sigma_{TPA}^s \langle P_s(t) \rangle^2}{C_r \sigma_{TPA}^r \langle P_r(t) \rangle^2}. \quad (7.27)$$

Rearranging Eq. (7.27), we find an expression with which we can calculate σ_{TPA}^s by measuring the emission from the sample compared to a reference dye of known σ_{TPA}^r :

$$\sigma_{TPA}^s = \frac{C_r \langle F_s(t) \rangle \sigma_{TPA}^r \langle P_r(t) \rangle^2}{C_s \langle F_r(t) \rangle \langle P_s(t) \rangle^2}. \quad (7.28)$$

This equation has been used previously to calculate σ_{TPA} of different fluorophores using fluorescein as a reference [214]. It requires that both measurements are taken within a intensity regime where two-photon emission dominates the signal and there is no appreciable signal from other sources, such as second harmonic generation (SHG), three-photon excited (3PE) emission, or white light supercontinuum (WLSC) generation. Because these phenomena have been observed from plasmonic nanoparticles under ultrafast excitation, we use a modified approach. Instead of measuring the emission counts at a single excitation power, which is given to the error in the power calibration and to that inherent in a single emission measurement, we compare the intercept, β , of a line with a slope of two fit to a plot of $\text{Log}\langle F_s(t) \rangle$ vs $\text{Log}\langle P_s(t) \rangle$. That is:

$$\text{Log}\langle F(t) \rangle = 2\text{Log}\langle P(t) \rangle + \beta \quad (7.29)$$

$$10^\beta = \frac{\langle F(t) \rangle}{\langle P(t) \rangle^2}. \quad (7.30)$$

Now substituting Eq. (7.30) into Eq. (7.28),

$$\sigma_{TPA}^s = 10^{(\beta_s - \beta_r)} \sigma_{TPA}^r \frac{C_r}{C_s}, \quad (7.31)$$

where β_s and β_r are the intercepts of best fit lines to the logarithmic emission vs. power plots for the sample of interest and the reference sample, respectively.

Because we observe a deviation from a pure second order dependence of MPL on excitation power, we take the MPL measurements at the lowest excitation intensities. Thus, we find β_s for a slope of two line that is fit at excitation intensities of 30-60 MW/cm². We also measure all cross sections at a short pulse duration (250 fs). The cross

section we measure may be more appropriately described as the effective two-photon action cross section because due to the non-quadratic relationship between MPL and I_p , and the deviation of MPL from a τ_p^{-1} dependence, there is a small difference in measured values when fitting β_s at different intensity regimes and pulse duration. For the measurements presented here, we took the most conservative estimates of the effective two-photon action cross section—at short τ_p and small I_p , the σ_{TPA} we calculate is significantly smaller than it would be if we used different excitation parameters.

Results

We validated our method by measuring the σ_{TPA} of fluorescein using a separate fluorescein measurement as a reference, and comparing a rhodamine 6G σ_{TPA} measurement to values found in the literature [214]. Fluorescein was prepared at 25 μM concentration in a pH 12 buffer, and rhodamine 6G was prepared at a 100 μM concentration, diluted in methanol. We found excellent agreement between consecutive measurements of fluorescein, and with published values of rhodamine 6G [Figure 6.23].

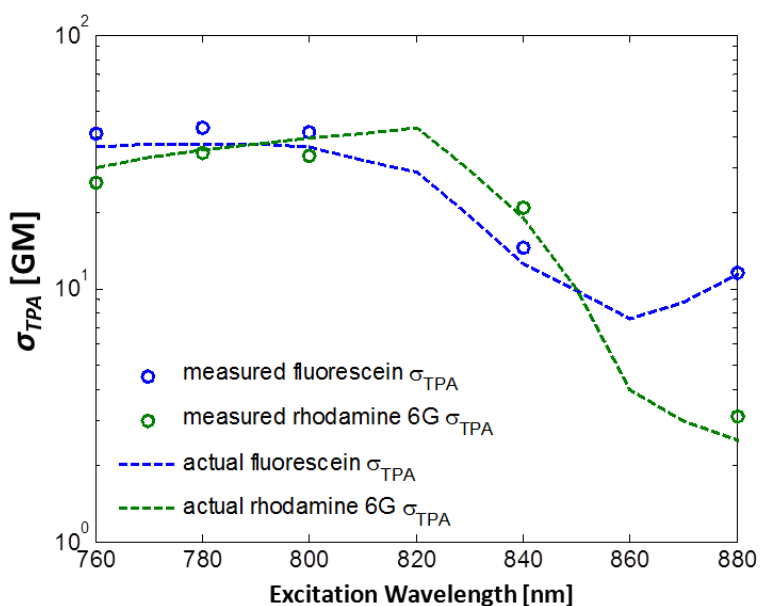


Figure 6.23: Validation of reference fluorophore technique for calculating σ_{TPA} . Using fluorescein as a reference, the calculated σ_{TPA} for a second fluorescein measurement and a rhodamine 6G sample (measured values) compare well to values reported in the literature (actual values). Actual values are from [214].

We measured the σ_{TPA} of each nanoparticle sample listed in Section 6.2 [Figure 6.24]. Cross sections were calculated based on the concentration values found in Section 6.5, using a 25 μM solution of fluorescein in a pH 12 buffer as the reference. Outside of the SHG signal reported in Figure 6.14, the GNS630 sample exhibited negligible MPL and its cross section is not compared in this section.

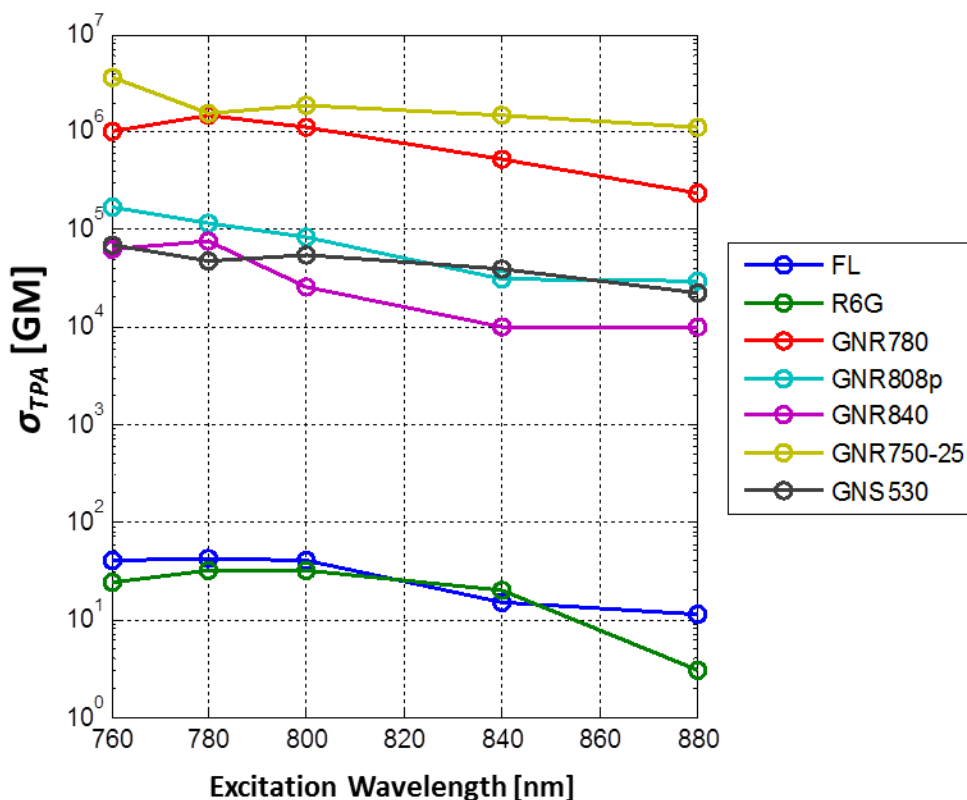


Figure 6.24: Measured two-photon action cross sections of gold nanoparticles. Two-photon action cross sections, σ_{TPA} , were measured relative to a sample of 25 μM fluorescein in pH 12 buffer. All nanoparticle solutions were used at concentrations necessary to have a peak absorbance of 10. FL: fluorescein, R6G: rhodamine 6G.

Several trends can be interpreted from this data. Most noticeably, the σ_{TPA} of both gold nanospheres and nanorods are many orders of magnitude larger than fluorescein and rhodamine 6G. Moreover these measured σ_{TPA} are comparable or larger than the brightest quantum dots reported, which are in the range of 10,000-50,000 GM [162]. For all samples, the σ_{TPA} either decreased or stayed constant above 800 nm excitation wavelength. This is even true for the GNR840 sample, which has twice the absorption at 840 nm than it does at 780 nm [Figure 6.4 and Table 6.2]. Considering the relatively fast nonradiative relaxation times of the *sp* and *d* band holes, we expect a large number of low energy emission photons in any excitation configuration. Thus, for a fair comparison of

absolute σ_{TPA} at larger excitation wavelengths, the dichroic and excitation filters should be adjusted to a constant energy difference below the excitation wavelength. It is possible that if our detection system was sensitive to luminescence up to 820 nm, the GNR840 sample excited at 840 nm would produce more MPL photon counts than we measured in our current setup. There is some correlation between the linear absorbance peaks and σ_{TPA} —the GNR756 and GNR 780 samples were brightest at 760 and 780 nm excitation, respectively. The GNS530 sample which has very little change in linear absorption from 760 nm to 880 nm showed only a very slight decay in brightness as the excitation wavelength was increased.

One way meaningful way of comparing the σ_{TPA} data between different particles and molecules is to normalize measurements by the geometric cross section and by the particle volume. The size of individual fluorescein and rhodamine 6G molecules is assumed to be a sphere with radius 5.9 Å [215]. The measure of brightness per area or per volume of contrast agent is useful for some imaging applications where the concern for delivery, toxicity, or target density might influence the type of particle chosen. Though the absolute σ_{TPA} of gold nanoparticles are many orders of magnitude larger than fluorescein and rhodamine 6G, when normalized by the physical cross section and volume, the brightness amongst contrast agents is more similar, with the exception of the gold nanospheres, which are noticeably dimmer per volume [Figure 6.25]. Comparing to quantum dots, which have reported σ_{TPA} of up to 50,000 GM, and volumes on the order of 100 nm^3 , we find that gold nanorods can generate up nearly one order of magnitude more luminescence per nm^3 of contrast agent.

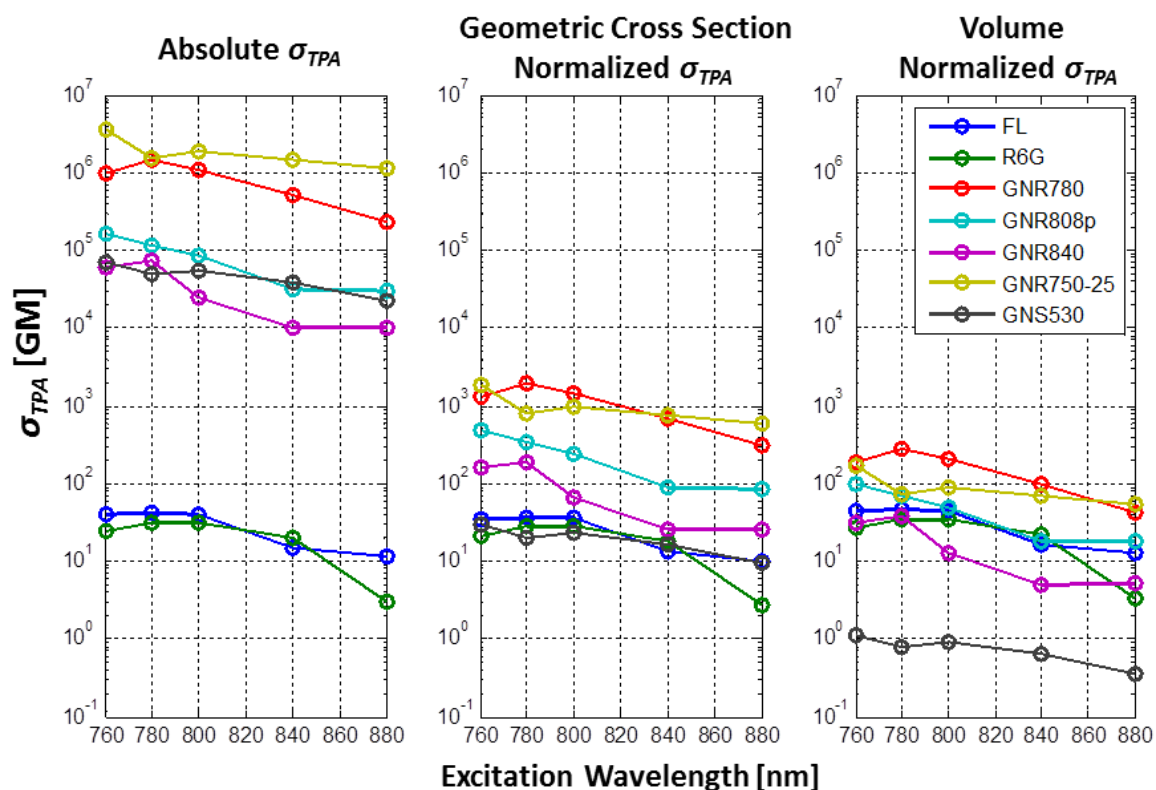


Figure 6.25: Absolute, area-normalized, and volume normalized σ_{TPA} of gold nanoparticles

Gold nanoparticles were 3 to 5 orders of magnitude brighter than fluorescein and rhodamine 6G per particle. But normalized for the physical area of the particles, nanorods are only 1 order of magnitude brighter, and nanospheres are similar brightness to fluorescein and rhodamine 6G. When normalized by the contrast agent's volume, nanorods and the organic fluorophores have similar brightness, while the nanosphere sample is orders of magnitude dimmer.

Comparison of σ_{TPA} to previous reports

Comparing the two previous calculations of gold nanorod σ_{TPA} with results from similar samples in our study, our values are two to four times larger. Wang *et al.* measured a σ_{TPA} of 2,320 at 840 nm excitation by comparing the brightness of a single gold nanorod dried on a coverslip to a single rhodamine 6G molecule [51]. For a similarly sized particle, we measured a σ_{TPA} of 10,000 at 840 nm excitation. Zijlstra *et al.* calculated a σ_{TPA} of 30,000 at 760 nm excitation by measuring the emission photon

counts of gold nanorods embedded in polyvinyl alcohol (PVA) and using Eq. (7.23) [52]. For a similarly sized particle, we measured a σ_{TPA} of 62,000 at 760 nm excitation. A summary of previous measurements of σ_{TPA} in gold nanorods and other nanoparticles is listed in Table 6.5.

There are a number of sources of error in the experimental methods of previous studies that could contribute to inaccurate σ_{TPA} values. Wang *et al.* used average fluences that are well above the saturation fluences we observe (many GW/cm²) [51]. This is also corroborated by the slope of two they observe, which we can reproduce by measuring MPL above the saturation intensity. They use rhodamine 6G and gold nanorods dried on a coverslip, but the σ_{TPA} of each would be expected to change with in an aqueous environment, thus their reference value may be off. Additionally, drying the gold nanorods on a coverslip restricts their orientation relative to that expected for gold nanorods floating in solution. It is unclear from their experiment whether they compared brightness values when the excitation polarization was aligned to the gold nanorod, or in some other orientation. Finally, they do not report the measured pulse duration at the imaging plane, so, given the results of Section 6.6.4, the effective cross section could change by an order of magnitude depending on how long their pulse duration was. The values by Zijlstra *et al.* suffer from some of the same sources of error [97]. Additionally, since they rely on a calculated system collection efficiency rather than a reference dye, any error in their collection efficiency value linearly affects their reported σ_{TPA} . Given the many sources of error, our values are surprisingly close to these previous reports. We show measured values of similar nanorods and excitation parameters used by Wang *et al.* and Zijlstra *et al.* in Table 6.5.

Reference	Sample	λ_{abs}^{peak} [nm]	λ_x [nm]	σ_{TPA} [GM]	Measurement Method
Gold Nanorods					
This work	GNR750-25	750	760	3,500,000	In solution, fluorescein and R6G reference
Wang <i>et al.</i> [51]	GNR 48 x 15 nm	820	830	2,320	Single particle on coverslip, R6G reference
This work	GNR840	840	840	10,000	In solution, fluorescein and R6G reference
Zijlstra <i>et al.</i> [97]	GNR 45 x 12 nm	810	760	30,000	Single particle in PVA, absolute measurement
This work	GNR840	840	760	62,000	In solution, fluorescein and R6G reference
Other Nanoparticles					
Liu <i>et al.</i> [216]	Gold Nanodot D = 1.3 nm	--	800	189	In solution, Coumarin 480 reference
Patel <i>et al.</i> [217]	Silver Nanodot D = 2.3 nm	400, 645	830	50,000	In solution, fluorescein and R6G reference
Larson <i>et al.</i> [50]	QD D = 7-14 nm	710	710	45,000	In solution, fluorescein reference
Stellacci <i>et al.</i> [218]	Cluster of fluorophores D = 10 nm	770	770	90,000	Compares cluster of 2500 fluorophores to a single one
Rahim <i>et al.</i> [219]	Conjugated polymer D = 8 nm	740	740	30,000	In solution, Fluorescein reference

Table 6.5 Two-photon action cross sections of gold nanorods and other nanoparticles.

λ_{abs}^{peak} is the peak linear absorbance of the sample. λ_x is the excitation wavelength used. The fluence used to probe the MPL, if reported, is indicated. The measurement method for determining the two-photon action cross section (σ_{TPA}) values are also described. Highlighted rows indicate measurements of similarly sized gold nanorods. We found reasonable agreement between the two published measurements of gold nanorod σ_{TPA} and our measurements. Sizes for nanorods are length x width. For spherical particles, sizes are described by the particle diameter, D.

6.6.6. Polarization dependence

Setup

We tested the dependence of MPL on excitation polarization by analyzing images of GNR780 nanorods dried on a coverslip. The excitation polarization was adjusted by

rotating a half wave plate inserted at the entrance to the laser scanning microscope. We used an excitation wavelength of 780 nm and a pulse duration of ~ 270 fs. Unlike the previous luminescence experiments in this chapter, for polarization experiments, we attempted to image single gold nanorods. Since this is better accomplished with a smaller excitation spot size, we used a higher NA objective (Nikon 40x/1.3 oil) and inserted an additional beam expander to overfill the back aperture. The higher NA also increased collection efficiency by 3 times over the NA=0.75 objective lens (collection \propto NA²). We found that the slight adjustments in the rotation of the half wave plate led to an appreciable lateral offset in consecutive images. We used an automated particle-finding script written in ImageJ to identify average bead drift over each frame. The offset was corrected and identified beads were tracked as the polarization angle was adjusted [Figure 6.26 (a) and (b)].

Linear polarization

Each particle identified in the image in Figure 6.26 (b) was fit with a cosine function. We identified the phase shift from the fit of each particle and plotted the raw and averaged data from 320 particles in Figure 6.26 (c). Spots that exhibited less than 10% deviation over the range of polarization were assumed to be clustered and neglected in this analysis. The particles exhibited a strong polarization dependence, but due to the noise of the data, we are unable to convincingly determine which order cosine offers the best fit. There is some discrepancy among previous studies on whether the best fit follows a \cos^2 or \cos^4 dependence[39],[92],[186],[204]. In simultaneous two-photon absorption, the two excitation photons must be coherent, and a \cos^4 dependence is expected. On the other hand, in the sequential absorption model the two excitation photons can be incoherent and a \cos^2 dependence is expected[208].

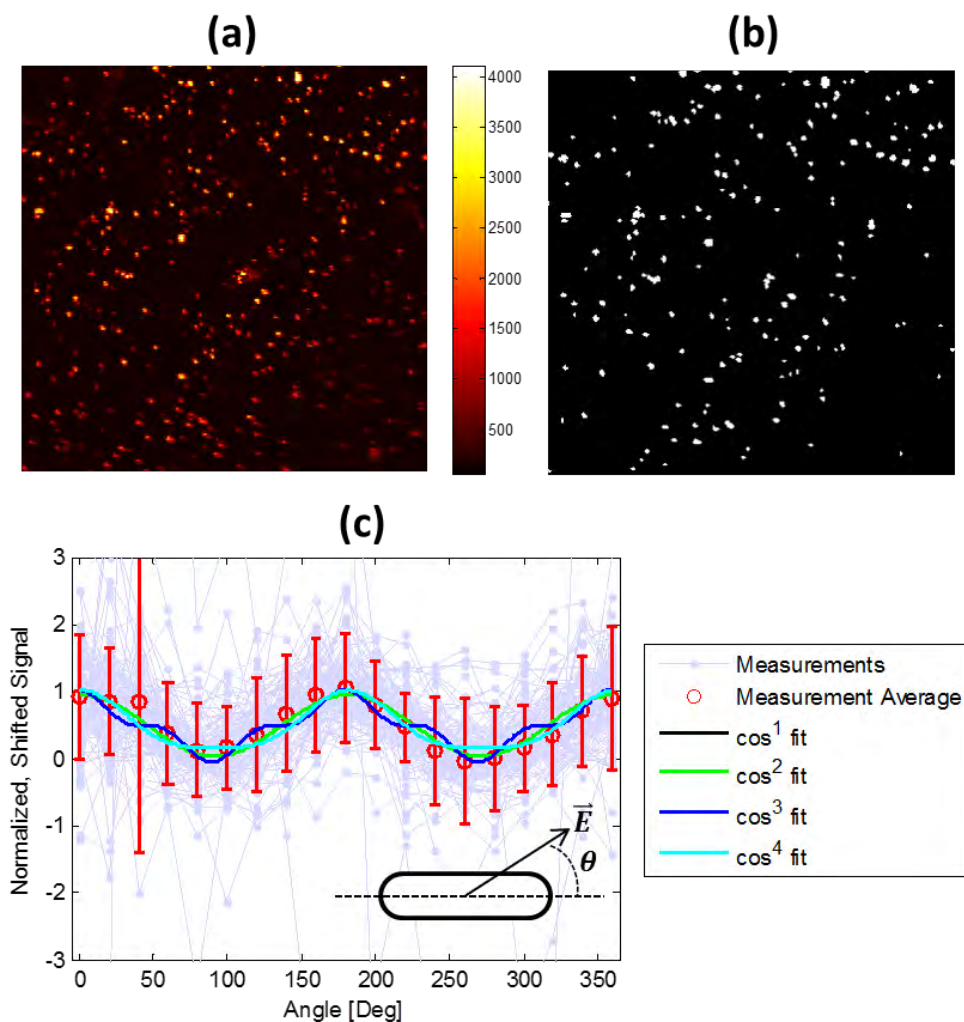


Figure 6.26: Dependence of MPL on excitation polarization--GNR780 on coverslip.

(a) A maximum projection image from a set of 19 MPL images taken at different excitation polarizations at 10° increments. (b) Binary image of particles found in image stack. (c) Measurements from individual particles and best fit cosines. Gray dots and lines show the measurement data after fitting, aligning, and normalizing. Red circles are average signals found at each polarization angle, and error bars represent the standard deviation. Due to the measurement noise, it is difficult to determine which order cosine fits the polarization dependence best. Inset image defines the polarization angle.

Circular Polarization

The polarization dependence of gold nanorod MPL has been shown to be useful for identifying particle orientation [97],[220]. We found good contrast between spots

illuminated at different polarizations. As expected, all spots that were visible under either vertical or horizontal excitation polarization were visible with circularly polarized light[221]. The relative signal of a spot at different polarizations could presumably be used to determine particle orientation. For example, (0, 1, 0.5) indicates a nanorod which horizontally aligned, while (0.8, 0.9, 1.0) indicates a nanorod which is aligned at close to 45° relative to the horizontal axis [Figure 6.27].

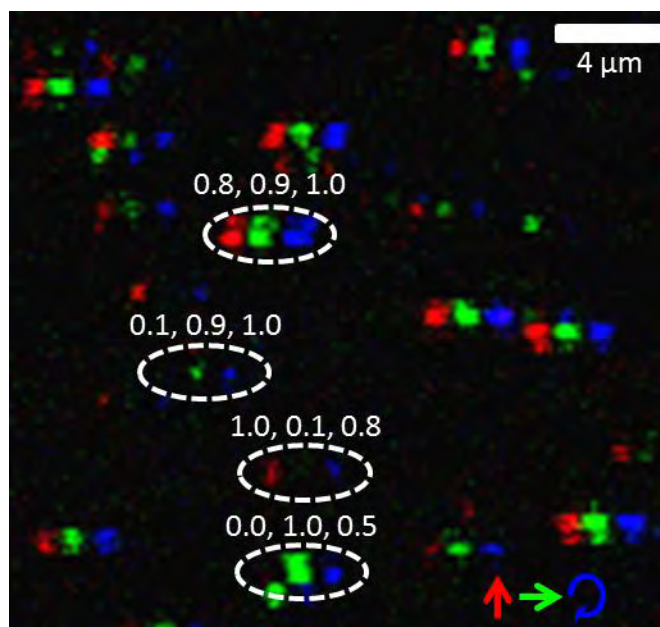


Figure 6.27: Determining orientation of gold nanorods from polarization dependence.

Images of GNR780 gold nanorods dried on a coverslip under vertical (red), horizontal (green), and circular (blue) polarized light. The three color images are overlaid horizontally offset to visualize the response of the same spot under different polarizations. Number sequences, X, Y, Z, represent normalized signal from vertical (X), horizontal (Y), and circular (Z) polarization for the spot highlighted in the dotted ovals.

6.7. CONCLUSION

We have measured effective σ_{TPA} values in the range $10^4 - 10^6$ GM for gold nanospheres and nanorods. The brightest values are, to the best of our knowledge, more

than an order of magnitude larger than any σ_{TPA} reported before. However, given the large size of these nanoparticles, when one normalizes σ_{TPA} by the size of the particle, the amount of luminescence generated per nm^3 is similar to that from fluorescein and rhodamine 6G. However, in many biomedical applications, fluorescence signal is limited to a small number of available ligands, or the fluorophore must be attached to a large antibody. In these cases, it is advantageous to use a single bright fluorophore rather than a large number of dimmer contrast agents.

Surprisingly, we found a strong deviation of MPL from the τ_p^{-1} dependence on pulse durations that is commonly observed in bandgap fluorophores. MPL is nearly constant for pulse durations below ~ 1 ps. This result has not been reported in colloidal metal nanoparticles before, but has recently been observed recently in long gold nanowires[86]. In addition to providing evidence for the sequential absorption mechanism for MPL, this result has important implications for endoscopic nonlinear microscopy, where it is often challenging to deliver short pulses and high fluences to the sample. It is conceivable that gold nanoparticles will become useful contrast agents in systems using picosecond pulse durations for three dimensional microscopy. This result also highlights the importance of carefully characterizing the pulse duration at the focal volume for MPL studies that use a reference fluorophore to calculate σ_{TPA} for metallic nanoparticles. We also described how the non-integer and higher order nonlinear dependencies we observe in our samples can be explained by incorporating nonlinear effects into the sequential absorption model. Using values from previous reports, where nonlinear absorption increases with longer pulse durations, reproduce the trends observed in our experimental data. Thus the non-quadratic dependence of MPL on average excitation power can be explained by sequential nonlinear absorption events.

Finally, we note that the results that the origin of MPL in gold nanoparticles is sequential absorption and that the effective σ_{TPA} values are extremely large may be directly related. Looking at Eq. (7.13), the effective σ_{TPA} in a sequential absorption process may be described as the product of two linear absorption cross sections: $\sigma_{d \rightarrow sp}$ and $\sigma_{sp \rightarrow sp}$. Linear absorption cross sections are many orders of magnitude larger than the nonlinear ones, even under focused femtosecond excitation. Thus, one would expect for the effective σ_{TPA} to be much larger in sequentially excited particles than the traditional particles which require simultaneous absorption for two-photon excitation.

Chapter 7

Nonlinear imaging of cancer cells with plasmonic contrast agents

In this chapter, we demonstrate the use of gold nanospheres and gold nanorods as bright nonlinear plasmonic contrast agents. Targeting these gold nanoparticles to epidermal growth factor receptor (EGFR), an important biomarker for carcinogenesis, we are able to perform molecularly specific, three-dimensional imaging of cancer cells in a single cell layers, and formed in a tissue phantom. We note that we refer to the luminescence observed from gold nanoparticles here as multiphoton luminescence (MPL), rather than two-photon luminescence (TPL). In light of the findings in Chapter 6, this is the most appropriate term, though the luminescence in gold nanoparticle labeled cells is more commonly referred to as TPL[51],[92],[97],[193],[93],[199],[198],[222-225].

7.1. PREPARATION OF CONTRAST AGENTS

7.1.1. CTAB coated gold nanorods

CTAB-coated gold nanorods were synthesized using a seed-mediated, surfactant-assisted growth method in a two-step procedure [226-228]. Hereafter, we call these gold nanorods GNR754. Figure 7.1 (a) shows a TEM image of synthesized gold nanorods that have an average aspect ratio of 3.4 ± 0.6 . Figure 7.1 (b) shows that the longitudinal plasmon mode of these nanorods is centered at 754 nm. To functionalize the GNR754 gold nanorods, the positive surface potential was converted to a negative surface potential by coating the CTAB with polystyrene sulfonate. We used anti-EGFR antibody (clone 29.1, Sigma) for targeting to EGFR. For the control, a nonspecific antibody was used in place of the anti-EGFR antibody (clone MOPC 21, Sigma). Details of the synthesis and functionalization can be found in Durr *et al.*[92].

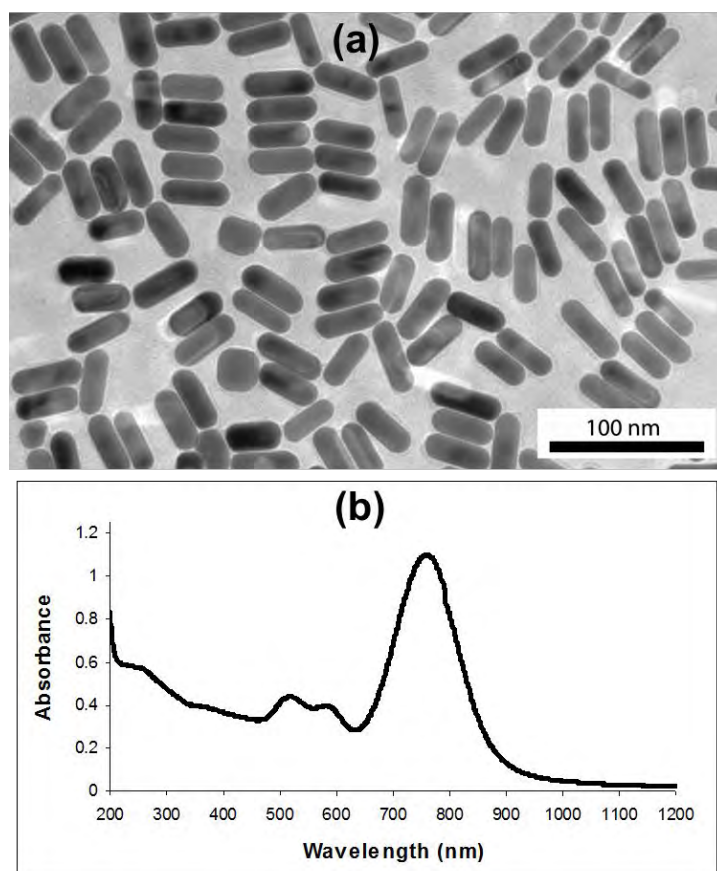


Figure 7.1: Properties of the CTAB-coated gold nanorods used as contrast agents.

(a) TEM image indicate an average length and width of 48.1 x 5.5 nm and 14.3 x 2.2 nm, respectively. (b) Gold nanorod absorbance in aqueous solution showed a longitudinal and latitudinal peak at 754 nm and 520 nm, respectively.

7.1.2. PEGylated gold nanorods

Given the cytotoxicity of CTAB surfactant coating (which is addressed in Section 7.6), we also explored labeling with a more biocompatible coating. We used the PEG coated sample studied in Chapter 6 (GNR808p). This sample consists of 39 ± 6 nm x 9 ± 1 nm gold nanorods, with a neutravidin-terminated PEG coating [Figure 6.1 (e)]. The exact size the PEG used in the CTAB dialysis is a trade secret, but the manufacturer did specify that it is less than 5 kDa. Our stock solution for labeling had an optical density of 56 at 808 nm, and a specified concentration of 3.3×10^{13} nanorods per mL. Based on our

characterization, we believe the actual concentration is closer to 1.2×10^{13} nanorods per mL at an optical density of 56 [Section 6.5].

We conjugated the neutravidin functionalized gold nanorods to biotin labeled antibodies for EGFR (clone 111.6, MS-378-B0, Thermo Scientific). The density of the stock antibody solution was 200 $\mu\text{g/mL}$ and the size of an individual antibody is 145kDa, which gives an approximate antibody density of 8.3×10^{14} antibodies/mL. We mixed the GNR808p, antibody, and 40 mM HEPES solution at a 1:1:4 volume ratio, which results in an interaction of ~ 67 antibodies for every nanorod. The mixture was allowed to interact for 20 minutes, and then centrifuged at $2,000 \times g$ for 30 minutes to remove unbound antibodies. We performed a second washing step, resuspending the pellet in 2 mL of 40 mM HEPES, and centrifuging at $2,000 \times G$ for 30 minutes to further remove unbound antibodies.

7.1.3. Nanospheres

We imaged the $54 \pm 5 \text{ nm} \times 44 \pm 4 \text{ nm}$ nanospheres from Chapter 6 (GNS530) labeled to cancer cells by conjugation to EGFR antibodies. 2 mL of the stock GNS530 solution were centrifuged at $2,000 \times G$ and resuspended in 2 mL of 20 mM HEPES buffer. 2 μL anti-EGFR monoclonal antibodies (clone 225, 1.5 mg/mL, Sigma) were suspended in 1.98 mL of 20 mM HEPES buffer. The gold solution was added dropwise to the dilute antibody solution while stirring, to allow for an even coating of the nanospheres. The mixture was allowed to interact for 45 minutes. 400 μL of 2% PEG was added to the mixture for stability. Unbound antibodies were removed by centrifuging at $300 \times G$ for 45 minutes. This left some nanospheres in solution, but we found that centrifuging the nanospheres at greater force led to irreversible agglomeration. The

functionalized nanosphere pellet was resuspended in 300 μL DPBS without Ca^{2+} and Mg^{2+} and stored at 4° C until use.

7.2. SAMPLE PREPARATION

We labeled MDA-MB-468 breast cancer cells and American Type Culture Collection ATCC A431 human epidermoid carcinoma cells, both of which are known to overexpress EGFR. Cells were cultured in DMEM supplemented with 5-10% Fetal Bovine Serum (Sigma) and maintained at 37° C in a humidified 5% CO_2 incubator. In preparation for labeling, cells were harvested via trypsinization and resuspended in 1x PBS. We then mixed the cell solution with varying amounts of functionalized nanoparticles and allowed them to interact for 30-45 minutes. We separated unbound nanoparticles from labeled cells with centrifugation at $200 \times G$ for 5 minutes. We deposited this solution on a #1.5 glass-bottom petri dish and incubated the sample for approximately 1 hour for the cells to stabilize on the top of the coverslip.

7.2.1. Tissue phantoms

Three-dimensional tissue phantoms were prepared using rat tail collagen as a scaffold. Labeled cells were centrifuged at $200 \times G$ for 5 minutes and the resulting pellet was resuspended in a buffered collagen solution at a concentration of 7.5×10^7 cells/mL. The collagen/cell mixture was pipetted into a 120 μm spacer (Molecular Probes) and sealed with a coverslip for imaging.

7.3. IMAGING SYSTEMS

Imaging was performed on one of two multiphoton microscopes, as indicated in each section. We used the upright microscope described in Chapter 3 with the 20x/0.95 water dipping objective (Olympus) for deep imaging experiments with phantoms. We

also used an inverted microscope described in Section 6.6.1 for phantom and single cell layer experiments with a high NA objective lens (Zeiss 63x/1.4 and Olympus 40x/1.3) for brightness comparison and polarization experiments. Images presented with the Olympus objective were also taken with an improved filter set that efficiently passed up to 720 nm luminescence to the detector.

7.4. SINGLE LAYER OF LABELED CANCER CELLS

7.4.1. Brightness characterization

Figure 7.2 presents nonlinear images of a single layer of labeled and unlabeled cells at 760 nm excitation wavelength. The images demonstrate successful labeling, indicating the cellular distribution of EGFR. The unlabeled cells [Figure 7.2 (a)] show a relatively uniform distribution of 2PAM signal throughout cellular cytoplasm. No signal is associated with the nuclei, which do not have significant concentrations of endogenous fluorophores that can be excited in the visible region. In labeled cells [Figure 7.2 (b)], bright rings can be seen; this is a characteristic pattern of EGFR labeling and has been also reported in confocal reflectance imaging of EGFR using spherical gold nanoparticles [71]. The discrete bright spots in the cytoplasm of nanorod-labeled cells are indicative of endosomal uptake of EGF receptors labeled with nanorods inside cells. The endosomal recycling of EGFR molecules is a normal biological function of living cancer cells.^{26, 27} MPL images of cells treated with nonspecifically conjugated nanorods shows agglomeration of contrast agent and little attachment to cell membranes [Figure 7.2 (d)]. Using the same excitation power of 140 μW , the two-photon imaging of unlabeled cells gave a pure background noise black image [Figure 7.2 (c)].

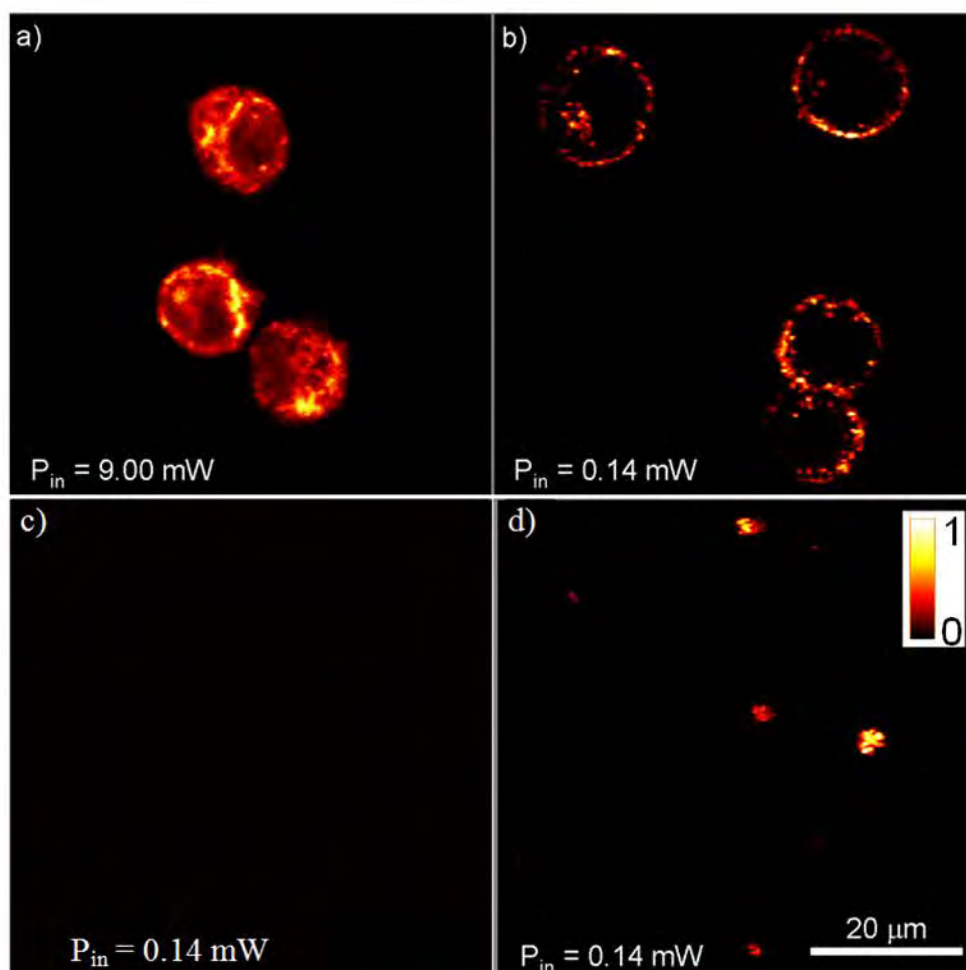


Figure 7.2: MPL images of GNR754 labeled and unlabeled A431 cancer cells. (a) 2PAM image of unlabeled cells. (b) MPL image of nanorod-labeled cells. Imaging required 9 mW of excitation power in unlabeled cells to get same signal level obtained with only 140 μW for nanorod labeled cells, indicating that MPL from nanorods can be more than 4000 times brighter than 2PAM from intrinsic fluorophores. (c) TPI of unlabeled cells at power levels used for labeled imaging shows a pure background noise image. (d) MPL image of nonspecifically labeled cells. Image was acquired with a 63x/1.4 objective lens.

By tuning the wavelength from 710 to 910 nm, it was found that 760 nm excitation wavelength yielded the brightest MPL signal from the nanorods as well as the brightest 2PAM signal from the cancer cells. This wavelength corresponds to the longitudinal plasmon resonance frequency of the nanorods. For the cancer cells, this finding is consistent with other reports that show that the biological molecules that are

primarily responsible for the signal in 2PAM imaging (NADH and flavins) have two-photon cross-sections that increase with decreasing excitation wavelength from 1000 to 750 nm, and level off around 750 nm[8]. The similarity of the optimal excitation wavelengths for both the gold nanorods and cellular autofluorescence allows a comparison of the two imaging modalities under identical excitation conditions. We found that MPL imaging of nanorod-labeled cells required 64 times less power than 2PAM imaging of unlabeled cells in order to achieve the similar collected intensity. Given the quadratic dependence of emission intensity on the incident power, this observation implies that, for equal excitation powers, MPL imaging of nanorod-labeled cancer cells can generate more than 4000 times larger emission signal than 2PAM imaging of unlabeled cells.

7.4.2. Signal from nanoparticle agglomerates

During functionalization, nanoparticle agglomerates are sometimes formed. We incorporated a widefield CCD imaging system into our upright microscope to visualize sequential images of the same field of view under MPL imaging and white-light transmission imaging. We found that large clusters of nanoparticles that are visible under white-light illumination are not sources of bright MPL signal. This is likely due to the loss of surface plasmon effects as nanorods form very large aggregates.

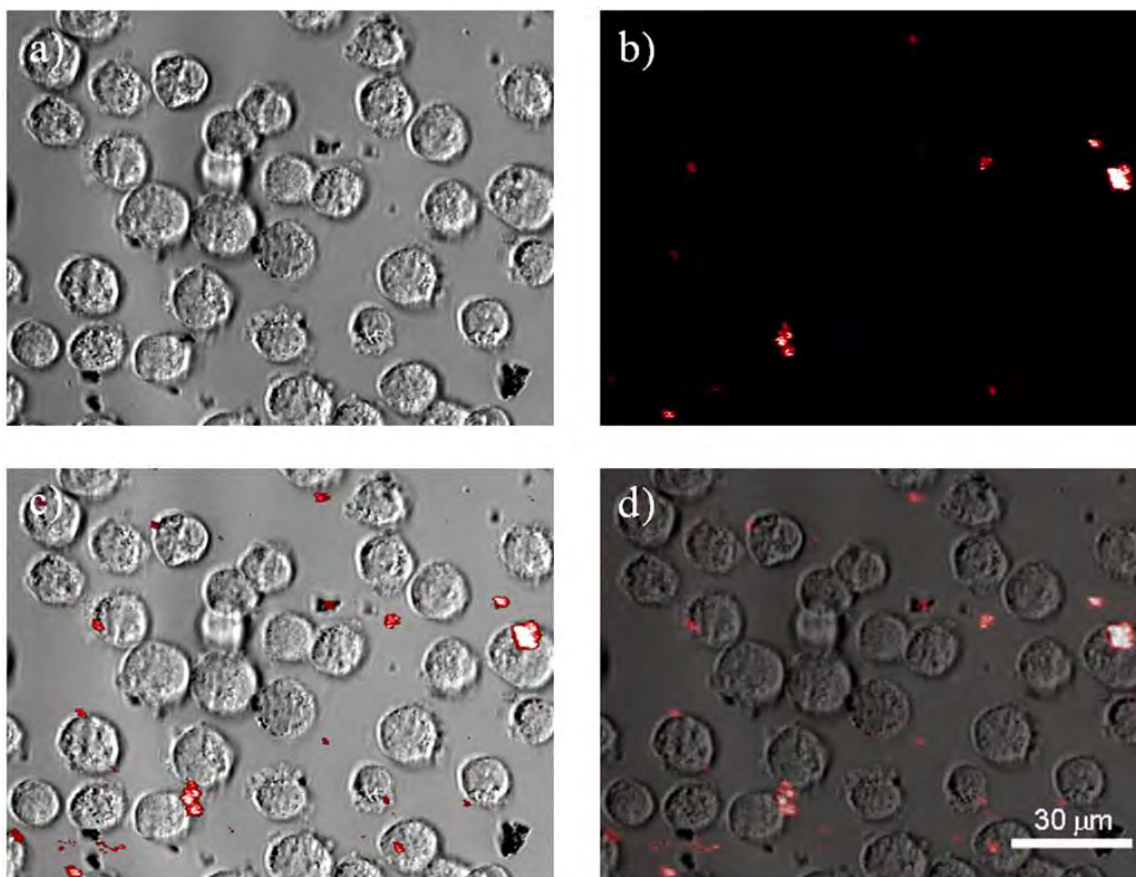


Figure 7.3: Wide-field white light and MPL images of non-specifically labeled GNR754 clusters with cells.

(a) White-light transmission image of a single layer of non-specifically nanorod labeled A431 cells. (b) MPL z-projection image of the same field of view over $15 \mu\text{m} \Delta z$. (c) Overlap of MPL image on top of white-light transmission image with blacker areas of MPL image deleted. (d) Overlap of MPL image on optical image, with transparency of MPL image increased to 50%. Time between imaging (a) and (b) was roughly 5 minutes, so some cellular movement was possible, and movement in the extracellular environment may have been even more drastic. Dark black spots appearing in the (a) are aggregated nanorods. Note that only a small MPL signal comes from some of the nanorods aggregates, and no MPL signal comes from some of the large aggregates.

7.4.3. Labeling with PEGylated gold nanorods

We successfully labeled A468 cancer cells with PEGylated GNR, using sample GNR808p. In this set of experiments, we found an even brighter MPL signal from the GNRs, as evidenced by the low excitation powers required [Figure 7.4]. Again, we

observed no signal from the cell cytoplasm, indicating that the MPL is much brighter than any autofluorescence.

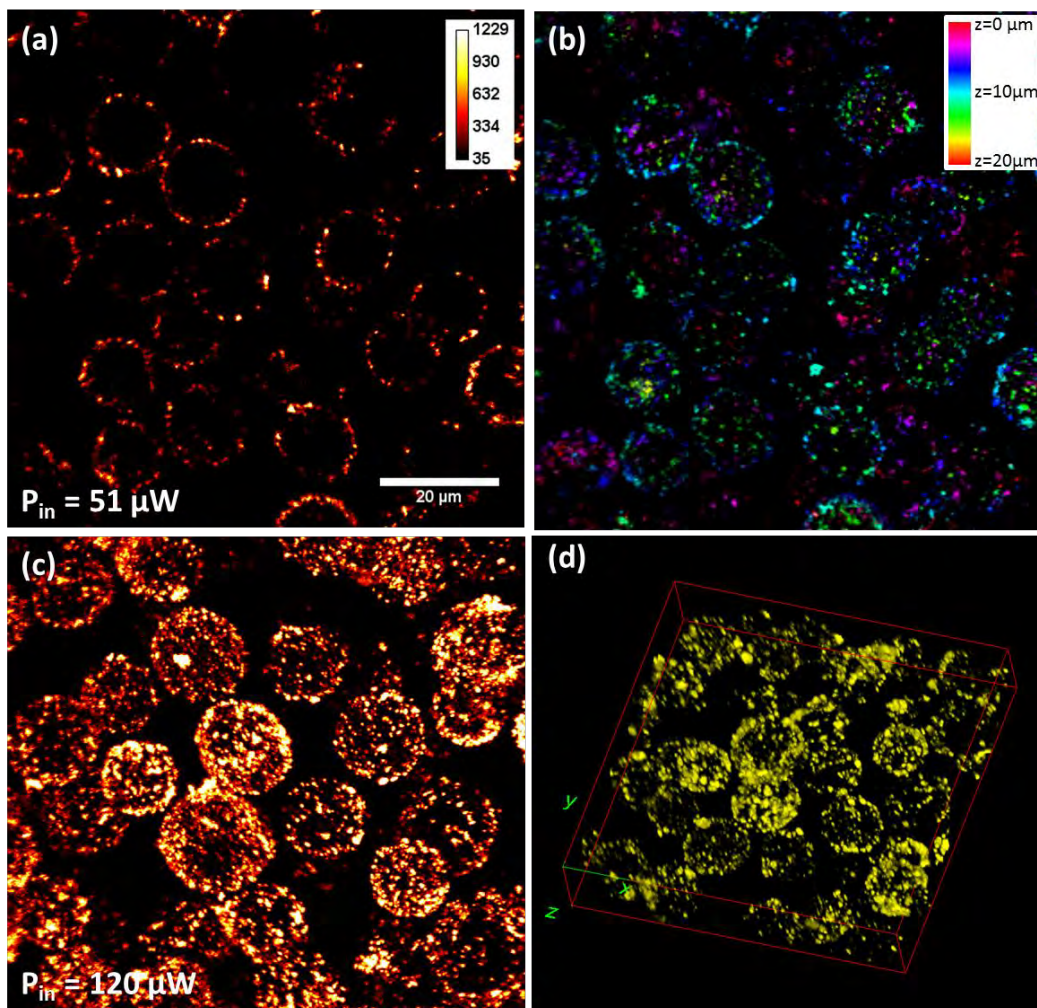


Figure 7.4: GNR808p labeling of A468 cancer cells.

(a) MPL image of A468 cancer cells labeled with PEGylated gold nanorods (GNR808p) with 40x/1.3 objective lens at 780 nm excitation. (b) Presentation of data from 21 images taken at different z positions. Each position is coded by a different color, as indicated by the calibration bar, and superimposed. Thus, the blue color is an image taken through the middle of the cells, and the purple and red colors are images taken at the top and bottom of the cells, respectively. (c) Maximum projection of image stack from a second sample imaged at higher excitation power (120 μW). This provided higher signal to noise at the expense of saturating the signal from bright GNRs. (d) a three dimensional rendering of data from (c). The images here show excellent axial resolution is achieved. Field of view is 100 x 100 μm^2 for all images.

7.4.4. Optical properties of labeled gold nanorods

The increased clustering of GNRs as they bind to EGFR molecules and/or are endocytosed will likely affect their nonlinear optical properties [229],[230]. To test this hypothesis, we monitored MPL signal as a function of excitation power, polarization, and labeling density for A468 cells labeled with GNR808p. We also tested the optical properties of individual functionalized gold nanorods deposited on a coverslip as a reference. These experiments proved to be challenging because small movements of the GNRs in any dimension significantly affect the measurement. Even in the stationary sample—the GNRs deposited on a coverslip—we observed small lateral movements in the imaging plane in time and as our power attenuator was rotated. To correct for image movement, we implemented a Matlab script that tracked particles from one frame to another. Each particle was shifted back to its original position and the resulting image stack could then be analyzed for response to changes in excitation power and polarization. As an example, Figure 7.5 shows images of before and after correction for GNR808p deposited on a coverslip. For GNR labeled cells, the movement was even more pronounced. We were unable to correct for GNR that moved in the axial direction because we kept at one imaging plane throughout each experiment.

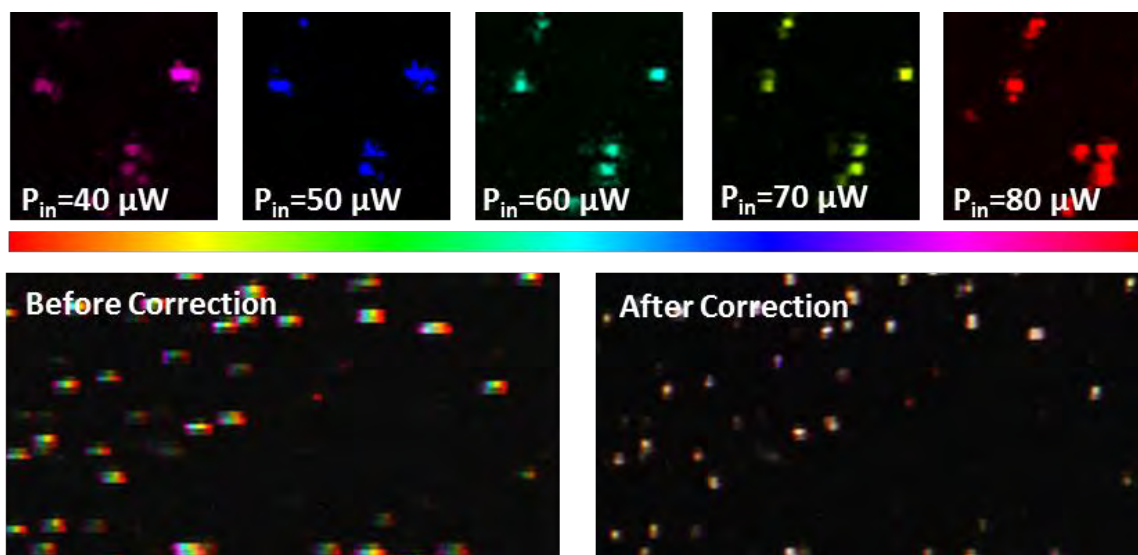


Figure 7.5: Sample movement correction algorithm.

Top: color images representing different excitation powers. Bottom Left: merge of all the images taken at different powers. The smearing of the colors demonstrates that the image moves slightly relative to the sample as the excitation power is changed. Bottom Right: After correcting for sample movement, our data stacks show much less particle movement.

Dependence of MPL on excitation fluence

We examined the dependence of MPL signal as a function of power on both GNR-labeled cells and GNRs deposited on a coverslip. Unfortunately, we were unable to image at the low fluences studied in Chapter 6, where we saw saturation effects above peak intensities of 300 MW/cm^2 . The setup in Chapter 6 allowed for more sensitive imaging because we used a large focal spot and simultaneously sampled many nanoparticles, whereas in this chapter, we aim to achieve high resolution images of gold nanoparticle labeled samples. Thus we expect that in the regimes probed here, we are saturating the signal from the nanorods.

We demonstrate MPL from GNR808p on a coverslip and labeled to cells in Figure 7.6. As expected, we see a smaller order nonlinear dependence than observed at the lower I_p probed in Chapter 6. Nonetheless, we can make two important observations

with the experiments presented here: (1) we observe irreversible photodamage (possibly due to melting, ablation, and electron emission), evidenced by the MPL signal failing to return to the original value after raising and lowering the fluence, and (2) there is a clear nonlinear dependence of MPL on excitation power.

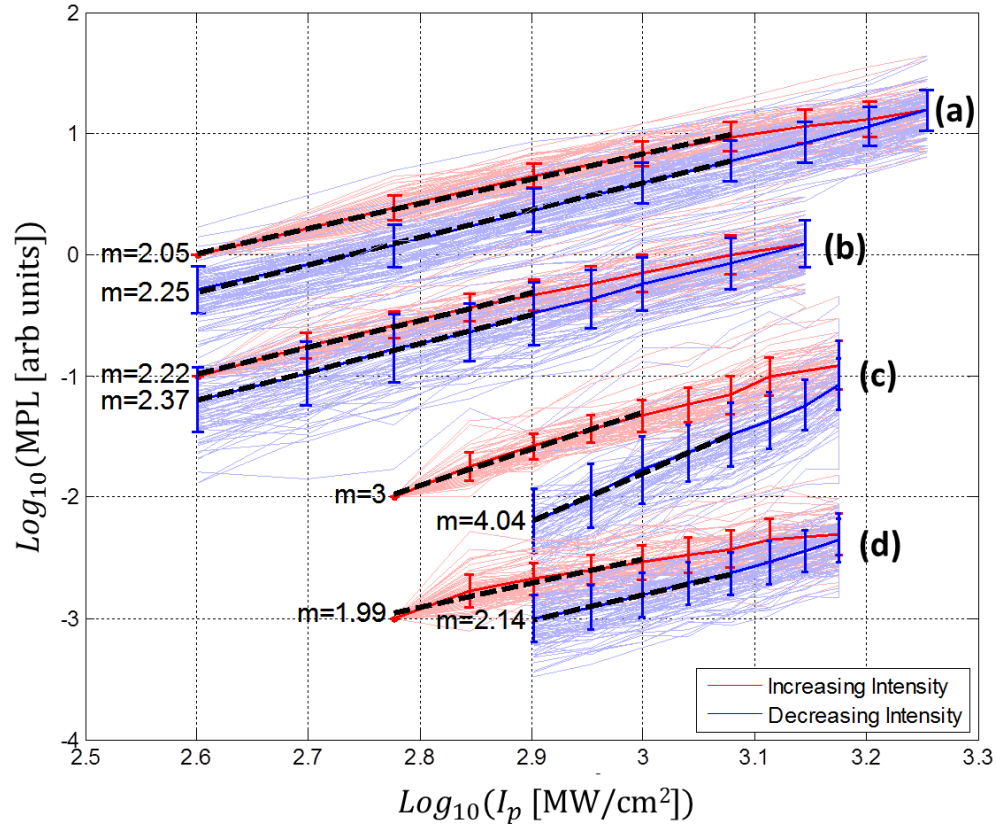


Figure 7.6: MPL vs. I_p for GNR808p on a coverslip and labeled to cells. (a) and (b): GNR808p deposited on coverslip. (c) and (d): GNR808p labeled to cells. All power sweeps are normalized to an MPL of one at first measurement. (b), (c), and (d), are shifted to more easily view on this plot by multiplying by 0.1, 0.01, and 0.001, respectively. Thick colored lines are average MPL signal for each power point. Thick dotted lines are linear best fit with slope indicated by m . Though we only observed appreciable signal above the saturation thresholds found in Chapter 6, we observe a nonlinear dependence of MPL on excitation power for GNR. We also observe irreversible photodamage, as the MPL measured after the power sweep was always lower than the starting point.

Dependence of MPL on excitation polarization

We examined the MPL dependence of gold nanorods labeled to cancer cells on excitation polarization in the same way as on the coverslip in Section 6.6.6 [Figure 7.7]. As expected, we see a weaker polarization dependence when gold nanorods are labeled to cancer cells because there is more likely to be clusters [229],[230]. Also, unlike gold nanorods dried on a coverslip, where the geometry is restricted to one degree of freedom, labeled gold nanorods are expected to be oriented more isotropically in three dimensions.

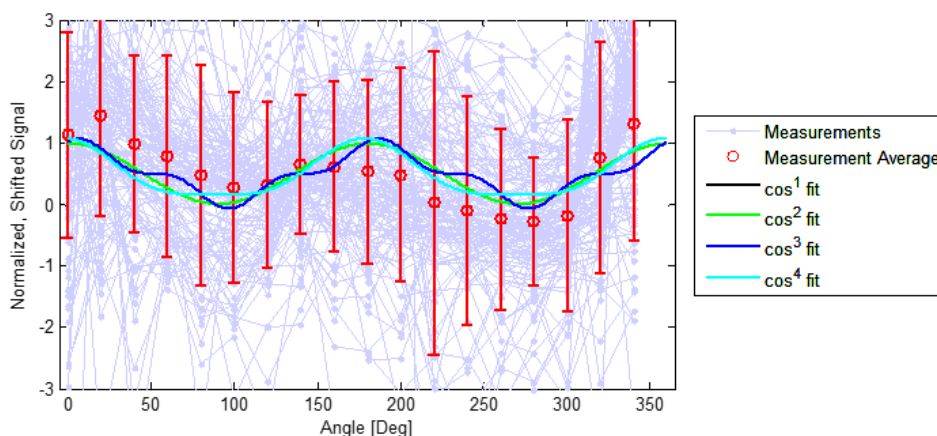


Figure 7.7: Polarization dependence of GNR808p labeled to cells. Same experiment as in Figure 6.19, but with nanorods labeled to cancer cells instead of on a coverslip. Note the error bars are much larger in this case, indicating a significant number of spots that do not exhibit polarization dependence. This is expected, since labeled nanorods are expected to exhibit more aggregation, are oriented in an extra dimension (GNR on a coverslip are not isotropically oriented), and experience more sample movement.

7.5. GNP-LABELED TISSUE PHANTOMS

To test the imaging ability of MPL deep into tissue, we imaged cancer cells embedded in a collagen matrix that mimics the epithelium tissue. Figure 7.8 compares MPL and 2PAM images of cancer cells obtained at different depths. To avoid delivery of large powers at deep levels, we increased our PMT gain and reduced imaging power

compared to the configuration in single cell layer imaging. The high gain allowed imaging at ten times less power than the single layer cell experiments. To maintain a constant detected intensity throughout the phantoms, a 26% power increase was required for each 20 μm increase in imaging depth. This is consistent with the predicted influence of GNR labeling on the bulk tissue optical properties discussed in Section 6.4.2. For 2PAM and MPL imaging, the excitation power was increased from 0.9 to 1.8 mW and from 35 to 70 μW , respectively. The excitation power ratio of 26 between the two imaging modalities indicates 675 times brighter MPL than 2PAM.

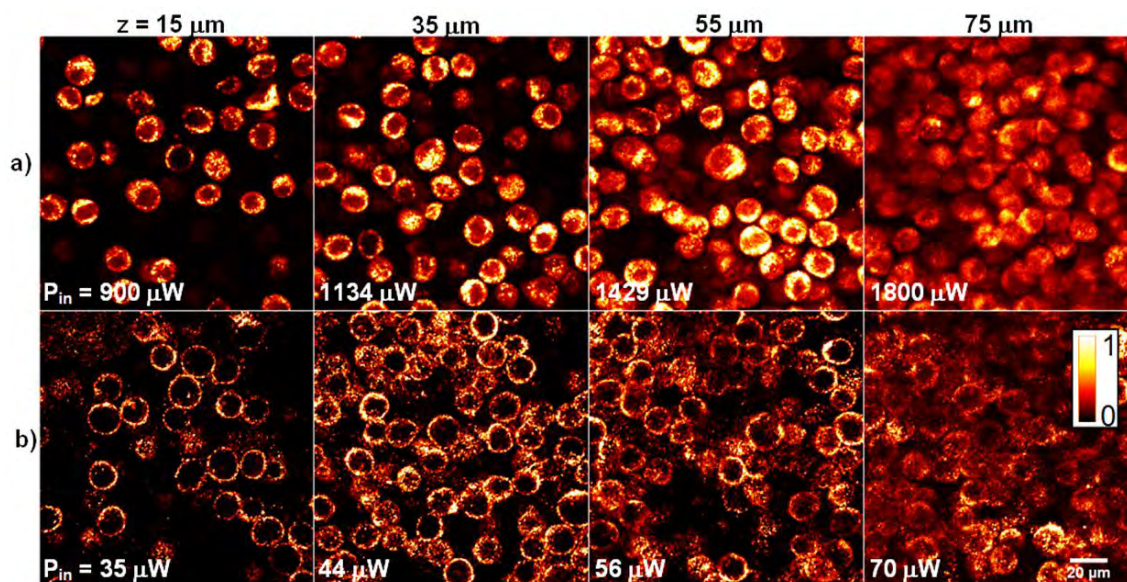


Figure 7.8: 2PAM and MPL images of tissue phantom.

Two-photon imaging of cancer cells embedded in a collagen matrix at increasing depths. (a) 2PAM imaging of unlabeled cells and (b) MPL imaging of nanorod-labeled cells. Both samples required the same excitation power increase of 26% at each 20 μm depth increment to maintain constant emission intensity.

To increase imaging depth, we imaged labeled cancer cell phantoms in the upright MPM with a water dipping objective lens. Figure 5 shows MPL images obtained down to 200 μm deep using the upright system. With this system, we are able to image in excess of 150 μm deep with sub-cellular resolution. Similar aberrations to those that occur with

the oil immersion lens are observed but the onset of these aberrations occur at approximately twice the depth. The power increase necessary to obtain similar collected signal as imaging depth was increased was not a smooth exponential function, as observed with the oil immersion objective. This could be due to the signal degradation being simultaneously dependent on multiple factors such as excitation light attenuation due to scattering, as well as optical aberrations. From the XZ image shown in Figure 6, we can see that the point spread function become drastically larger, especially in the axial direction, at depths greater than 150 μm .

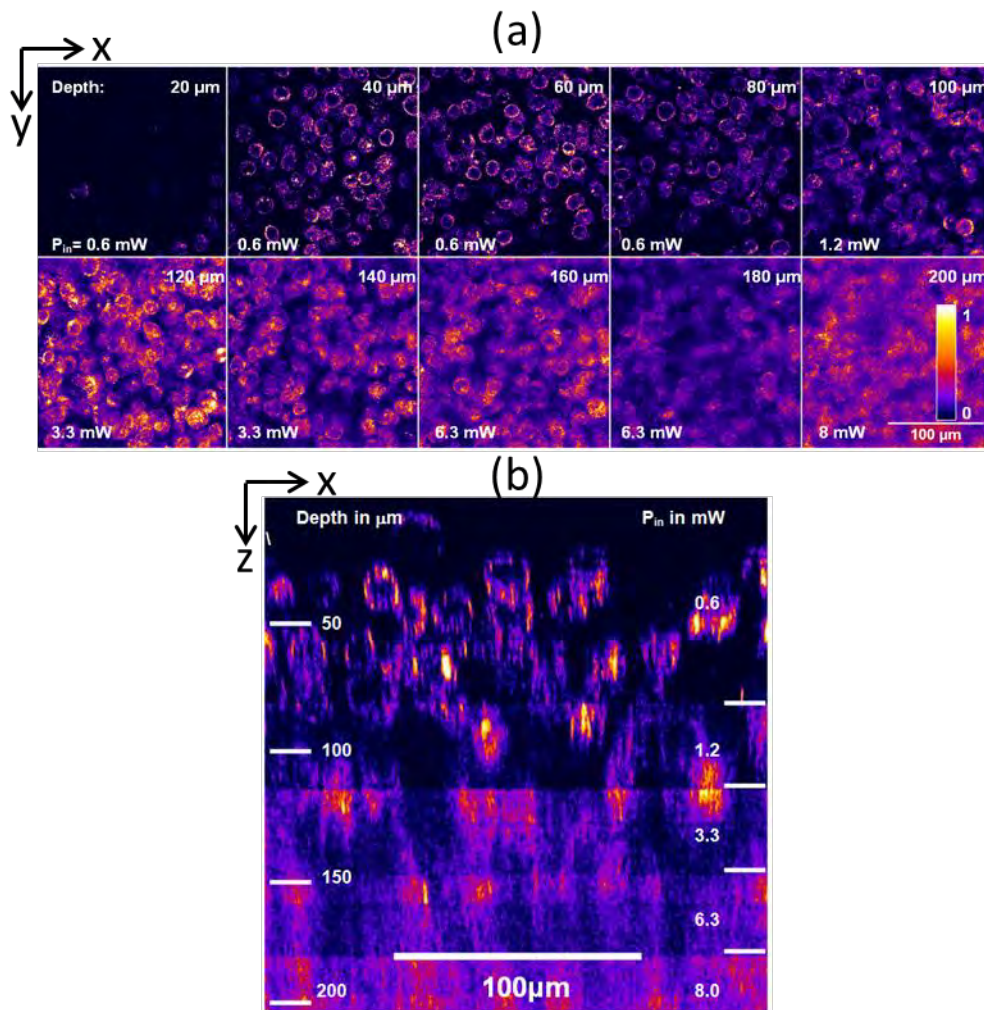


Figure 7.9: Deep MPL imaging in tissue phantom.

(a) Lateral images at increasing imaging depths. (b) Reconstructed cross section shows resolution gradually decreasing with larger imaging depths. Imaging tissue phantoms with a water-immersion rather than oil objective lens results in less spherical aberrations and allows for deeper imaging. Here imaging is demonstrated approximately twice as deep as in Figure 7.8.

In order to obtain similar emission signal in the upright setup as we measure in the inverted setup, it is necessary to use an order of magnitude more excitation power. This power increase is partially due to the increased spot size and thus decreased irradiance at the imaging plane resulting from the lower numerical aperture objective used in the upright setup, as well as the reduced collection efficiency of the upright

system resulting from the large back aperture of the water immersion objective. The measured lateral spot size of the upright setup was approximately 2.2x larger in area than in the inverted setup. With additional optimization of the collection optics, it will be possible to further improve the upright MPM collection efficiency.

7.6. BIOCOMPATIBILITY

CTAB is known to be cytotoxic at the concentrations used in nanorod labeling, raising concerns about the *in vivo* use of nanorods for molecular imaging [231],[222],[232],[233]. However, CTAB can be exchanged with PEG, a much more biocompatible material, in a dialysis reaction [234]. We conducted a preliminary test of the biocompatibility of gold nanospheres (GNS530), CTAB-coated gold nanorods (GNR780), and PEGylated gold nanorods (GNR808p) by using an MTT assay (Promega CellTiter Aqueous One kit). We used this assay to quantify the proliferation of A468 cancer cells when incubated with these three particle types at different concentrations for 24 and 48 hours. At each time point, the density of cells incubated with each solution was compared to the density of cells incubated in DMEM supplemented with 5-10% Fetal Bovine Serum (Sigma). Cells were incubated at 37° C in a humidified 5% CO₂ incubator. Concentrations in the 100 pM range are generally sufficient for dense labeling of cancer cells. We tested incubation with concentrations of 4 to 4,000 pM of each nanoparticle sample [Figure 7.10]. Gold nanospheres showed no significant cytotoxic effects at either timepoint. We found that the CTAB-coated GNR780 sample at concentrations equal to and above 400 pM exhibited significant cytotoxicity within 24 hours of application to human cancer cells. After 48 hours of incubation, even GNR780 concentrations of low as 40 pM, began to show some cytotoxic effects. On the other hand, PEGylated gold nanorods showed very little cytotoxic effects at all concentrations after 24 hours of

incubation, and only a small effect on cell proliferation after 48 hours at concentration of 4,000 pM.

Rayavarapu *et al.* recently conducted a similar assay and found 100% cell death from four different types of cells incubated gold nanorods for 24 hours at all tested concentrations of CTAB coated gold nanorods, down to 0.1 pM[235]. Our results find no observed cytotoxicity at this level, perhaps due to different amounts of free CTAB in the gold nanorod solutions. In sequential wash cycles, as the concentration of free CTAB decreases, the gold nanorods begin to irreversibly agglomerate. Thus it is advantageous to maintain surplus CTAB in the gold nanorod solution. Generally, the particle concentrations are well characterized and reported, but most studies do not quantify the absolute concentration of CTAB in the gold nanorod solutions. It is possible that if Rayavarapu *et al.* would have further washed their gold nanorods to eliminate excess CTAB, they would have observed reduced cytotoxicity. They also found that PEGylated gold nanorods exhibit much less cytotoxicity, up to 200 pM, consistent with our results.

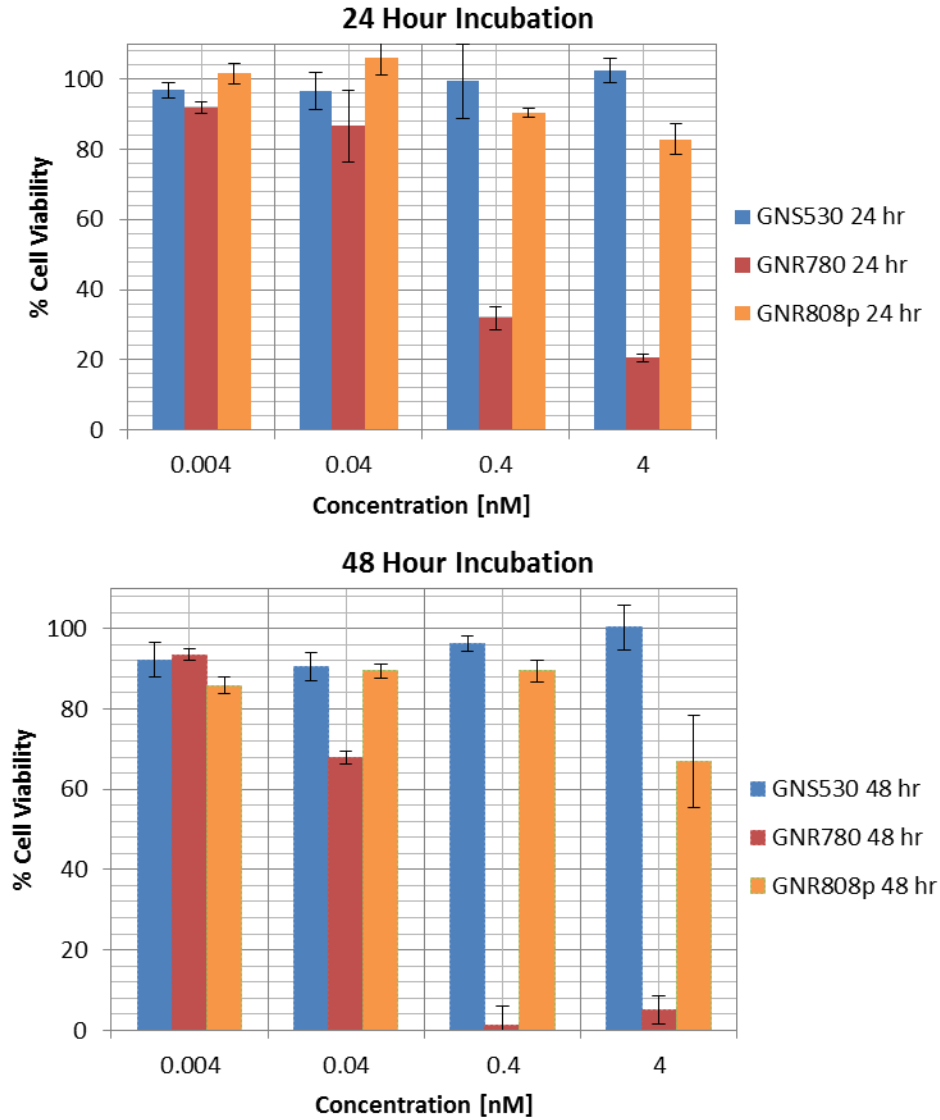


Figure 7.10: MTT assay after incubation with GNS, GNR, and GNRp
 We incubated A468 cancer cells with 4 pM to 4 nM of gold nanospheres (GNS530), CTAB coated gold nanorods (GNR780), and PEGylated gold nanorods (GNR808p) for 24 hours and 48 hours. While the CTAB coated nanorods exhibited strong cytotoxicity above 0.4 nM, the PEGylation is shown to drastically reduce cell death.

Chapter 8

Conclusions and future directions

This dissertation addressed two aspects in which nonlinear microscopy can be extended towards clinical use—optimizing and understanding the limits of 2PAM imaging depths in epithelial tissues, and the use of extremely bright plasmonic nonlinear contrast agents for molecularly specific imaging of cancer cells.

We found that 2PAM imaging could be performed down to approximately 320 μm deep in a healthy human skin biopsy before the contrast was degraded to below one, presumably by out-of-focus fluorescence generation. This result was corroborated by tissue phantom experiments and a Monte Carlo model. As previous 2PAM studies in mammalian skin have been limited to imaging depths of less than approximately 150 μm deep, this represents a significant improvement in imaging depth capabilities. Our measured maximum imaging depth is significantly less than that obtained in stained brain tissue, even when the imaging depth is normalized by the different scattering lengths used [11],[236]. Through Monte Carlo models and tissue phantoms, we demonstrate that the origins for this difference are: (1) the maximum imaging depth does not scale linearly with scattering length, and (2) the staining inhomogeneity is two orders of magnitude less in 2PAM of epithelial tissues than typically encountered in two-photon imaging of stained brain tissue. Fortunately, an imaging depth of 320 μm is still useful for probing epithelial tissue disease[237]. Though 2PAM might not reach the *stratum basale* in some cases, the majority of human epithelial tissues are less than a few hundred microns thick.

Still, there are several ways to improve the maximum 2PAM imaging depth. Spherical aberrations due to refractive index mismatch can significantly degrade the spot size in nonlinear imaging. Though we verified no significant aberrations were present in tissue phantom experiments, the slightly larger imaging depths achieved in tissue

phantoms than in the biopsy may be explained by appreciable specimen-induced aberrations by the biopsy. Future studies could use an objective lens with a correction collar compensate for spherical aberrations to mitigate these effects, possibly moderately increasing the maximum imaging depth in biopsies.

Alternative approaches to conventional two-photon microscopy show some promise for reducing contributions of out-of-focus fluorescence. Temporal focusing[163],[164], differential aberration imaging[165], optical clearing[166],[167], and spatial filtering[11],[168] could all potentially increase maximum imaging depth. Though these methods have shown the *potential* for increasing imaging depth, currently each has only been demonstrated as a proof-of-concept for deep nonlinear imaging; larger maximum imaging depths are generally reported using conventional two-photon microscopes. Expected gains in imaging depths using these methods are approximately 0.5-1.0 mean free scattering length, and it is debatable whether the increased complexity in implementing any of these methods is worth the additional $\sim 50 \mu\text{m}$ in maximum imaging depth one might achieve in epithelial tissues.

In the second part of this dissertation, we demonstrated the use of gold nanoparticles for bright, molecularly specific imaging of cancer cells. Interestingly, we found a deviation from the inverse relation of gold nanoparticle MPL on pulse duration. This provides evidence that the mechanism of absorption in MPL is a sequential rather than simultaneous one. We observed effective two-photon action cross sections that were an order of magnitude larger than that reported from any previously reported particle, including quantum dots. However, normalizing for the large size of gold nanoparticles, we find that the luminescence generated per volume of particle is only slightly larger than that from the brightest quantum dots. Still, in cases where the density of antigens is limited, gold nanoparticles likely provide a more appealing option than quantum dots,

because in addition to being dimmer than gold nanoparticles, quantum dots are also well-known to be cytotoxic. An additional advantage of nonlinear imaging with nanoparticles compared to quantum dots is that although quantum dots are generally limited to one emission photon per particle per excitation pulse, based on the large number of free electrons in gold nanoparticles, it is likely that gold nanoparticles can produce more than one emission photon per excitation pulse.

The origin of the enhanced nonlinear luminescence from gold nanoparticles is still poorly understood. Though recent results, included those from this dissertation, point to sequential absorption as the mechanism for MPL, the role of the plasmon resonance in increasing MPL has only been described empirically[89], and is a poor match to ours and others[193] observed σ_{TPA} spectra. Currently, there is no accurate model to reconcile the disparate atomic model, from which MPL can be described as emission close to the symmetry points in the Brillouin zone of gold, and the classical picture, where the spectral dependency of the plasmon resonance is weakly correlated to enhanced MPL signal. With improved understanding the mechanisms of MPL, better particle geometries and compositions can be engineered.

We only tested commonly synthesized (and now commercially available) particle geometries, but future studies characterizing MPL from nanorice[238], nanostars[239], and silver nanorods[227] could yield even brighter nonlinear contrast agents because of the sharp tips and large simulated near-field enhancements. In engineering gold nanoparticles specifically for nonlinear imaging, it would be advantageous to create particles with SPR peaks even further into the NIR region. For instance, at 1350 nm, excitation light may penetrate even deeper into epithelial tissues. In moving to larger excitation wavelengths, the disadvantage in the increased spotsize will likely be outweighed by the increase in maximum imaging depth[170].

To achieve molecularly specific nonlinear imaging of tissues with plasmonic contrast agents, several challenges remain. The biggest disadvantage of using gold nanoparticles as contrast agents is likely their large size. Though some groups have had success in the topical application of gold nanoparticles (notably, by using permeation enhancers, such as chitosan[229],[240]), the delivery of gold nanoparticles, which are orders of magnitude larger than molecular fluorophores, remains a challenge. Additionally, more detailed studies exploring the biodistribution and clearance of gold particles are necessary to understand the true biocompatibility of this class of contrast agents.

The melting of gold nanoparticles has been thoroughly characterized in previous studies, both experimentally[241],[242] and theoretically[243]. In nonlinear imaging, where high intensities are necessary to generate appreciable signal, care must be taken to stay below the particle damage threshold. It is possible that one may tune the excitation wavelength for a compromise between minimizing linear absorbance of light and maximizing the effective σ_{TPA} value. For our experiments, we found irreversible photodamage could largely be avoided by using sub-mW excitation powers, and typically, we could image with one order of magnitude lower intensity below the melting threshold. However, for deep imaging, melting could become more problematic, as more luminescence must be generated at the imaging plane to compensate from increasing losses in collection efficiency.

There are a few notable promising applications of gold nanoparticles as nonlinear contrast agents worth reiterating. The large size of gold nanoparticles, which makes delivery and clearance challenging, can actually be advantageous in killing cancer cells[78]. Because of the “leaky vasculature” phenomenon, their large size may even be beneficial in preferentially heating tumors[80]. Furthermore, gold nanoparticles can be

combined as a therapeutic and diagnostic (“theragnostic”) contrast agent, or nonlinear imaging can be used to understand the distribution of nanoparticle therapeutic agents [93]. Finally, the large brightness of gold nanoparticles can enable molecularly specific imaging in systems with poor collection efficiencies and/or limited excitation fluence, such as that typically found in nonlinear endoscopic probes[12-15].

References

- [1] G.J. Tearney, M.E. Brezinski, B.E. Bouma, S.A. Boppart, C. Pitris, J.F. Southern, and J.G. Fujimoto, "In Vivo Endoscopic Optical Biopsy with Optical Coherence Tomography," *Science*, vol. 276, Jun. 1997, pp. 2037-2039.
- [2] W. Denk, J. Strickler, and W. Webb, "Two-photon laser scanning fluorescence microscopy," *Science*, vol. 248, Apr. 1990, pp. 73-76.
- [3] B.R. Masters, P.T. So, and E. Gratton, "Multiphoton excitation fluorescence microscopy and spectroscopy of in vivo human skin.," *Biophys. J.*, vol. 72, Jun. 1997, pp. 2405-2412.
- [4] E. Dimitrow, M. Ziemer, M.J. Koehler, J. Norgauer, K. Konig, P. Elsner, and M. Kaatz, "Sensitivity and Specificity of Multiphoton Laser Tomography for In Vivo and Ex Vivo Diagnosis of Malignant Melanoma," *J Invest Dermatol*, vol. 129, Jan. 2009, pp. 1752-1758.
- [5] K. König, M. Speicher, R. Bückle, J. Reckfort, G. McKenzie, J. Welzel, M.J. Koehler, P. Elsner, and M. Kaatz, "Clinical optical coherence tomography combined with multiphoton tomography of patients with skin diseases," *Journal of Biophotonics*, vol. 2, 2009, pp. 389-397.
- [6] I. Pavlova, M. Williams, A. El-Naggar, R. Richards-Kortum, and A. Gillenwater, "Understanding the Biological Basis of Autofluorescence Imaging for Oral Cancer Detection: High-Resolution Fluorescence Microscopy in Viable Tissue," *Clinical Cancer Research*, vol. 14, Apr. 2008, pp. 2396-2404.
- [7] R. Alfano, D. Tata, J. Cordero, P. Tomashefsky, F. Longo, and M. Alfano, "Laser induced fluorescence spectroscopy from native cancerous and normal tissue," *IEEE Journal of Quantum Electronics*, vol. 20, Dec. 1984, pp. 1507-1511.
- [8] W.R. Zipfel, R.M. Williams, R. Christie, A.Y. Nikitin, B.T. Hyman, and W.W. Webb, "Live tissue intrinsic emission microscopy using multiphoton-excited native fluorescence and second harmonic generation," *Proceedings of the National Academy of Sciences*, vol. 100, 2003, pp. 7075-7080.
- [9] C. Xu, W. Zipfel, J.B. Shear, R.M. Williams, and W.W. Webb, "Multiphoton fluorescence excitation: new spectral windows for biological nonlinear microscopy," *Proceedings of the National Academy of Sciences of the United States of America*, vol. 93, Oct. 1996, pp. 10763 -10768.
- [10] P.J. Campagnola, H.A. Clark, W.A. Mohler, A. Lewis, and L.M. Loew, "Second-harmonic imaging microscopy of living cells," *Journal of Biomedical Optics*, vol. 6, Jul. 2001, pp. 277-286.
- [11] P. Theer and W. Denk, "On the fundamental imaging-depth limit in two-photon microscopy," *Journal of the Optical Society of America A*, vol. 23, 2006, pp. 3139-3149.
- [12] K. König, A. Ehlers, I. Riemann, S. Schenkl, R. Bückle, and M. Kaatz, "Clinical two-photon microendoscopy," *Microscopy Research and Technique*, vol. 70, May. 2007, pp. 398-402.
- [13] B.A. Flusberg, E.D. Cocker, W. Piyawattanametha, J.C. Jung, E.L.M. Cheung, and

- M.J. Schnitzer, "Fiber-optic fluorescence imaging," *Nature Methods*, vol. 2, Dec. 2005, pp. 941-950.
- [14] C.L. Hoy, N.J. Durr, P. Chen, W. Piyawattanametha, H. Ra, O. Solgaard, and A. Ben-Yakar, "Miniaturized probe for femtosecond laser microsurgery and two-photon imaging," *Optics Express*, vol. 16, Jun. 2008, pp. 9996-10005.
- [15] J.C. Jung and M.J. Schnitzer, "Multiphoton endoscopy," *Optics Letters*, vol. 28, Jun. 2003, pp. 902-904.
- [16] Garcia M, Jemal A, Ward EM, Center MM, Hao Y, Siegel RI, and Thun MJ, "Global Cancer Facts and Figures 2007," 2007.
- [17] V. Kumar, N. Fausto, and A. Abbas, *Robbins & Cotran Pathologic Basis of Disease, Seventh Edition*, Saunders, 2004.
- [18] E.J. Kort, N. Paneth, and G.F. Vande Woude, "The Decline in U.S. Cancer Mortality in People Born since 1925," *Cancer Research*, vol. 69, 2009, pp. 6500-6505.
- [19] J.V. Frangioni, "Translating in vivo diagnostics into clinical reality," *Nature biotechnology*, vol. 24, 2006, pp. 909-913.
- [20] "Blue Histology," *Human Thin Skin. Keratinized stratified squamous epithelium*.
- [21] M.C. Skala, J.M. Squirrell, K.M. Vrotsos, J.C. Eickhoff, A. Gendron-Fitzpatrick, K.W. Eliceiri, and N. Ramanujam, "Multiphoton microscopy of endogenous fluorescence differentiates normal, precancerous, and cancerous squamous epithelial tissues," *Cancer Research*, vol. 65, Feb. 2005, pp. 1180-1186.
- [22] I. Pavlova, K. Sokolov, R. Drezek, A. Malpica, M. Follen, and R. Richards-Kortum, "Microanatomical and Biochemical Origins of Normal and Precancerous Cervical Autofluorescence Using Laser-scanning Fluorescence Confocal Microscopy & para;" *Photochemistry and Photobiology*, vol. 77, 2003, pp. 550-555.
- [23] M. Rajadhyaksha, R.R. Anderson, and R.H. Webb, "Video-Rate Confocal Scanning Laser Microscope for Imaging Human Tissues In Vivo," *Applied Optics*, vol. 38, Apr. 1999, pp. 2105-2115.
- [24] J.T.C. Liu, M.J. Mandella, J.M. Crawford, C.H. Contag, T.D. Wang, and G.S. Kino, "Efficient rejection of scattered light enables deep optical sectioning in turbid media with low-numerical-aperture optics in a dual-axis confocal architecture," *Journal of Biomedical Optics*, vol. 13, 2008, p. 034020.
- [25] B.R. Masters, G. Gonnord, and P. Corcuff, "Three-dimensional microscopic biopsy of in vivo human skin: a new technique based on a flexible confocal microscope," *Journal of Microscopy*, vol. 185, Mar. 1997, pp. 329-338.
- [26] B.R. Masters, "Three-dimensional confocal fluorescence microscopic visualization of the living human skin," *Proceedings of SPIE*, San Jose, CA, USA: 1995, pp. 188-192.
- [27] J.V. Burstin, S. Eser, B. Seidler, A. Meining, M. Bajbouj, J. Mages, R. Lang, A.J. Kind, A.E. Schnieke, R.M. Schmid, G. Schneider, and D. Saur, "Highly sensitive detection of early-stage pancreatic cancer by multimodal near-infrared molecular imaging in living mice," *International Journal of Cancer*, vol. 123, 2008, pp.

- 2138-2147.
- [28] M. Ignat, M. Aprahamian, V. Lindner, A. Altmeyer, S. Perretta, B. Dallemagne, D. Mutter, and J. Marescaux, "Feasibility and Reliability of Pancreatic Cancer Staging Using Fiberoptic Confocal Fluorescence Microscopy in Rats," *Gastroenterology*, vol. 137, 2009, pp. 1584-1592.e1.
 - [29] T. Gambichler, A. Orlikov, R. Vasa, G. Moussa, K. Hoffmann, M. Stücker, P. Altmeyer, and F.G. Bechara, "In vivo optical coherence tomography of basal cell carcinoma," *Journal of Dermatological Science*, vol. 45, Mar. 2007, pp. 167-173.
 - [30] E.Z. Zhang, J.G. Laufer, R.B. Pedley, and P.C. Beard, "In vivo high-resolution 3D photoacoustic imaging of superficial vascular anatomy," *Physics in Medicine and Biology*, vol. 54, Feb. 2009, pp. 1035-1046.
 - [31] H.F. Zhang, K. Maslov, G. Stoica, and L.V. Wang, "Functional photoacoustic microscopy for high-resolution and noninvasive in vivo imaging," *Nature Biotechnology*, vol. 24, Jul. 2006, pp. 848-851.
 - [32] A.J. Welch and M.J.C.V. Gemert, *Optical-thermal response of laser-irradiated tissue*, Springer, 1995.
 - [33] A.N. Bashkatov, E.A. Genina, V.I. Kochubey, and V.V. Tuchin, "Optical properties of human skin, subcutaneous and mucous tissues in the wavelength range from 400 to 2000 nm," *Journal of Physics-London-D Applied Physics*, vol. 38, 2005, p. 2543.
 - [34] A. Knüttel and M. Boehlau-Godau, "Spatially confined and temporally resolved refractive index and scattering evaluation in human skin performed with optical coherence tomography," *Journal of Biomedical Optics*, vol. 5, Jan. 2000, pp. 83-92.
 - [35] G.J. Tearney, M.E. Brezinski, J.F. Southern, B.E. Bouma, M.R. Hee, and J.G. Fujimoto, "Determination of the refractive index of highly scattering human tissue by optical coherence tomography," *Optics Letters*, vol. 20, Nov. 1995, pp. 2258-2260.
 - [36] E. Salomatina, B. Jiang, J. Novak, and A.N. Yaroslavsky, "Optical properties of normal and cancerous human skin in the visible and near-infrared spectral range," *Journal of Biomedical Optics*, vol. 11, Nov. 2006, pp. 064026-9.
 - [37] Michael Sheik-Bahae M and Hasselbeck MP, "Third Order Nonlinearities," *OSA Handbook of optics*, 2001.
 - [38] Boyd, Yu, and Shen, "Photoinduced luminescence from the noble metals and its enhancement on roughened surfaces," *Physical review. B, Condensed matter*, vol. 33, Jun. 1986, pp. 7923-7936.
 - [39] K. Imura, T. Nagahara, and H. Okamoto, "Near-Field Two-Photon-Induced Photoluminescence from Single Gold Nanorods and Imaging of Plasmon Modes," *Journal of Physical Chemistry B*, vol. 109, Jul. 2005, pp. 13214-13220.
 - [40] V.E. Centonze and J.G. White, "Multiphoton excitation provides optical sections from deeper within scattering specimens than confocal imaging.," *Biophysical Journal*, vol. 75, Oct. 1998, pp. 2015-2024.
 - [41] W. Denk and K. Svoboda, "Photon upmanship: why multiphoton imaging is more

- than a gimmick,” *Neuron*, vol. 18, Mar. 1997, pp. 351-357.
- [42] W. Zipfel, R. Williams, and W. Webb, “Nonlinear magic: multiphoton microscopy in the biosciences,” *Nature Biotechnology*, vol. 21, Nov. 2003, pp. 1368-1376.
- [43] P.J. Campagnola, A.C. Millard, M. Terasaki, P.E. Hoppe, C.J. Malone, and W.A. Mohler, “Three-dimensional high-resolution second-harmonic generation imaging of endogenous structural proteins in biological tissues,” *Biophysical Journal*, vol. 82, Jan. 2002, pp. 493-508.
- [44] E. Brown, T. McKee, E. diTomaso, A. Pluen, B. Seed, Y. Boucher, and R.K. Jain, “Dynamic imaging of collagen and its modulation in tumors in vivo using second-harmonic generation,” *Nat Med*, vol. 9, Jun. 2003, pp. 796-800.
- [45] D.A. Dombeck, K.A. Kasischke, H.D. Vishwasrao, M. Ingelsson, B.T. Hyman, and W.W. Webb, “Uniform polarity microtubule assemblies imaged in native brain tissue by second-harmonic generation microscopy,” *Proceedings of the National Academy of Sciences of the United States of America*, vol. 100, Jun. 2003, pp. 7081 -7086.
- [46] D. Debarre, W. Supatto, A. Pena, A. Fabre, T. Tordjmann, L. Combettes, M. Schanne-Klein, and E. Beaurepaire, “Imaging lipid bodies in cells and tissues using third-harmonic generation microscopy,” *Nat Meth*, vol. 3, Jan. 2006, pp. 47-53.
- [47] S. Tai, W. Lee, D. Shieh, P. Wu, H. Huang, C. Yu, and C. Sun, “In vivo optical biopsy of hamster oral cavity with epi-third-harmonic-generation microscopy,” *Optics Express*, vol. 14, Jun. 2006, pp. 6178-6187.
- [48] D. Debarre and E. Beaurepaire, “Quantitative characterization of biological liquids for third-harmonic generation microscopy,” *Biophysical journal*, vol. 92, 2007, pp. 603-612.
- [49] M. Albota, D. Beljonne, J. Brédas, J.E. Ehrlich, J. Fu, A.A. Heikal, S.E. Hess, T. Kogej, M.D. Levin, S.R. Marder, D. McCord-Maughon, J.W. Perry, H. Röckel, M. Rumi, G. Subramaniam, W.W. Webb, X. Wu, and C. Xu, “Design of Organic Molecules with Large Two-Photon Absorption Cross Sections,” *Science*, vol. 281, Sep. 1998, pp. 1653-1656.
- [50] D.R. Larson, W.R. Zipfel, R.M. Williams, S.W. Clark, M.P. Bruchez, F.W. Wise, and W.W. Webb, “Water-Soluble Quantum Dots for Multiphoton Fluorescence Imaging in Vivo,” *Science*, vol. 300, May. 2003, pp. 1434-1436.
- [51] H. Wang, T.B. Huff, D.A. Zweifel, W. He, P.S. Low, A. Wei, and J.X. Cheng, “In vitro and in vivo two-photon luminescence imaging of single gold nanorods,” *Proceedings of the National Academy of Sciences*, vol. 102, 2005, pp. 15752-15756.
- [52] P. Zijlstra, J.W.M. Chon, and M. Gu, “Five-dimensional optical recording mediated by surface plasmons in gold nanorods,” *Nature*, vol. 459, May. 2009, pp. 410-413.
- [53] N.W. Ashcroft and N.D. Mermin, *Solid State Physics*, Brooks Cole, 1976.
- [54] M.A. El-Sayed, “Some interesting properties of metals confined in time and nanometer space of different shapes,” *Accounts of Chemical Research*, vol. 34,

- 2001, pp. 257-264.
- [55] G. Mie, "Beiträge zur Optik trüber Medien, speziell kolloidaler Metallösungen," *Annalen der Physik*, vol. 330, 1908, pp. 377-445.
- [56] U. Kreibig and M. Vollmer, *Optical Properties of Metal Clusters*, Springer, 1995.
- [57] S. Link and M.A. El-Sayed, "Shape and size dependence of radiative, non-radiative and photothermal properties of gold nanocrystals," *International Reviews in Physical Chemistry*, vol. 19, 2000, pp. 409-454.
- [58] M.A. Yurkin and A.G. Hoekstra, "The discrete dipole approximation: An overview and recent developments," *Journal of Quantitative Spectroscopy and Radiative Transfer*, vol. 106, Jul. 2007, pp. 558-589.
- [59] P.K. Jain, K.S. Lee, I.H. El-Sayed, and M.A. El-Sayed, "Calculated absorption and scattering properties of gold nanoparticles of different size, shape, and composition: applications in biological imaging and biomedicine," *Journal of Physical Chemistry B*, vol. 110, 2006, p. 7238.
- [60] M. Abrams and B. Murrer, "Metal compounds in therapy and diagnosis," *Science*, vol. 261, Aug. 1993, pp. 725-730.
- [61] N. Lewinski, V. Colvin, and R. Drezek, "Cytotoxicity of nanoparticles," *Small (Weinheim an Der Bergstrasse, Germany)*, vol. 4, Jan. 2008, pp. 26-49.
- [62] K. Sokolov, D. Nida, M. Descour, A. Lacy, M. Levy, B. Hall, S. Dharmawardhane, A. Ellington, B. Korgel, and R. Richards[hyphen (true graphic)]Kortum, "Molecular Optical Imaging of Therapeutic Targets of Cancer," *Genomics in Cancer Drug Discovery and Development*, Academic Press, 2006, pp. 299-344.
- [63] M. Horisberger, "Colloidal gold : a cytochemical marker for light and fluorescent microscopy and for transmission and scanning electron microscopy," *Scanning Electron Microscopy*, 1981, pp. 9-31.
- [64] W. Geoghegan and G. Ackerman, "Adsorption of horseradish peroxidase, ovomucoid and anti-immunoglobulin to colloidal gold for the indirect detection of concanavalin A, wheat germ agglutinin and goat anti-human immunoglobulin G on cell surfaces at the electron microscopic level: a new method, theory and application," *J. Histochem. Cytochem.*, vol. 25, Nov. 1977, pp. 1187-1200.
- [65] I. Nabiev, H. Morjani, and M. Manfait, "Selective analysis of antitumor drug interaction with living cancer cells as probed by surface-enhanced Raman spectroscopy," *European Biophysics Journal*, vol. 19, 1991.
- [66] K. Kneipp, A.S. Haka, H. Kneipp, K. Badizadegan, N. Yoshizawa, C. Boone, K.E. Shafer-Peltier, J.T. Motz, R.R. Dasari, and M.S. Feld, "Surface-Enhanced Raman Spectroscopy in Single Living Cells Using Gold Nanoparticles," *Applied Spectroscopy*, vol. 56, Feb. 2002, pp. 150-154.
- [67] S. Nie and S.R. Emory, "Probing Single Molecules and Single Nanoparticles by Surface-Enhanced Raman Scattering," *Science*, vol. 275, Feb. 1997, pp. 1102-1106.
- [68] R. Elghanian, J.J. Storhoff, R.C. Mucic, R.L. Letsinger, and C.A. Mirkin, "Selective Colorimetric Detection of Polynucleotides Based on the Distance-

- Dependent Optical Properties of Gold Nanoparticles,” *Science*, vol. 277, Aug. 1997, pp. 1078-1081.
- [69] R. Yasuda, H. Noji, M. Yoshida, K. Kinosita, and H. Itoh, “Resolution of distinct rotational substeps by submillisecond kinetic analysis of F1-ATPase,” *Nature*, vol. 410, Apr. 2001, pp. 898-904.
- [70] S. Schultz, D.R. Smith, J.J. Mock, and D.A. Schultz, “Single-target molecule detection with nonbleaching multicolor optical immunolabels,” *Proceedings of the National Academy of Sciences of the United States of America*, vol. 97, Feb. 2000, pp. 996 -1001.
- [71] K. Sokolov, M. Follen, J. Aaron, I. Pavlova, A. Malpica, R. Lotan, and R. Richards-Kortum, “Real-time vital optical imaging of precancer using anti-epidermal growth factor receptor antibodies conjugated to gold nanoparticles,” *Cancer Research*, vol. 63, May. 2003, pp. 1999-2004.
- [72] S.A. Boppart, A.L. Oldenburg, C. Xu, and D.L. Marks, “Optical probes and techniques for molecular contrast enhancement in coherence imaging,” *Journal of Biomedical Optics*, vol. 10, Aug. 2005, p. 41208.
- [73] A.L. Oldenburg, M.N. Hansen, D.A. Zweifel, A. Wei, and S.A. Boppart, “Plasmon-resonant gold nanorods as low backscattering albedo contrast agents for optical coherence tomography,” *Optics Express*, vol. 14, Jul. 2006, pp. 6724-6738.
- [74] M.C. Skala, M.J. Crow, A. Wax, and J.A. Izatt, “Photothermal Optical Coherence Tomography of Epidermal Growth Factor Receptor in Live Cells Using Immunotargeted Gold Nanospheres,” *Nano Letters*, vol. 8, Oct. 2008, pp. 3461-3467.
- [75] A.A. Oraevsky, A.A. Karabutov, and E.V. Savateeva, “Enhancement of optoacoustic tissue contrast with absorbing nanoparticles,” *Hybrid and Novel Imaging and New Optical Instrumentation for Biomedical Applications*, A. Boccara and A.A. Oraevsky, Eds., Munich, Germany: SPIE, 2001, pp. 60-69.
- [76] J.A. Copland, M. Eghtedari, V.L. Popov, N. Kotov, N. Mamedova, M. Motamedi, and A.A. Oraevsky, “Bioconjugated gold nanoparticles as a molecular based contrast agent: implications for imaging of deep tumors using optoacoustic tomography,” *Molecular Imaging and Biology: MIB: The Official Publication of the Academy of Molecular Imaging*, vol. 6, Oct. 2004, pp. 341-349.
- [77] S. Mallidi, T. Larson, J. Aaron, K. Sokolov, and S. Emelianov, “Molecular specific optoacoustic imaging with plasmonic nanoparticles,” *Optics Express*, vol. 15, May. 2007, pp. 6583-6588.
- [78] X. Huang, I. El-Sayed, W. Qian, and M. El-Sayed, “Cancer cell imaging and photothermal therapy in the near-infrared region by using gold nanorods,” *J Am Chem Soc*, vol. 128, Feb. 2006, pp. 2115-20.
- [79] L.R. Hirsch, R.J. Stafford, J.A. Bankson, S.R. Sershen, B. Rivera, R.E. Price, J.D. Hazle, N.J. Halas, and J.L. West, “Nanoshell-mediated near-infrared thermal therapy of tumors under magnetic resonance guidance,” *Proceedings of the National Academy of Sciences of the United States of America*, vol. 100, Nov. 2003, pp. 13549 -13554.

- [80] D.P. O'Neal, L.R. Hirsch, N.J. Halas, J.D. Payne, and J.L. West, "Photo-thermal tumor ablation in mice using near infrared-absorbing nanoparticles," *Cancer Letters*, vol. 209, Jun. 2004, pp. 171-176.
- [81] C. Loo, A. Lowery, N. Halas, J. West, and R. Drezek, "Immunotargeted Nanoshells for Integrated Cancer Imaging and Therapy," *Nano Letters*, vol. 5, Apr. 2005, pp. 709-711.
- [82] X. Huang, "Gold Nanoparticles Used in Cancer Cell Diagnostics, Selective Photothermal Therapy and Catalysis of NADH Oxidation Reaction," 2006.
- [83] I.H. El-Sayed, X. Huang, and M.A. El-Sayed, "Selective laser photo-thermal therapy of epithelial carcinoma using anti-EGFR antibody conjugated gold nanoparticles," *Cancer Letters*, vol. 239, Jul. 2006, pp. 129-135.
- [84] R.S. Norman, J.W. Stone, A. Gole, C.J. Murphy, and T.L. Sabo-Attwood, "Targeted photothermal lysis of the pathogenic bacteria, *Pseudomonas aeruginosa*, with gold nanorods," *Nano Lett*, vol. 8, 2008, pp. 302-306.
- [85] J.R. Lakowicz, *Principles of Fluorescence Spectroscopy*, Springer, 2006.
- [86] P. Biagioni, M. Celebrano, M. Savoini, G. Grancini, D. Brida, S. Matefi-Tempfli, M. Matefi-Tempfli, L. Duo, B. Hecht, G. Cerullo, and M. Finazzi, "Dependence of the two-photon photoluminescence yield of gold nanostructures on the laser pulse duration," *Physical Review B*, vol. 80, Jul. 2009, p. 045411.
- [87] C. Sun, F. Vallee, L.H. Acioli, E.P. Ippen, and J.G. Fujimoto, "Femtosecond-tunable measurement of electron thermalization in gold," *Physical Review B*, vol. 50, Nov. 1994, p. 15337.
- [88] A. Mooradian, "Photoluminescence of Metals," *Physical Review Letters*, vol. 22, 1969, pp. 185-187.
- [89] M.B. Mohamed, V. Volkov, S. Link, and M.A. El-Sayed, "The 'lightning' gold nanorods: fluorescence enhancement of over a million compared to the gold metal," *Chemical Physics Letters*, vol. 317, 2000, pp. 517-523.
- [90] D. Yelin, D. Oron, S. Thiberge, E. Moses, and Y. Silberberg, "Multiphoton plasmon-resonance microscopy," *Opt. Express*, vol. 11, 2003, pp. 1385-1391.
- [91] R. Farrer, F. Butterfield, V. Chen, and J. Fourkas, "Highly Efficient Multiphoton-Absorption-Induced Luminescence from Gold Nanoparticles," *Nano Letters*, vol. 5, Jun. 2005, pp. 1139-1142.
- [92] N. Durr, T. Larson, D. Smith, B. Korgel, K. Sokolov, and A. Ben-Yakar, "Two-photon luminescence imaging of cancer cells using molecularly targeted gold nanorods," *Nano Letters*, vol. 7, Apr. 2007, pp. 941-945.
- [93] J. Park, A. Estrada, K. Sharp, K. Sang, J.A. Schwartz, D.K. Smith, C. Coleman, J.D. Payne, B.A. Korgel, A.K. Dunn, and J.W. Tunnell, "Two-photon-induced photoluminescence imaging of tumors using near-infrared excited gold nanoshells," *Optics Express*, vol. 16, Feb. 2008, pp. 1590-1599.
- [94] T.B. Huff, M.N. Hansen, Y. Zhao, J. Cheng, and A. Wei, "Controlling the Cellular Uptake of Gold Nanorods," *Langmuir*, vol. 23, Feb. 2007, pp. 1596-1599.
- [95] L. Tong, Y. Zhao, T.B. Huff, M.N. Hansen, A. Wei, and J. Cheng, "Gold Nanorods Mediate Tumor Cell Death by Compromising Membrane Integrity,"

- Advanced materials (Deerfield Beach, Fla.)*, vol. 19, 2007, pp. 3136-3141.
- [96] L. Tong, C.M. Cobley, J. Chen, Y. Xia, and J. Cheng, "Bright Three-Photon Luminescence from Gold/Silver Alloyed Nanostructures for Bioimaging with Negligible Photothermal Toxicity," *Angewandte Chemie International Edition*, 2010, pp. NA-NA.
- [97] P. Zijlstra, J.W.M. Chon, and M. Gu, "Five-dimensional optical recording mediated by surface plasmons in gold nanorods," *Nature*, vol. 459, 2009, pp. 410-413.
- [98] B. Holfeld, "Study of the imaging depth in turbid tissue with two-photon microscopy," Masters Thesis, University of Texas at Austin, 2008.
- [99] Tsai PS, Nishimura N, Yoder EJ, Dolnick EM, White GA, and Kleinfeld D, "Principles, design, and construction of a two-photon laser scanning microscope for in vivo brain imaging," *In vivo optical imaging of brain function*, CRC Press, 2002.
- [100] Stelzer EHK, "The intermediate optical system of laser-scanning confocal microscopes," *Handbook of Biological Confocal Microscopy*, Springer, 2006.
- [101] C.J. de Grauw, J.M. Vroom, H.T. van der Voort, and H.C. Gerritsen, "Imaging properties in two-photon excitation microscopy and effects of refractive-index mismatch in thick specimens," *Applied Optics*, vol. 38, Oct. 1999, pp. 5995-6003.
- [102] H. Jacobsen, P. Hanninen, and S. Hell, "Refractive-index-induced aberrations in 2-photon confocal fluorescence microscopy," *Journal of Microscopy-Oxford*, vol. 176, 1994, pp. 226-230.
- [103] K. Carlsson, "The influence of specimen refractive-index, detector signal integration, and nonuniform scan speed on the imaging properties in confocal microscopy," vol. 163, 1991, pp. 167-178.
- [104] M. Oheim, E. Beaurepaire, E. Chaigneau, J. Mertz, and S. Charpak, "Two-photon microscopy in brain tissue: parameters influencing the imaging depth," *Journal of Neuroscience Methods*, vol. 111, Oct. 2001, pp. 29-37.
- [105] T. Kasahara, "United States Patent: 6501603 - Microscope objective lens," U.S. Patent 6501603, December 31, 2002.
- [106] H. Urey, "Spot Size, Depth-of-Focus, and Diffraction Ring Intensity Formulas for Truncated Gaussian Beams," *Applied Optics*, vol. 43, Jan. 2004, pp. 620-625.
- [107] F. Helmchen and W. Denk, "Deep tissue two-photon microscopy," *Nat Meth*, vol. 2, Dec. 2005, pp. 932-940.
- [108] V. Andresen, S. Alexander, W. Heupel, M. Hirschberg, R.M. Hoffman, and P. Friedl, "Infrared multiphoton microscopy: subcellular-resolved deep tissue imaging," *Current Opinion in Biotechnology*, vol. 20, Feb. 2009, pp. 54-62.
- [109] C. Xu, C. Vinegoni, T.S. Ralston, W. Luo, W. Tan, and S.A. Boppart, "Spectroscopic spectral-domain optical coherence microscopy," *Optics Letters*, vol. 31, Apr. 2006, pp. 1079-1081.
- [110] A.K. Dunn, V.P. Wallace, M. Coleno, M.W. Berns, and B.J. Tromberg, "Influence of optical properties on two-photon fluorescence imaging in turbid samples," *Applied Optics*, vol. 39, 2000, pp. 1194-1201.

- [111] C.Y. Dong, K. Koenig, and P. So, "Characterizing point spread functions of two-photon fluorescence microscopy in turbid medium," *Journal of Biomedical Optics*, vol. 8, 2003, p. 450.
- [112] M. Muller, J. Squier, and G.J. Brakenhoff, "Measurement of femtosecond pulses in the focal point of a high-numerical-aperture lens by two-photon absorption," *Optics Letters*, vol. 20, May. 1995, pp. 1038-1040.
- [113] J.B. Guild, C. Xu, and W.W. Webb, "Measurement of group delay dispersion of high numerical aperture objective lenses using two-photon excited fluorescence," *Applied Optics*, vol. 36, Jan. 1997, pp. 397-401.
- [114] R. Trebino, *Frequency-Resolved Optical Gating: The Measurement of Ultrashort Laser Pulses*, Springer, 2002.
- [115] *The effects of dispersion on ultrashort pulses*, Newport Corporation, .
- [116] J.T. Zinter and M.J. Levene, "Optimizing Fluorescence Collection in Multiphoton Microscopy," *Biomedical Optics, OSA Technical Digest*, vol. BMD70, 2008.
- [117] D. Feng, D. Marshburn, D. Jen, R.J. Weinberg, R.M. Taylor, and A. Burette, "Stepping into the Third Dimension," *J. Neurosci.*, vol. 27, Nov. 2007, pp. 12757-12760.
- [118] P. Carmeliet and R. Jain, "Angiogenesis in cancer and other diseases," *Nature*, vol. 407, Sep. 2000, pp. 249-257.
- [119] C.K. Hayakawa, V. Venugopalan, V.V. Krishnamachari, and E.O. Potma, "Amplitude and Phase of Tightly Focused Laser Beams in Turbid Media," *Physical Review Letters*, vol. 103, Jul. 2009, p. 043903.
- [120] Theer, Patrick, "On the Fundamental Imaging-Depth Limit in Two-Photon Microscopy," Dissertation, University of Heidelberg, 2004.
- [121] C.J.R. Sheppard, M. Gu, Y. Kawata, and S. Kawata, "Three-dimensional transfer functions for high-aperture systems," *Journal of the Optical Society of America A*, vol. 11, 1994, pp. 593-598.
- [122] J. Ying, F. Liu, and R.R. Alfano, "Spatial distribution of two-photon-excited fluorescence in scattering media," *Applied Optics*, vol. 38, Jan. 1999, pp. 224-229.
- [123] J. Ying, F. Liu, and R.R. Alfano, "Effect of Scattering on Nonlinear Optical Scanning Microscopy Imaging of highly scattering media," *Applied Optics*, vol. 39, Feb. 2000, pp. 509-514.
- [124] A. Leray, C. Odin, and Y. Le Grand, "Out-of-focus fluorescence collection in two-photon microscopy of scattering media," *Optics Communications*, 2008.
- [125] J.W. McLean, J.D. Freeman, and R.E. Walker, "Beam Spread Function with Time Dispersion," *Applied Optics*, vol. 37, Jul. 1998, pp. 4701-4711.
- [126] L. Wang, S.L. Jacques, and L. Zheng, "MCML--Monte Carlo modeling of light transport in multi-layered tissues," *Computer Methods and Programs in Biomedicine*, vol. 47, Jul. 1995, pp. 131-146.
- [127] E. Beaurepaire, M. Oheim, and J. Mertz, "Ultra-deep two-photon fluorescence excitation in turbid media," *Optics Communications*, vol. 188, 2001, pp. 25-29.
- [128] C. Simpson, M. Kohl, M. Essenpreis, and M. Cope, "Near-infrared optical properties of ex vivo human skin and subcutaneous tissues measured using the

- Monte Carlo inversion technique,” *Phys Med Biol*, vol. 43, Sep. 1998, pp. 2465-78.
- [129] J.A. Palero, H.S. de Bruijn, A. van der Ploeg-van den Heuvel, H.J.C.M. Sterenborg, and H.C. Gerritsen, “In vivo nonlinear spectral imaging in mouse skin,” *Optics Express*, vol. 14, May. 2006, pp. 4395-4402.
- [130] J.A. Palero, H.S. de Bruijn, A. van der Ploeg van den Heuvel, H.J.C.M. Sterenborg, and H.C. Gerritsen, “Spectrally Resolved Multiphoton Imaging of In Vivo and Excised Mouse Skin Tissues,” *Biophys. J.*, vol. 93, Aug. 2007, pp. 992-1007.
- [131] A. Leray, C. Odin, E. Huguet, F. Amblard, and Y.L. Grand, “Spatially distributed two-photon excitation fluorescence in scattering media: Experiments and time-resolved Monte Carlo simulations,” *Optics Communications*, vol. 272, 2007, pp. 269-278.
- [132] C.M. Blanca and C. Saloma, “Monte carlo analysis of two-photon fluorescence imaging through a scattering medium,” *Applied Optics*, vol. 37, Dec. 1998, pp. 8092-8102.
- [133] A. Tycho, T.M. Jørgensen, H.T. Yura, and P.E. Andersen, “Derivation of a Monte Carlo method for modeling heterodyne detection in optical coherence tomography systems,” *Applied Optics*, vol. 41, Nov. 2002, pp. 6676-6691.
- [134] “Forming a hyperboloid with strings,” *Forming a hyperboloid with strings*, Jul. 2010.
- [135] E. Beaufort and J. Mertz, “Epifluorescence collection in two-photon microscopy,” *Applied optics*, vol. 41, 2002, pp. 5376-5382.
- [136] B. Masters, P. So, and E. Gratton, “Optical Biopsy of In Vivo Human Skin: Multiphoton Excitation Microscopy,” *Lasers in Medical Science*, vol. 13, Oct. 1998, pp. 196-203.
- [137] P. Wilder-Smith, K. Osann, N. Hanna, N. El Abbadi, M. Brenner, D. Messadi, and T. Krasieva, “In vivo multiphoton fluorescence imaging: a novel approach to oral malignancy,” *Lasers in Surgery and Medicine*, vol. 35, 2004, pp. 96-103.
- [138] S. Lin, S. Jee, C. Kuo, R. Wu, W. Lin, J. Chen, Y. Liao, C. Hsu, T. Tsai, Y. Chen, and C. Dong, “Discrimination of basal cell carcinoma from normal dermal stroma by quantitative multiphoton imaging,” *Optics Letters*, vol. 31, Sep. 2006, pp. 2756-2758.
- [139] N.D. Kirkpatrick, M.A. Brewer, and U. Utzinger, “Endogenous Optical Biomarkers of Ovarian Cancer Evaluated with Multiphoton Microscopy,” *Cancer Epidemiology Biomarkers & Prevention*, vol. 16, 2007, pp. 2048-2057.
- [140] J. Paoli, M. Smedh, A. Wennberg, and M.B. Ericson, “Multiphoton Laser Scanning Microscopy on Non-Melanoma Skin Cancer: Morphologic Features for Future Non-Invasive Diagnostics,” *Journal of Investigative Dermatology*, vol. 128, 2007, pp. 1248-1255.
- [141] C. Wang, F. Li, R. Wu, V.A. Hovhannisyanyan, W. Lin, S. Lin, P.T.C. So, and C. Dong, “Differentiation of normal and cancerous lung tissues by multiphoton imaging,” *Journal of Biomedical Optics*, vol. 14, 2009, p. 044034.

- [142] R.R. Anderson and J.A. Parrish, "The Optics of Human Skin," *J Investig Dermatol*, vol. 77, Jul. 1981, pp. 13-19.
- [143] D.L. Heintzelman, U. Utzinger, H. Fuchs, A. Zuluaga, K. Gossage, A.M. Gillenwater, R. Jacob, B. Kemp, and R.R. Richards-Kortum, "Optimal excitation wavelengths for in vivo detection of oral neoplasia using fluorescence spectroscopy," *Photochemistry and Photobiology*, vol. 72, Jul. 2000, pp. 103-113.
- [144] R. Drezek, C. Brookner, I. Pavlova, I. Boiko, A. Malpica, R. Lotan, M. Follen, and R. Richards-Kortum, "Autofluorescence Microscopy of Fresh Cervical-Tissue Sections Reveals Alterations in Tissue Biochemistry with Dysplasia," *Photochemistry and Photobiology*, vol. 73, 2001, p. 636.
- [145] B. Masters, "Three-dimensional confocal microscopy of human skin in vivo: autofluorescence of human skin," *Bioimaging*, vol. 4, 1996, pp. 13-19.
- [146] P. Theer, M.T. Hasan, and W. Denk, "Two-photon imaging to a depth of 1000 μm in living brains by use of a Ti: Al₂O₃ regenerative amplifier," *Optics letters*, vol. 28, 2003, pp. 1022-1024.
- [147] K. Koenig and I. Riemann, "High-resolution multiphoton tomography of human skin with subcellular spatial resolution and picosecond time resolution," *Journal of Biomedical Optics*, vol. 8, 2003, p. 432.
- [148] S. Chen, H. Wu, and C. Sun, "Three-dimensional confocal microscopy of human skin in vivo: autofluorescence of human skin," *Journal of Biomedical Optics*, vol. 14, 2009, p. 060505.
- [149] R. Cicchi, D. Massi, S. Sestini, P. Carli, V. De Giorgi, T. Lotti, and F.S. Pavone, "Multidimensional non-linear laser imaging of Basal Cell Carcinoma," *Optics Express*, vol. 15, 2007, pp. 10135-10148.
- [150] M.B. Ericson, C. Simonsson, S. Guldbrand, C. Ljungblad, J. Paoli, and M. Smedh, "Two-photon laser-scanning fluorescence microscopy applied for studies of human skin," *Journal of Biophotonics*, vol. 1, 2008, pp. 320-330.
- [151] D. Li, W. Zheng, and J.Y. Qu, "Imaging of epithelial tissue in vivo based on excitation of multiple endogenous nonlinear optical signals," *Optics Letters*, vol. 34, 2009, pp. 2853-2855.
- [152] B.R. Masters, P.T.C. So, and E. Gratton, "Multiphoton Excitation Microscopy of In Vivo Human Skin: Functional and Morphological Optical Biopsy Based on Three-Dimensional Imaging, Lifetime Measurements and Fluorescence Spectroscopy," *Annals of the New York Academy of Sciences*, vol. 838, 1998, pp. 58-67.
- [153] A.J. Radosevich, M.B. Bouchard, S.A. Burgess, B.R. Chen, and E.M.C. Hillman, "Hyperspectral in vivo two-photon microscopy of intrinsic contrast," *Optics Letters*, vol. 33, 2008, pp. 2164-2166.
- [154] P. So, H. Kim, and I. Kochevar, "Two-Photon deep tissue ex vivo imaging of mouse dermal and subcutaneous structures," *Optics Express*, vol. 3, Oct. 1998, pp. 339-350.
- [155] J. Sun, T. Shilagard, B. Bell, M. Motamedi, and G. Vargas, "In vivo multimodal nonlinear optical imaging of mucosal tissue," *Optics Express*, vol. 12, May. 2004,

- p. 2478.
- [156] S. Zhuo, J. Chen, X. Jiang, S. Xie, R. Chen, N. Cao, Q. Zou, and S. Xiong, "The layered-resolved microstructure and spectroscopy of mouse oral mucosa using multiphoton microscopy," *Physics in Medicine and Biology*, vol. 52, 2007, pp. 4967-4980.
 - [157] S. Zhuo, J. Chen, T. Luo, X. Jiang, S. Xie, and R. Chen, "Two-layered multiphoton microscopic imaging of cervical tissue," *Lasers in Medical Science*, vol. 24, 2008, pp. 359-363.
 - [158] J. Paoli, M. Smedh, A. Wennberg, and M.B. Ericson, "Multiphoton Laser Scanning Microscopy on Non-Melanoma Skin Cancer: Morphologic Features for Future Non-Invasive Diagnostics," *J Invest Dermatol*, vol. 128, Nov. 2007, pp. 1248-1255.
 - [159] C. Matzler, *Matlab functions for mie scattering and absorption*, University of Bern: Institut fur Angewandte Physik, 2006.
 - [160] R. Drezek, K. Sokolov, U. Utzinger, I. Boiko, A. Malpica, M. Follen, and R. Richards-Kortum, "Understanding the contributions of NADH and collagen to cervical tissue fluorescence spectra: modeling, measurements, and implications," *Journal of Biomedical Optics*, vol. 6, 2001, p. 385.
 - [161] S. Guldbrand, C. Simonsson, M. Smedh, and M.B. Ericson, "Point spread function measured in human skin using two-photon fluorescence microscopy," *Proceedings of SPIE*, Munich, Germany: 2009, pp. 73671R-73671R-6.
 - [162] D.R. Larson, W.R. Zipfel, R.M. Williams, S.W. Clark, M.P. Bruchez, F.W. Wise, and W.W. Webb, "Water-soluble quantum dots for multiphoton fluorescence imaging in vivo," *Science (New York, N.Y.)*, vol. 300, May. 2003, pp. 1434-6.
 - [163] G. Zhu, J. van Howe, M. Durst, W. Zipfel, and C. Xu, "Simultaneous spatial and temporal focusing of femtosecond pulses," *Optics Express*, vol. 13, Mar. 2005, pp. 2153-2159.
 - [164] D. Oron, E. Tal, and Y. Silberberg, "Scanningless depth-resolved microscopy," *Optics Express*, vol. 13, Mar. 2005, pp. 1468-1476.
 - [165] A. Leray, K. Lillis, and J. Mertz, "Enhanced background rejection in thick tissue with differential-aberration two-photon microscopy," *Biophysical Journal*, vol. 94, 2008, pp. 1449-1458.
 - [166] G. McConnell, "Improving the penetration depth in multiphoton excitation laser scanning microscopy," *Journal of Biomedical Optics*, vol. 11, 2006, p. 054020.
 - [167] R. Cicchi, D. Sampson, D. Massi, and F. Pavone, "Contrast and depth enhancement in two-photon microscopy of human skin ex vivo by use of optical clearing agents," *Optics Express*, vol. 13, 2005, pp. 2337-2344.
 - [168] Y. Le Grand, A. Leray, T. Guilbert, and C. Odin, "Non-descanned versus descanned epifluorescence collection in two-photon microscopy: Experiments and Monte Carlo simulations," *Optics Communications*, vol. 281, Nov. 2008, pp. 5480-5486.
 - [169] V. Andresen, S. Alexander, W. Heupel, M. Hirschberg, R.M. Hoffman, and P. Friedl, "Infrared multiphoton microscopy: subcellular-resolved deep tissue

- imaging,” *Current Opinion in Biotechnology*, vol. 20, Feb. 2009, pp. 54-62.
- [170] D. Kobat, M.E. Durst, N. Nishimura, A.W. Wong, C.B. Schaffer, and C. Xu, “Deep tissue multiphoton microscopy using longer wavelength excitation,” *Optics Express*, vol. 17, 2009, pp. 13354-13364.
- [171] Y. Abate, A. Schwartzberg, D. Strasser, and S.R. Leone, “Nanometer-scale size dependent imaging of cetyl trimethyl ammonium bromide (CTAB) capped and uncapped gold nanoparticles by apertureless near-field optical microscopy,” *Chemical Physics Letters*, vol. 474, May. 2009, pp. 146-152.
- [172] J. Turkevich, P.C. Stevenson, and J. Hillier, “The Formation of Colloidal Gold,” *The Journal of Physical Chemistry*, vol. 57, Jul. 1953, pp. 670-673.
- [173] G. Frens, “Controlled nucleation for regulation of particle-size in monodisperse gold suspensions,” *Nature-Physical Science*, vol. 241, 1973, pp. 22, 20.
- [174] J. Kimling, M. Maier, B. Okenve, V. Kotaidis, H. Ballot, and A. Plech, “Turkevich Method for Gold Nanoparticle Synthesis Revisited,” *The Journal of Physical Chemistry B*, vol. 110, 2006, pp. 15700-15707.
- [175] S. Link, M.B. Mohamed, and M.A. El-Sayed, “Simulation of the Optical Absorption Spectra of Gold Nanorods as a Function of Their Aspect Ratio and the Effect of the Medium Dielectric Constant,” *The Journal of Physical Chemistry B*, vol. 103, Apr. 1999, pp. 3073-3077.
- [176] R. Harrison and A. Ben-Yakar, “Role of near-field enhancement in plasmonic laser nanoablation using gold nanorods on a silicon substrate,” *In preparation*.
- [177] A. Oldenburg, “Characterization of plasmon-resonant gold nanorods as near-infrared optical contrast agents investigated using a double-integrating sphere system,” *Proceedings of SPIE*, San Jose, CA, USA: 2005, pp. 50-60.
- [178] W. Ni, X. Kou, Z. Yang, and J. Wang, “Tailoring Longitudinal Surface Plasmon Wavelengths, Scattering and Absorption Cross Sections of Gold Nanorods,” *ACS Nano*, vol. 2, Apr. 2008, pp. 677-686.
- [179] K. Lee and M.A. El-Sayed, “Dependence of the Enhanced Optical Scattering Efficiency Relative to That of Absorption for Gold Metal Nanorods on Aspect Ratio, Size, End-Cap Shape, and Medium Refractive Index,” *The Journal of Physical Chemistry B*, vol. 109, Nov. 2005, pp. 20331-20338.
- [180] C.J. Orendorff and C.J. Murphy, “Quantitation of Metal Content in the Silver-Assisted Growth of Gold Nanorods,” *The Journal of Physical Chemistry B*, vol. 110, Mar. 2006, pp. 3990-3994.
- [181] B. Nikoobakht, J. Wang, and M.A. El-Sayed, “Surface-enhanced Raman scattering of molecules adsorbed on gold nanorods: off-surface plasmon resonance condition,” *Chemical Physics Letters*, vol. 366, Nov. 2002, pp. 17-23.
- [182] H. Liao and J.H. Hafner, “Gold Nanorod Bioconjugates,” *Chemistry of Materials*, vol. 17, 2005, pp. 4636-4641.
- [183] R. Jin, G. Wu, Z. Li, C.A. Mirkin, and G.C. Schatz, “What Controls the Melting Properties of DNA-Linked Gold Nanoparticle Assemblies?,” *Journal of the American Chemical Society*, vol. 125, Feb. 2003, pp. 1643-1654.
- [184] O. Martinez, “3000 times grating compressor with positive group velocity

- dispersion: Application to fiber compensation in 1.3-1.6 μm region,” *IEEE Journal of Quantum Electronics*, vol. 23, Jan. 1987, pp. 59-64.
- [185] M. Lai, S.T. Lai, and C. Swinger, “Single-grating laser pulse stretcher and compressor,” *Applied Optics*, vol. 33, Oct. 1994, pp. 6985-6987.
- [186] H. Wang, T.B. Huff, D.A. Zweifel, W. He, P.S. Low, A. Wei, and J.X. Cheng, “In vitro and in vivo two-photon luminescence imaging of single gold nanorods,” *Proceedings of the National Academy of Sciences*, vol. 102, 2005, p. 15752.
- [187] X. Su, M. Li, Z. Zhou, Y. Zhai, Q. Fu, C. Huang, H. Song, and Z. Hao, “Microstructure and multiphoton luminescence of Au nanocrystals prepared by using glancing deposition method,” *Journal of Luminescence*, vol. 128, 2008, pp. 642–646.
- [188] M.J. Pelletier, “Quantitative Analysis Using Raman Spectrometry,” *Applied Spectroscopy*, vol. 57, Jan. 2003, pp. 20A-42A.
- [189] D.J. Roaf, “The Fermi Surfaces of Copper, Silver and Gold II. Calculation of the Fermi Surfaces,” *Royal Society of London Philosophical Transactions Series A*, vol. 255, Nov. 1962, pp. 135-152.
- [190] K. Imura and H. Okamoto, “Properties of Photoluminescence from Single Gold Nanorods Induced by Near-Field Two-Photon Excitation,” *The Journal of Physical Chemistry C*, vol. 113, 2009, pp. 11756-11759.
- [191] P. Muhlschlegel, “Resonant Optical Antennas,” *Science*, vol. 308, 2005, pp. 1607-1609.
- [192] Q. Wang, J. Han, D. Guo, S. Xiao, Y. Han, H. Gong, and X. Zou, “Highly Efficient Avalanche Multiphoton Luminescence from Coupled Au Nanowires in the Visible Region,” *Nano Letters*, vol. 7, 2007, pp. 723-728.
- [193] D.S. Wang, F.Y. Hsu, and C.W. Lin, “Surface plasmon effects on two photon luminescence of gold nanorods,” *Optics Express*, vol. 17, 2009, pp. 11350–11359.
- [194] H.M. Gong, Z.K. Zhou, S. Xiao, X.R. Su, and Q.Q. Wang, “Strong Near-infrared Avalanche Photoluminescence from Ag Nanowire Arrays,” *Plasmonics*, vol. 3, 2008, pp. 59-64.
- [195] J. Pawley, *Handbook of Biological Confocal Microscopy*, Springer, 2006.
- [196] M. Pelton, M. Liu, S. Park, N.F. Scherer, and P. Guyot-Sionnest, “Ultrafast resonant optical scattering from single gold nanorods: Large nonlinearities and plasmon saturation,” *Physical Review B*, vol. 73, Apr. 2006, p. 155419.
- [197] S. Park, M. Pelton, M. Liu, P. Guyot-Sionnest, and N.F. Scherer, “Ultrafast Resonant Dynamics of Surface Plasmons in Gold Nanorods,” *The Journal of Physical Chemistry C*, vol. 111, Jan. 2007, pp. 116-123.
- [198] P. Biagioni, M. Celebrano, M. Savoini, G. Grancini, D. Brida, S. Mátéfi-Tempfli, M. Mátéfi-Tempfli, L. Duò, B. Hecht, G. Cerullo, and M. Finazzi, “Dependence of the two-photon photoluminescence yield of gold nanostructures on the laser pulse duration,” *Physical Review B*, vol. 80, 2009.
- [199] H. Kim, C. Xiang, A.G. Güell, R.M. Penner, and E.O. Potma, “Tunable Two-Photon Excited Luminescence in Single Gold Nanowires Fabricated by Lithographically Patterned Nanowire Electrodeposition,” *Journal of Physical*

- Chemistry C*, vol. 112, 2008, pp. 12721-12727.
- [200] M. Beversluis, A. Bouhelier, and L. Novotny, "Continuum generation from single gold nanostructures through near-field mediated intraband transitions," *Physical Review B*, vol. 68, 2003.
- [201] P.J. Schuck, D.P. Fromm, A. Sundaramurthy, G.S. Kino, and W.E. Moerner, "Improving the Mismatch between Light and Nanoscale Objects with Gold Bowtie Nanoantennas," *Physical Review Letters*, vol. 94, 2005.
- [202] T. Kempa, R.A. Farrer, M. Giersig, and J.T. Fourkas, "Photochemical Synthesis and Multiphoton Luminescence of Monodisperse Silver Nanocrystals," *Plasmonics*, vol. 1, 2006, pp. 45-51.
- [203] G. Ramakrishna, O. Varnavski, J. Kim, D. Lee, and T. Goodson, "Quantum-sized gold clusters as efficient two-photon absorbers," *J. Am. Chem. Soc.*, vol. 130, 2008, pp. 5032–5033.
- [204] A. Bouhelier, R. Bachelot, G. Lerondel, S. Kostcheev, P. Royer, and G.P. Wiederrecht, "Surface Plasmon Characteristics of Tunable Photoluminescence in Single Gold Nanorods," *Physical Review Letters*, vol. 95, 2005.
- [205] M. Eichelbaum, B.E. Schmidt, H. Ibrahim, and K. Rademann, "Three-photon-induced luminescence of gold nanoparticles embedded in and located on the surface of glassy nanolayers," *Nanotechnology*, vol. 18, 2007, p. 355702.
- [206] S. Pang, A.T. Yeh, C. Wang, and K.E. Meissner, "Beyond the $\frac{1}{2}T$ limit: two-photon-excited fluorescence using pulses as short as sub-10-fs," *Journal of Biomedical Optics*, vol. 14, 2009, p. 054041.
- [207] R.H.M. Groeneveld, R. Sprik, and A. Lagendijk, "Femtosecond spectroscopy of electron-electron and electron-phonon energy relaxation in Ag and Au," *Physical Review B*, vol. 51, May. 1995, p. 11433.
- [208] K. Imura, T. Nagahara, and H. Okamoto, "Near-Field Two-Photon-Induced Photoluminescence from Single Gold Nanorods and Imaging of Plasmon Modes," *The Journal of Physical Chemistry B*, vol. 109, 2005, pp. 13214-13220.
- [209] N. Rotenberg, A.D. Bristow, M. Pfeiffer, M. Betz, and H.M. van Driel, "Nonlinear absorption in Au films: Role of thermal effects," *Physical Review B*, vol. 75, Apr. 2007, p. 155426.
- [210] M. Pollnau, D.R. Gamelin, S.R. Luthi, H.U. Gudel, and M.P. Hehlen, "Power dependence of upconversion luminescence in lanthanide and transition-metal-ion systems," *Physical Review B*, vol. 61, Feb. 2000, p. 3337.
- [211] C. Xu and W. Webb, "Measurement of two-photon excitation cross sections of molecular fluorophores with data from 690 to 1050 nm," *Journal of the Optical Society of America B-Optical Physics*, vol. 13, Mar. 1996, pp. 481-491.
- [212] R. Loudon, *The Quantum Theory of Light*, Oxford University Press, USA, 2000.
- [213] C. Xu, R.M. Williams, W. Zipfel, and W.W. Webb, "Multiphoton excitation cross-sections of molecular fluorophores," *Bioimaging*, vol. 4, 1996, pp. 198-207.
- [214] M.A. Albota, C. Xu, and W.W. Webb, "Two-photon fluorescence excitation cross sections of biomolecular probes from 690 to 960 nm," *Applied optics*, vol. 37, 1998, pp. 7352-7356.

- [215] Acemioglu B., Arik M., Efeoglu H., and Onganer Y., "Solvent effect on the ground and excited state dipole moments of fluorescein," *Journal of Molecular Structure: theochem*, vol. 548, Jul. 2001, pp. 165-171.
- [216] C. Liu, M. Ho, Y. Chen, C. Hsieh, Y. Lin, Y. Wang, M. Yang, H. Duan, B. Chen, J. Lee, J. Hsiao, and P. Chou, "Thiol-Functionalized Gold Nanodots: Two-Photon Absorption Property and Imaging In Vitro," *The Journal of Physical Chemistry C*, vol. 113, 2009, pp. 21082-21089.
- [217] S.A. Patel, C.I. Richards, J. Hsiang, and R.M. Dickson, "Water-Soluble Ag Nanoclusters Exhibit Strong Two-Photon-Induced Fluorescence," *Journal of the American Chemical Society*, vol. 130, 2008, pp. 11602-11603.
- [218] F. Stellacci, C.A. Bauer, T. Meyer-Friedrichsen, W. Wenseleers, S.R. Marder, and J.W. Perry, "Ultrabright Supramolecular Beacons Based on the Self-Assembly of Two-Photon Chromophores on Metal Nanoparticles," *Journal of the American Chemical Society*, vol. 125, Jan. 2003, pp. 328-329.
- [219] N.A.A. Rahim, W. McDaniel, K. Bardon, S. Srinivasan, V. Vickerman, P.T.C. So, and J.H. Moon, "Conjugated Polymer Nanoparticles for Two-Photon Imaging of Endothelial Cells in a Tissue Model," *Advanced Materials*, vol. 21, 2009, pp. 3492-3496.
- [220] O. Schwartz and D. Oron, "Background-free third harmonic imaging of gold nanorods," *Nano Letters*, vol. 9, Dec. 2009, pp. 4093-4097.
- [221] J.L. Li, D. Day, and M. Gu, "Ultra-Low Energy Threshold for Cancer Photothermal Therapy Using Transferrin-Conjugated Gold Nanorods," *Advanced Materials*, vol. 20, 2008, pp. 3866-3871.
- [222] X. Huang, S. Neretina, and M.A. El-Sayed, "Gold Nanorods: From Synthesis and Properties to Biological and Biomedical Applications," *Advanced Materials*, vol. 21, 2009, pp. 4880-4910.
- [223] T.B. Huff, M.N. Hansen, L. Tong, Y. Zhao, H. Wang, D.A. Zweifel, J.X. Cheng, and A. Wei, "Plasmon-resonant nanorods as multimodal agents for two-photon luminescent imaging and photothermal therapy," *Colloidal Quantum Dots for Biomedical Applications II. Edited by Osinski, Marek; Jovin, Thomas M.; Yamamoto, Kenji. Proceedings of the SPIE*, 2007, p. 64480D.
- [224] T. Huff, M. Hansen, Y. Zhao, J. Cheng, and A. Wei, "Controlling the cellular uptake of gold nanorods," *Langmuir*, vol. 23, Feb. 2007, pp. 1596-9.
- [225] H. Kim, C. Xiang, A.G. Güell, R.M. Penner, and E.O. Potma, "Tunable Two-Photon Excited Luminescence in Single Gold Nanowires Fabricated by Lithographically Patterned Nanowire Electrodeposition," *Journal of Physical Chemistry C*, vol. 112, 2008, pp. 12721-12727.
- [226] L. Gou and C.J. Murphy, "Fine-Tuning the Shape of Gold Nanorods," *Chemistry of Materials*, vol. 17, Jul. 2005, pp. 3668-3672.
- [227] N.R. Jana, L. Gearheart, and C.J. Murphy, "Wet Chemical Synthesis of High Aspect Ratio Cylindrical Gold Nanorods," *The Journal of Physical Chemistry B*, vol. 105, May. 2001, pp. 4065-4067.
- [228] B. Nikoobakht and M.A. El-Sayed, "Preparation and growth mechanism of gold

- nanorods (NRs) using seed-mediated growth method,” *Chemistry of Materials*, vol. 15, 2003, pp. 1957-1962.
- [229] J. Aaron, N. Nitin, K. Travis, S. Kumar, T. Collier, S.Y. Park, M. Jose-Yacaman, L. Coghlan, M. Follen, and R. Richards-Kortum, “Plasmon resonance coupling of metal nanoparticles for molecular imaging of carcinogenesis in vivo,” *Journal of Biomedical Optics*, vol. 12, 2007, p. 034007.
- [230] J. Aaron, K. Travis, N. Harrison, and K. Sokolov, “Dynamic imaging of molecular assemblies in live cells based on nanoparticle plasmon resonance coupling,” *Nano Letters*, vol. 9, Oct. 2009, pp. 3612-3618.
- [231] C.L. Didychuk, P. Ephrat, M. Belton, and J.J.L. Carson, “Synthesis and in vitro cytotoxicity of mPEG-SH modified gold nanorods,” *Photons Plus Ultrasound: Imaging and Sensing 2008: The Ninth Conference on Biomedical Thermoacoustics, Optoacoustics, and Acousto-optics*, San Jose, CA, USA: SPIE, 2008, pp. 68560M-8.
- [232] H. Takahashi, Y. Niidome, T. Niidome, K. Kaneko, H. Kawasaki, and S. Yamada, “Modification of gold nanorods using phosphatidylcholine to reduce cytotoxicity,” *Langmuir: The ACS Journal of Surfaces and Colloids*, vol. 22, Jan. 2006, pp. 2-5.
- [233] L. Tong, Q. Wei, A. Wei, and J. Cheng, “Gold nanorods as contrast agents for biological imaging: optical properties, surface conjugation and photothermal effects,” *Photochemistry and Photobiology*, vol. 85, Feb. 2009, pp. 21-32.
- [234] T. Niidome, M. Yamagata, Y. Okamoto, Y. Akiyama, H. Takahashi, T. Kawano, Y. Katayama, and Y. Niidome, “PEG-modified gold nanorods with a stealth character for in vivo applications,” *Journal of Controlled Release*, vol. 114, Sep. 2006, pp. 343-347.
- [235] R.G. Rayavarapu, W. Petersen, L. Hartsuiker, P. Chin, H. Janssen, F.W.B. van Leeuwen, C. Otto, S. Manohar, and T.G. van Leeuwen, “In vitro toxicity studies of polymer-coated gold nanorods,” *Nanotechnology*, vol. 21, 2010, p. 145101.
- [236] P. Theer, M.T. Hasan, and W. Denk, “Two-photon imaging to a depth of 1000 μm in living brains by use of a Ti:Al₂O₃ regenerative amplifier,” *Optics Letters*, vol. 28, Jun. 2003, pp. 1022-4.
- [237] H. Hong, J. Sun, and W. Cai, “Anatomical and molecular imaging of skin cancer,” *Clinical, cosmetic, and investigational dermatology*, vol. 1, 2008, pp. 1-17.
- [238] H. Wang, D.W. Brandl, F. Le, P. Nordlander, and N.J. Halas, “Nanorice: A Hybrid Plasmonic Nanostructure,” *Nano Letters*, vol. 6, Apr. 2006, pp. 827-832.
- [239] C.L. Nehl, H. Liao, and J.H. Hafner, “Optical Properties of Star-Shaped Gold Nanoparticles,” *Nano Letters*, vol. 6, Apr. 2006, pp. 683-688.
- [240] B. Ghosn, A.L. van de Ven, J. Tam, A. Gillenwater, K.V. Sokolov, R. Richards-Kortum, and K. Roy, “Efficient mucosal delivery of optical contrast agents using imidazole-modified chitosan,” *Journal of Biomedical Optics*, vol. 15, Jan. 2010, pp. 015003-11.
- [241] S. Link, C. Burda, M.B. Mohamed, B. Nikoobakht, and M.A. El-Sayed, “Laser Photothermal Melting and Fragmentation of Gold Nanorods: Energy and Laser Pulse-Width Dependence,” *The Journal of Physical Chemistry A*, vol. 103, Mar.

1999, pp. 1165-1170.

- [242] S. Link, C. Burda, B. Nikoobakht, and M.A. El-Sayed, "Laser-induced shape changes of colloidal gold nanorods using Femtosecond and Nanosecond Laser Pulses," *Journal of Physical Chemistry B*, vol. 104, 2000, pp. 6152-6163.
- [243] O. Ekici, R. Harrison, N. Durr, D. Eversole, M. Lee, and A. Ben-Yakar, "Thermal analysis of gold nanorods heated with femtosecond laser pulses," *Journal of Physics D: Applied Physics*, vol. 41, Sep. 2008.

Vita

Nicholas James Durr was born in McMinnville, Oregon on March 22, 1981, the son of Joseph and Lynn Durr. He graduated from McKinleyville High School in 1999. He graduated in May 2003 from the University of California, Berkeley with a degree in Electrical Engineering and Computer Science. He was introduced to the field of biomedical optics while employed as a research engineer in the advanced technology development department at Nellcor from 2003 to 2004. In August 2004, he left Nellcor to enter the Graduate School of The University of Texas at Austin as an NSF Integrative Research and Training Fellow. He received a Master of Science in Biomedical Engineering in the Fall of 2007.

Permanent address: 4209 Burnet Rd, Apt #209, Austin, TX, 78756

This dissertation was typed by the author